Title
Microfluidic Homogeneous Mobility Shift Assays at the Bench and the Bedside

Author
Karns, Kelly Melia

Publication Date
2013

Peer reviewed|Thesis/dissertation

Microfluidic Homogeneous Mobility Shift Assays at the Bench and the Bedside

by

Kelly Melia Karns

A dissertation submitted in partial satisfaction of the

requirements for the degree of

Joint Doctor of Philosophy

with University of California, San Francisco

in

Bioengineering

in the

Graduate Division

of the

University of California, Berkeley

Committee in Charge:

Professor Amy E. Herr, Chair

Professor Shuvo Roy

Professor Albert P. Pisano

Spring 2013

Microfluidic Homogeneous Mobility Shift Assays

at the Bench and Bedside

Abstract

Microfluidic Homogeneous Mobility Shift Assays

at the Bench and Bedside

by

Kelly Melia Karns

Doctor of Philosophy in Bioengineering

University of California, Berkeley

Professor Amy E. Herr, Chair

Binding interactions underpin all biological processes. As a result, understanding binding interactions has implications in the development of novel diagnostics as well as advancing our understanding of biological processes and the molecular mechanisms of human disease.

Electrophoresis is a widely used chemical separation technique that is used to study molecular binding interactions. In this technique, molecules are separated based on differences in their electrophoretic mobilities. By harnessing the molecular binding interactions that are prevalent throughout biology and medicine, electrophoretic mobility shift assays rely on the evolutionarily-derived binding affinity and specificity of biomolecules to induce a change in electrophoretic mobility between molecular populations. These assays use a molecular probe that binds with a target molecule, causing a change in weight or size, shape, and/or charge that leads to a detectable change in electrophoretic mobility.

Electrophoretic mobility shift assays benefit from operation on the microscale. Microfluidic assays have emerged as powerful tools that can be used to study and detect binding interactions between many of the major classes of biological macromolecules. Performing electrophoresis on the microscale enables the application of higher electric fields which in turn speeds up separations and enables increased resolution of analyte fractions.

This dissertation reports the development of microfluidic electrophoretic mobility shift assays and their application to relevant research questions affecting both clinical medicine and basic research. The unifying theme of the assays presented here is the use of induced mobility differences in order to probe for the functionality of a target biomolecule of interest. All the applications presented here take advantage of a specific benefit imparted by adapting electrophoresis to the microscale including the small sample volume requirements which are appropriate for analysis of volume-limited tear fluid from dry eye patients and the enhanced mobility resolution enabled by lower diffusion timescales as is appropriate for detecting the small conformational changes of functional riboswitch aptamers.

In this work, I first demonstrate and characterize a first-in-kind microfluidic homogeneous immunoassay that is able to probe for protein biomarkers in human tear fluid. This format capitalizes on the binding affinity and specificity of antibodies to impart a mobility shift between the bound and unbound forms of a target protein biomarker. I optimize the assay conditions including gel pore-size and pH to minimize the nonspecific binding interactions that complicate measurement of tear proteins. As a result, I demonstrate detection of tear protein biomarkers with a specificity and speed that outperforms conventional tools such as ELISA or slab gel electrophoresis. With the target-user and the applicability of the assay to the broader community in mind, gaps in the literature that are relevant to translation of the assay presented here are also considered including the impact of upstream biospecimen sample processing on the assay read-out and the integration of additional ophthalmological tests for dry eye severity assessment into a single device. This work has the potential to revolutionize our understanding of ocular disease pathology, enable non-invasive diagnosis of systemic disease (where biomarkers are available) using tears, and may be used to stratify Sjögren's syndrome patients from those with other forms of dry eye. Taken in sum, this work has broad implications in the proteomic analysis of tear fluid and can be used in the advancement of both basic science and clinical medicine.

Secondly, I demonstrate and characterize a first-in-kind microfluidic mobility shift assay for riboswitch screening applications. Riboswitches are RNA sequences that undergo a conformational change in response to binding by a regulatory small molecule ligand, resulting in modulation of gene expression. I optimize assay conditions in order to demonstrate the ability to utilize a ligand binding-induced conformational change to impart a mobility shift to the bound and unbound riboswitch populations. As a result, I utilize the assay to screen five never-before characterized riboswitch candidates for functionality. I also demonstrate the ability to utilize the fine mobility resolution of microfluidic formats to be able to study the binding affinity of both fast and slow interconverting riboswitch pairs.

In sum, this work makes important contributions toward creating robust analytical tools capable of probing the binding interactions that underpin all of biology. By harnessing the speed, resolution, and portability of electrophoresis on the microscale, this work has the potential to enable these powerful analytical techniques to increasingly be used both at the bench and the bedside.

Acknowledgements

I am so grateful for the tremendous amount of mentorship and support I have received over these four and a half challenging years of graduate school. I entered with the determination to deepen my technical skills and the desire to earn a title that I could then take with me into my career. However, I am leaving with much more. I now possess a deeper appreciation for the many wonderful and exciting technologies that are being developed in biology and medicine, an ability to sit down and think through complicated problems, and a network of extremely talented scientists, engineers, and friends. Thank you to everyone who has helped to make that possible.

First and foremost, I would like to thank my PhD adviser, Dr. Amy E. Herr. The first day that I sat down in Amy's office, she asked me to build a photo-multiplier tube (PMT) for the lab's microscope. Being an eager first year, I willingly agreed to do it, only to realize once I left her office that I had no idea what a PMT was. But, after much 'googling,' reading, and mentorship from Amy, we ended up with a functional dual-color PMT. Amy, thank you for taking me into your nascent laboratory as a young and inexperienced scientist. Your dedication to each and every graduate student in your laboratory is unparalleled. You always showed a respect for my time and talents that made me feel like a valued member of the laboratory. Our weekly research updates and meetings and the countless practice talks and manuscript drafts required a lot of your valuable (and limited) time but were critical in deepening my ability and comfort with technical communication and experimental design. You taught me how to write, how to communicate effectively and concisely, and just how far hard work and attention to detail can get you. Further, your willingness to acknowledge and help to correct weaknesses in those around you make everyone around you better, despite being the more difficult route. A wise graduate student in our lab once said that "working with Amy is like going running with someone who is more in shape than you are. It's really hard during the run, but afterwards you come out so much stronger than you were before." Amy, thank you for your time, your talents, your energy, your support, your mentoring, and your friendship.

I would also like to thank those people who helped shape my path to graduate school. Uncle Dennis and Auntie Jeri, thank you for introducing me to engineering and for being the first people to tell me that engineers don't just drive trains and wear cool hats. Thank you to the Engineering Department at Yale University for exposing me to research and helping to convince me that a PhD would be a worthwhile investment in my career. I would especially like to thank my research advisers and mentors at Yale including Dr. Mitchell Smooke, Dr. Mark Saltzman, Dr. Jacek Cholewicki, Dr. Hur Koser, and Dr. Eric Stern. Finally, I would like to acknowledge Dr. Gregory Jordan for making a PhD seem like a perfectly reasonable thing to do.

I have been honored to have made many remarkable friends here at Berkeley. I trust that you all know how much I value your friendship and how much I have treasured our adventures together. Here, I would like to just extend a special thank you to Tenzing Joshi, for always being there to catch me when I fell and for always being ready with a hug, glass of wine, and a supportive ear when things weren't going well or even when they were. Thank you also to

Lowry Kirkby and Maria Daderlat for all of our girls nights out and quiet nights in. You two possess a rare combination of scientific brilliance, humility, sincerity, and a sense of adventure.

I would also like to thank Bob Calonico and the many talented musicians of the UC Berkeley Wind Ensemble. There were many weeks when going to band was the only thing I could look forward to. Plato was right when he said that "music gives a soul to the universe, wings to the mind, flight to the imagination, and life to everything." Thank you for giving me the gift of music to keep my spirits up, for giving me a family and a group to belong to on campus, and for providing a safe haven away from the stresses of lab. Bob, you bring a smile and a carefree laugh to every day and I appreciate all of your support both personally and professionally. I could not have done this without you all and the beautiful music we shared.

Thank you to all the past and present members of the Herr Laboratory especially Dr. Akwasi Apori, Sam Tia, Monica Kapil, Dr. Chenlu Hou, and Dr. Mei He. Thank you for the valuable feedback in my many practice talks and for your help in preparing for my qualifying examination. I am certain that I learned more from you than you learned from me. I would especially like to thank Dr. Chenlu Hou for training me in the lab and for providing the foundation for the device on which the majority of my work is based. Thank you also to Sasha Denisin for your unwavering enthusiasm for research. It was a pleasure having the opportunity to help you grow into the budding scientist that you are now. Walt Disney once said, "if you can dream it, you can do it." I can't wait to see what you all are going to do. I am confident that it, and you, will be great. Finally, I am so grateful to have had to the pleasure to join such a friendly and social department. Thank you to my fellow BioE graduate students for all the laughs and fun adventures.

Thank you to my collaborators including Dr. Nancy McNamara for providing samples, for the helpful discussions, and for exposing me to ophthalmologists and clinicians who could lend unique insight on the validity, need, and demand for our work. Thank you also to Dr. Ming Hammond and the members of the Hammond laboratory especially Qian Qin, Jacob Vogan, and Scott Hickey for helpful discourse and for teaching me more about riboswitches and gene regulation.

Thank you to my thesis committee, Dr. Shuvo Roy and Dr. Albert Pisano, for all of your encouragement and time spent reading my thesis. Thank you to my academic advisor, Dr. Song Li, for the privilege of rotating in your lab and for taking an active interest in my success. Thank you also to Rebecca Pauling and the staff members in the Bioengineering office for all of your help in navigating the complicated bureaucracy of getting a PhD. You always seemed to answer my questions with a smile. Thank you to my funding sources including the National Science Foundation Graduate Research Fellowship and a Defense Advanced Research Projects Agency (DARPA) Young Faculty Award.

Most importantly, I would like to thank my family. Thank you to my sister, Lori, and cousins, Heather and Andrea. You have shown me all the many and diverse adventures that are possible in ones career and inspired me to seek them in my own. Thank you to the entire

Gardner/Hrinya family for welcoming me unconditionally into their family and supporting me throughout this process. I am deeply grateful to my fiancé, John, who constantly amazes and inspires me. John, thank you for the hours you spent listening and supporting me. You always knew the difference between when I needed help solving a problem and when I just needed someone to talk to. Thank you for all the coffee shops you've patiently sat in with me while I worked and for understanding when I needed to work weekends. It is no wonder that others are now seeking your advice on how to be a supportive partner through a PhD. This accomplishment and milestone is something we did together and I look forward to all the challenges and adventures we will face together in the future. Finally, I would like to acknowledge my deep gratitude for my parents who set an outstanding example for the last 28 years. You gave me a world-class education, put me in challenging situations, raised me to believe that I could do anything I put my mind and effort toward, and showed me what hard work can get you. I am profoundly sad that Dad won't be able to read my final dissertation, but I know he would be so proud. He was thrilled and excited to see the world's first 'Dr. Karns.' Mom and Dad, you prepared and pushed me to become Dr. Karns. This thesis is dedicated to you both.

To My Parents

Table of Contents

Table of Figures

List of Tables

List of Common Acronyms

SS: Sjögren's syndrome
KCS: Keratoconjunctivitis sicca (dry eye)
Lf: Lactoferrin
pI: Isoelectric point
µMSA: Microfluidic mobility shift assay

Chapter 1: Binding Interactions Form the Core of All Biological Processes

1.1 Binding Interactions Enable Molecular Tagging and Trigger Molecular Signaling Pathways

Molecular binding interactions mediate virtually every process in biology. Complimentary binding sites on two different molecules can allow for specific molecular identification and tagging as in the case of antibodies and their protein targets. Proteins that are found on cell surfaces or circulating throughout the body are recognized and bound by their corresponding antibody, enabling diverse processes ranging from activation of an immune response to a foreign pathogen to facilitating the identification and clearance of toxins in the blood. Molecular binding interactions can also act to trigger a series of subsequent events as in the case of certain sequences of RNA strands called riboswitches and their small molecule ligands. Riboswitches that are bound by their corresponding ligand undergo a conformational change that induces regulation of gene transcription. As a result, binding interactions of all forms are be harnessed by researchers to enable targeted detection of molecules and to trigger complicated molecular signaling pathways.

Within the cytosol of all cells are thousands of molecules ranging from small, organic molecules to large macromolecules which are the central actors and metabolites in the pathways that mediate all cellular functions. These molecules interact with each other in numerous and diverse ways. As a result, when exploring the molecular mechanisms of any biological process, biochemists almost inevitably study one or more binding interactions between biological macromolecules.

Proteins are one class of biomolecules that engage in varied binding interactions throughout biology. Proteins are the most abundant biological macromolecules and exhibit an almost endless diversity of functions.[1] All proteins are created from the same 20 amino acids; yet from these basic building blocks, cells can produce diverse products such as enzymes, hormones, antibodies, transporters, muscle fiber, hair, optical lenses in the eye, feathers, mushroom poisons, and myriad other objects with unique and distinct biological functions.[1]

Understanding the intramolecular binding interactions that led to protein folding and structure is important in order to understand and mitigate many common diseases. The three dimensional structure of a protein influences its functionality by exposing some regions to the environment, while sequestering other (typically nonpolar) regions in the interior of the protein. This protein folding relies on all types of binding interactions including hydrogen bonds, hydrophobic interactions, and van der Waals forces. Defects in protein folding form the molecular basis for a large number of human genetic disorders including type 2 diabetes, Alzheimer's disease, Huntington's disease, and Parkinson's disease.[1] These diseases typically

arise because of the accumulation of insoluble extracellular amyloid loidoses, which are soluble proteins that are secreted from cells in a misfolded state that renders them insoluble.[1] Cystic fibrosis is another disease caused by folding defects in a membrane-bound protein called cystic fibrosis transmembrane conductance regulator (CFTR), which serves to allow chloride ions to pass through the cell membrane. If one of a few mutations occurs in CFTR, it will fold improperly, leading to protein degradation and a loss of function.[1]

Protein-ligand binding interactions are also prevalent throughout all biological processes. The function of many proteins is largely influenced by reversible binding with molecules from the environment. The transient nature of protein-ligand binding allows a cell to respond to changing environmental conditions and metabolic needs. Typically, protein-ligand interactions are also specific since a ligand binding site on a protein is complementary to the ligand in size, shape, charge, and hydrophobic or hydrophilic properties.[1]

Understanding the relationship between proteins and their specific ligands has implications in diverse fields including immunology, oxygen transport, and locomotion. For example, hemoglobin is a protein that specifically recognizes and binds oxygen. Hemoglobin is found in almost all mammals and plays an essential role in transporting oxygen in the blood stream to distal tissues. The immune system also relies on the reversible binding of proteins and ligands in order to distinguish molecular 'self' from 'non-self.' For example, immunoglobulins bind bacteria, viruses, or other large molecules that are identified as being foreign and target them for destruction by the host cells.[1] Recognition of infected cells also involves protein T-cell receptors found on the surface of cytotoxic T cells that recognize and bind extracellular ligands and trigger changes within the cell.[1] The interactions between motor proteins such as myosin and actin are also critical to enabling locomotion and muscle contraction. These interactions rely on complementary arrangements of ionic, hydrogen bonding, hydrophobic, and van der Waals interactions at protein binding sites.

Enzymes are a class of proteins that catalyze virtually all cellular reactions. In enzyme reactions, a substrate is bound in the active site of the enzyme and acted upon by the enzyme. Enzymes are highly varied and specialized and understanding their function can advance our understanding of reactions for nutrient degradation, the conservation and transformation of chemical energy, and the synthesis of biological macromolecules from their precursor molecules.[1] Enzymes also play a large role in the regulation of metabolic pathways in cells, which often rely on reversible binding of a specific modulator molecule. Many inheritable genetic diseases are due to a deficiency or lack of one or more enzymes, warranting their study. Meanwhile, other diseases are caused by the over-activity of an enzyme. In addition, because of the ability of an enzyme to facilitate the conversion of a substance into another form, many drugs act through interactions with enzymes or act to inhibit the enzymes themselves. For example, penicillin interferes with the synthesis of peptidoglycan, a major component of the rigid cell wall found in many bacteria which shields the bacteria from osmotic lysis. In the presence of penicillin, synthesis of the bacterial cell wall is disrupted, causing bacterial death when the inner membrane bursts under osmotic pressure.[1]

Lectins are a class of proteins that specifically bind carbohydrates with high affinity. Lectin-carbohydrate binding interactions influence cell-cell recognition, signaling, and adhesion reactions.[1] For example, luteinizing hormone and thyrotropin circulating in the blood are recognized by a lectin receptor of hepatocytes, which mediates their uptake and destruction, and lowers their concentration in the blood. This explains the periodic rise and fall of these hormonal levels in the blood.[1] Selectins are a family of plasma lectins that mediate cell-cell recognition and adhesion. Human selectins influence the inflammatory response involved in autoimmune diseases such as rheumatoid arthritis, asthma, psoriasis, and multiple sclerosis.[1] As a result, there is a great deal of interest in developing drugs that inhibit selectin-mediated cellular processes. Finally, restriction endonucleases, or restriction enzymes, recognize and cleave DNA strands at specific sequence locations (restriction sites). These enzymes rely on transient binding interactions to function and have played a central role in DNA cloning and recombinant DNA technology.

DNA and RNA molecules also participate in a wide variety of binding interactions. Intra-molecular binding interactions are critical in defining Watson-Crick base pairing which impart the unique three-dimensional structure of DNA and RNA molecules. Further, proteins bind to DNA for a variety of functions and protein-DNA interactions are critical in DNA replication and transcription. These and other protein factors also play a large role in regulating RNA translation into proteins. Small molecule metabolites in cells have also been shown to bind RNA to influence gene regulation. These RNA sequences are called riboswitches.[2] Synthetic DNA strands have been designed to pair with specific sequences on DNA strands in order to form triplex DNA or other secondary structures such as hairpins or cruciforms that can disrupt gene expression.

Lipids are another major class of biomolecules that engage in numerous diverse binding interactions. A unifying feature of lipids is that they are insoluble in water and many are found in fats and oils, which are the principal stored forms of energy in many organisms.[1] In addition, biological membranes are created by a double layer of lipids which blocks the passage of polar molecules and ions into the cell. One example of a lipid-binding interaction involves steroid hormones, or oxidized derivatives of sterols (a class of membrane lipids), which circulate in the blood stream on protein carriers. When they enter cells, steroid hormones such as male and female sex hormones bind to highly specific receptor proteins on the nucleus of some cells and trigger changes in gene expression and metabolism.[1] Because of their extremely high affinity for their receptors, these hormones can produce cellular responses even when present in very low concentrations.

G protein-coupled receptors (GPCRs) and second messengers are another major class of biological molecules whose function is tightly coupled to binding. Cellular membranes contain many proteins that are specialized in promoting or catalyzing various cellular processes.[1] For example, transporter proteins move organic and inorganic ions across the membrane, receptors such as GPCRs sense extracellular signals and trigger reactions within the cell, and adhesion proteins hold neighboring cells together. The human genome contains approximately 350 GPCRs for detecting hormones, growth factors, and other endogenous ligands in the cell.

Approximately 500 additional GPCRs are known that play a role as olfactory or gustatory receptors.[1] GPCRs have been implicated in many diseases such as allergies, depression, blindness, diabetes, and various cardiovascular illnesses.[1] Further, almost half of all drugs on the market target GPCRs. For example, "beta blockers," which are commonly prescribed for illnesses ranging from hypertension to cardiac arrhythmia and glaucoma, target the β-adrenergic receptor which mediates the effects of epinephrine.[1]

It is clear that binding interactions form the core of all biological processes, making them fundamental to life. Understanding their tremendous diversity is of central importance in advancing our knowledge of the molecular mechanisms of many diseases and will undoubtedly enable the development of new, more effective drug classes, improve our awareness of the early signs of some diseases, and lead to novel medical products to improve human health.

1.2 Theory and Types of Binding Reactions in Biology

Binding between two molecules can be described by the equation:

$$A + B \underset{K_{off}}{\overset{K_{on}}{\Longleftrightarrow}} AB$$

In this equation, the top arrow represents the molecules binding with a rate constant of K_{on} (units of $M^{-1}s^{-1}$) while the bottom arrow represents the molecules dissociating with a rate constant of K_{off} (units of s^{-1}). The dissociation constant (K_d) is therefore equal to:

$$K_d = \frac{k_{off}}{k_{on}}$$

Throughout this dissertation, we presume that the reaction is at equilibrium and there are no changes to the net concentrations of A, B and AB.[3]

Looking more closely at K_d, we can see that an interaction with a low K_d (high affinity) will likely have a large K_{on} and a small K_{off}. In other words, A ad B will associate rapidly and then the AB complex will dissociate slowly. Likewise, an interaction with a high K_d (low affinity) will likely have a small K_{on} and a large K_{off}, or A and B will associate slowly and the AB complex will dissociate rapidly.[3]

There are several types of binding interactions that occur throughout biology. Covalent bonds are prevalent; yet weak hydrogen bonds, hydrophobic interactions and van der Waals forces, when acting in concert, can also have a significant influence on the structure as well as the interactions of these molecules. Covalent bonds involve the sharing of pairs of electrons between atoms and therefore are very strong. Hydrogen bonds are weak and involve the attractive interaction between a hydrogen atom and an electronegative atom such as nitrogen (N), oxygen (O) or fluorine (F). Hydrophobic interactions occur due to the tendency of nonpolar substances to aggregate in aqueous solution. Hydrophilic interactions occur since polar

biomolecules will dissolve readily in water because of their ability to replace water-water interactions with energetically favorable water-solute interactions.[1] Van der Waals interactions are also weak interatomic attractions that occur when two uncharged atoms are brought close enough together for their electron clouds to induce transient electric dipoles which weakly attract one another.

Weak interactions significantly influence macromolecular structure and function. They are constantly forming and breaking. As such, the dissociation of two biomolecules that are bound noncovalently by a combination of several weak interactions requires that all the weak binding interactions must be disrupted at the same time. Because of the random nature of these dissociation events, this is very unlikely. As a result, both covalent and weak binding interactions occur throughout biology and are important for understanding the biological relevance of the molecular binding event.

1.3 Motivation for Studying Biological Binding Interactions

In addition to the importance of understanding biological binding interactions in order to gain insight into the molecular mechanisms of many diseases, there are many practical applications made possible by harnessing the power of biological binding interactions. Many different types of sensors have been developed which take advantage of the astonishing specificity of biological affinity molecules. For example, enzyme-linked immunoassays (ELISAs) utilize surface immobilized antibodies to specifically detect low levels of a target protein in a complex solution. Within this same application, enzyme reactions are harnessed to continually convert a clear substrate into a fluorescent signal for amplified, high sensitivity analyte detection. In addition, understanding the impact of a binding event within a biological system or pathway and characterizing the binding affinity of that particular biological binding interaction can clarify the role of a particular molecule in genetic regulation or cellular metabolism. This can potentially expand the number and scope of drug targets and drug-able compounds.

Chapter 2: Electrophoretic Assays to Study Biomolecular Interactions

2.1 What is Electrophoresis?

Electrophoresis is a widely used chemical separation technique that is used to separate species that have different electrophoretic mobilities. In this technique, a charged particle moves under the application of an applied electric field which creates a force on the particle equal to qE, where q is particle charge and E is the strength of the applied electric field. As the particle moves in the direction of the electric field, it is also subject to a Stokes drag force equal to $6\pi\eta rU$, where η is the viscosity of the separation medium, r is the hydrodynamic radius of the particle, and U is the particle migration velocity (Figure 1).

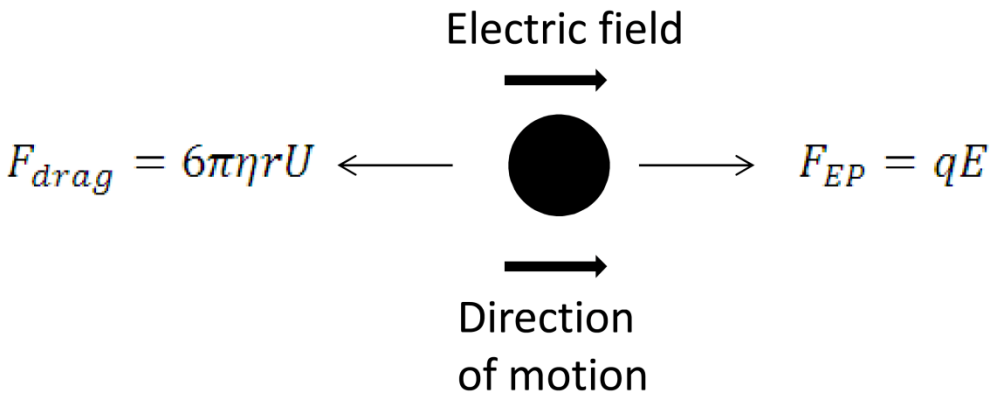

Figure 1. Electrophoretic mobility is a result of a balance of electrophoretic and drag forces on a particle in an applied electric field.

Balancing the forces on the force-body diagram therefore yields the equation

$$F_{drag} = F_{EP} = 6\pi\eta rU = qE$$

or

$$U = \frac{qE}{6\pi\eta r}$$

Since the mobility (μ) of a particle is defined as $\mu = U / E$, we can derive the equation for the electrophoretic mobility of a particle:

$$\mu = \frac{q}{6\pi\eta r}$$

Electrophoretic mobility is therefore dependent on the charge (q) to size (r) ratio of the particle and electrophoresis can be used to separate particles that differ in their charge, radius, or the ratio of the two.

Particle charge can be made uniform by using a charged surfactant, such as the ubiquitous sodium dodecyl sulfate (SDS) which imparts a negative surface charge to all particles in the system, in order to separate particles based on radius alone. Further, due to the fact that frequently, a direct relationship exists between radius (r) and other properties such as molecular weight or size, electrophoresis can also be used in many cases to separate particles that differ in weight or size.

Because of the mobility dependence on the η, the viscosity of the separation medium, a high viscosity sieving matrix is often introduced which serves to slow down particle mobility, suppress electroosmotic flow, and impart finer electrokinetic control. Polymer gels such as polyacrylamide or agarose are commonly used as the sieving matrix owing to their inert properties and robustness. In the case of polyacrylamide gels, used throughout the work presented here, the viscosity is related to the pore-size of the polymer network and the total acrylamide concentration (T). Therefore, the particle mobility is related to the total acrylamide concentration according to the equation

$$\mu = \mu_0 10^{-k_r T}$$

where k_r is the retardation coefficient of the particle in the matrix, and μ_0 is the particle mobility in free solution. Experimentally, electrophoresis has been implemented in slab gel as well as capillary and microchip formats.[4-6]

2.2 Electrophoretic Mobility Shift Assays

Electrophoretic mobility shift assays rely on the evolutionarily-derived binding affinity and specificity of biomolecules to impart a change in electrophoretic mobility between populations. As a result, mobility shift assays are able to separate populations based on differences in charge, charge to mass ratio, mass or radius of gyration.

For example, homogeneous electrophoretic immunoassays are electrophoretic mobility shift assays which rely on a binding-induced molecular weight difference that leads to an electrophoretic mobility shift between bound and unbound populations. In this case, an antibody with molecular weight of ~150 kDa will be used to probe for a target protein. Upon binding, the antibody will contribute ~150 kDa to the protein and the resultant immune complex will migrate at a much slower mobility owing to the added weight and radius.

Electrophoretic mobility shift assays can also be used to measure a binding-induced conformational change of a molecule if the conformation change affects the effective radius of the molecule (r) which leads to an electrophoretic mobility shift between bound and unbound

populations. In the case of riboswitch RNA aptamers, when a ligand binds, a conformational change is induced in the aptamer molecule, conferring a more compact structure and smaller molecular radius. Therefore, the bound aptamer molecule will migrate at a faster electrophoretic mobility owing to the smaller radius and diminished drag force.

2.3 Benefits of Performing Electrophoresis on the Micro Scale

There are numerous benefits gained by performing electrophoresis at the microscale. The low sample volume requirements (nL) enable analysis of volume-limited samples such as tear fluid or stem cell lysate. This characteristic was critical to the novel tear assay presented in Chapters 3-7. Further, the high surface to volume ratio enables enhanced heat dissipation and the application of higher electric fields, which results in rapid species resolution (seconds). Rapid assay times reduce time-based diffusive dispersion and enable enhanced resolution of small differences in species mobility, enabling the discrimination of smaller mobility shifts such as those caused by small differences in the effective particle radius. The scaling involved in this enhanced mobility resolution is presented in Chapter 9.4. These high speed assays can also be utilized in high throughput screening assays where samples are run serially. Further, the small footprint of the device and channels enables a higher device density in a given surface area, enabling parallelization of assays for high throughput screening. The enhanced mobility resolution and high throughput capabilities were critical to the successful development of a riboswitch screening mobility shift assay presented in Chapters 8-10. The small device footprint also eases the translation of electrophoretic devices into point-of-care settings such as the clinic or other research laboratories. Finally, the automation and control of assay steps afforded by automated electrokinetic particle movement is amendable to the incorporation of multiple assay steps on one device, as is necessary for multiplexing to integrate many clinically relevant measurements in one device.

2.4 Microfluidic Electrophoretic Mobility Shift Assays

Affinity-based assays have been implemented in microfluidic formats since the late 90s. Microfluidic electrophoretic affinity assays can be either homogeneous or heterogeneous in format. In both homogeneous and heterogeneous affinity assay formats, affinity reagents (e.g., antibodies, lectins, aptamers, enzymes) are selected *a priori* to be highly specific for the target analyte(s) of interest. In heterogeneous formats, the affinity reagent is then immobilized on a solid substrate within the assay (e.g., plate, channel or bead surface) typically through a covalent binding interaction. When the sample, which contains the target analyte, interacts with the immobilized affinity reagent, the target is specifically captured. After washing away unbound analytes in solution, the bound analytes can be detected through a variety of detection techniques (e.g., fluorescence, electrochemical, colorimetric).

In contrast, homogeneous affinity based assays do not require immobilization of the affinity reagent and instead rely on a mobility shift to detect the analyte of interest. In this format, the target is allowed to bind to the affinity reagent in free solution and a mobility shift is induced. Separation of the bound complex and unbound affinity reagent then allows for specific

detection of the analyte. When an antibody is used as the affinity reagent to form an immune complex, this assay is called a homogeneous immunoassay. When an RNA aptamer binds to a ligand and bound and unbound forms are separated, this assay is called an RNA mobility shift assay.

Microfluidic affinity-based homogeneous formats offer several advantages over heterogeneous formats. Microfluidic homogeneous assays combine the high-efficiency separation power of microfluidic electrophoresis with the specificity and selectivity of immunoaffinity reactions in a reusable platform. Homogeneous microfluidic affinity assays also have the ability to improve assay specificity compared to heterogeneous formats, which is critical for precise biomarker quantification within the complexity of biological matrices. The specificity of any immunoaffinity-based assay is dependent on the quality of the selected affinity probe, yet specificity typically decreases when analysis is conducted in the presence of highly complex biological fluids such as plasma, saliva, or tears. Plasma in particular is thought to contain tens of thousands of proteins that span ten to twelve orders of magnitude in concentration[7] and can interact non-specifically with the affinity probe. Distinct from heterogeneous formats, microfluidic homogeneous affinity assays can access mobility information for the band of interest as well as affinity information, thus enabling the positive identification of the target of interest and offering an additional degree of specificity over conventional ELISA or other heterogeneous formats. This mobility-based identification can eliminate the confounding matrix effects that are common when analyzing complex biological fluids, thus enabling more specific target detection than is currently achievable with ELISAs.

Integration of homogeneous immunoassays on microfluidic chips has enabled highly sensitive and quantitative protein measurements, improvements in measurement specificity over conventional techniques, and unprecedented assay times (seconds) and reagent volume requirements (μL). From the earliest demonstrations of microfluidic homogeneous immunoassays, protein biomarkers have also been quantified with sufficient sensitivity to reach clinically relevant concentrations. Human plasma is one of the most attractive biological fluids for protein biomarker detection as it is thought to comprise a circulating representation of the full human proteome and is composed of markers from all body tissues and both pathological and normal conditions.[7] The majority of disease-specific protein biomarkers in plasma are thought to be in the nanogram per milliliter concentration range. In one of the first demonstrated microfluidic homogeneous immunoassays, Chiem and Harrison,[8] developed a laser-induced fluorescence (LIF)-based competitive microfluidic homogeneous immunoassay capable of quantifying theophylline, a therapeutic drug used for asthma, in human serum with a 1.25 ng/mL detection limit. Kawabata and co-workers subsequently reported on a direct homogeneous immunoassay for α-fetoprotein (AFP) which utilized DNA-coupled antibody probes and LIF detection to achieve a 21 ng/mL detection limit and linear concentration range up to 1.4 mg/mL.[9] Utilizing electrochemical detection to extend assay sensitivity, Wang, et. al. also demonstrated integration of sample incubation, injection, separation, post-separation enzyme reaction, and amperometric detection on-chip, and achieved a lower limit of detection of 0.256 fg/mL for mouse IgG.[10]

Multiplexing of protein biomarker targets has also been demonstrated in microfluidic homogeneous immunoassay formats. Microfluidic homogeneous immunoassays using different DNA-tagged antibody probes have been demonstrated for simultaneous detection of two distinct targets (AFP and prostate-specific antigen) in buffer.[9] Spectral multiplexing has also been used to detect two distinct targets (C-reactive protein and tumor necrosis factor-α) on-chip using homogeneous immunoassays.[11] Further, Phillips[12] demonstrated the use of heterogeneous immunoaffinity capture, subsequent release, and electrophoretic separation for homogeneous multiplexed detection of six cytokines in CSF. Using LIF-based detection, he achieved clinically relevant (pg/mL) detection limits.

However, the theoretical limitations of affinity-based assays prevent the further extension of these multiplexing approaches.[13] Immunoassays are limited in the number of multiplexed targets they can simultaneously detect owing to the inherent cross-reactivity of antibodies. In fact, antibodies found in healthy volunteers (excluding people with known autoimmune disorders) were found to react with roughly 28% of human proteins.[14] Therefore, given the orders of magnitude difference in protein concentration levels, even if abundant proteins have micromolar-level dissociation constants for the capture antibodies specific to the analyte of interest, a significant fraction the analytes captured from a complex fluid will be due to off-target effects owing only to equilibrium binding.[14] Further, microfluidic immunoassays tend to be highly sensitive to buffer conditions and significant assay optimization is often required to detect a single target of interest. As a result, simultaneous optimization of conditions for multiple analytes presents practical challenges and approximately forty distinct targets appears to be the limit of multiplexing in ELISA formats while maintaining acceptable specificity levels.[15] Additional advancements in multiplexing in microfluidic formats are needed in order to facilitate biomarker validation.

One way in which researchers have begun working around these limitations is by taking advantage of the re-usable, universal format, and rapid (sec) timescales of microfluidic homogeneous immunoassays. These characteristics make multiplexing achievable through the sequential analysis of different affinity probes in homogeneous formats. Using this approach, Koutny, et. al. demonstrated that 100 serum cortisol measurements could be performed on a sample within an hour using a competitive homogeneous immunoassay format.[16] In addition, Bromberg, et. al. used multiplexed channel networks to demonstrate simultaneous homogeneous immunoassay detection of TNT in 48 distinct samples in < 1 min.[17] However, further work in this area is warranted.

2.5 Thesis Organizational Overview

This dissertation reports the development of microfluidic electrophoretic mobility shift assays and their application to relevant research questions affecting both clinical medicine and basic research. The first part of my thesis work (Chapters 3-7) focuses on the development and application of efficient homogeneous immunoassays to detect protein biomarkers in human tear fluid. We capitalize on the binding affinity and specificity of antibodies to impart a mobility shift between the bound and unbound forms of our target protein, thus enabling

electrophoretic detection. We optimize separation conditions including gel pore-size and pH to minimize the nonspecific binding interactions that complicate measurement of tear proteins. As a result, we are able to detect tear protein biomarkers with a specificity and speed that outperforms conventional tools such as ELISA or slab gel electrophoresis.

The second part of my thesis work (Chapters 8-10) focuses on the development of microfluidic electrophoretic mobility shift assays for riboswitch screening applications. Riboswitches are RNA sequences that undergo a conformational change in response to binding by a regulatory small molecule ligand, resulting in modulation of gene expression. We optimized separation conditions in order to demonstrate the ability to utilize a ligand binding-induced conformational change to impart a mobility shift to the bound and unbound riboswitch populations. As a result, we were able to screen five putative riboswitches for functionality and demonstrated the ability to measure the binding kinetics that dictate the ligand-binding interaction.

The unifying theme of the assays presented here is the use of induced mobility differences in order to probe for functionality of a target biomolecule of interest. Further, all applications presented here take advantage of a specific benefit imparted by adapting electrophoresis to the microscale including the small sample volume requirements which are appropriate for analysis of volume-limited tear fluid from dry eye patients and the enhanced mobility resolution enabled by lower diffusion timescales as is appropriate for detecting the small conformational changes of functional riboswitch aptamers. With the target-user and the applicability of the assay to the broader community in mind, gaps in the literature that are relevant to translation of the assays presented here are also considered including the impact of upstream biospecimen sample processing on the assay read-out and the integration of additional ophthalmological tests for dry eye severity assessment into a single device.

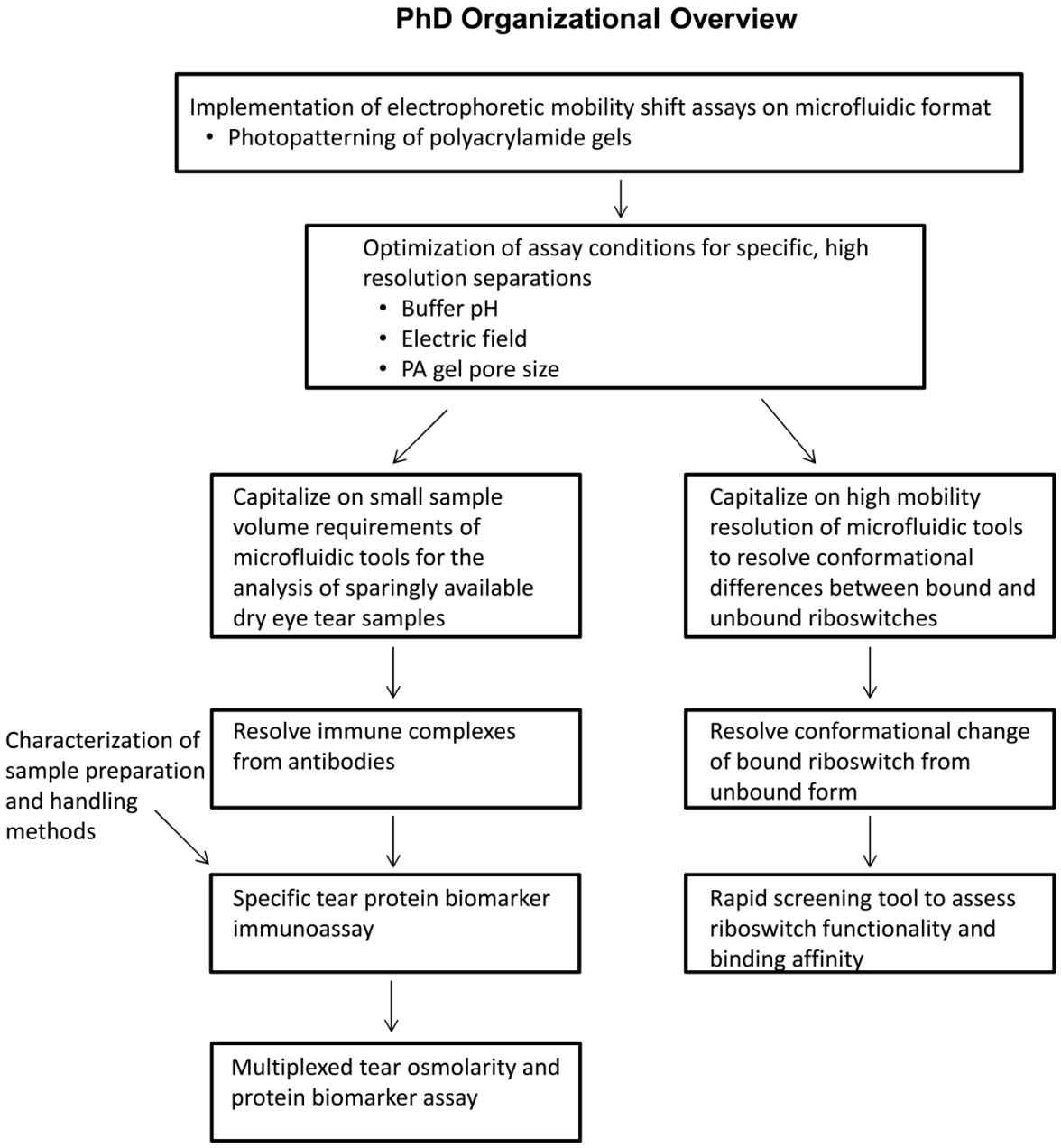

Figure 2. Techniques introduced in this dissertation are focused on the development and application of mobility shift assays on the micro-scale. The small volume requirements and high mobility resolution of microfluidic formats enable biomarker analysis of sparingly available tear fluid from dry eye patients and the resolution of small molecular conformation differences between bound and unbound functional riboswitch aptamers.

Chapter 3: Tear Fluid in Ophthalmologic Medicine

3.1 Tear Fluid

Much like blood or serum, human tear fluid is an information-rich biological fluid composed of an aqueous mixture of electrolytes (e.g. Na+, K+, Ca^{2+}, Mg^{2+}, Cl^-, HCO_3^-), low molecular-weight organic molecules (e.g. glucose, urea, hormones, amino acids and lipids) and both locally produced and serum-derived proteins.[18-23] The tear film covers the surface of the eye, providing lubrication, protection from disease and injury and nutrition for the cornea,[19,21,23] and is important for the undistorted passage of light into the eye.[20,23] The tear film is also important for keeping the optical surface distortion-free and removing foreign and cellular bodies from the surface of the eye.[21] It is composed of three layers: an inner mucin layer, a middle protein-rich aqueous layer and an outer lipid layer[19] (Figure 3). These layers contain proteins, lipids, and glycoproteins, which increase the wetting effect of the aqueous layer and act to slow down evaporation from the ocular surface.[21]

There are two primary types of tears including basal tears which are present on the ocular surface at all times, and reflex tears which are formed when the ocular surface is exposed to light, cold, foreign bodies, or irritants.[21] Other tear types have been reported including psychogenic tears, which arise in response to emotional stress, and fourth type of tearing that is induced when war gases are administered systemically, ultimately reaching the tear glands by way of the blood stream.[21] Normal tear volume is 5-10 µL and the secretion rate is about 1.2 µL per minute (decreasing with age) with an average renewal rate of 12-16%/min.[24,20,21]

The mean pH value of tear fluid is 7.6, but the pH becomes more alkaline the longer the eye remains open due to equilibration of the bicarbonate in the tear film fluid with the CO_2 in the atmosphere.[21] The bicarbonate buffering system is thought to contribute to buffering of tears, but all the buffering capacity mechanisms have not yet been determined.[21]

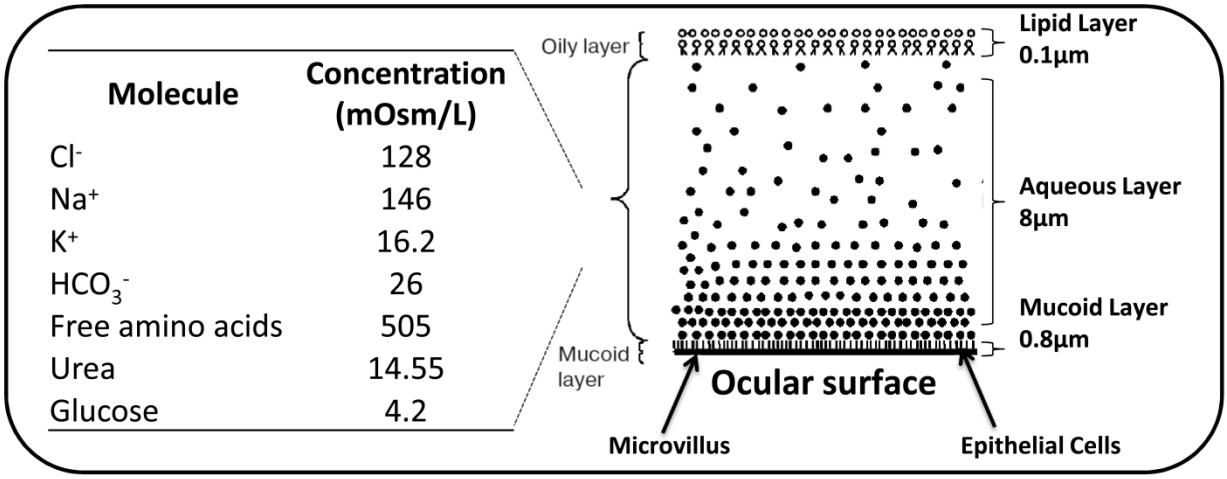

Figure 3. Trilaminar structure of the tear film on the ocular surface[25] and major tear components listed by concentration.[26,27] Tear diagram reprinted from R. Sariri & H. Ghafoori, Tear Proteins in Health, Disease, and Contact Lens Wear, *Biochemistry (Moscow), 2008,73(4) 381-392 with kind permission from Springer Science and Business Media.*

Tears are produced in the lacrimal and accessory lacrimal glands and flow onto the surface of the eye through the superior cul-de-sac.[21] A portion of the tear fluid remains on the eye during the blinking process of the eye lids and the remaining drains away through small holes in the eyelids called puncta and along small canals to a tear sac.[21] Normal tears contain 10% of the total protein concentration of plasma[21] and more than 400 proteins have been identified in human tear fluid through current analytical technologies.[20,28,29] The most abundant proteins in tears include lipophilin (7-8 kDa), lysozyme (14.2 kDa), lipocalin (previously called tear-specific prealbumin) (17 kDa), human serum albumin (65 kDa), lactoferrin (77 kDa), secretory IgA (150 kDa in its monomeric form). Tear proteins such as lactoferrin and epidermal grown factor (EGF) are produced and secreted by the lacrimal gland.[30] Other tear proteins and enzymes are produced and released from epithelial cells of the cornea and conjunctiva. In conditions where conjunctival vessels have increased permeability, proteins that originate in the plasma can also enter the tear fluid.[21] Basal and reflex tears have different proteomic compositions and are suggested to contain tear-specific proteins that are not detectable in blood, offering the potential for the use of novel tear-specific biomarkers to diagnose ocular and systemic disease.

Changes in the expression of tear proteins are associated with many systemic and ocular diseases.[20,21,30-33] For example, eotaxin-1 is implicated in seasonal ocular allergy; IL-1β in dry eye disease; IL-2 in atopic keratoconjunctivitis, a severe and potentially blinding form of eye allergy; lacryglobin in cancer; lactoferrin in Sjögrens syndrome, a systemic autoimmune disease; malate dehydrogenase and fibronectin in corneal epithelium injury; MMP-9 in keratoconus, or degeneration in the structure of the cornea; and Pro-MMP-3, Pro-MMP-9, and TIMP-1 in ocular rosacea[20].

Yet, the current understanding of the repertoire and function of tear film proteins and other tear biomolecules is limited.[34] A key roadblock in achieving a deeper understanding of tear film fluid molecules stems from limitations in analytical technologies.[33] Robust technologies capable of making quantitative measures of human tear biomolecule levels are of great interest in understanding ocular disease pathology, identifying and validating novel disease biomarkers and creating robust clinical diagnostic tests.

3.2 Tear Fluid in Ocular Diagnostics: Clinical and Research Tools

Blood and serum are routinely collected and analyzed in the medical clinic to diagnose disease, monitor treatment efficacy, and assess patient health. In fact, human plasma has been characterized as the most comprehensive human proteome – a circulating representation of all body tissues and of both physiological and pathological processes.[7] For example, glucose is routinely measured to assess the blood sugar levels of diabetic patients and their need for insulin. Further, blood proteins can be measured that indicate a wide variety of conditions including heart attack (e.g., creatine kinase), inflammation (e.g., C-reactive protein), or cancer (e.g., prostate-specific antigen).

In contrast, the biochemical make-up of tear fluid is rarely utilized in the ophthalmologist's office to inform diagnosis or treatment. Corneal pressure readings and slit-lamp microscopy are commonly used to visually inspect the anatomy of ocular structures in detail and to look for abnormalities in structure or morphology. Other ocular diagnostic techniques employ bulk measurements of tear volume, assess the health and cellular morphology of epithelial cells on the surface of the eye, and utilize symptomatic questionnaires to assess the severity of specific symptomatic complaints made by the patient. A summary of the most common diagnostic tests employed in the ophthalmology clinic is shown in Table 1 below.

Table 1. Summary of common ocular diagnostic tests used in the clinic for diseases including keratoconjunctivitis (KCS) and Sjogren's syndrome (SS).[30,35-38]

Name of Test	What is measured?	Description	Clinical relevance	Reference
Tear Volume Measurements				
Schirmer-I test	Reflex tear volume	Two Whatman 41 paper strips are placed in the inferior fornices and the extent of paper wetting is measured after 5 minutes	Decreased tear volume in KCS	Bjerrum, 2000; Lemp, 1992
Schirmer-II test	Reflex tear volume	Same as Schirmer-I but a stimulant is placed in the conjunctival sac or under the nostrils	Decreased tear volume in KCS	Bjerrum, 2000
Schirmer strip test (with anesthetic)	Basal tear volume	Same as Schirmer-I but a topical anesthetic is used to supress reflex tearing caused by the local irritation of the filter paper	Decreased tear volume in KCS	Bjerrum, 2000
Lacrimal scintigraphy	Basal tear turn-over	10 µL saline with 200 µCi technetium introduced in conjunctival sac and imaged with a gamma-camera oscilloscope display and the turn-over rate in the basal phase measured.	Pathological values indicate nasolacrimal duct occlusion or dry eye	Lemp, 1992
Assessment of Ocular Surface Cell Health				
Lissamine green staining	Epithelial cell damage and death on the ocular surface	Lissamine green stain specifically stains cells that are degenerated or dead. The stain is visualized with red light and stings less with introduction to the eye than Rose Bengal.	Positive staining indicates poor protection of the epithelial cells by the preocular tear film and KCS or SS.	Asbell, 2006
Rose Bengal staining	Loss of or insufficient protection by ocular surface mucin	Rose Bengal stain specifically stains cells that are degenerated or dead, mucous strands, and living corneal cells unless blocked by mucin and albumin in tears. Each eye is given a maximum score of 9 (intense staining). The stain is visualized with green light.	Positive staining indicates poor protection of the epithelial cells by the preocular tear film and KCS or SS.	Bjerrum, 2000; Farris, 1983; Asbell, 2006
Fluorescein staining	Identifies areas of the conjunctiva ad cornea where epithelia lack cellular and junctional integrity	Fluorescein dye is introduced into the eye on an impregnated strip & dye patterns are visualized using blue light	Staining indicates disruption of cellular junctions and increased membrane permability. Epithelial cell damage is associated with dry eye	Asbell, 2006
Tear Quality & Composition				
Lactoplate	Lactoferrin concentration	Lactoferrin is synthesized & secreted in the lacrimal gland. The Lactoplate test consists of two filter-discs, 4 mm in diameter, which are placed in the eye. After careful blotting of excess tear fluid, the discs are placed on a gel which contains anti-lactoferrin antibody. Afer three days, a ring-shaped immuno-precipitate has formed, the diameter of which corresponds to Lf concentration.	Lactoferrin may be a marker for lacrimal gland function. Decreased levels in KCS and SS patients. Sensitivity and specificity of Lactoplate test are low	Ohashi, 2003; Bjerrum, 2000
Crystallization	Tear crystalization	Tears dried on a glass slide produce fern-like crystals. Less crystallization is observed if tear quality is poor.	Low crystallization may indicate altered protein composition, osmolarity, etc.	Lemp, 1992
Tear osmolarity	Tear osmolarity	All forms of dry eye have increased osmolarity which causes epithelial damage. Clifton osmometry, vapor pressure osmometry, or the TearLab tear osmometer can also be used	Tear osmolarity increases in KCS	Asbell, 2006
Tear Meniscus Dilution Test	Tear meniscus quality	Using a mixture of 1% rose bengal and 1% fluorescein in the eye, the diltion after 5 min is measured in the interior tear meniscus.	Yellow color indicates normal meniscus, red or orange indicates KCS	Lemp, 1992
Tear film break-up time (BUT)	Time for tear film to rupture when eye is left open	If eyes are left open, the tear film will become unstable and rupture with dry spot formation over the cornea and conjunctiva. Fluorescein is introduced to the eye for visualization and the time to rupture is the tear film break-up time (BUT). BUT is typically longer than the time between blinks.	BUT decreases in KCS patients. A primary cause is a defective mucus layer.	Bjerrum, 2000; Lemp, 1992

Name of Test	What is measured?	Description	Clinical relevance	Reference
Mucus Tests				
Alcian blue staining	Stains mucus	10 µL is instilled in the eye and staining of mucous coatings on the epithelium are shown.	In KCS, pronounced staining is observed	Lemp, 1992
Staining with mixture of tetrazolium & alcian blue	Differentiates between mucus and neutrophilic leukocytes	Red color indicates many live, but affected epithelial cells.	In KCS, pronounced blue and red staining	Lemp, 1992
Lipid Tests				
Tear film interference	Lipid layer thickness	Interference pattern of lipid layer is measured with a slit lamp	Increased thickness in KCS and SS patients. May indicate decrease in lipid layer drainage or increase in Meibomian gland secretion	Bjerrum, 2000; Lemp, 1992
Symptom Assessment				
Patient symptom questionnaire	Subjective scoring of patient symptoms	Several standardized questionnaires exist for dry eye and other ocular diseases. Patients are asked to rate the severity of several symptoms and symptom classes.	Severe reported symptoms may indicate KCS	Asbell, 2006

Additional tools have been used by laboratory researchers to measure the biochemical composition of tears. 1D and 2D SDS polyacrylamide gel electrophoresis (PAGE) slab gels are commonly used[39-41] (Figure 4). Yet, native slab gels, which allow for the maintenance of antibody-antigen binding during the gel run and resulting biochemical affinity information, are rarely used in tear protein analysis due to the commonly observed non-specific binding of the tear fluid proteins. SDS is used to denature proteins and impart a uniform negative charge on their surface, thus minimizing any electrostatic binding. Protein microarrays[33] and enzyme-linked immunosorbent assays (ELISAs)[30] are also used, but suffer from high levels of background and nonspecific protein adsorption (Figure 5). Further, reverse-phase high performance liquid chromatography (HPLC) and mass spectrometry have been used, but are not appropriate for use in a clinical setting.[19,42,43]

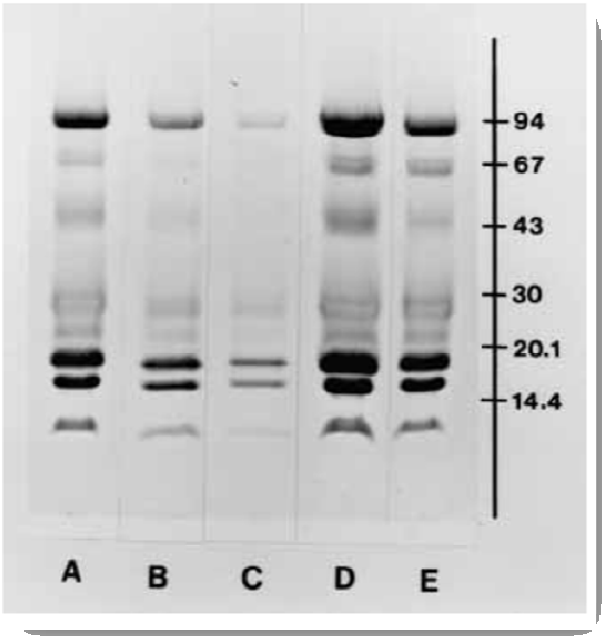

Figure 4. SDS-PAGE analysis of undiluted tear fluid (A), tear fluid diluted 1:3 with distilled water (B), eye flush fluid (C), diluted tears after concentration by centrifugation (D), eye flush fluid after concentration (E). Reprinted from Bjerrum, KB, Primary Sjogren's Syndrome and Keratoconjunctivitis Sicca: Diagnostic Methods, Frequency and Social Disease Aspects*, Acta Ophthalmologica Scandinavica, 2000, 78, 3-37 with kind permission from John Wiley and Sons.*

In much the same way that quantitative blood measurements have revolutionized the practice of medicine, taking it from a symptomatic, observation-based occupation to one equipped with quantitative biomarker-based measurements of disease pathology, the use of quantitative measurements in proximal fluids has the potential to push the boundary of our understanding of local disease pathology and revolutionize diagnosis of tissue-specific diseases. The use of proximal fluids (i.e., a biofluid close to, or in direct contact with, a site of disease) in diagnostic medicine has increased in recent years.[7] Since biomarkers originating from a specific tissue (e.g., a malignant tumor) likely arise locally, it is likely that the signal generated by that biomarker will decrease with distance from the diseased tissue and dilution into plasma.[7] Therefore, fluids close to a site of malignancy, or proximal fluids, are likely to have higher local concentrations of soluble proteins that are actively secreted from the tissue microenvironment[44] and may also have biomarkers that cannot be detected in blood.

Yet, in order to take advantage of tears as a rich proximal-fluid source of biomarkers for diagnostics, ophthalmologists are in need of improved instrumentation capable of making robust biochemical measurements of tear molecules at the point-of-care. Quantitative tools of tear composition would advance our understanding of ocular disease pathologies and provide an opportunity for much needed molecular biomarker-based ocular diagnostics.

3.3 Challenges Associated with Making Measurements in Tear Fluid

Major technological hurdles hinder routine clinical assessment of tear fluid biomolecules. Specific challenges in tear protein analysis include 1) the high alkalinity of many major tear proteins (e.g. lactoferrin, isoelectric (pI) point 8.7, lysozyme, pI 9.28 and SPRR1B, pI 8.85)[45] which are known to rapidly associate with other analytes in solution[46], 2) the low sample volume availability especially in dry eye diseases (< 10 µL), 3) the high ion content and resulting high conductivity of tear fluid, and 4) the presence of factors in human tear fluid that can interfere with traditional assay readouts. Highly alkaline proteins, such as those commonly found in tear fluid, are known to rapidly associate with other analytes in solution.[46] Further, the interfering factors in tear fluid include constituents that decrease the binding efficiency of antibodies through selective cleaving of the Fab region or steric hindrance of the epitope through complexing,[47,48] block the interaction of proteins with plastic surfaces to interfere with tear protein ELISAs,[47,49] and contribute high background signals, blooming effects, matrix effects and cross-talk between capture and probe antibodies in micro-well arrays and immunoassays (Figure 5).[31,33,50] Tears may also contain a protease that can selectively cleave micro-well bound IgG molecules, resulting in an overall reduction in ELISA efficiency.[48] Various fluid types including intestinal secretions, saliva, nasal mucus, and lacrimal fluid have been shown to inhibit antigen-antibody binding *in vivo*.[48] In a separate study, immunoglobulin G binding affinity was shown to be substantially lower in the presence of tear fluid when compared to other biological fluids (e.g. saliva and nasal mucous) (Figure 6).[48]

Historically, matrix effects have confounded measurements that utilize affinity probes in a heterogeneous format to specifically detect proteins in tear fluid. One study that utilized commercially available stationary phase antibody protein arrays for a panel of inflammatory cytokines in tear samples found that multiplex microplate array assays present an 'unanticipated challenge due to the unique nature of tear fluid.'[33] In this study, components in the tear fluid exhibited an affinity for plastic, capture antibodies and IgG, creating elevated levels of background and a reduced ability for the target proteins to bind. These effects were reduced in tears collected with Schirmer strips, but nonetheless, made protein measurement with this technique impossible and pointed to effects that may contribute to the wide range of discrepancies in dot sandwich ELISA reports in the literature.[33] It has been suggested that one contributor to these matrix effects is a high molecular weight factor(s) that has a high affinity for micro-well plastic, similar to a previously presented tear 'clumping factor' that aggregates IgG-sensitized sheep red blood cells[50], but characterization of this factor has not occurred to date.[31] Further, blocking activity has been observed when tears are in the presence of receptors, binding proteins, inhibitors, and/or proteases.[31] For example, a protease inhibitor,

alpha-2 macroglobulin, is known to complex with several cytokines in serum and closed-eye tear fluid, making it difficult to analyze with ELISA.[31]

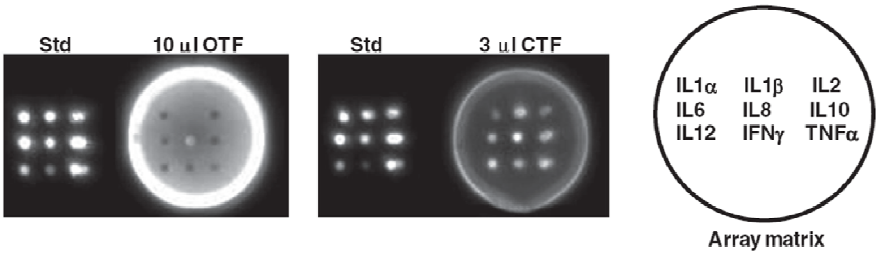

Figure 5. Matrix effects and background signal obtained when open tear fluid (OTF) and closed eye tear fluid (CTF) is added to a microwell protein antibody array. Figure reprinted from Li, et. al., Antibody Protein Array Analysis of the Tear Film Cytokines*, Optometry & Vision Science, 2008, 85(8) E653-E660 with kind permission from Wolters Kluwer Health.*

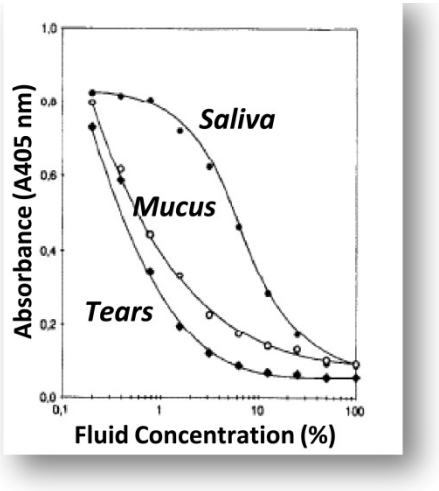

Figure 6. Inhibition of antigen-antibody interactions by saliva, mucus, and tears in ELISAs. Tear fluid has the largest decrease in observed IgG binding. Reprinted from R. Poethke, et. al., A putative enzyme from various secretions specifically inhibits antibody-antigen interactions*, Journal of Immunological Methods, 1996, 191, 149-157 with permission from Elsevier.*

The tear-specific moieties that are responsible for these interfering effects have not yet been identified[33] and given these confounding factors and the high variability of tear fluid, the degree to which tear fluid impacts the reliability of an assay can be highly dependent on the volume, type of assayed tear sample, individual donor and assay employed. Consequently, obtaining quantitative data for proteins in the presence of tear fluid is difficult.[31] Thus, analytical technologies optimized to quantify specific tear proteins within the complex tear matrix would go far to aid in elucidating ocular – as well as systemic- disease pathogenesis. Such enhanced understanding would, in turn, inform treatment.

Additional gaps exist in the suitability of current technologies for use in a clinical, point-of-care setting. These gaps include: low throughput (> 5 hours for analysis for ELISA), lack of automation potential, consumption of large sample volumes, and limited sensitivity levels for clinical assessment. Taken together, these gaps make current assays (i.e., protein sizing slab gels, ELISA) unsuitable for point-of-care diagnostics and rapid quantification of molecular concentrations in clinically relevant ranges.

Acknowledging the need for improved instrumentation, we sought to design and implement next-generation tools for tear protein analysis. The goal of this project was the design and application of new technologies to enable tear biomarker (e.g., protein, osmolarity) measurements, both for research and point-of-care settings.

We believe a tool that is able to measure tear proteins as well as small molecules (e.g., salt content) would comprise a major advance towards first-in-kind tear-based diagnostic tests at the point of care and would enable the study of several interesting medical and research questions. For example, we are interested in using such a tool in research for biomarker validation and discovery in diseases such as dry eye disorder, a collection of diseases that remain poorly differentiated, difficult to accurately diagnose, and that affect millions of people. We would like to investigate the possibility of using tears, a biological fluid that can be non-invasively collected and which equilibrates with blood in some conditions, to diagnose systemic disease. Further, we are interested in studying the impact of biospecimen collection, storage and handling on the analytical results of an assay.

We envision the use of this tool in other point-of-care settings including the developing world and believe the device could be extended to quantify biomarkers in infectious ocular diseases such as trachoma, a widespread disease in the developing world and the number one cause of preventative blindness in those countries.[51] Finally, it is poorly understood what enables the eye to be the only external surface of our bodies that remains sterile. We expect that this analytical tool could be used to investigate what factors in tears contribute to commonly observed matrix effects and what also might impart surface sterility to the eye.

Chapter 4: Tear Sample Collection, Storage, and Handling

4.1 The Problem with Current Tear Sample Preparation Methods

The biochemical composition of human tear fluid is of increasing interest in clinical medicine and basic research. More specifically, tear fluid is a potentially rich and untapped reservoir of disease-specific protein biomarkers for emerging disease diagnostics and therapies.[33,52-56] However, sample preparation remains a significant bottleneck in tear fluid biochemical analysis due to variability introduced by sample collection and handling methods. More broadly, the US National Institutes of Health (NIH) has identified biospecimen science as "the most pressing problem facing 21st century molecular medical research."[57] They cite the quandary as "limited availability of carefully collected and controlled, high quality human biospecimens."[57]

While the impact of diverse tear collection methods on tear composition as well as the variability of tear protein levels among patient populations and within a single patient over time or disease progression have been studied extensively,[34,58-63] few studies have focused specifically on evaluating the effect of subsequent post-collection processing on sample composition. This is especially true when considering processing protocols that process proteins in native conditions that are relevant to downstream measurements conducted using immunoassays or other immunoaffinity-based analytical techniques. In this chapter, we focus on characterizing tear fluid biospecimen collection and handling losses; however, biospecimen integrity and handling, more broadly, has emerged as a major concern in proteomics studies.[64]

In particular, the impact of processing tears collected with Schirmer strips remains poorly understood. The Schirmer strip is a commercially available nitrocellulose Whatman membrane measuring 5 x 35 x 0.22 mm. In the clinic, Schirmer strips are commonly used to assess aqueous tear volume (e.g., Schirmer I and II tests) and are increasingly used "off label" for tear collection and storage. As a result, large well-characterized registries of Schirmer strip-collected tear samples have been established to run retrospective clinical studies for protein biomarker discovery and validation (e.g., SICCA patient library at the University of California, San Francisco).[33] Yet, despite the availability of large repositories of patient samples and their potential in biomarker discovery and validation, tears collected with Schirmer strips remain poorly characterized and no well-characterized protocol exists to extract tear proteins off of Schirmer strips for downstream analysis.

Table 2 Review of studies utilizing tear samples collected with Schirmer strips from 1983 to 2011. Highlighted columns illustrate the controls used to characterize the sample processing technique, if any.[33,34,43,49,54,59,60,63,65-89]

Protein Target	Elution Technique	Analysis Technique	Control Used for Elution Efficiency	Elution Efficiency	Year Published
Protein profile	Diffusion in PBS with 1% Triton X-100	ProteinChips SELDI-TOF, MALDI-TOF MS, BCA	None	None reported	2011
MMPs & cytokines	Diffusion in 0.5 M NaCl with 0.5% Tween-20	Luminex 10 cytokine and 5 MMP kit	Spiked MMPs & cytokines onto Schirmer strips	>60% recovery for cytokines & MMPs	2011
Protein profile	Diffusion in PBS	iTRAQ, BCA	None	None reported	2011
Protein profile	Spin filter with extraction buffer, followed by centrifugation	iTRAQ, LC-MS/MS, Bradford	None	None reported	2010
Cytokines	Diffusion in PBS	Antibody coated beads, BCA	Total protein	None reported	2010
Protein profile (Lf, Lz, sIgA, Lipocalin, IgA, cytalins)	Incubate strip in ammonium bicarbonate, followed by centrifugation	SDS PAGE, Bradford, Mass spec	Capillary tube	None reported	2010
Protein profile	Diffusion in PBS	iTRAQ, BCA	Total protein	None reported	2009
Lz, lipocalin-1 & Lf	Centrifugation immediately after collection	SDS-PAGE, BCA	Capillary tube & total protein	None reported	2009
Cytokines	Diffusion in MEGA Block 3, followed by centrifugation	Microwell plate immunoassay	None	None reported	2008
Tear proteome	Acetone precipitation at -20C for 1 hour	2D LC-MS/MS, 1D- and 2D-SDS–PAGE	Capillary tube	None reported	2008
Secretory IgA	Diffusion in PBS with NaCl and 0.5% Tween 20	Antibodies against sIgA	None	None reported	2007
Diadenosine Polyphosphates	Immediate incubation with DI water, precipitation of proteins, centrifugation	HPLC	None	None reported	2006

Secretory IgA	Diffusion in PBS with NaCl and 0.5% Tween 20	ELISA	None	None reported	2006
Lz, lipocalin, Lf, HSA, IgA	Diffusion in PBS with 1% Triton X-100	SELDI-TOF-MS ProteinChip Array	Capillary tube	None reported	2005
Protein profile	Incubation in PBS, followed by centrifugation	SELDI-TOF-MS	None	None reported	2004
Staphylococcal enterotoxin A + B	Diffusion in PBS	IMMULIZEsystem (Ab detection)	None	None reported	2003
Diadenosine polyphosphates	Diffusion in water & precipitation	HPLC	None	None reported	2002
Eosinophil cationic protein, chemokines, cytokines	Diffusion in PBS with NaCl and 0.1% Tween 20	ELISA	None	None reported	2003, 2006
Cysteine, ascorbate, glutathione, urate & tyrosine	Diffusion in phosphate buffer	HPLC	Capillary tube	None reported	2001
MUC5AC mRNA	Diffusion in SDS PAGE buffer, followed by centrifugation	RT-PCR	None	None reported	1999
Cystatins	Diffusion in DI water	BCA, ELISA	Capillary tube	98%, based on preliminary unreported experiments	1991
Lz, Lf & HSA	Diffusion in TIMED acetic acid buffer	Immunochemical (rocket electrophoresis)	Capillary tube	None reported	1986
Lf, tear properties	Diffusion in PBS	ELISA, Lowry	Capillary tube	None reported	1985
Lz, Lf, HSA, transferrin & IgG	Diffusion in TMED-acetic acid buffer	Electroimmunochemical	Capillary tube	None reported	1984
Lysozymal enzymes	Incubation in water, followed by centrifugation	Lowry for total protein, enzyme assays	None	None reported	1984
Lf	Immediate diffusion in PBS with NaCl	ELISA	Capillary tube	90% (Lf)	1983

Uncontrolled upstream processing of tear samples obfuscates quantitative cross-study comparisons of Schirmer strip-collected tear protein measurements and explains, in part, the large disparity in measured protein levels reported in the literature. From a survey of the literature spanning from 1983 to 2011 (Table 2), tears collected with Schirmer strips for subsequent quantitative protein expression studies are often analyzed with the assumption that the Schirmer strip has no impact on the absolute or relative concentrations of the collected tear proteins.[43,58,69,72,78,80] Further, numerous studies have compared protein levels in tears collected with capillary tubes and Schirmer strips without taking into account the additional elution and processing steps that can influence the composition of Schirmer strip-collected samples. These additional elution and processing steps required to process Schirmer strip samples very likely impact sample composition.[34,58-60]

In this work, we examine the impact of post-collection sample handling on the protein composition of human tear samples. In particular, we characterize diffusion-based protein extraction from Schirmer strips and characterize the efficiency, repeatability, and time-, concentration- and protein-dependence of a simple and widely reported method of using diffusion to process tear samples collected with Schirmer strips. Specifically, we isolate protein loss due to interactions with the Schirmer strip and protein loss due to other sample handling steps. We focus our attention on diffusion-based tear protein extraction, although several tear protein extraction protocols from Schirmer strips are documented (e.g., diffusion,[33,58,60,69] centrifugation,[59,73 74] and acetone precipitation[34,65]). To date, two studies have examined the impact of diffusion-based sample reconstitution on the composition of tears collected with Schirmer strips.[66,67] These studies examined the impact of the Schirmer strip on protein recovery but did not evaluate the protein lost due to the extraction protocol itself or attempt to investigate the effect of protein surface properties on elution efficiency. As a result, no well-characterized method of reconstituting tear proteins collected with Schirmer strips exists that is compatible with subsequent downstream functional protein assays.

Three major reasons guide the rationale for our focus on diffusion-based protein extraction under native conditions:

(1) The approach has found widespread use in recent research studies.[54,60,66,69,70,72] Reconstitution of tear proteins from banked Schirmer strip samples typically relies on a diffusion-based protein extraction, with at least 9 recent studies published employing this technique (Table 2).
(2) The protocol preserves the native state of endogenous tear proteins in an effort to be compatible with downstream functional protein assays, and
(3) This method can be easily integrated with a novel microfluidic homogeneous immunoassay recently developed by our group and presented in Chapter 5.[68]

The study presented in Chapter 4 utilizes Schirmer strips spiked with known protein concentrations to characterize native protein losses resulting from diffusion-based reconstitution of tear samples collected with Schirmer strips. Levels of protein irrecoverable from the Schirmer strip and lost during sample handling are isolated and compared for several

major tear proteins. Further, the impact of the Schirmer strip and sample handling on the downstream concentration of proteins ranging in molecular weight, surface charge, and surface hydropathicity is quantified. The significance of this study arises from our ability to isolate and quantify sources of protein loss during sample processing of the Schirmer strip (Figure 7).

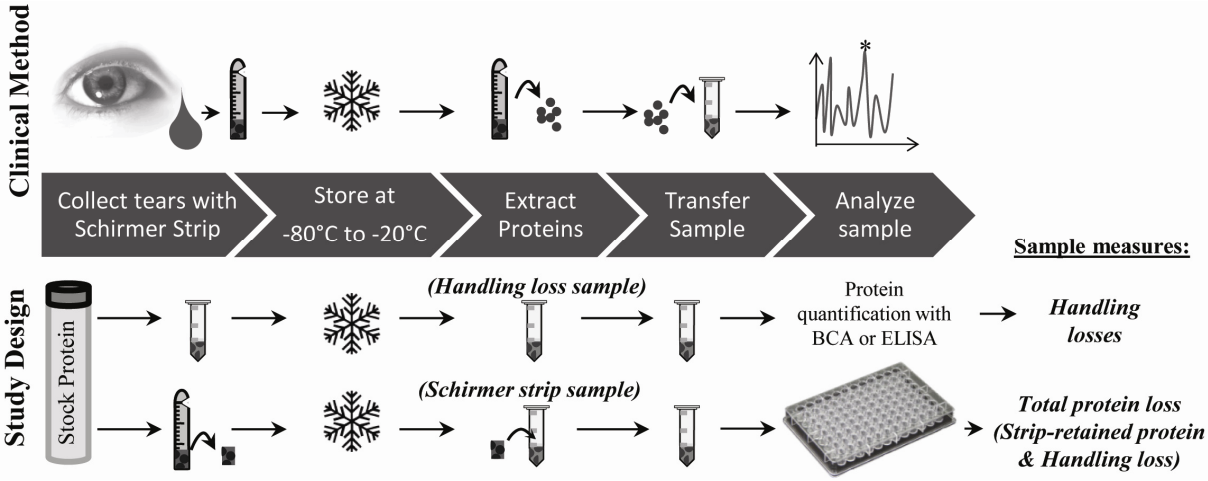

Figure 7. Schematic illustrating the standard method of Schirmer-based tear collection and analysis and our experimental design for isolating two major sources of protein loss: sample handling and retention of protein on the Schirmer strip. Reprinted with permission from Denisin, Karns & Herr, Post-collection processing of Schirmer strip-collected human tear fluid impacts protein content, *Analyst, 2012, 137, 5088-5096*

Our work includes consideration of protein retention on the Schirmer strip and protein loss during subsequent sample handling. The study detailed here introduces:

a) **Novelty and need:** The first well-characterized protocol to reconstitute tear proteins collected with Schirmer strips, which enables relation of downstream protein quantitation to ocular protein levels for cross-study comparison
b) **Methodical, quantitative approach**: Demonstration of the variable impact of post-collection sample processing on downstream tear protein concentration,
c) **Wide ranging relevance to proteinaceous biospecimens**: A systematic study to reveal the impact of protein size and charge on protein loss mechanisms, including appropriate statistically-driven conclusions.

We find, for the first time, that diffusion-based processing of Schirmer strip-collected tear fluid is highly protein-dependent. Optimization of the characterized protocol for high yield protein extraction is beyond the scope of the present report. Importantly, this work has implications in the interpretation of previously reported tear studies and paves the way for well-controlled, clinically meaningful tear studies which utilize tear samples collected with Schirmer strips.

4.2 Materials and Methods

Proteins and Reagents

Phosphate buffered saline (10× PBS) was purchased from Fisher Bioreagents (Pittsburg, PA) and diluted to 1× with DI water. Sterile, standardized Schirmer strips were obtained from Alcon (Fort Worth, TX). Polypropylene 0.65 mL microcentrifuge tubes from VWR (Brisbane, CA) were used in all experiments.

Tear proteins human lactoferrin (Lf) (77 kDa, pI 8.7), human serum albumin (HSA) (69 kDa, pI 5.92), and synthetic mucin 4 peptide (MUC4) (930 kDa, pI 5.85) were purchased from Abcam (Cambridge, MA). Secretory IgA (sIgA) (320 kDa, pI 4.3-6.85) was purchased from Genway Biotech (San Diego, CA) and recombinant human lysozyme (Lz) (14 kDa, pI 10.2-11) was purchased from RayBiotech (Norcross, GA). Model proteins for size, surface charge, and surface hydrophobicity studies were purchased from Sigma Aldrich: α-lactalbumin (AL) (14.2 kDa, pI 4.8), carbonic anhydrase (CA) (29 kDa, pI 6.4), chicken ovalbumin (OVA) (45 kDa, pI 5.35), bovine serum albumin (BSA) (66 kDa, pI 5.6), alcohol dehydrogenase (ADH) (150 kDa, pI 5.6), β-amylase (BMY) (200 kDa, pI 5.1), urease (UR) (272 kDa dimer, 545 kDa tetramer, pI 6.05), horse apoferritin (HAF) (443 kDa, pI 4.0), thyroglobulin (THG) (670 kDa, pI 4.58). Isoelectric points were obtained from the vendor and from estimates on ExPASy Proteomics Server of the Swiss Institute for Bioinformatics.[45] Each tested protein was made into a 1.5 mg/mL stock solution with 1× PBS.

Unless otherwise indicated, the protein content of all samples was measured with the bicinchoninic acid total protein assay (BCA) (Thermo Fisher Scientific, Pierce, Rockford, IL). The BCA assay relies on colorimetric detection of protein-induced Cu reduction and thus measures total protein in a sample. The BCA protocol used 4 µl of sample and 80 µl of reagent and was conducted according to the manufacturer's directions. Corning Costar 96 well EIA/RIA flat bottom, transparent polystyrene (medium binding) plates (Sigma Aldrich) were used for sample incubation and absorbance measurements. Absorbance measurements at 562 nm were obtained using the Infinite 200 PRO plate reader (Tecan Group, Switzerland). A human lactoferrin ELISA Kit was used where indicated according to the manufacturer's protocol and was obtained from Bethyl labs (Montgomery, TX).

Human tear fluid from healthy patients was collected to compare the characterization studies performed in buffer with sample preparation of clinical samples. Healthy subjects were recruited from the University of California, San Francisco (UCSF) Sjögren's syndrome clinic with informed consent according to the guidelines established by the Association for Research in Vision and Ophthalmology. All procedures adhered to the tenets of the Declaration of Helsinki. Tear samples were collected using Schirmer strips in standardized fashion (unanaesthetized eye with strip inserted in the inferior cul-de-sac for 5 min) from both eyes of each subject. Subjects were anonymized and strips were snap frozen at -80°C in 1.5 mL Eppendorf microcentrifuge (Sigma Aldrich) tubes until reconstitution and analysis.

Protocol to Replicate Tear Protein Collection by Schirmer Strips

To study the effects of post-collection Schirmer strip processing on protein content, we replicate the clinical method of Schirmer strip tear protein collection and storage as described in the 'Clinical Method' section of Figure 7.

The 'Study Design' section of Figure 7 details our protein collection and storage protocol, which is comprised of the following steps: 1) pipette 5 µL of recombinant protein with a known concentration ('stock protein') into a polypropylene microcentrifuge tube (handling loss sample), 2) load 5 µL of stock protein sample onto a 5 mm^2 square of clean, dry Schirmer strip (Schirmer strip sample), 3) allow the Schirmer strip to dry for 35 min at room temperature, and 4) store both samples overnight at -20°C.

The handling loss sample is used to isolate and measure protein losses due only to sample manipulation during the elution protocol. The Schirmer strip sample measures the impact of both the Schirmer strip and sample handling and thus accounts for total protein loss due to the protocol.

Diffusion-Based Tear Protein Extraction from Schirmer Strips and Sample Handling

After protein collection on Schirmer strips, the proteins were extracted and processed according to the protocol outlined in the 'Study Design' section of Figure 7. Briefly, we performed the following steps: 1) each of the frozen 5 mm^2 Schirmer strip sections spiked with a known protein concentration (Schirmer strip sample) was placed in a microcentrifuge tube using clean tweezers, 2) 10 µL of 1× PBS was added to both the sample handling and Schirmer strip tube, 3) tubes were incubated on a benchtop shaker for 3 hours at room temperature, and 4) protein concentrations in each tube were quantified using a BCA total protein assay.

This extraction protocol replicates sample preparation protocols commonly published in the literature.[33,58,60,69] In addition, the protocol does not require any specialized lab equipment and can be performed on stored Schirmer strip samples since it does not require *a priori* modifications of the strip before sample collection. Thus, the protocol is applicable to established libraries of stored Schirmer strip samples.

Sources of Post-Collection Variability in Protein Content

In order to characterize the post-collection processing of tear fluid collected with Schirmer strips, we tracked two major sources of protein loss: 1) the Schirmer strip itself (*Strip-retained Protein*) and 2) sample handling (*Handling Loss*). Protein lost to the Schirmer strip quantifies only the protein that is retained on the Schirmer strip and is unrecoverable in solution after extraction is allowed to proceed to steady-state. Meanwhile, protein lost during sample handling includes all other sources of protein loss from the moment the sample is introduced to the strip through final BCA quantification. These sources of handling loss include protein adsorption to the stock protein tube, frozen storage, defrosting, polypropylene sample tube adsorption, pipette transfer to the BCA plate, and protein adsorption to the BCA plate. ELISA measurements included exposure to an additional polypropylene sample tube during serial

dilution resulting in a higher observed handling loss as compared to eluted protein quantification using the BCA.

The amount of protein retained on the Schirmer strip was calculated as follows:

$$Strip\ retained\ Protein\ (\%) = \left(\frac{Protein\ in\ handling\ loss\ sample - Protein\ in\ Schirmer\ strip\ sample}{Stock\ protein}\right) \times 100\%$$

Handling loss was calculated as follows:

$$Handling\ Loss\ (\%) = \left(1 - \frac{Protein\ in\ handling\ loss\ sample\ \left(\frac{mg}{mL}\right)}{Stock\ protein\ \left(\frac{mg}{mL}\right)}\right) \times 100\%$$

The sum of these two sources of protein loss is equal to the 'total protein loss,' which represents the fraction of initial protein ultimately unrecoverable from the extraction protocol. Total protein loss was used to assess the overall efficiency of the protocol.

Controls

In order to control for background signal observed in the BCA assay from the Schirmer strip, matched blank Schirmer strips spiked with 5 µL of PBS were used as controls. These controls were processed simultaneously and identically to all protein-containing strips with the exception that they contained no protein. The 562 nm absorbance signal obtained from these blank (no protein) control samples was 0.0883 ± 0.0067 (n = 32, from BCA). This background signal from blank strips was, on average, 1.52 ± 0.135 times the absolute absorbance signal of PBS (0.0581 ± 0.0027, n = 14) and was subtracted from all signals acquired from protein-containing Schirmer strip samples. We hypothesize that this observed BCA background signal is caused by endogenous Schirmer strip components that also diffuse off the strip into the sample during reconstitution and interact with the BCA reaction.

Characterization of Diffusion-Based Schirmer Strip Processing Protocol

Time-Dependence of Protocol: The time at which the protein extraction from Schirmer strips reached steady-state represents the time for maximal protein extraction from the Schirmer strips. In order to determine this time point, we measured the amount of Lf eluted from a Schirmer strip over time. Lf is a notoriously 'sticky' protein[46] and therefore was used as a model protein since it would likely take longer to reach maximal extraction than other proteins. The extracted Lf concentration in the eluate was measured at various time points using ELISA. The data was fit to a one-dimensional limited source diffusion model[90,91] with the equation $C(t) = C_{max} - Q/(A\sqrt{\pi D t})$ where $C(t)$ is the concentration of Lf measured in the eluate at each time point, C_{max} is the maximum extracted protein after 3 hours, Q is the mass of Lf loaded on the strip (0.0075 mg), A is the cross-sectional area of the Schirmer strip (0.25 cm^2), and t is time in seconds. When the data was fit to this curve, the diffusion coefficient, D, was determined to be 7.01E-6 cm^2/sec using a non-linear least squares curve fitting algorithm. This value is on-par with literature values.[92,93] The change in concentration in the eluate over time

was determined by taking the derivative of C(t). Finally, the change in concentration over time was normalized by the maximum observed concentration change to determine the percent change in Lf concentration at each time point.

Concentration-Dependence of Protocol: The speed and extent of protein extraction from Schirmer strips using diffusion is dependent on the protein concentration gradient that exists between the Schirmer strip and the surrounding medium. Therefore, we characterized the range of starting protein concentrations that exhibit concentration-independent extraction from Schirmer strips by tracking total loss for proteins AL, CA, OVA, BSA, and UR over a concentration range of 0.75 to 2 mg/mL.

Protocol Repeatability: The repeatability of the protocol was assessed by comparing the strip-retained protein and handling loss for BSA over a 12 month period of experimentation. 90 experiments were compared over this period (270 Schirmer strip samples spiked with BSA).

Protocol Efficiency: Total protein loss (the sum of strip-retained protein and sample handling protein loss) was tracked to assess the amount of initial protein ultimately unrecoverable from the extraction protocol. Protocol efficiency (100% – total protein loss(%)) was then calculated.

Protein-Dependence of Protocol: To assess the protein-dependence of the extraction protocol, protocol efficiency was measured for model proteins specifically chosen to span a range of physicochemical properties. These proteins were selected based on their diversity in molecular weight, surface charge, and surface hydropathicity. Protein losses during extraction and sample handling were then tracked to assess the effect of protein size, surface charge, and surface hydropathicity on these sources of protein loss. Further, strip-retained protein and handling loss were measured for 5 major tear proteins to understand the relationship between the results obtained from the model proteins and those commonly found in tears. The tear proteins studied were Lz, HSA, sIgA, MUC4, and Lf.

The effect of protein molecular weight on protein loss: Proteins with matched isoelectric (pI) points (average pI = 5.40 $\pm$ 0.72) and varying molecular weights (ranging from 14.2 – 930 kDa) were used to isolate the impact of protein weight on protein lost to the Schirmer strip and sample handling.

The effect of protein surface charge on protein loss: PyMOL software (DeLano Scientific, LLC) was used to analyze all proteins in this study, with structures taken from the RCSB Protein Data Bank (PDB)[94] via the SWISS-MODEL Repository.[95] The negatively and positively charged surface area of each protein was calculated by 1) identifying which amino acids are negatively or positively charged at pH 7.4 (PBS), 2) using the software to highlight the surface amino acids that are accessible by solvent, and 3) using the software to calculate the surface area of the amino acids on the surface that are negatively or positively charged at pH 7.4. Negatively and positively charged surface areas were normalized by total surface area accessible by solvent (1.4 Å water molecule), as shown previously.[96] Protein lost to the Schirmer strip and sample handling was plotted over a range of the proportion of total surface area that is negatively or positively charged.

The effect of protein surface hydropathicity on protein loss: The surface areas of hydrophobic residues (Ala, Val, Ile, Leu, Met, Phe, Tyr, Trp) and hydrophilic residues (Arg, His, Lys, Asp, Glu, Ser, Thr, Asn, Gln) on the surface of the protein were calculated using PyMOL software in a manner similar to how the negatively and positively charge surface areas were calculated (explained above). Hydrophobic and hydrophilic surface areas were normalized by total solvent-accessible surface area as above. Protein lost to the Schirmer strip and sample handling was plotted over a range of the proportion of total surface area that is hydrophobic or hydrophilic.

Impact of Tear Matrix on Protocol: Tear fluid has been shown to interfere with assay readouts.[33] Therefore, we sought to assess the impact of the complex proteinaceous tear matrix on elution of specific proteins and bridge our findings on the extent of protein loss that was obtained using purified model proteins. We intended to identify if there was a different loss pattern in the presence of tear fluid compared to the amount of purified protein lost in the presence of tear fluid. We therefore compared Lf protein lost to the Schirmer strip and sample handling loss both in the presence of Lf-depleted human tear samples and in 1× PBS buffer. The presence of about 500 other tear proteins,[29] as well as salts, lipids, and other tear components, are likely to alter the properties of the tear sample (e.g., matrix stability, contact angle, pH),[97] interact with the proteins studied here, and compete for protein adsorption sites, among other effects. For example, published studies suggest that tear fluid components can inhibit protein interaction with plastic surfaces.[47,49] Lf was chosen as a model protein for this study because of its notorious tendency to interact with other tear components and assay structures,[46,68] making this protein particularly susceptible to altered loss profiles in the presence of the tear matrix. Lf is also a clinically relevant biomarker for diagnosing Sjögren's syndrome, a serious systemic autoimmune disease.[30] However, it should be noted that the observed effect of the tear matrix on Lf losses should not necessarily be generalized to all tear proteins.

Schirmer strip-collected healthy human tear fluid was reconstituted by incubating 5 mm^2 strips in 20 µL of 1x PBS buffer overnight. Dynabeads antibody coupling kit and DynaMag-2 magnet were purchased from Invitrogen (Carlsbad, CA). Endogenous Lf was removed from the tear matrix by conjugating polyclonal goat anti-human Lf antibodies (Bethyl Laboratories, Montgomery, TX) to magnetic Dynabeads. Conjugated beads were incubated with the healthy human tear fluid overnight. Lf-bound Dynabeads were then magnetically removed. The final concentration of Lf in the depleted sample (measured by ELISA) was 0.0098 mg/mL (1.95% of original Lf concentration). 1.5 mg/mL of recombinant Lf was then spiked into the Lf-depleted tear sample and loaded onto a Schirmer strip and into a processing tube. Lf spiked into PBS and loaded onto a Schirmer strip and into a processing tube served as controls. Extracted Lf concentrations were quantified using ELISA.

Statistical Methods

The Spearman Rank Correlation test was used to assess the association between protein molecular weight, extent of positively and negatively charged surface area, and the extent of

hydrophobic and hydrophilic surface area on the amount of protein retained on the Schirmer strip and lost during sample handling. The Spearman Rank Correlation test allows quantitation of the trend strength between two variables measured on an ordinal scale.[98] Normality conditions in the data were not assumed, further motivating the choice of the nonparametric Spearman correlation test over a parametric test (e.g., Pearson Correlation Coefficient). Sample sizes of 14 and 12 were used for the molecular weight and charge/hydropathicity analyses, respectively. As such, all calculated Spearman Rank Correlation Coefficients were compared to a reference table for critical values[98] to assess the association between the two variables. Using an $\alpha = 0.05$ significance level, Spearman coefficients below the critical values of 0.587 (n=12) and 0.538 (n=14) indicated no association between the two variables. All studies focusing on elucidating protein properties that may impart protein-dependence to the sample preparation protocol were observational in nature owing to the practical difficulties of actively manipulating a single, independent physicochemical protein property (e.g., protein surface charge) in order to observe changes in protein loss patterns. As such, the analysis used here measures associations between variables and not causality. Experiments in this portion of the study do not rule out the possibility that both variables are independently responding to an unknown third factor and that the independent variable does not causally affect the dependent variable.

4.3 Experimental Results

It is critical to develop a steady-state, concentration-independent, repeatable, efficient, and protein-independent protocol for extracting proteins off of Schirmer strips. This will ensure preservation of the relative and absolute concentrations of tear proteins in the downstream sample.[99]

In order to characterize the time-dependence of the protocol, we tracked diffusion-based extraction of Lf off the Schirmer strip over time. After 37 min of extraction, less than 5% change in Lf concentration in the eluate was observed. Less than 1% change in Lf concentration in the eluate was observed after 1.8 hours. Thus, a 3 hour diffusion time appeared to be sufficient to achieve time-independent extraction for Lf. A 3 hour diffusion time is on-par with times reported in the literature.[70,72]

In order to characterize the concentration-dependence of the protocol, we measured total protein loss for proteins AL, CA, OVA, BSA, and UR over a concentration range of 0.75 to 2 mg/mL. There was no significant change observed in the total protein eluted after 3 hours across these concentrations for any of the tested proteins ($p > 0.05$, ANOVA test, power = 0.8). This indicates steady elution of protein regardless of initial protein concentration within the range of 0.75 mg/mL to 2 mg/mL.

In order to characterize the repeatability of the protocol, we monitored both strip-retained protein and handling losses for a model protein, BSA, over a 12 month period. There was no observed variation among the measured strip-retained protein and handling losses over all

studies run under the same conditions ($p > 0.05$, ANOVA test, power = 0.972). This attests to the repeatability of the experimental protocol.

We assessed overall protocol efficiency and protein-dependence by tracking total protein loss after 3 hours of elution. Table 3 shows the overall extraction efficiencies (100% - total protein loss (%)) of the protocol for 14 model proteins. The protocol extraction efficiency is protein dependent, ranging from highly efficient (e.g., Lz 84%) to inefficient (e.g., BMY 7%).

Table 3. Overall protocol efficiency is calculated as 100% - total protein loss (%). The average elution efficiency is followed by the maximum and minimum values for each protein. The number of trials is as follows: n = 2 for BSA, HAF, ADH, CA, OVA, AL, THG, BMY; n = 3 for Lz, HSA, Lf, sIgA, MUC4; n =8 for UR.

Protein	Protocol Efficiency (%)	(max, min)
Lz	84	(88, 78)
BSA	83	(92, 74)
HAF	81	(84, 79)
HSA	79	(80, 79)
ADH	73	(78, 68)
CA	71	(71, 70)
OVA	69	(74, 63)
AL	63	(67, 60)
Lf	63	(70, 59)
UR	48	(61, 36)
sIgA	44	(46, 41)
THG	36	(38, 34)
MUC4	28	(29, 27)
BMY	7	(7, 6)

To more fully characterize the protein-dependence of the protocol and determine whether this observed variability holds true for tear proteins, we isolated and measured the impact of the Schirmer strip and sample handling on the downstream concentrations of several predominant tear proteins including Lz, HSA, sIgA, MUC4 and Lf. Figure 8A and Figure 8B show the amount of each tear protein retained on the Schirmer strip after extraction and the level of tear protein handling losses, respectively. The average measured levels of strip-retained protein are: 14.2% for Lz, 9.5% for HSA, 27.7% for sIgA, 30.9% for MUC4, and 17.1% for Lf. The average percentages of tear protein lost during sample handling are: 2.0% for Lz, 11.2% for HSA, 28.4% for sIgA, 41.2% for MUC4, and 20.0% for Lf. The handling losses observed here are within the range of losses observed by others and reported in the literature using the same protocol.[100-102]

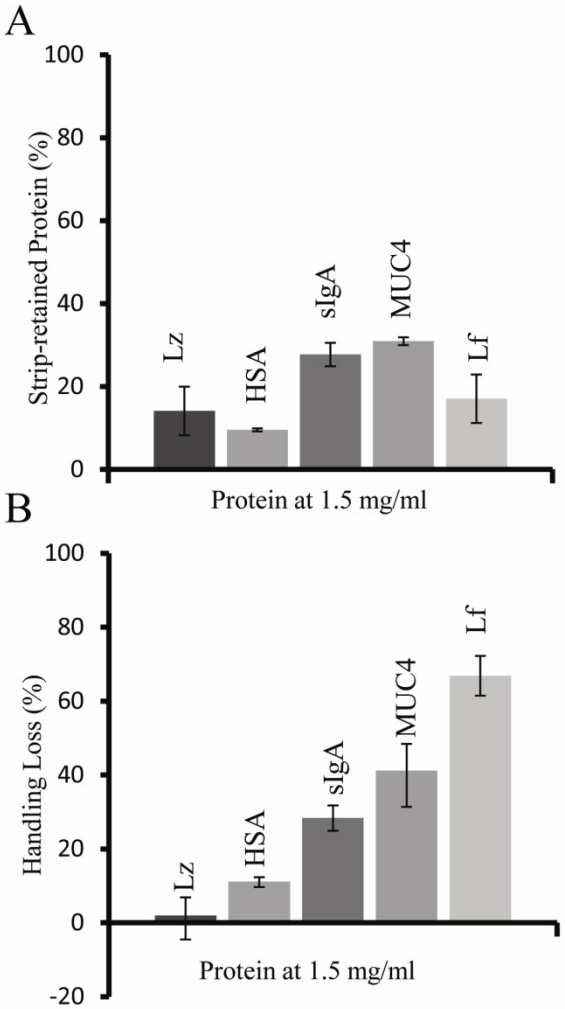

Figure 8. Processing of Schirmer strip-collected tear samples impacts tear protein levels. A) The amount of protein retained on the Schirmer strip for abundant tear proteins. B) The extent of sample handling loss for several predominant tear proteins. Total protein loss is the sum of losses shown in A and B (strip-retained protein (%) plus handling loss (%)). For both histograms, the average value is shown. Error bars indicate the measurement range. Lf is measured by ELISA (n = 2), all other proteins measured by BCA (n = 3). Adapted with permission from Denisin, Karns & Herr, Post-collection processing of Schirmer strip-collected human tear fluid impacts protein content, *Analyst, 2012, 137, 5088-5096*

To investigate the impact of biochemical and biophysical protein properties on the protein-dependency of the extraction protocol, we tracked protein losses across three major protein properties: molecular weight, surface charge, and surface hydropathicity. Surface hydropathicity encompasses both surface hydrophobicity and surface hydrophilicity. Figure 9 presents the association between Schirmer strip protein retention, protein handling loss, and protein molecular weight. A histogram of total protein loss as a function of molecular weight is overlaid above to show the relationship between overall protocol efficiency and molecular

weight. Spearman coefficients of 0.526 ($p < 0.001$, $n = 39$) and 0.538 ($p < 0.001$, $n = 39$) for strip-retained protein and protocol loss, respectively, suggest that there is a significant association between protein molecular weight and both the amount of protein retained on the Schirmer strip and the amount of protein lost during sample handling.

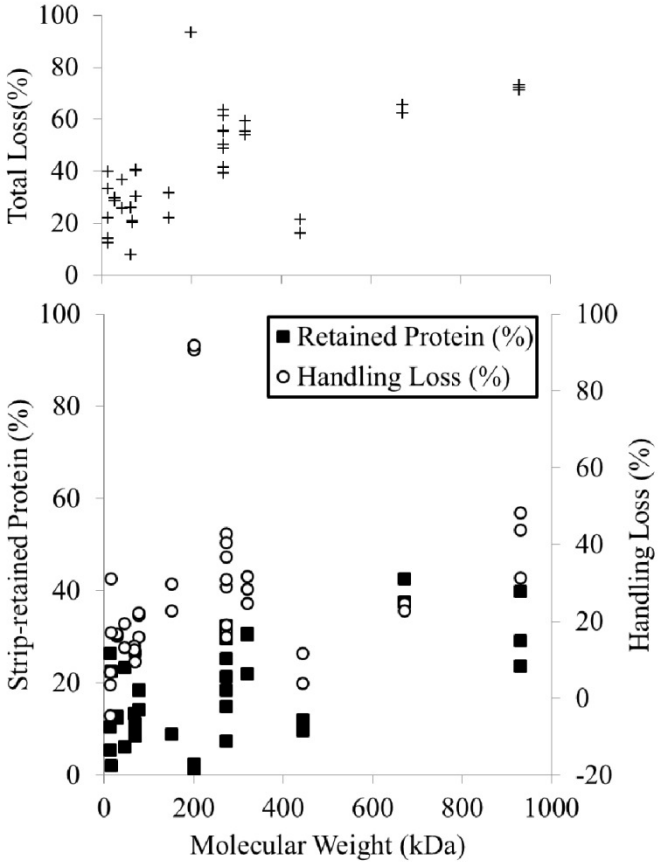

Figure 9. Molecular weight dependence of the extraction protocol. Bottom plot shows the association between protein retention, protein handling loss, and protein molecular weight. Losses due to irreversible Schirmer strip protein retention appear in black squares (axis on the left), while protein losses due to sample handling appear in open circles (axis on the right). There is a significant association between protein molecular weight and both strip-retained protein (Rs = 0.526, p < 0.001) and handling losses (Rs = 0.538, p < 0.001). Top plot shows the total protein lost as a function of protein molecular weight. Adapted with permission from Denisin, Karns & Herr, Post-collection processing of Schirmer strip-collected human tear fluid impacts protein content, *Analyst, 2012, 137, 5088-5096*

Figure 10A and Figure 10B present the association between Schirmer strip protein retention, protein handling loss, and the positive and negative protein surface charge, respectively.

Scatterplots of total protein loss as a function of positive and negative protein surface charge are overlaid above the graphs to show the relationship between overall protocol efficiency and protein surface charge. Spearman coefficients of -0.121 and 0.033 for strip-retained protein and protocol loss, respectively, suggest no significant association between negative surface charge and either the amount of protein retained on the Schirmer strip or the amount of protein lost during sample handling. Likewise, Spearman coefficients of -0.131 and -0.146 for strip-retained protein and protocol loss, respectively, suggest no significant association between positive surface charge and either the amount of protein retained on the Schirmer strip or the amount of protein lost during sample handling.

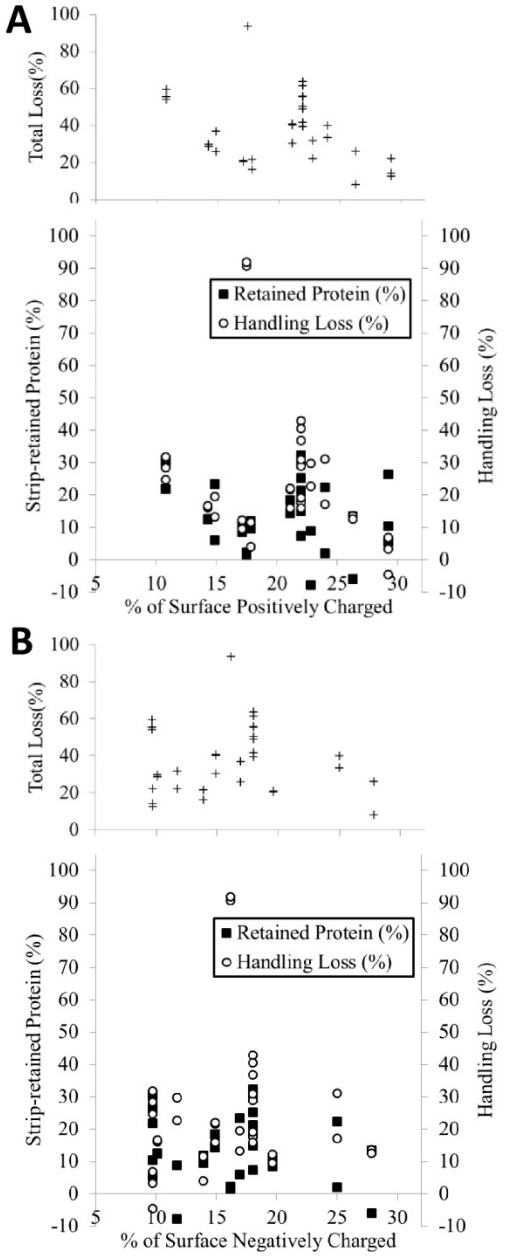

Figure 10. Association between fraction of positive (A) and negative (B) residues on protein surface and Schirmer strip protein retention (black squares, left axis) and protein loss due to handling (open circles, right axis). A) There is no significant association between positive surface charge and strip-retained protein or handling loss. B) There is no significant association between negative surface charge and strip-retained protein or handling loss. Top plots show the total protein lost as a function of the percentage of the protein surface that is positively (A) and negatively (B) charged. Adapted with permission from Denisin, Karns & Herr, Post-collection processing of Schirmer strip-collected human tear fluid impacts protein content, *Analyst, 2012, 137, 5088-5096*

Figure 11A and Figure 11B show the association between Schirmer strip protein retention, protein handling loss, and protein surface hydrophobicity and hydrophilicity, respectively. Scatterplots of total protein loss as a function of protein surface hydrophobicity and hydrophilicity are overlaid above each plot to show the relationship between overall protocol efficiency and protein surface hydropathicity. A Spearman coefficient of 0.422 ($p < 0.02$, $n= 4$) for strip-retained protein suggests that there is a significant association between surface hydrophobicity ad the amount of protein retained on the Schirmer strip. A Spearman coefficient of 0.334 for protocol loss suggests that the protocol protein loss is not significantly associated. Spearman coefficients of 0.215 and -0.073 for strip-retained protein and protocol loss, respectively, also suggest no significant association between surface hydrophilicity and either the amount of protein retained on the Schirmer strip or the amount of protein lost during sample handling.

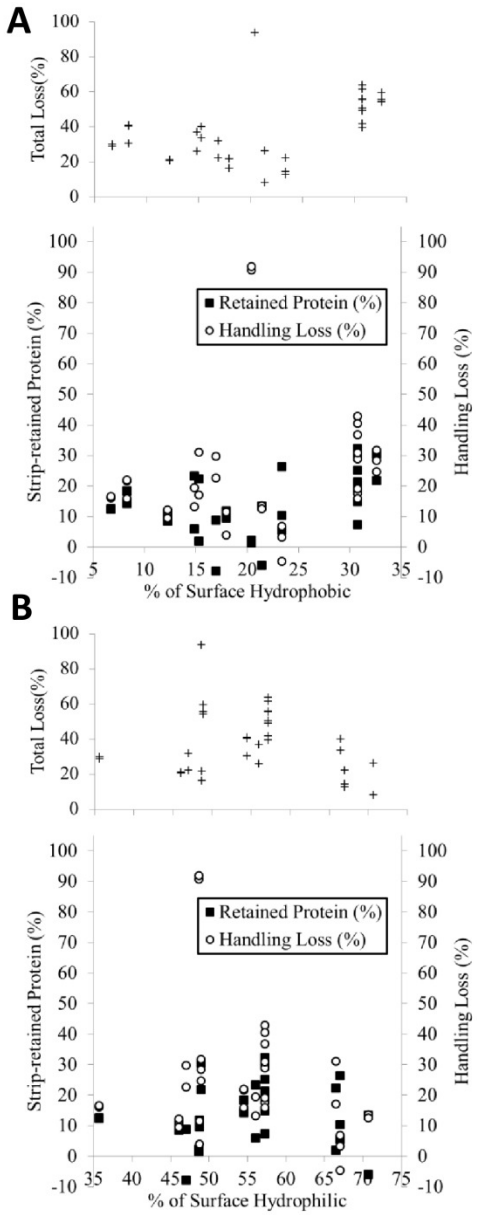

Figure 11. Association between fraction of hydrophobic (A) and hydrophilic (B) residues on the protein surface and Schirmer strip protein retention (black squares, left axis) and protein loss due to handling (open circles, right axis). A) There is a significant association between degree of protein surface hydrophobicity and retained protein or handling loss (Rs = 0.422, 0.01 < p < 0.02). B) There is no significant association between degree of protein surface hydrophilicity and retained protein or handling loss. Top plots show the total protein lost as a function of the percentage of the protein surface that is hydrophobic (A) and hydrophilic (B). Adapted with permission from Denisin, Karns & Herr, Post-collection processing of Schirmer strip-collected human tear fluid impacts protein content, *Analyst, 2012, 137, 5088-5096*

Finally, in order to evaluate the effects of the tear fluid matrix on the extent of protein losses measured using recombinant purified proteins in buffer, we compared protein losses in the presence of Lf-depleted healthy tear matrix to Lf losses in the presence of buffer. Lf in the presence of tear matrix is retained on the Schirmer strip to a similar degree (5.27%) when compared to Lf in PBS (6.55%), and the observed difference is not statistically significant ($p = 0.526$, unpaired equal variance 2-tailed Students t-test, $n = 6$). Lf losses during sample handling were also comparable in the presence of tear fluid, as compared to Lf in buffer (65.2% in the tear matrix, 66.8% in PBS). This observed difference in Lf losses during sample handling of the tear matrix (as compared to buffer) was not statistically significant ($p = 0.937$, unpaired 2-tailed equal variance test, $n = 4$).

4.4 Discussion

The biochemical and proteomic profile of a tear sample can be influenced by each point of intervention including collection, storage, extraction, handling, and analysis. In response to a gap in knowledge, we focus here on the effect of extraction of tear proteins from Schirmer strips using published diffusion-based protocols because these methods are used widely in current and past literature[33,58,60,69] yet the effect of sample processing on downstream protein yield and analyte composition have not been characterized. To identify and isolate the sources of material loss, we characterized the time- and concentration-dependence, repeatability, efficiency and protein-dependence of the protocol. Results of the characterization study suggest that use of >1 hour incubation times to reconstitute high abundance tear proteins (0.75 – 2 mg/mL) yields a sample processing protocol that is independent of time and analyte concentration. We observed that the protocol was very repeatable with no notable variation in the elution efficiency over 90 replicates.

The extensive total post-collection protein loss in Schirmer strip-collected tear samples that we observed here is protein-dependent. As such, the Schirmer strip and sample handling processes substantially impact the absolute and relative downstream concentrations of collected tear proteins. The altered relative and absolute concentration profile of collected tear proteins confounds downstream quantitative protein measurements. These results point to the need for additional controls in tear studies utilizing Schirmer strip-collected samples. Namely, controls are needed to verify the impact of the Schirmer strip and sample handling on the protein(s) of interest. Further, tear fluid samples collected with Schirmer strips may not be an appropriate sample collection modality for multiplexed studies assessing the relative concentrations of a panel of tear proteins (e.g., protein microarray studies), without careful design of controls.

We hypothesized that protein size, surface charge, and/or surface hydropathicity may impact the observed protein-dependent elution profile. Domains on the surface of proteins can participate in interactions with the Schirmer strip, elution buffer, and sample handling vessels.[103] Furthermore, proteins may be retained on the Schirmer strip due to protein-strip interactions (e.g., electrostatic, steric, van der Waals) that cannot be reversed by diffusion alone. For example, Schirmer strips are manufactured from Whatman No. 41 cellulose filter

paper,[104-106] and thus have a negative surface charge in pH 7 buffers such as the PBS buffer used in our elution buffer,[107,108] imparting a negative charge to the Schirmer strip in the conditions used in our study. As a result, we hypothesized that this may contribute to preferential retention of positively charged proteins. Protein adsorption to polypropylene surfaces has been shown previously to occur through electrostatic and hydrophobic interactions[100] and we hypothesized that exposed hydrophobic patches on the surface of a protein may also contribute to altered protein levels in solution. However, characterization of protein losses revealed that the extent of protein retained on the Schirmer strip and lost during sample handling is not associated with protein surface charge, or surface hydrophilicity for the spectrum of proteins studied here. Protein molecular weight was observed to have a positive, direct association with the amount of protein retained on a Schirmer strip and the observed protocol losses, suggesting that larger proteins are lost to a greater degree on the Schirmer strip and during sample handling. Further, hydrophobic surface area has a positive, direct association with the amount of protein retained on a Schirmer strip, supporting our proposed hypothesis that more hydrophobic patches on the surface of a protein lead to additional protein loss. In total, these results suggest that the effect of sample preparation on protein concentration cannot be accurately predicted in full based on a cursory knowledge of the protein surface properties.

Although changes in surface charge and surface hydrophilicity did not affect the extent of protein loss, an average of 25.1% ± 21.6% of protein mass was lost during sample handling. This represents a sizable loss which will ultimately limit the sensitivity of downstream protein assays. These observed handling losses were most substantial for β-amylase (BMY), which was lost at strikingly high levels (3.6x higher than average) with an overall 7% extraction efficiency. BMY has been shown previously to participate in hydrophobic interactions with surrounding proteins and system components, even at low salt concentrations.[109] In fact, the hydrophobicity of BMY is sometimes used to immobilize the protein in gels and other substrates.[109] Thus, it is likely that condensed hydrophobic patches on BMY contributed to the high levels of observed protein adsorption and loss during sample handling. Multivalent hydrophobic protein-polypropylene surface interactions in sufficient number and energies can cause enhanced protein adsorption that cannot be overcome by diffusive forces.[103]

Based on the demonstrated protein-dependent variability in tear protein retention on Schirmer strips and protein losses during sample handling, we recommend that researchers utilizing Schirmer strip-collected tear samples should characterize their specific elution protocols using model studies matched to their target proteins of interest, materials, and methods. Further, to avoid significant handling losses, we suggest employing elution techniques that minimize or eliminate sample transfers using integrated strategies with downstream analytical systems.

4.5 Conclusions

In sum, these results demonstrate that while diffusion-based processing of Schirmer strip-collected tear fluid is widespread throughout the literature, it results in total post-collection protein losses that are considerable, consistent, and protein-dependent. As a result, diffusion-

based processing of Schirmer strips after tears are collected affects both the absolute and relative concentrations of human tear proteins collected. This protein-dependency is impacted by protein molecular weight and surface hydrophobicity. Meanwhile, surface charge and surface hydrophilicity are not significantly associated with protein losses due to the Schirmer strip or elution protocol. As a result, the relative and absolute concentrations of eluted tear proteins collected with Schirmer strips are dependent on the protocol used and the protein target of interest.

These results point to the need for all tear studies that utilize Schirmer strip-collected tear samples to include additional controls (e.g., 'spike and recover' experiments such as those demonstrated here) to characterize the efficiency of the sample processing method used for the particular protein of interest. Because of the demonstrated variability in sample composition introduced by sample processing, quantitative measurements of tear proteins collected with Schirmer strips may only be comparable across studies if disparate assay measurements are related back to the starting ocular concentration, necessitating additional calibration studies. In lieu of this, tear fluid samples collected with Schirmer strips may not be an appropriate sample collection modality for multiplexed studies assessing the relative concentrations of a panel of tear proteins (e.g., protein microarray studies) since each target protein in the panel may exhibit different elution behavior. Thus, although often overlooked in research and clinical laboratories, carefully controlled and well-characterized tear sample preparation is critical in yielding scientifically and clinically meaningful results.

Chapter 5: Microfluidic Homogeneous Lactoferrin Immunoassay for Sjögren's Syndrome Diagnosis

5.1 Pathophysiology and Classification of Dry Eye Disease

Collectively dry eye disease, or keratoconjunctivitis sicca (KCS), affects 30-50 million Americans and can cause ocular burning, stinging, itching, pain, redness and, ultimately threaten a patient's vision.[37] Dry eye disease was historically defined as "a disorder of the tear film due to tear deficiency or excessive evaporation which causes damage to the interpalpebral ocular surface and is associated with symptoms of ocular discomfort."[110] However, conflicting results from the major tests for lacrimal deficiency and excessive evaporation continued to complicate a physician's ability to arrive at a definitive diagnosis for dry eye disease.[38] Further, subsequent research suggested that additional knowledge about the physiology of dry eye disorder and the role of ocular surface inflammation needed to be incorporated in the disease definition and clinical practice. As a result, the central mechanisms involved in each form of dry eye were reclassified in 2007 in the Dew report.[111] Dry eye is now defined as "a multifactorial disease of the tears and ocular surface that results in symptoms of discomfort, visual disturbance, and tear film instability with potential damage to the ocular surface. It is accompanied by increased osmolarity of the tear film and inflammation of the ocular surface."[111]

There are several distinct pathophysiological mechanisms that can lead to dry eye symptoms. The two primary causes of dry eye are an insufficient production of tears (aqueous-deficient dry eye) and excessive evaporation of tears (evaporative dry eye) (Figure 12). Both aqueous-deficient and evaporative dry eye have several potential underlying causes. Aqueous-deficient dry eye is due to a failure of lacrimal gland tear secretion and results in tear hyperosmolarity owing to the reduced tear volume present on the surface of the eye. Tear film hyperosmolarity in turn causes hyperosmolarity of the ocular surface epithelial cells and the initiation of a cascade of inflammatory events such as the release of inflammatory cytokines interleukin (IL)-1α, IL-1β, tumor necrosis factor (TNF)-α, and matrix metalloproteinases (MMP-9).[111-113] As such, tear film osmolarity has emerged as a putative biomarker to assess the extent of dry eye disease.

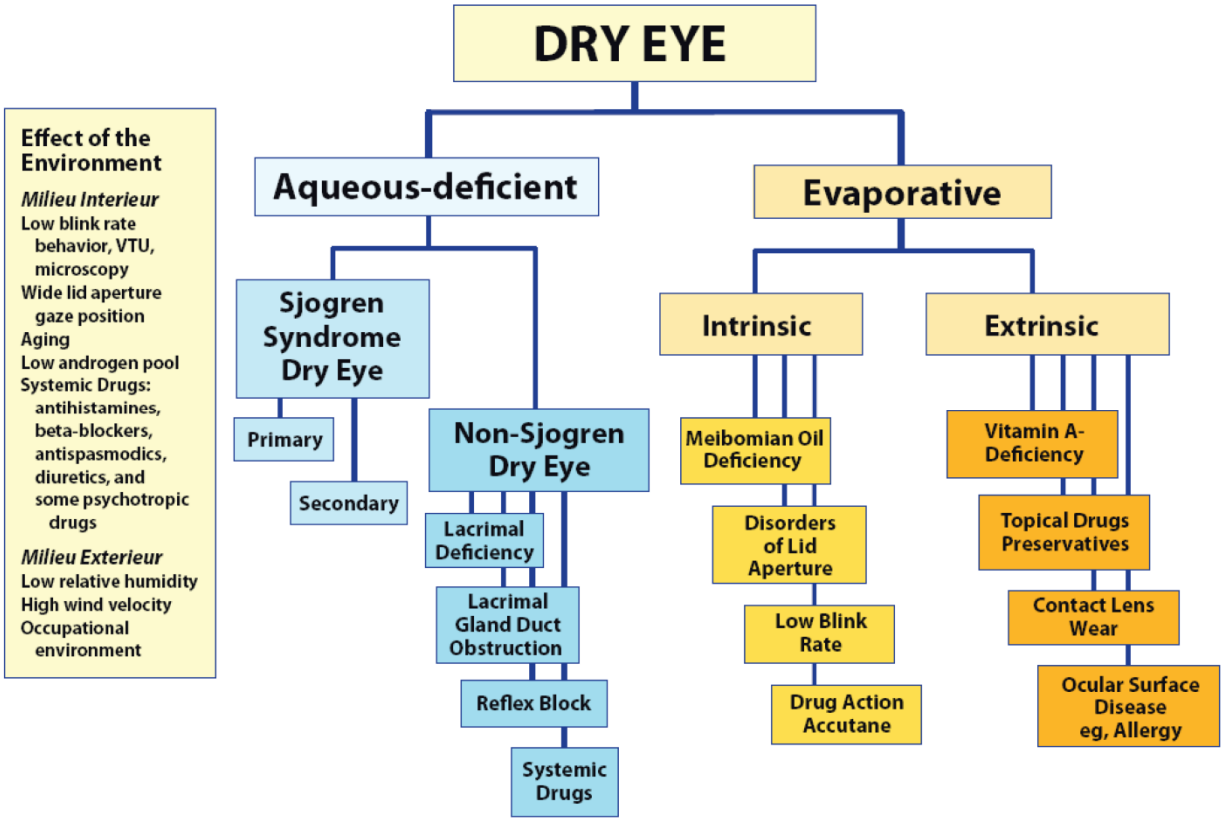

Figure 12. Major causes of dry eye disorder. The left hand box lists environmental factors that impact an individual's risk of developing dry eye. Reprinted from Lemp, et. al., The Definition and Classification of Dry Eye Diseases: Report of the Definition and Classification Subcommittee of the International Dry Eye Workshop *(2007), The Ocular Surface, 5(2) 75-92 with permission from Elsevier.*

Aqueous-deficient dry eye can be caused by Sjögren's syndrome (SS), a systemic autoimmune disease in which the lacrimal and salivary glands are targeted by the body's immune response. Alternatively, aqueous-deficient dry eye can be caused by non-Sjögren's syndrome causes such as lacrimal deficiencies such as lacrimal gland inflammatory infiltration in sarcoidosis (infiltration by sarcoid granulomata), lymphoma (infiltration by lymphomatous cells), AIDS (infiltration by T-cells), and graft-vs-host disease (lacrimal gland fibrosis). Another non-Sjögren's syndrome cause of aqueous deficient dry eye includes obstruction of the lacrimal gland ducts which transport tears from the lacrimal glands to the surface of the eye. This has been observed in diseases such as trachoma, cicatricial pemphigoid and mucous membrane perphigoid, erythema multiforme, and chemical or thermal burns. Hyposecretion of reflex tears can also arise from a blocking of the reflex sensory drive, which results in a reduction in lacrimal secretion or blink rate, or a block of the reflex motor system through central damage to the VII cranial nerve.[111]

Evaporative dry eye disease, in contrast, is due to excessive water loss from the surface of the eye while lacrimal gland function remains normal.[111] Evaporative dry eye can be intrinsic, where an intrinsic disease directly affects the regulation of tear evaporation (Figure 12). For example, the lipids produced in the meibomian gland, which form a lipid layer on the outer surface of the tear film may be defective or produced in insufficient quantities to prevent tear evaporation.[111] Meibomian gland dysfunction, or obstruction, is the most common cause of evaporative dry eye.[114] Poor lid congruity and lid dynamics, or a low blink rate, may also lead to longer periods of time where the eye is open, leading to additional time for evaporative tear loss to occur.[111]

In extrinsic evaporative dry eye disease, excessive evaporation occurs due to an extrinsic exposure. Extrinsic evaporative dry eye encompasses etiologies that increase evaporation through their pathological effects on the ocular surface. These causes include a deficiency of vitamin A, which is necessary for the development of goblet cells in mucous membranes and the formation of mucins, the action of toxic topical drugs such as preservatives which cause surface epithelial cell damage, prolonged contact lens wear, and a range of ocular surface diseases such as allergic conjunctivitis and others.

In addition to these accepted causes of dry eye, the left-hand box in Figure 12 lists several environmental factors that can increase an individual's risk of developing dry eye.[111]

5.2 Sjögren's Syndrome (SS)

Sjögren's syndrome (SS) is a serious form of aqueous-deficient dry eye disease. First published in 1933 by the Swedish ophthalmologist Henrik Sjögren,[115] SS is a systemic automimmune disease affecting 1-2% of the general population[36] that is characterized by decreased lacrimal and salivary gland function which results in severe dry eyes and dry mouth.[30] In Sjögren's syndrome, activated T-cell lymphocytes infiltrate the epithelium of the lacrimal and salivary glands, which causes acinar and ductular cell death, cytolysis of lacrimal gland cells, and reduced production and secretion of tears or saliva. Inflammation in the glands leads to the expression of autoantigens at the surface of epithelial cells (e.g., fodrin, Ro, and La) and the accumulation of tissue-specific CD4 and CD8 T-cells.[111] In non-SS dry eye, the lacrimal gland is not destroyed by lymphocytic infiltration and the gland can often still produce tears. An estimated 90% of SS patients are elderly women and the mean age at diagnosis is 50 years.[115]

Two forms of SS are recognized. Primary SS consists of the occurrence of aqueous deficient dry eye disease along with symptoms of dry mouth, a detection of autoantibodies in the blood or tears, evidence of reduced salivary secretion, and a positive focus score in a minor salivary gland biopsy.[111,115]

Secondary SS incorporates the features of primary SS along with the presence of an overt autoimmune connective tissue disease. Rheumatoid arthritis is the most common contributor to secondary SS, but others include systemic lupus erythematosis, polyarteritis nodosa, Wegener's granulomatosis, systemic sclerosis, primary biliary sclerosis, or mixed connective tissue disease.[111] Accurately distinguishing between primary and secondary SS is important

owing to the genetic, clinical, and diagnostic differences between them.[115] Further, since a diagnosis of primary SS results in increased risk for salivary gland cancers and co-occurrence with other connective tissue diseases such as rheumatoid arthritis and lupus, early diagnosis can lead to early clinical intervention, and avoidance of more severe manifestations of the these diseases.

Although there is no cure for SS, it is important to be able to differentiate this form of aqueous deficient dry eye from other forms of dry eye in order to treat the systemic as well as the ocular forms of the disease. The severity of some of its features can be minimized with proper identification and targeted treatment.[115]

5.3 Diagnosis and Treatment of Dry Eye Disease and Sjögren's Syndrome

When a patient presents with dry eye symptoms in an ophthalmologist's office, the clinician will run a series of tests that make general measurements of tear volume, ocular surface epithelial cell health, tear salt concentration (osmolarity), mucin staining patterns, and lipid layer thickness. Many of these diagnostic tests (outlined in Table 1 above) address either one or more aspect of the condition and generally more than one test is needed to diagnose KCS. Yet to date, there is no rigorous standard series of tests for clinicians to use, leading to widespread differences in the diagnosis of dry eye and the prevalence of each test in clinical practice.[113]

Some attempts to standardize the diagnosis of KCS have been published including a composite grading system that can be used to assess dry eye severity (Figure 13). When testing for a general KCS diagnosis, Schirmer testing without anesthetic and Rose Bengal staining are the most specific tests (100%) but suffer from low sensitivity (10% and 58%, respectively).[38] The most sensitive tests were an increase in lactoferrin concentration from basal to reflex tears or percent increase in lactoferrin (96%) and tear osmolarity (76%).[38]

Dry Eye Severity Level	1	2	3	4*
Discomfort, severity & frequency	Mild and/or episodic; occurs under environmental stress	Moderate episodic or chronic, stress or no stress	Severe frequent or constant without stress	Severe and/or disabling and constant
Visual symptoms	None or episodic mild fatigue	Annoying and/or activity-limiting episodic	Annoying, chronic and/or constant, limiting activity	Constant and/or possibly disabling
Conjunctival injection	None to mild	None to mild	+/–	+/++
Conjunctival staining	None to mild	Variable	Moderate to marked	Marked
Corneal staining (severity/location)	None to mild	Variable	Marked central	Severe punctate erosions
Corneal/tear signs	None to mild	Mild debris, ↓ meniscus	Filamentary keratitis, mucus clumping, ↑ tear debris	Filamentary keratitis, mucus clumping, ↑ tear debris, ulceration
Lid/meibomian glands	MGD variably present	MGD variably present	Frequent	Trichiasis, keratinization, symblepharon
TFBUT (sec)	Variable	≤ 10	≤ 5	Immediate
Schirmer score (mm/5 min)	Variable	≤ 10	≤ 5	≤ 2

*Must have signs AND symptoms. TBUT: fluorescein tear break-up time. MGD: meibomian gland disease

Reprinted with permission from Behrens A, Doyle JJ, Stern L, et al. Dysfunctional tear syndrome. A Delphi approach to treatment recommendations. *Cornea* 2006;25:90-7

Figure 13. Grading scheme commonly used to assess dry eye severity. Reprinted from Lemp, et. al., The Definition and Classification of Dry Eye Diseases: Report of the Definition and Classification Subcommittee of the International Dry Eye Workshop *(2007), The Ocular Surface, 5(2) 75-92 with permission from Elsevier.*

Accurate diagnosis of Sjögren's syndrome also remains a critical challenge in clinical ophthalmology. Relying on the same analytical tools as those available for reaching a general diagnosis of KCS, current practice in diagnosing Sjogren's syndrome is non-standardized[36,115,116] and reliant on subjective symptoms and crude measures of tear volume (Schirmer's test), tear film quality (tear break-up time) and corneal and conjunctival epithelial integrity (corneal and conjunctival staining).[23,43,116] There is often good agreement on the diagnosis of patients with extreme symptoms for SS, but diagnosis of those with milder sicca symptoms remains controversial due to a lack of good non-invasive methods of quantifying dry eye and dry mouth symptoms.[117]

Many different diagnostic criteria exist for SS including those from San Francisco, Tokyo, La Jolla[118], Copenhagen, Ioannina (Greece), and the European Community.[119] Differences in the specific requirements of each criteria add to variability in the disease definition, prevalence numbers, and diagnostic accuracy.[115] For example, the demonstration of focal lymphocytic infiltrates in a minor salivary gland biopsy remains the gold standard for the oral component of the diagnosis. A cluster of 50 or more lymphocytes is considered a "focus." However, the number of foci required to return a positive diagnosis differs across the geographic criteria.

Greater than one foci per 4 mm^2 of tissue is considered a positive diagnosis of SS using the San Francisco criteria.[117,120] In the San Francisco criteria, patients must also have KCS as demonstrated by characteristic rose Bengal staining patterns and a Schirmer test of < 10 mm/5 min of wetting time. Meanwhile, in the Tokyo criteria, SS requires two of the following: (1) ocular rose Bengal stain (++) and Schirmer test < 10 mm/5 min and/or positive fluorescein stain; (2) > 1 lymphocytic focus in a lacrimal or salivary gland (the tissue size was not specified); and/or (3) a sialogram showing diffuse nodular or globular sialectasis with diameter > 1mm.[115] In the Copenhagen criteria, KCS was diagnosed when unanesthetized Schirmer test ≤ 10 mm/5 min, tear break-up time ≤ 10 seconds, and/or rose Bengal staining ≥ 4. Xerostomia required two of the following: unstimulated whole salivary glow < 1.5 mL/15 min, labial salivary gland biopsy with focus score > 1 focus per 4 mm^2 of tissue, decreased uptake or secretion in salivary scintigraphy, or abnormal sialography.[115] The European Community (EC) criteria requires four of the following six criteria to be met: (1) one of three specified ocular symptoms, (2) one of three specified oral symptoms, (3) a Schirmer test ≤ 5 mm/5 min or ocular rose Bengal stain ≥ 4, (4) a labial salivary gland biopsy with ≥ 1 focus per 4 mm^2 of tissue, (5) positive results in either scintigraphy, sialography, or unstimulated whole flow salivary tests, and (6) presence of rheumatoid factor, antinuclear antibody, anti-SS-A or anti-SS-B serum autoantibodies.[115] It is clear that the lack of diagnostic standardization makes it especially challenging to diagnose SS.

The requirement for a salivary or lacrimal gland biopsy is a critical component to reaching a definitive diagnosis of SS. However, this invasive salivary gland biopsy (Figure 14) is often refused,[77,116] making the average time from the onset of symptoms to a positive diagnosis approximately 6.5 years (Figure 15).[121] Since the severity of the disease can lead to debilitating complications, there is a need for an improved diagnostic test for SS that is quantitative, definitive, rapid and, importantly, non-invasive.

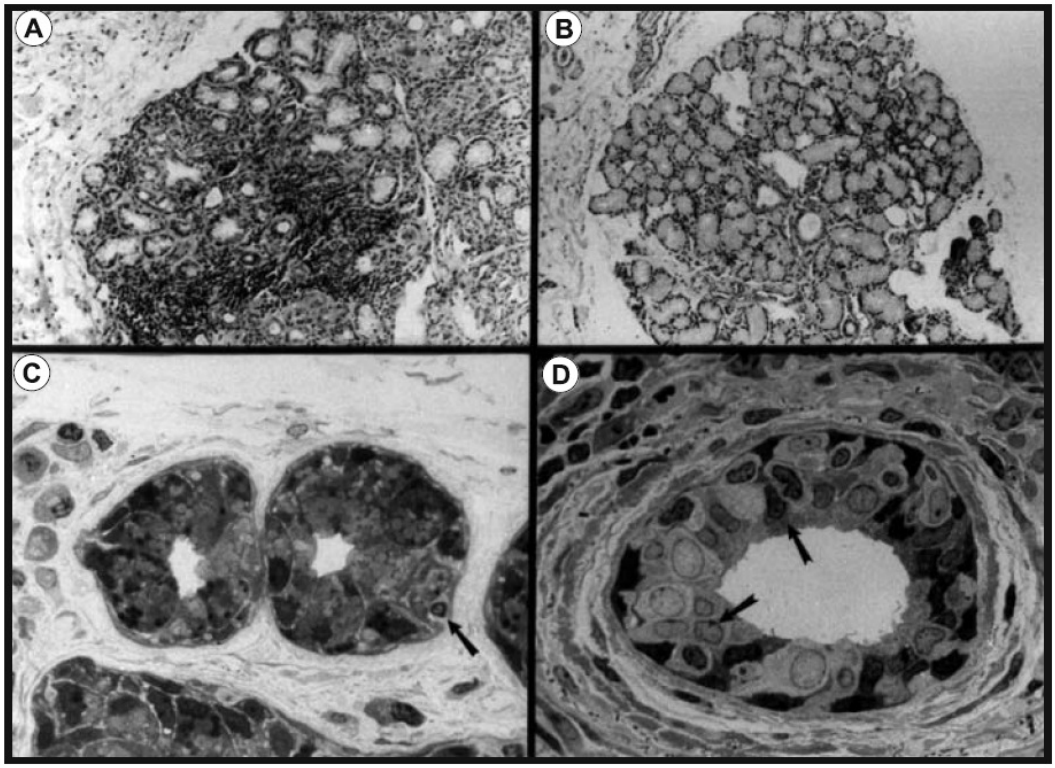

Figure 14. Minor salivary gland biopsy from a patient with Sjögren's syndrome (A) and fibromyalgia (B). Higher power views of the Sjögren's syndrome biopsy are given in (C) and (D). Reprinted from RJ Fox and I Saito, Autoimmune Diseases of the Skin, *Springer, 2005, 261-289 with kind permission from Springer.*

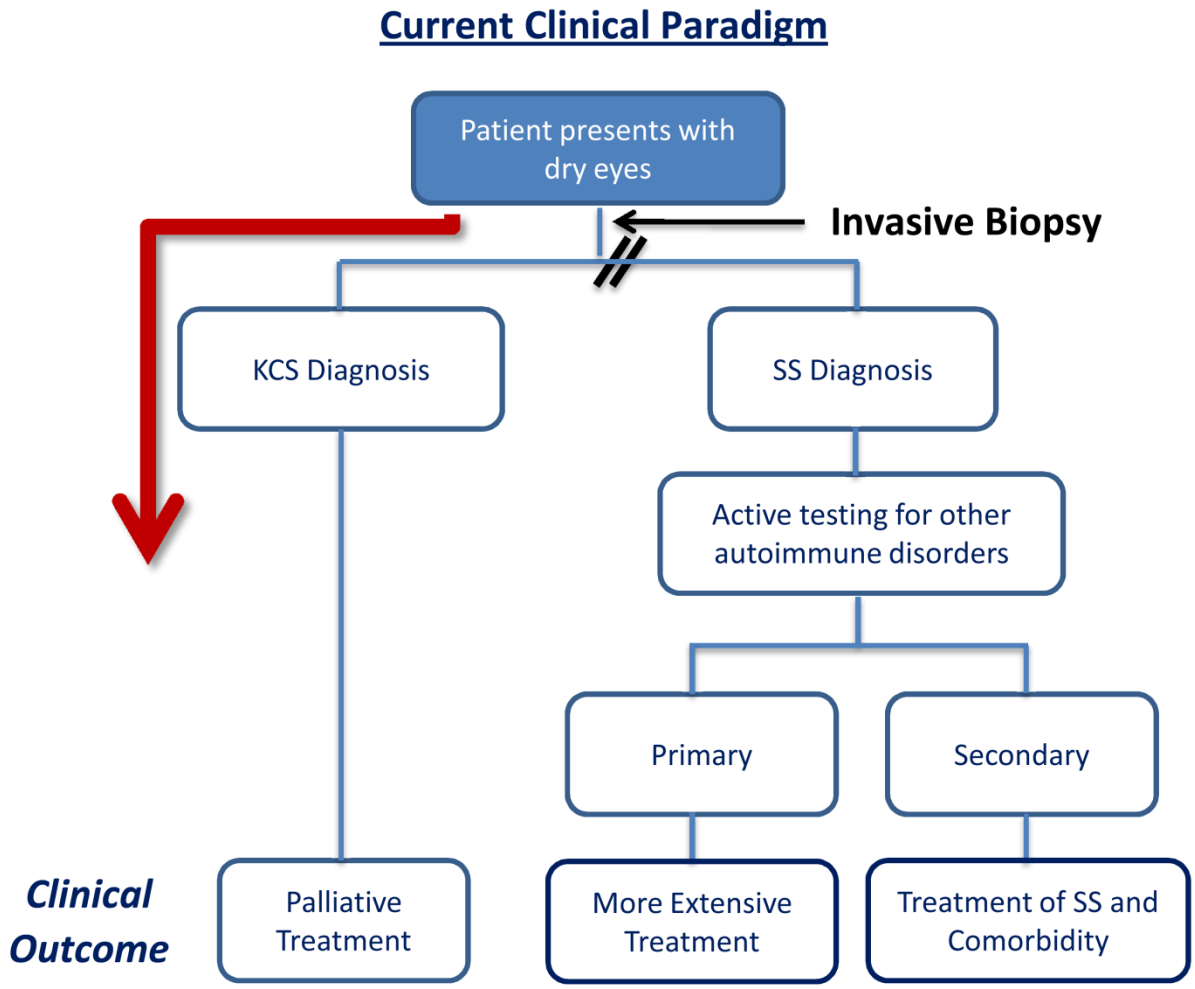

Figure 15. Current clinical paradigm in SS diagnostics. An invasive salivary or labial gland biopsy prevents effective diagnosis of SS and any associated co-morbidities as well as early and effective treatment.

Proper treatment of dry eye disease and SS includes addressing the systemic as well as the ocular manifestations and causes of the disease, underlying the importance of distinguishing between these numerous and diverse disease mechanisms. Therefore, the primary goal in diagnosing dry eye disease is to determine the underlying cause of the dry eye symptoms so as to enable targeted treatment aimed at correcting the underlying physiological cause of the symptoms. In practice, artificial tears and ointments are commonly used to replace tear volume in KCS patients.[37] However, these palliative treatments do little to augment the quality of the tears themselves by replacing essential proteins, mucins, or lipids, or suppressing the underlying immune response. There is a need to add tear proteins with biologic activity to supplement tear quality as well as quantity.[30] For example, autologous serum, when applied to the ocular surface, has been shown to provide essential components to the ocular surface and improve ocular health.[30] Further, artificial tears do not help in many evaporative forms of dry eye when tear volume may be normal and evaporation will not be reduced merely by artificially

increasing tear volume further. Treatment of SS is also important since early identification and intervention can lead to the avoidance of more severe manifestations of other co-morbidities such as rheumatoid arthritis or lupus, which are commonly associated with SS.

Despite the need to distinguish between the diverse disease mechanisms of dry eye in order to appropriately administer treatment, currently available ophthalmology tests are largely unable to differentiate between the various forms of the disease and are further unable to differentiate SS dry eye. For example, a measurement of tear volume returns a general diagnosis of dry eye disorder or lack thereof. Information about ocular surface cell health returns a general diagnosis of poor ocular surface health. A quantitative measurement of tear salt concentration returns a general diagnosis of dry eye disease and an indication of the severity of disease. Importantly, none of these tests give information about whether the dry eye disease is aqueous deficient or evaporative in mechanism. Further, mucin staining patterns and lipid layer thickness measurements may only suggest deficiencies in mucin or lipid layers and are subject to qualitative interpretation.

New, quantitative analytical tools are needed in ophthalmology to (1) differentiate between evaporative and aqueous deficient dry eye disease mechanisms, and (2) specifically identify SS from other forms of KCS. An objective, non-invasive differential diagnosis between KCS and SS would eliminate the need for an invasive labial or salivary gland biopsy and lead to early SS disease management, earlier diagnosis and treatment of systemic autoimmune diseases and offer the possibility of pre-symptomatic testing for autoimmune diseases (Figure 16). Next-generation dry eye diagnostic tests may include assays capable of quantitatively assessing lacrimal gland function, which would enable the differentiation evaporative dry eye and aqueous deficient dry eye patients. Further, a non-invasive, quantitative test for a biochemical biomarker of SS could have implications in the improved diagnosis, treatment and understanding of SS and its common co-morbidities.

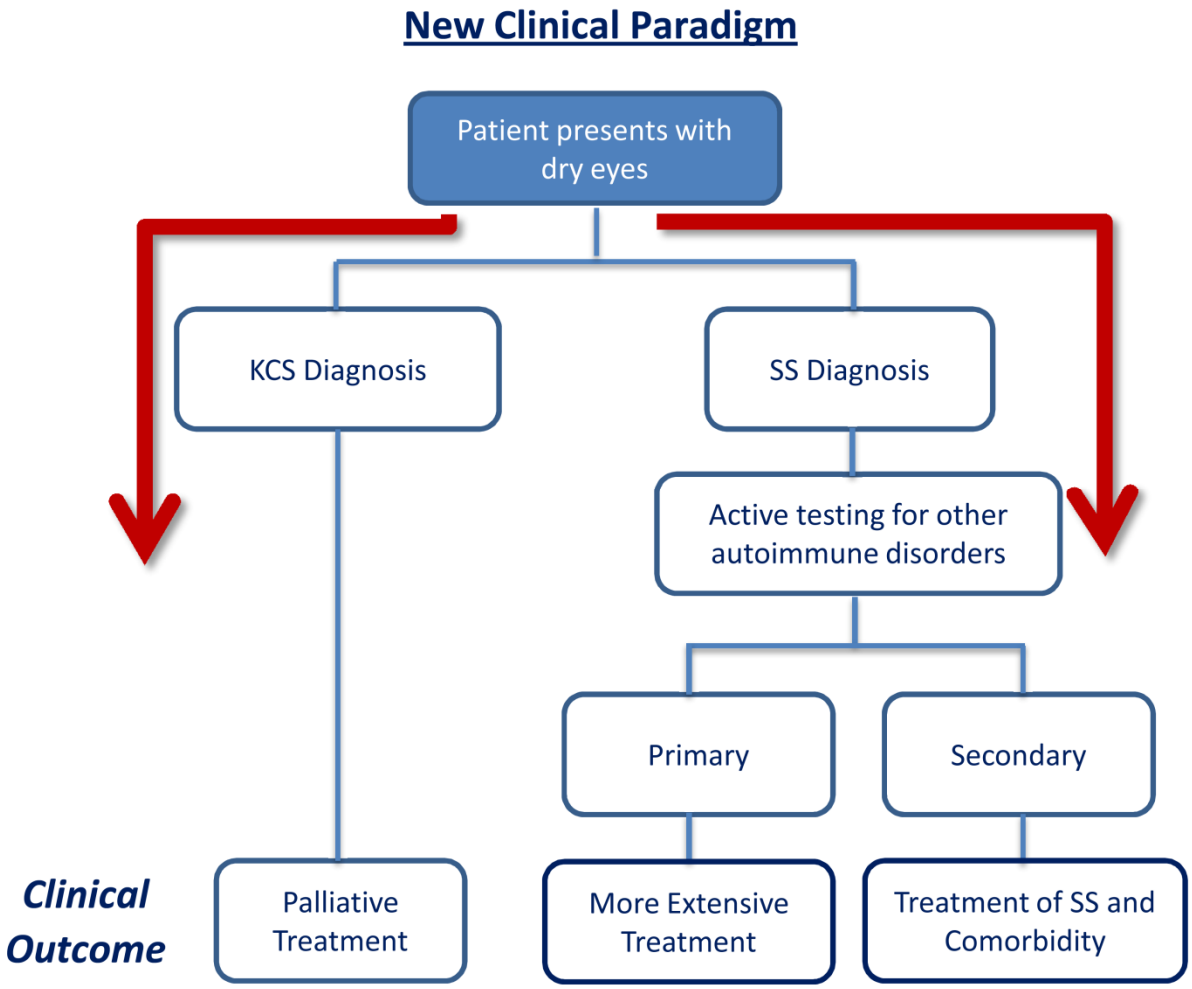

Figure 16. An improved diagnostic tests able to differentiate between KCS and SS dry eye patients would eliminate the need for an invasive labial or salivary gland biopsy and provide a standardized diagnostic metric.

5.4 Lactoferrin as a Candidate Biomarker for Sjögren's Syndrome Stratification

Lactoferrin (Lf) is a protein that is found in tears, milk, saliva, serum, mucosal secretions and neutrophils, among other fluids.[122,123] Tear Lf is one of the five principal tear proteins with an average concentration of 1.84 mg/mL, or 25% of total tear proteins.[21] Tear Lf is produced in the lacrimal gland and excreted into the tear fluid. As such, tear Lf has been identified as a putative tear protein biomarker for primary SS.[30] Lf is down regulated in SS tears compared to the tears of patients with other forms of dry eye disorders (non-SS KCS patients) as well as normal, healthy patients (Figure 17).[30] Lf, when applied to the ocular surface, has also been shown to reduce the loss of corneal epithelial cell integrity.[124,125] This suggests that the absence of Lf on

the ocular surface may amplify ocular cell death and dry eye symptoms. Albumin has also been suggested as an internal control that should not change with disease state and an albumin to lactoferrin ratio above 2:1 has been proposed as a diagnostic threshold for primary SS.[55] Preliminary results suggest that such a test would have a sensitivity of 67% and specificity of 100%.[55]

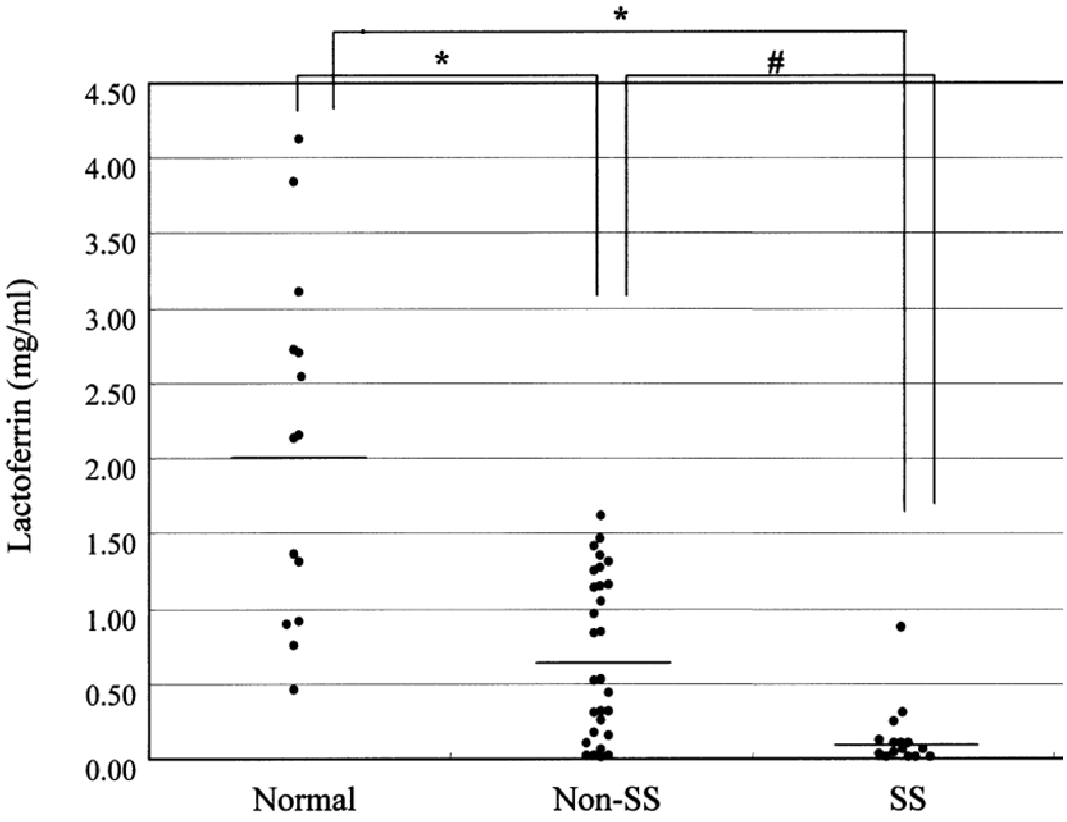

Figure 17. Lactoferrin concentration in normal, non-SS KCS tears, and SS tears. '' and '#' indicate significant differences between the groups with $p < 0.05$ (Mann-Whitney test). Reprinted from Ohashi, et al.,* Abnormal Protein Profiles in Tears with Dry Eye Syndrome*, American Journal of Ophthalmology, 2003, 136(2),291-299, with kind permission from Springer.*

Towards the clinical goal of developing quantitative analytical tools to differentiate between evaporative and aqueous deficient dry eye disease mechanisms and specifically identify SS from other forms of KCS, we endeavored to create an assay capable of making specific, targeted measurements of Lf concentration in human tears. Such an assay has several major motivations including:

(1) Tear fluid as a non-invasive, peripheral fluid sample matrix: The use of tear fluid in SS diagnosis would have the benefit of being non-invasive, obfuscating the need for an invasive salivary or lacrimal gland biopsy as is currently required. Further, tear fluid,

being a peripheral fluid located in proximity to the site of immune attack (e.g., the lacrimal gland), is likely to contain the largest detectable signal from the disease. Biochemical markers of Sjögren's syndrome are likely to be the most concentrated in tears compared to systemic fluids such as blood.

(2) Differentiation of evaporative vs. aqueous deficient dry eye: Lf is produced in the lacrimal gland and therefore may provide a quantitative marker for lacrimal gland function. A quantitative assessment of lacrimal gland function would enable the differential diagnosis of evaporative (no lacrimal gland involvement) vs. aqueous deficient dry eye (lacrimal gland dysfunction), providing important information not attainable with current techniques.

(3) Differentiation of SS from other forms of dry eye: Based on the preliminary results from Ohashi, et al.,[30] Lf may be able to differentially diagnose SS from other forms of dry eye disease with the establishment of proper concentration thresholds. In Ohashi, et al., KCS patients were diagnosed according to the following criteria: (1) symptoms of dry eye, (2) abnormalities of test dynamics determined by the Schirmer (< 5 mm/5 min) and clearance tests (< 8 x), and (3) abnormalities of the ocular surface determined by rose Bengal or fluorescein vital staining (> 3+).[30] Meanwhile, diagnosis of SS was made using the La Jolla criteria[118] which requires the following to make a diagnosis of "definite SS": (1) objective evidence of KCS as documented by rose Bengal or fluorescein dye staining, (2) objective evidence of diminished salivary gland flow, (3) minor salivary gland biopsy, obtained through normal mucosa, with the specimen containing at least 4 evaluable salivary gland lobules, and having an average of at least 2 foci/4 mm^2, and (4) evidence of a systemic autoimmune process, as manifested by the presence of autoantibodies, such as rheumatoid factor and/or anti-nuclear antibody.[118] As Ohashi, et al. reported (Figure 17), Lf levels in SS patient tears are lower and much less variable than those of patients with other forms of KCS. Further, Lf levels are lower in both SS and KCS patients compared to healthy controls, suggesting that Lf may be able to differentiate between SS and other forms of non-SS KCS.

Lactoferrin is a 77 kDa polycationic, iron-binding glycoprotein with a maximal positive charge located in the arginine-rich N-terminal region (Figure 18, N-terminal region highlighted in blue).[22,126] Lf is alkaline with an isoelectric (pI) point of 8.7[45] and is known to associate rapidly with acidic proteins.[46] In addition to its potential as a SS biomarker, it has also been shown to have antimicrobial and anti-inflammatory activity in tears through reducing the availability of the iron necessary for microbial growth and inhibiting biofilm formation.[22]

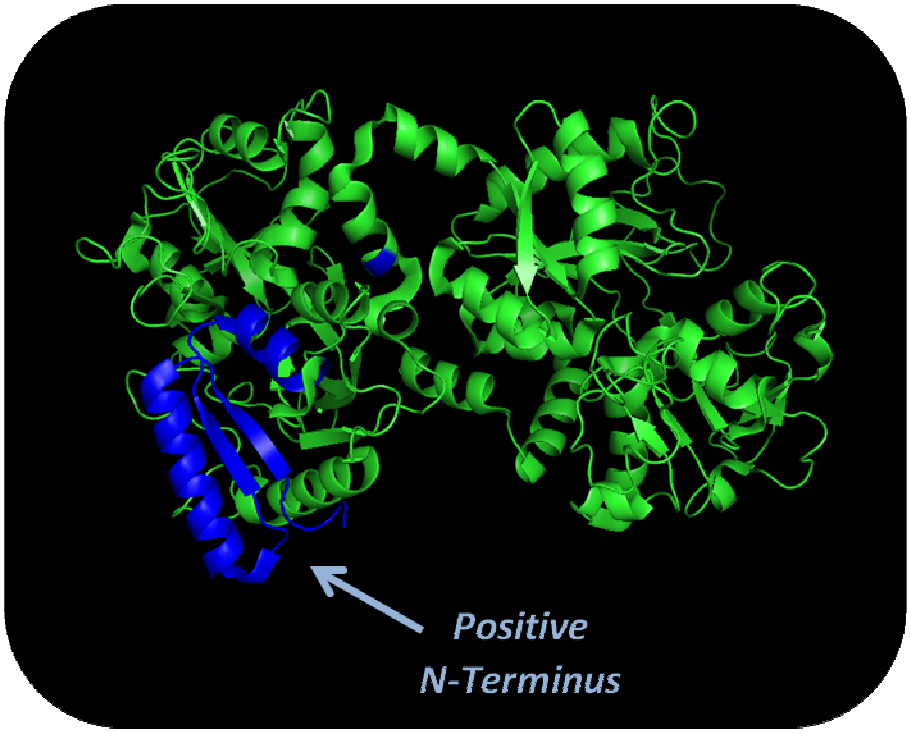

Figure 18. 3D structure of human diferric lactoferrin. The last 50 residues of the N-terminus, which contribute positive charge at physiological pH, are highlighted in blue. Structural information was obtained from the Protein Data Bank[127] and displayed using pymol. The original protein crystal structure is from Sun, et al., 1999[128]

Quantitative measurements of Lf levels in tears to date have been done through ELISA,[30] radial immunodiffusion assays (e.g., Lactoplate),[32,129-131] colorimetric solid phase ELISA (e.g., Lactocard),[130] and iTRAQ technology coupled with 2D-nanoLC-nano-ESI MS/MS.[43] Non-quantitative and semi-quantitative detection of Lf levels in tears have been done with PAGE slab gel assays.[55] However, measuring Lf in tear fluid remains challenging owing to the low sample volume availability inherent to dry eye tear fluid analysis, propensity of Lf to non-specifically bind to acidic proteins in tears or other positively charged molecules or structures in the system, and other interfering signals contributed by the tear matrix. There is a clear motivation for improved instrumentation, especially when working toward tear-based assays with clinical relevance.

5.5 Microfluidic Homogeneous Immunoassays for Measurement of Tear Proteins in Sparingly Available Ocular Fluid

Homogeneous electrophoretic microfluidic immunoassays are a powerful technique for the rapid quantification of proteins in low volumes of complex biological fluids and have been demonstrated previously in saliva,[132] serum,[5,16,133-135] plasma,[136] and cerebral spinal fluid.[137] In this technique, an antibody probe specifically captures the analyte of interest and the unbound antibody probe is electrophoretically separated from the bound immune complex. Binding of the antibody probe to the free protein target of interest induces a mobility shift caused by the molecular weight difference between the antibody-antigen immune complex and free antibody in the system. This mobility shift between the bound and unbound forms of the target antigen enables the effective separation of the antigen from the other components in the complex fluid.

Introduction of a sieving matrix within the microfluidic channels eliminates bulk driving flow (i.e. electroosmotic flow, Poiseuille flow) and enables enhanced analyte control, elimination of bulk flow-induced dispersion and a resulting increase in resolution capacity. Direct detection of the resultant immune complex allows for quantification of analyte concentration in a matter of seconds[11,138] to minutes.[132,139-141] The assay returns both charge-to-mass ratio ('size') and immunoaffinity information. The size of the detected immune complex peak(s) can therefore be used to positively identify the specifically-bound Lf-antibody pair for targeted detection of Lf amidst the background and non-specific binding commonly observed in other tear protein detection modalities.

Microfluidic technology is particularly appropriate for analysis of tear proteins because of the small sample volume requirements, which are especially important when analyzing sparingly available tear fluid from dry eye patients, which averages approximately 1 µL. The rapid analysis time of microfluidic homogeneous immunoassays is beneficial for point-of-care settings where time-to-diagnosis must be minimized to enable rapid transmission of information from doctor to patient and to accelerate treatment initiation. Further, the ability to use sizing information obtained by the electrophoretic migration to discriminate between specifically and nonspecifically bound immune complex peaks provides an additional – and important – piece of information over other purely affinity-based techniques. As such, microfluidic homogeneous immunoassay techniques pair the targeted specificity of immuno-detection with the sizing information needed to discriminate between the true signal and non-specific antibody binding interactions.

A successful electrophoretic immunoassay conducted without a bulk driving flow requires all analytes to possess the same net charge (e.g., anionic or cationic). The pI points of antibodies and resultant immune complexes are dependent on epitope and paratope locations and binding configuration, making prediction of pI point difficult. As such, most assay developers must either theoretically or experimentally determine the pI points of their analytes before the assay is performed. Practically, this limits the analytes that can be separated with this technique. A review of reported homogeneous electrophoretic immunoassay targets

conducted in said format shows that such assays have been most successful for a narrow range of weakly acidic proteins. Successful targets include: C-Reactive Protein (pI 5.28) and TNF-α (pI 7.0);[142] human serum proteins transferrin (pI 6.7), albumin (pI 5.67) and α-1-antitrypsin (pI 5.37);[143] matrix metalloproteinase 8 (pI 5.49);[132] interleukin-6 (pI 6.21);[144] human prostate specific antigen (pI 7.36);[145] ovalbumin (pI 5.19);[138] and ricin (pI 7.09) and shiga (pI 5.59) toxins.[146] Further, protein ladders that are commonly used for native separations employ proteins with a narrow pI range (e.g. Sigma ladder: pI range 4.6 to 6.4; Invitrogen ladder: pI range 4.61 to 6.19).[45]

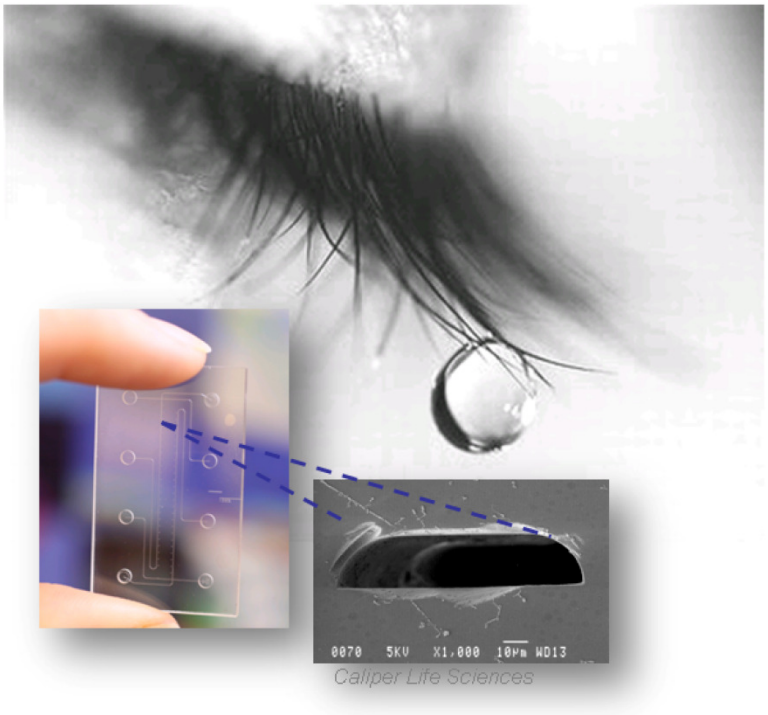

Figure 19. The small sample requirements of microfluidic homogeneous immunoassays make them well-suited for human tear protein analysis. A picture of the microfluidic chip used in this work is shown as well as a scanning-electron-microscope image of the channel cross-section, courtesy of Caliper Life Sciences. Image of tear is from wallpaperswide.com[147]

Owing to the potential benefits of using microfluidic immunoassays to measure tear protein biomarker levels, we endeavored to develop an alkaline microfluidic immunoassay capable of making rapid, quantitative measurements of endogenous lactoferrin concentrations in the human tear film fluid of healthy and SS patients. We believe this work would improve the analytical toolkit available for tear fluid proteomic measurements and would enable the creation of a translatable assay with real clinical relevance to SS diagnostics. Further, the development of a highly alkaline microfluidic immunoassay capable of separating analytes irrespective of their pI point would eliminate the need to predict complex and antibody pI

points, would expand the range of proteins that can be detected in an electrophoretic immunoassay format to include more alkaline proteins, and would have direct utility in the analysis of the highly alkaline proteins, such as Lf, that are commonly found in tear fluid.

In the following sections, we present the development, optimization and demonstration of a microfluidic immunoassay capable of quantifying the concentration of endogenous Lf in healthy and SS tear fluid in a clinically relevant range for SS diagnostics. We discuss the implications of using a high pH buffer for polyacrylamide (PA) gel polymerization and stability, effects caused by the addition of the tear matrix and characterize assay sensitivity, specificity, accuracy and predictive value. The final assay is shown to measure down-regulated Lf levels in diseased patients and be highly specific for endogenous Lf, highly correlative to ELISA measurements, and predictive of known concentrations of Lf spiked into the confounding tear matrix. Further, we are able to take steps in addressing the problem of rampant sample collection variability for the first time in the literature by relating the final measured concentration of Lf in the collected tear sample back to the actual concentration in the eye, using our sample preparation protocol.

Taken in total, our results suggest that this alkaline microfluidic immunoassay is capable of rapidly measuring tear protein biomarkers for a wide variety of uses in both basic research and clinical medicine.

5.6 Electrophoretic Separations of Alkaline Proteins

Although many proteins in the body have isoelectric (pI) values in the range of pH 4-7, proteins with pI > 7 are also known.[148] Proteins with a pI value lower than the pH of the surrounding buffer conditions carry a net negative charge and migrate toward the anode during electrophoresis. Meanwhile, proteins with a pI value higher than the pH of the surrounding buffer conditions carry a net positive charge and migrate toward the cathode during electrophoresis.[148] Proteins with a pI value that is the same as the pH of the surrounding buffer are neutrally charged and do not migrate under the application of an electric field. Therefore, while the polarity of the electrodes in an electrophoresis apparatus can be reversed to either detect positively charged or negatively charged proteins, it is not possible to detect both positively and negatively charged proteins in the same gel.[148]

The most common electrophoresis buffers follow the Good's buffers closely and are chosen to buffer in a range of physiological pH. The Goods Buffers (Figure 20), which were published in 1966 and chosen for their relevance for biological research applications, range in pKa from 6.15 (MES) to 8.35 (Bicine).[149] This narrow range of buffer pH values limits the range of proteins that can be separated with electrophoresis. Antibody samples typically have heterogeneous pI points that are in a physiological range. Therefore, electrophoretic separations that aim to separate both an antibody and a protein must use a buffer that imparts the same charge to both the antibody and the protein. Practically speaking, this means that the buffer pH must either be below physiological pH, making both the antibody and protein net positive, or above physiological pH, making both the antibody and protein net negative. Since Goods Buffers only have a pH range of 6.15 to 8.15, they often do not provide a wide enough range of pH values to

separate more acidic or alkaline proteins. As a result, a challenge in electrophoretic protein analysis is separating very acidic and alkaline proteins.

Proposed Name	pK, at 20°
MES	6.15
ADA	6.6
PIPES	6.8
ACES	6.9
Cholamine chloride	7.1
BES	7.15
TES	7.5
HEPES	7.55
Acetamido-glycine	7.7?
Tricine	8.15
Glycinamide	8.2
Tris	8.3
Bicine	8.35
Glycylglycine	8.4

Figure 20. Twelve 'Goods Buffers' commonly used in biological research and electrophoretic protein separations. The range of pKa values indicates their buffering range (6.15 – 8.4). Reprinted with permission from Good, et al., Hydrogen Ion Buffers for Biological Research, Biochemistry, 1966, 5(2) 476-477. Copyright (1966) American Chemical Society.

Several approaches to separating alkaline proteins have been published. Su, et al., utilized a horizontal electrophoresis system and pH 8.9 tris-glycine buffer to separate recombinant human phospholipiase A2 (pI > 10), cytochrome c (pI > 10.3), and recombinant interleukin-2 (pI < 7.8). The sample wells were along the center of the gel so that the positively and negatively charged proteins could migrate toward the cathode and anode, respectively.[148] Alternate buffers with more basic and acidic pH values have been published in order to impart the same

charge to all proteins in the system. For example, Zais et al. used tris(hydroxymethyl)amino-methane/ethylenediaminetetraacetic acid/borate buffer (pH 9.2) to separate a2-macroglobulin and haptoglobin type 2-2.[150] Kaltschmidt et al. used acetate buffer, pH 4.6 to separate proteins from the ribosomal subunits of *E. coli* bacteria several of which have pI > 8.6.[151] Despite these demonstrations, additional innovation is needed to push the range of proteins that can be analyzed with electrophoresis.

5.7 Homogeneous Microfluidic Immunoassay Design and Fabrication

Assay design and overview of operation

The assay hardware includes a glass slide with etched microfluidic channels filled with photopolymerized polyacrylamide gel. The channels intersect perpendicularly in a 'T' architecture (Figure 21). The operation of the assay is outlined in Figure 22. Briefly, we first collected the tear samples from the eye using a Schirmer strip, which is a nitrocellulose membrane that wicks tear fluid off the surface of the eye and is a widely used tool in clinical ophthalmology. We then reconstituted the tear sample in 1× buffer and incubated the sample with a fluorescently labeled antibody specific to our protein biomarker target (Lf) before pipetting it onto the microfluidic chip in well 'S'. An electric field was then applied from top to bottom (well 'S' to well 'SW', Figure 21) so that the charged protein molecules migrate and load into the chip. The field was then switched horizontally (well 'B' to well 'BW') so that a tight band of sample was injected into the 'separation channel.' The free antibody and bound immune complex were then allowed to migrate according to their differential mobilities and resolve from each other. Fluorescence was monitored in the 'imaging area' (Figure 21) using an inverted epi-fluorescence microscope and CCD camera. An intensity profile of the separation channel was then taken as the fluorescent protein bands migrate past the imaging region to quantify the amount of immune complex present in solution.

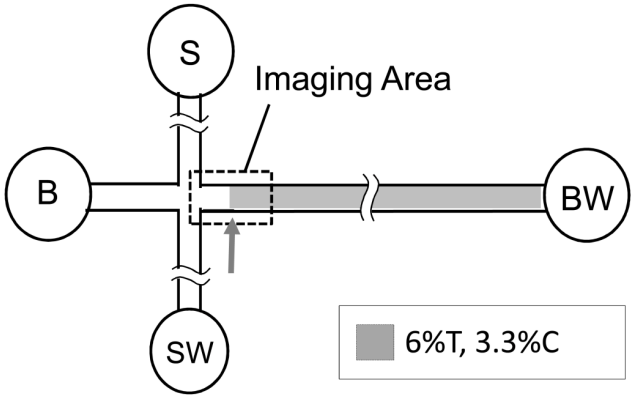

Figure 21. Schematic of channel lay-out of microfluidic chip used in this study including sample (S), sample waste (SW), buffer (B) and buffer waste (BW) wells. A 3-6%T (3.3%C) discontinuous pore-size PA gel is indicated by the shading in the separation channel.

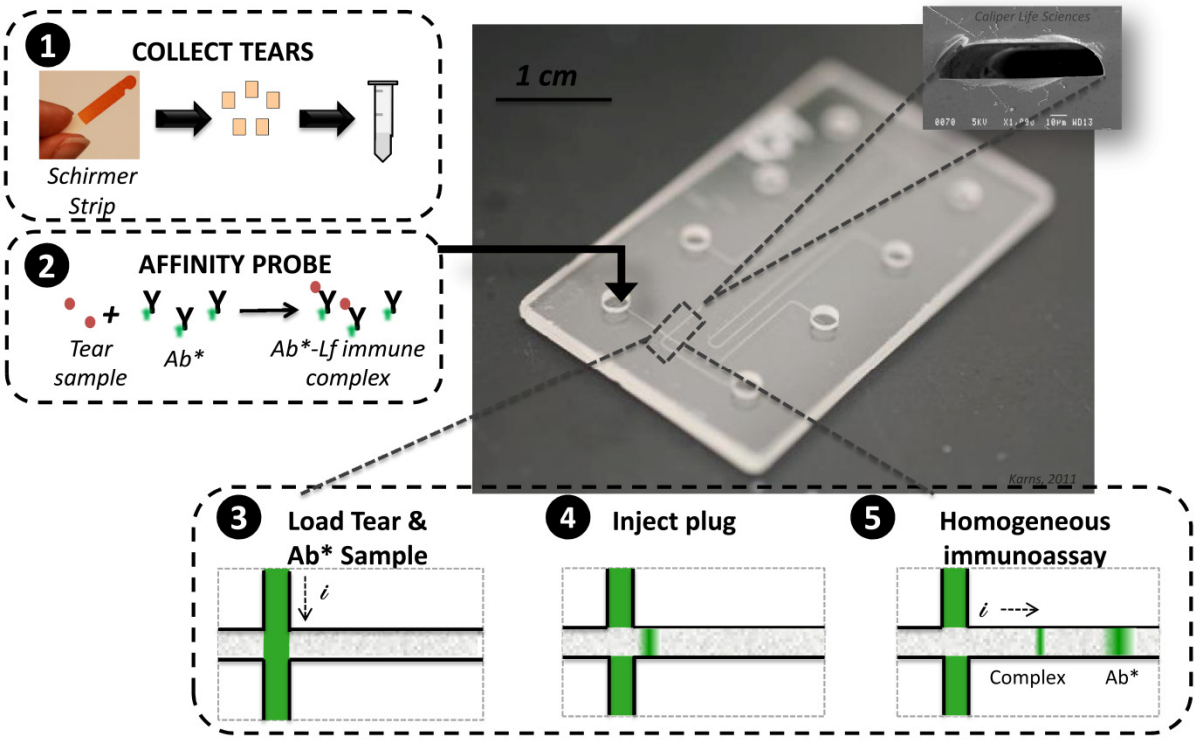

Figure 22. Assay concept for microfluidic tear Lf immunoassay. Assay steps include (1) collecting tears with a Shirmer strip, (2) reconstituting the tear proteins and incubating with a fluorescently-labeled antibody probe, (3) electrophoretically loading the sample on-chip, (4) injecting a plug of sample into the 'separation channel', and (5) resolving the unbound antibody and bound immune complex peaks.

Reagents and Protein Samples

3-(trimethoxysilyl)-propyl methacrylate (98%), glacial acetic acid, 30% (29:1) acrylamide/bis-acrylamide, 2-hydroxyethyl cellulose, methanol, N-cyclohexyl-3-aminopropanesulfonic acid (CAPS) and rabbit anti-human Lf polyclonal antibody were purchased from Sigma Aldrich (St. Louis, MO). Water-soluble photoinitiator 2,2-azobis[2-methyl-N-(2-hydroxyethyl) propionamide] (VA-086) was purchased from Wako Chemicals (Richmond, VA). Pre-mixed 10× tris-glycine native electrophoresis buffer (25 mM tris, 192 mM glycine, pH 8.3) was purchased from Bio-Rad Laboratories (Hercules, CA). Human lactoferrin purified from human breast milk and monoclonal anti-Lf antibody clones 2B8 (herein "clone 1"), 1C6 ("clone 2"), B97 ("clone 3") and CLB-13.17 ("clone 4") were purchased from Abcam (Cambridge, MA). Monoclonal anti-Lf antibody clones KT33 ("clone 5") and 1B8 ("clone 6"), DyLight-488 maleimide fluorescent dye and Slide-A-Lyzer Dialysis Cassettes (10k MWCO) were purchased from Thermo Scientific Pierce Protein Research Products (Rockford, IL). Goat anti-human Lf polyclonal antibody and human lactoferrin ELISA kits were purchased from Bethyl Laboratories (Montgomery, TX) to determine Lf concentration in patient samples and to characterize protein reconstitution protocol efficiency. 1A1 anti-Lf monoclonal antibody clone ("clone 7") was purchased from GeneTex

(Irvine, CA). Schirmer tear test strips were purchased from Alcon Laboratories (Fort Worth, TX) and Sigma Pharmaceuticals (Monticello, IA). Dynabeads antibody coupling kit and DynaMag-2 magnet were purchased from Invitrogen (Carlsbad, CA) for Lf-depletion studies. CAPS buffer was prepared by dissolving CAPS in water and titrating to pH 11 with 1 M NaOH before adding necessary water volume to bring it to the desired concentration of 500 mM (10× concentration).

Fluorescently-labeled antibody probes (Ab*) were labeled in-house with DyLight 488 fluorescent dye at 4°C overnight and purified to remove un-reacted dye using 10k MWCO Slide-A-Lyzer Dialysis Cassettes in PBS with 3 buffer exchanges overnight. All samples were prepared off-chip by adding the desired concentrations of regents to a final volume of 20 µL in the following order so as to establish a negative charge on Lf and tear matrix constituents before introducing the antibody probe (Ab*): 1) Lf, 2) 1x (50mM) CAPS buffer, 3) tear matrix. 4) Ab*. Samples were incubated at 4°C in the dark for at least 1 hour before running on-chip.

Human Tear Samples

SS patients (diagnosed according to the European criterion and SICCA ocular surface grading system[152]) and normal healthy subjects were recruited from the University of California, San Francisco (UCSF) SS clinic with informed consent according to the guidelines established by the Association for Research in Vision and Ophthalmology. All procedures adhered to the tenets of the Declaration of Helsinki. SS patients were instructed not to use any topical ocular medications other than artificial tears for 3 days before tear collection. Tear samples were collected using Schirmer strips in standardized fashion (unanaesthetized eye with strip inserted in the inferior cul-de-sac for 5 min) from both eyes of each subject. Subjects were anonymized and strips were snap frozen at -80°C in 1.5 mL eppendorf tubes until reconstitution and analysis. Frozen storage of Schirmer strips has been shown to have no effect on protein content (e.g. lysozyme activity).[153]

Tear fluid from the frozen Schirmer strips was reconstituted in phosphate-buffered saline (PBS). Frozen strips from each patient were cut into eight 5x5 mm^2 squares and each was incubated in a 0.65 mL Protein Lobind eppendorf tube with 20 µL PBS on a shaker overnight. The eluate from the eight squares of a single patient was then collected, pooled and frozen at -20°C until use. Storing tear samples at -20°C up to 2 months has been shown to have no effect on protein content.[154]

The volumetric measurement capabilities of the Schirmer strip also allows for a rapid method by which to normalize for potential disease-induced changes in tear volume in order to pull out actual changes in Lf mass on the ocular surface. An approximately equal observed distance of tear wicking for both healthy and SS tear samples indicates approximately equivalent volumes of collected tears for all analyzed samples. Therefore, measured variations in Lf concentration are entirely attributed to changes in Lf mass in the tear fluid.

Human tear fluid was depleted of Lf where indicated by conjugating polyclonal goat anti-human Lf antibodies to magnetic DynaBeads (20-30 µg Ab per mg DynaBeads to ensure at least 1.5:1

ratio of conjugated Ab to expected Lf present in tears), incubating with healthy and SS tear fluid overnight and magnetically removing Lf-bound Dynabeads. Final Lf concentration was confirmed through ELISA.

Microfluidic Device Fabrication

Standard glass t-channel microfluidic chips were fabricated with standard wet etch processing by Caliper Life Sciences (Hopkinton, MA). Channels were 20 µm deep x 80 µm wide and consisted of two intersecting channels to connect sample (S), sample waste (SW), buffer (B) and buffer waste (BW) wells (Figure 21). Before introducing polyacrylamide (PA) gel precursor solutions, channels were washed with 1M NaOH for 10 min, flushed with DI water 3× and then incubated with a degassed 2:3:5 (v/v/v) mixture of 98% 3-(trimethoxysilyl)-propyl methacrylate, glacial acetic acid, and DI water to form a silane monolayer for PA gel adherence to the glass walls. Channels were flushed 3× with alternating methanol and DI water solutions and purged with vacuum. All aqueous solutions were introduced into the channels through capillary action.

Polyacrylamide Gel Fabrication and Pore Size Optimization

Polyacrylamide sieving gels were fabricated *in situ* in the channels to suppress electro-osmotic flow and enable multi-step photopatterning of functional regions for improved assay performance. A large pore-size gel was fabricated in the loading channel to minimize sample loading bias and a sharp pore-size discontinuity was fabricated ~300 µm downstream of the injection junction. This discontinuous pore-size gel architecture has been shown to serve multiple roles including 1) decreasing assay time to <15 seconds for timely analysis, 2) enabling complex stacking to increase assay sensitivity and reduce complex dispersion, and 3) allowing assay completion within a short separation distance (<1 mm), opening the possibility for lower voltage separations and battery-powered operation.[11] The greater the difference in pore sizes used at the discontinuity, the more these benefits are amplified.[11] A 3%T (3.3%C) to 6%T (3.3%C) pore-size discontinuity was selected to maximize the pore-size difference across the discontinuity which amplifies these benefits. 3%T (3.3%C) was determined to be the minimum reliably polymerized acrylamide concentration in the optimized buffer conditions and 6%T (3.3%C) yielded the smallest pore-size that the endogenous complex could enter without being excluded at the interface.

The discontinuous polyacrylamide gel matrix was fabricated as described previously.[11] Briefly, gel precursor solutions were prepared by diluting 30% (w/v) acrylamide/bis-acrylamide with 10× CAPS buffer and water to achieve the desired total acrylamide concentration (3%T or 6%T) in 1× CAPS buffer with 0.2% (w/v) VA-086 photoinitiator. Precursor solutions were thoroughly degassed by sonication (~5 min) before use. 6%T precursor solution was than introduced into the device through capillary action and the chip was aligned over a transparency mask with a 4mm × 500 µm opening (designed in house and fabricated by Fineline Imaging, Colorado Springs, CO) so that a region of the separation channel directly downstream of the injection junction was exposed. The device was seated on an inverted Nikon Diaphot 200 microscope (Melville, NY), drops of highly viscous 5% (w/v) 2-hydroxyethyl cellulose (HEC) were applied to each well and the device was allowed to equilibrate for 5 min to minimize bulk flow in the

channels. UV light from a Hamamatsu LightningCure LC5 UV light source (Hamamatsu City, Japan) was directed into the lightpath of the microscope and through a UV-transmission objective lens (UPLANS-APO 4x, Olympus, Center Valley, PA). The intensity of the beam was measured with a UV513AB Digital Light Meter (General Tools, New York, NY) to an intensity of ~1.73mW/cm^2 and the masked chip was exposed to UV light for 4.5min. Unpolymerized precursor solution was removed from channel reservoirs S, SW and B and replaced with 3%T precursor solution by sequentially applying vacuum to each well. The entire chip was then flood exposed for 18 min at ~10mW/cm^2 on a 100W filtered mercury UV lamp (UVP B100-AP, Upland, CA) a distance of 5 inches from the chip.

Polymerization Theory

PA gels are formed by copolymerization of acrylamide and bis-acrylamide ("bis", N,N-methylene-bisacrylamide) in a vinyl addition polymerization reaction initiated by a free radical-generating photoinitiator.[155] Free radical polymerization reactions occur through chain reactions where monomers are added to a free-radical containing end of a polymer molecule. This site is known as an "active center."[156] The initiator used in this work, 2,2'-Azobis[2-methyl-N-(2-hydroxyethyl)propionamide] or VA-086 (Figure 23), is an azo-initiator and is used because it is water soluble and has a high 10-hour half-life decomposition temperature of 86°C.[157] In the case of polyacrylamide gel polymerization, the elongating polymer chains are randomly crosslinked by bis (Figure 24), which results in a porous gel. The specific porosity of PA gels are dependent on the polymerization conditions and monomer concentrations.[155]

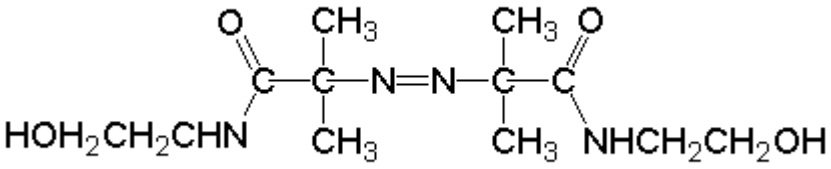

Figure 23. Chemical structure of VA-086 photoinitiator used throughout this work

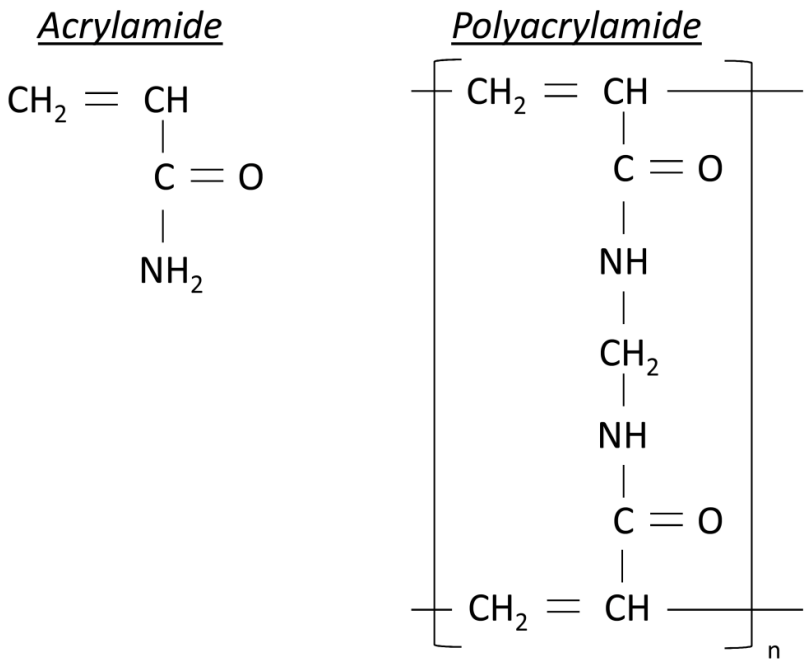

Figure 24. Chemical structure of acrylamide and cross-linked polyacrylamide.[155]

During the chain polymerization reaction of PA gel polymerization, monomers are added to the terminal free-radical reactive site on the ends of polymer molecules and after the addition of each monomer, the active center is transferred to the newly-created chain end. The reaction can be divided into three distinct stages: 1) initiation, 2) propagation and 3) termination. Initiation involves the formation of free radicals from the initiator and the addition of these free radicals to a monomer molecule and is governed by the equation:[156]

$$I \rightarrow nR^* + M \rightarrow RM_i^*$$

$R_i = 2\Phi\varepsilon I_0[I]$ is the rate governing this two step process of forming active centers on the monomer molecules, where I_0 is the intensity of incident light, ε is the molar absorptivity of the initiator and Φ is the quantum yield (i.e. photochemical equivalent of initiator efficiency).[156] Propagation involves growing the polymer chain through sequential addition of monomer to the active center and is governed by the equation:[156]

$$M_i^* + M \xrightarrow{k_p} M_{i+1}^*$$

where k_p is the rate constant of propagation. Termination involves a bimolecular reaction (e.g. combination or disproportionation) that terminates growth of the polymer chain and is governed by the equations:[156]

$$M_i^* + M_j^* \begin{array}{l} \xrightarrow{k_{tc}} M_{i+j} \\ \xrightarrow{k_{td}} M_i + M_j \end{array}$$

where k_{tc} is the rate constant of termination and k_{td} is the rate constant of disproportionation. The overall rate constant for termination, k_t, can therefore be given by

$$k_t = k_{tc} + k_{td}$$

Under steady state conditions (assumed for the majority of polymerization time), the rate of monomer consumption or rate of polymerization, R_p, is governed by the equation:

$$R_p = \left(\frac{k_p}{2^{\frac{1}{2}} k_t^{\frac{1}{2}}} \right) R_i^{\frac{1}{2}} [M]$$

where [M] is the concentration of monomers in solution. Substituting in the equation for R_i gives:

$$R_p = k_p \left(\frac{\Phi \varepsilon I_0}{k_t} \right)^{1/2} [M][I]^{1/2}$$

The above equations demonstrate that the rate of polymerization is primarily dependent on light intensity and monomer concentration. However, temperature also affects the rate of gel polymerization and the properties of the gel and it is important to maintain the environment around 25°C. Since the polymerization is exothermic,[155] the rate of reaction can be accelerated by the reaction itself. Further, cool temperatures during polymerization result in porous, inelastic gels with low reproducibility.[155] At temperatures around 25°C, PA gels are transparent, less porous, and more elastic.[155] At higher temperatures, the polymer chains can be terminated early resulting in short chains and brittle, non-elastic gels.[155]

Oxygen also serves as a free-radical trap which inhibits the polymerization reaction. Oxygen can enter the system through the air or by being dissolved in gel solutions. As a result, proper degassing of all gel precursor solutions is critical for gel integrity and reproducibility.[155]

Assay Control and Full-Field Imaging

Glass chips were secured in a custom-built Delrin manifold to augment sample reservoirs for each well and minimize external light interference. Five microliters of sample was loaded into the sample well and all other wells were filled with 50 µL of 1× pH 11 CAPS buffer. Platinum electrodes were inserted into each well and sample was electrophoretically loaded into the 3%T loading channel by applying 450 V to SW while grounding the S, B and BW reservoirs (E = 160 V/cm in the loading channel) for 3-5 minutes. Separation was initiated by switching the electric field to apply 800V to BW, grounding B, 400 V to S and 600 V to SW to inject a sample plug into the orthogonal channel (E = 102 V/cm in separation channel). After 5.5 seconds the pull-back voltage was decreased to 112V in both the S and SW wells (E = 150 V/cm in separation channel).

Migration and concentration distributions of fluorescent analytes were measured via an IX-70 inverted epi-fluorescent microscope equipped with a 100W mercury arc lamp (Olympus, Center Valley, PA), 10× objective (UPlanFL, NA 0.3, Olympus, Center Valley, PA), 0.63× demagnifier (Diagnostic Instruments Inc., Sterling Heights, MI) and a filter cube optimized for GFP (XF100-3, Omega Optical, Brattleboro, VT). Sequential image capture was performed using a 1392 x 1030 Peltier-cooled charge-coupled device (CCD) camera (CoolSNAP HQ2, Roper Scientific, Trenton, NJ), 200 msec or 75 msec exposure times, and 4 x 4 pixel binning. Image post-processing was done with ImageJ (National Institutes of Health). All images were background subtracted to account for variability in background signal (50 pixel rolling ball radius). Intensity profiles of the separation channel were generated using a standardized ROI (320 x 15 pixels or 1.26 x 0.06mm) along the length of the separation channel. Peak area measurements were done with a nonlinear Gaussian peak fitting algorithm (GaussAmp) using OriginPro 8.5 (OriginLab, Northampton, MA) with an $R^2 \geq 0.7$.

5.8 Alkaline Immunoassay Development & Troubleshooting

The remaining sections in Chapter 5 detail the development and optimization of the on-chip alkaline homogeneous electrophoretic immunoassay for Lf. The impact of separation buffer pH, operating conditions, and antibody clone selection are described. Further results concerning PA gel polymerization in the high pH buffer conditions are also presented. Introducing the CAPS molecule and operating in a high pH regime affects PA sieving gel polymerization and overall gel integrity. We characterize gel performance in this highly alkaline regime and establish metrics for determining assay performance limits. Lastly, we characterize the newly developed assay performance, quantitative capabilities and clinical relevance.

Observations of Protein Fouling, Non-specific Protein Binding, and Immune Complex Precipitation

Throughout the initial assay development stages, abundant complex precipitation (Figure 25), binding interactions between complex and PA gel ('gel staining') and large complex peak dispersion ('complex smearing') was observed in a standard pH 8.4 tris/glycine buffer system which precluded effective immune complex detection (Figure 26). Precipitation of the immune complex peak was evident in the loading channel following loading of samples containing both Ab* and Lf (Figure 25). The full field fluorescence microscopy separation montage in Figure 26 visually reports non-ideal exemplars of these behaviors, including visible smearing of the Lf immune complex after the pore-size discontinuity, loading channel staining, and precipitation of the immune complex in the loading channel region.

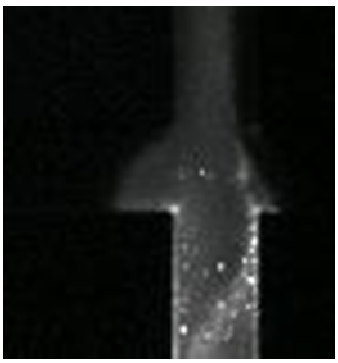

Figure 25. Lf immune complex precipitation in the loading channel using pH 8.4 tris-glycine buffer after 1 min of loading.

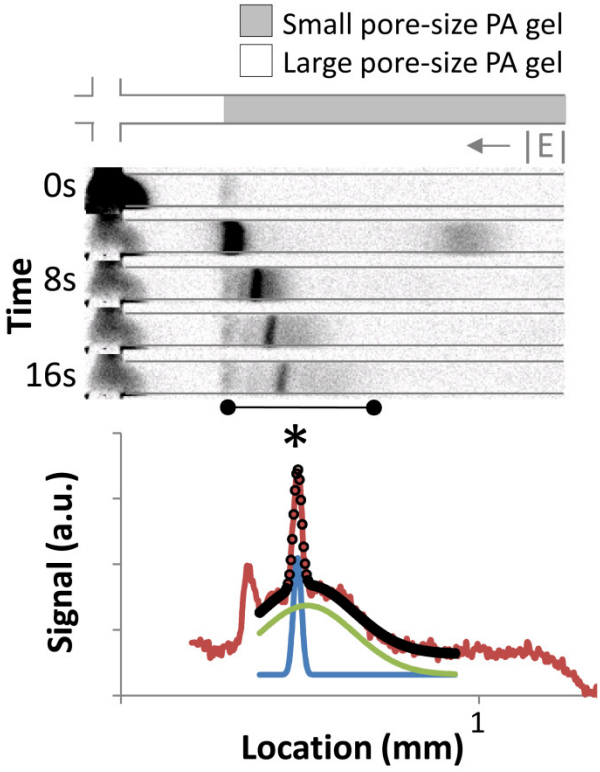

Figure 26. Non-specific antibody-antigen binding results in the resolution of two complex peaks after the pore-size discontinuity: a specifically bound immune complex ('') and a non-specifically bound complex ('barbell'). Gaussian peak fitting can be used to assess the separation resolution, complex dispersion, and signal overlap for assay development and optimization. Reprinted with permission from Karns and Herr,* Human Tear Protein Analysis Enabled by an Alkaline Microfluidic Homogeneous Immunoassay*, 2011, 83, 8115-8122. © 2011 American Chemical Society.*

In Figure 26, as the complex hits the pore-size discontinuity it is resolved into two populations: one strongly bound population (specific immune complex, '*') and one weakly bound population (non-specific immune complex peak and newly dissociated antibody, barbell). An intensity profile along the channel 16 s after injection is shown below in red. Both populations have gaussian shapes as they diffuse over time. The sum of non-linear gaussian curve fits to both the specific population (blue curve) and non-specific population (green curve) is overlaid in black. The presence of the non-specific (green) peak has the following negative impacts on assay performance: 1) poor resolution from the specifically-bound complex peak makes detection of the specific complex peak difficult, 2) large variance contributes to complex smearing and increases overall signal dispersion, and 3) non-specific peak signal reduces the detectable signal of the specifically-bound complex peak by obscuring the peak area. Furthermore, Figure 26 shows visible loading channel staining.

These non-ideal behaviors are attributed primarily to electrostatic interactions between highly alkaline Lf and the negatively charged PA gel and increase with gel-contact time. The abundant positively charged residues of alkaline Lf at physiological pH have been shown previously to electrostatically interact with surrounding negative residues on PA gels as well as in the surrounding matrix.[46] Electrostatic or hydrophobic interactions between the immune complex and the surrounding PA matrix can therefore result in complex smearing in small pore-size PA gel regions where complex-gel interactions are increased. Increased interaction time between analytes and the gel was observed to increase gel staining and sample loss (Figure 27).

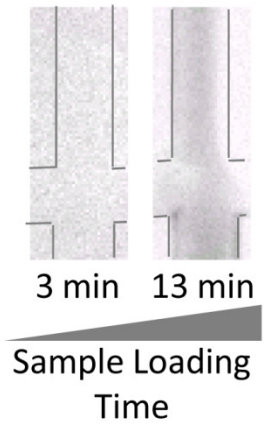

Figure 27. Increased complex resonance time in the gel increases protein-gel interactions and increases non-specific immune complex-PA gel immobilization. Reprinted with permission from Karns and Herr, Human Tear Protein Analysis Enabled by an Alkaline Microfluidic Homogeneous Immunoassay*, 2011, 83, 8115-8122. © 2011 American Chemical Society.*

Importantly, these non-ideal behaviors were observed only for the Lf immune complex. In the left panel of Figure 28, we see that, although Lf immune complex can be seen at the front of the

advancing complex peak, there is still a significant amount of complex smearing that occurs after the pore-size discontinuity. Because of the immune complex smearing and gel staining, the signal of this band decreases over time as more and more is retained in the post-discontinuity gel. In contrast, multiple CRP immune complex bands are observed on the same chip with little post-discontinuity stacking or staining in the loading channel (Figure 28, right panel). This shows that the immune complex smearing and gel staining observed for Lf is not due to the gel or chip itself, but rather to the Lf analyte.

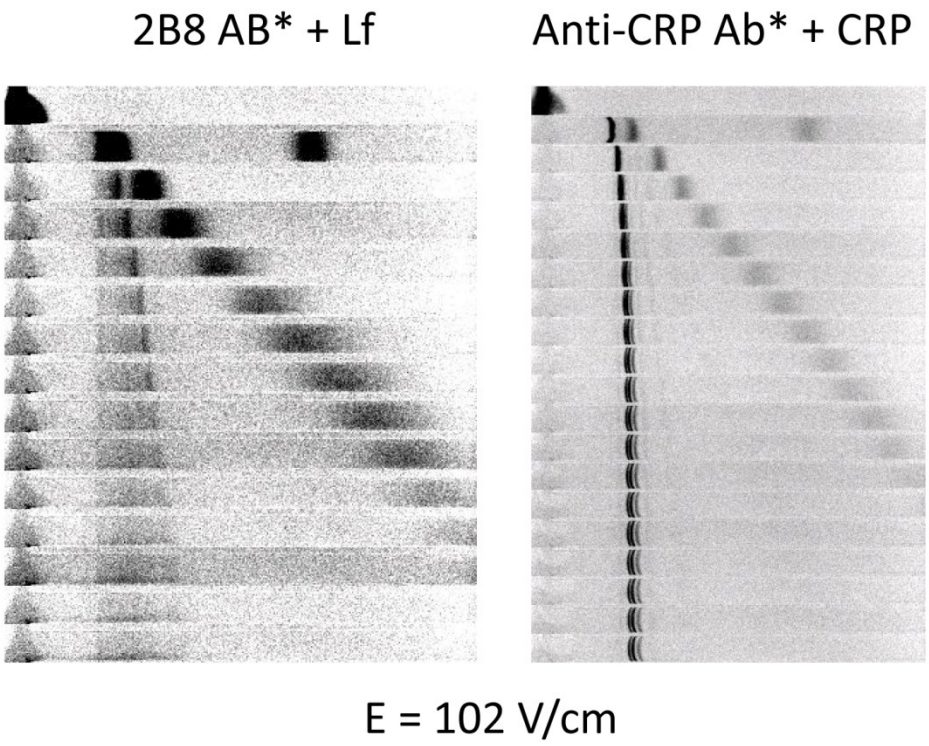

Figure 28. Separation montages of 2B8 anti-Lf Ab(clone 1) with Lf (left panel) and anti-CRP Ab* with CRP on the same 3-6%T discontinuous separation gel in pH 9.75 glycine buffer. Each frame is 2 seconds. Fabrication was done with a 4:00 exposure time on the UV objective at ~7.2mW/cm^2 and a 15:00 exposure time on UV lamp at ~12mW/cm^2*

Non-specific antibody-antigen binding is typically electrostatic, hydrophobic and/or non-polar in nature[46] and results in weak immune complex binding affinities and ready complex dissociation. A homogeneous electrophoretic separation of a sample of spectrally coded Lf (red) and antibody (green) shows the majority of the complex band dissociating into free Lf and free Ab bands as it migrates through the pore-size discontinuity, contributing to immune complex peak smearing (Figure 29). Specifically-bound antibody-antigen complexes remain bound while the newly dissociated antibody migrates more quickly through the interface. This results in observed smearing of the complex peak. Weak antibody-Lf binding affinity is further

confirmed by a high measured dissociation constant (K_d) for Lf and antibody (220 ± 27 nM) (data presented later). Protein staining and some immune complex precipitation in the loading channel are also observed in Figure 29.

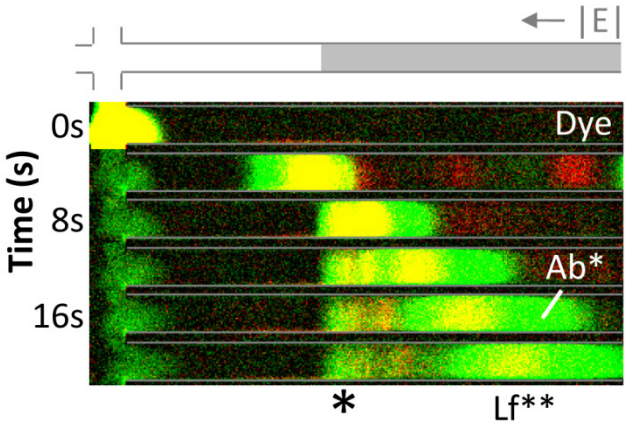

Figure 29. Weak binding affinity of Ab and Lf** in pH 8.4 buffer results in complex disruption after the discontinuity interface. A two color assay shows Ab* (green channel) and Lf** (red channel) species co-migrating before the discontinuity. Immediately after the discontinuity, the plug is resolved into complex, free Lf** and free Ab* peaks. The majority of species is in the unbound state and migrates through the small pore-size region. Reprinted with permission from Karns and Herr,* Human Tear Protein Analysis Enabled by an Alkaline Microfluidic Homogeneous Immunoassay*, 2011, 83, 8115-8122. © 2011 American Chemical Society.*

Alkaline Buffer Selection and Effects

To address the issues of gel staining, complex smearing, and complex precipitation in the past, Reisfeld buffer systems have been employed using β-alanine-acetic acid buffers (pH 4.5) for native electrophoretic separation of basic tear proteins in a slab gel format followed by Coomassie staining.[18]

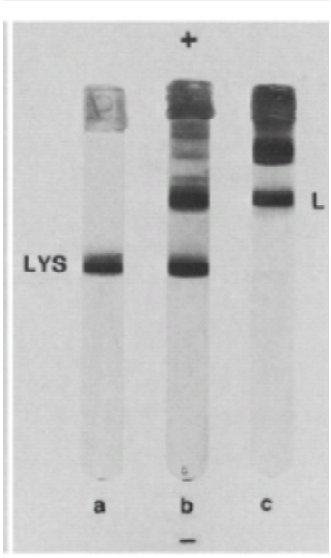

Figure 30. PAGE separation of (a) purified lysozyme, (b) native tears, and (c) human milk using the Reisfeld system with alanine-acetic acid buffer, pH 4.5. LYS indicates lysozyme, L indicates lactoferrin. Reprinted from Berta, A Polyacrylamide-Gel Electrophoretic Study of Human Tear Proteins*, 1982, 219: 95-99 with kind permission from Springer Science and Business Media.*

The purpose of using acidic buffer conditions is to impart all proteins in the system with a positive charge so that they migrate toward the negative electrode, but more importantly, so that there are fewer negatively charged protein residues and assay structures for nonspecific binding to occur. However, use of acidic buffer conditions for homogeneous electrophoretic immunoassays is problematic when the assay utilizes fluorescently labeled antibody probes as fluorophores suffer from reduced performance in low pH regimes.[158] Consequently, we sought to develop a homogeneous electrophoretic immunoassay utilizing a fluorescently-labeled antibody probe that obviates the need for acidic buffer conditions.

An alternative to using acidic buffers to impart the same net charge to all proteins in the system and minimize non-specific electrostatic binding was to use a high pH buffer. More specifically, the selection of an alkaline buffer system aimed to: (1) impart a net negative charge to all proteins in the system in order to have uniform migration toward the positive electrode, (2) retain the fluorescence activity of the fluorescently labeled antibody probe, and (3) minimize the non-ideal complex precipitation, gel staining, and complex smearing that was observed at pH 8.4. By increasing the buffer system to a pH where the majority of R groups on Lf amino acids are negative or at least neutrally charged, we hoped there would be negatively charged R groups exposed on the surface of the Lf molecule to give Lf and – therefore the immune complex – a net negative charge. My hypothesis was that this would both increase the amount of immune complex loaded into the gel, reduce the observed electrostatic interactions between

Lf, Ab, and the gel, and allow for specific antibody-Lf binding to occur which would have higher binding affinity.

Although the theoretical pI value for human Lf is 8.7,[45] a wide range of pI values (5.5-10) have been reported.[159,160,161,126] Experimentally, we observed that isoelectric focusing of Lf over a pH range of 3-10 showed ten distinct Lf subpopulations with pI points ranging from 7.88 to 10.3 (Figure 31). The measured Lf heterogeneity suggests that the Lf immune complexes, which will have pI points that are dictated by both the Ab* and Lf molecules that comprise them, will also have heterogeneous subpopulations with varying pI points. This further necessitated a buffer pH above that of the highest pI subpopulation to ensure that all Lf molecules were electrophoretically loaded onto the chip.

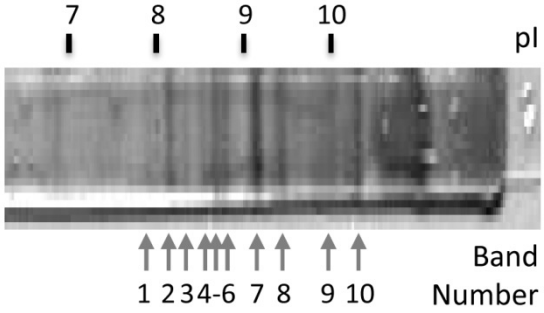

Figure 31. 3-10 pH range IEF gel of Lf shows 10 distinct bands ranging from pI 7.88 to 10.3. Reprinted with permission from Karns and Herr, Human Tear Protein Analysis Enabled by an Alkaline Microfluidic Homogeneous Immunoassay*, 2011, 83, 8115-8122. © 2011 American Chemical Society.*

The ability to change the surface charge of Lf by increasing buffer pH and de-protonating Lf amino acids depends on where the relevant amino acids are located in the Lf molecule. Amino acids that may become de-protonated at a certain pH but are hidden deep in the protein interior may not be exposed to the buffer and therefore may not have a direct impact on the effective protein charge or nonspecific electrostatic binding that the molecule undergoes. Amino acids, which make up proteins, each have a specific pKa indicating the pH at which that particular amino acid loses a hydrogen atom and loses a positive charge. Table 4, below, shows the alkaline amino acids with their pKa values and expected charge in different buffer conditions.

Table 4. Charge of amino acid side chains at the given pH.

Amino Acid	pKa (R group)	charge at pH 6.8	charge at pH 8.4	charge at pH 9.75	charge at pH 11
Aspartate	3.65	-	-	-	-
Glutamate	4.25	-	-	-	-
Histidine	6	-	-	-	-
Cysteine	8.18	+	-	-	-
Tyrosine	10.07	+	+	+	-
Lysine	10.53	+	+	+	-
Arginine	12.48	+	+	+	+

Noting that the location of each amino acid is important, Figure 32 below shows a 3D structure of the Lf molecule with cysteine residues (pKa of 8.18) highlighted in red, tyrosine residues (pKa of 10.07) highlighted in purple, lysine residues (pKa of 10.53) highlighted in white, and arginine residues (pKa of 12.48) highlighted in orange. Figure 32 shows that cysteines and tyrosines are almost entirely on the interior of the protein and therefore should have a small effect on the net charge of the molecule. In contrast, lysines and arginines are mostly on the surface of the protein and will have a larger impact on net charge. The first 50 amino acids of the N-terminus are also highlighted in blue. We can clearly see that this N-terminus region is exposed on the exterior of the protein and therefore likely also contributes to the effective charge of the molecule. In fact, this positive charge is known to cause Lf to nonspecifically associate with other proteins due to electrostatic interactions.[46] This may also augment the observed non-specific interactions with Lf.

Figure 32. 3D structure of Lf with alkaline amino acids highlighted. Cysteines are red, tyrosines are purple, lysines are white, arginines are orange and the last 50 residues of the N-terminus is highlighted in blue. At pH 11, all residues except arginine (orange) would be negatively charged. With DyLight 488 dye, cystein residues would be bound with dye and neutrally charged irrespective of pH. Structural information was obtained from the Protein Data Bank[127] and displayed using pymol. The original protein crystal structure is from Sun, et al., 1999[128]

As a result, we sought to alter the pH of the sample, gel, and run buffers to see the impact on the non-ideal observations we had noted. Comparing a separation of 2B8 antibody (clone 1) and Lf in pH 6.8 HEPES buffer, pH 8.4 tris-glycine buffer and pH 9.6 glycine buffer, we see in Figure 33 that the Ab* has much lower mobility in HEPES buffer as expected owing to its more positive charge. Further, although there is less staining in the loading channel, there was no immune complex detected during the separation, suggesting that at this lower pH, the immune complex is positively charged and therefore does not load onto the chip during the loading step. There was significant build-up at the beginning of the loading channel where the gel began which may be where the complex was accumulating (not shown).

In contrast, moving from pH 8.4 tris-glycine buffer to pH 9.6 glycine buffer, the separation montage shows an increased amount of immune complex. Further, unlike in the pH 8.4 conditions, the complex is now able to migrate through the discontinuity, suggesting that binding is maintained after passing the interface and a greater proportion of the immune complex molecules are specifically bound with higher affinity. Figure 33 also shows slightly lower loading channel staining and immune complex precipitation at pH 9.6 compared to pH 8.4. Proteins are lowest in solubility in solutions that have a pH equal to their pI point.

Therefore, it is possible that moving away from pH 8.4 increased the solubility of the immune complex by moving away from its pI point. Note that it is very difficult to measure the pI point of an immune complex peak since it relies on maintaining native conditions. We attempted to make this measurement (in collaboration with Sasha Denisin, data not shown), but were unable to maintain binding of the antibody and Lf molecules during the iso-electric focusing (IEF) process. In the pH 9.6 conditions, faster loading was observed for the complex-containing sample as well a higher intensity loading. In contrast, the immune complex-containing sample consistently had lower signal intensity in the loading channel. This improvement is likely due to the fact that more Ab*-containing complex is negatively charged at the buffer pH and can migrate into the loading channel rather than remaining in the well.

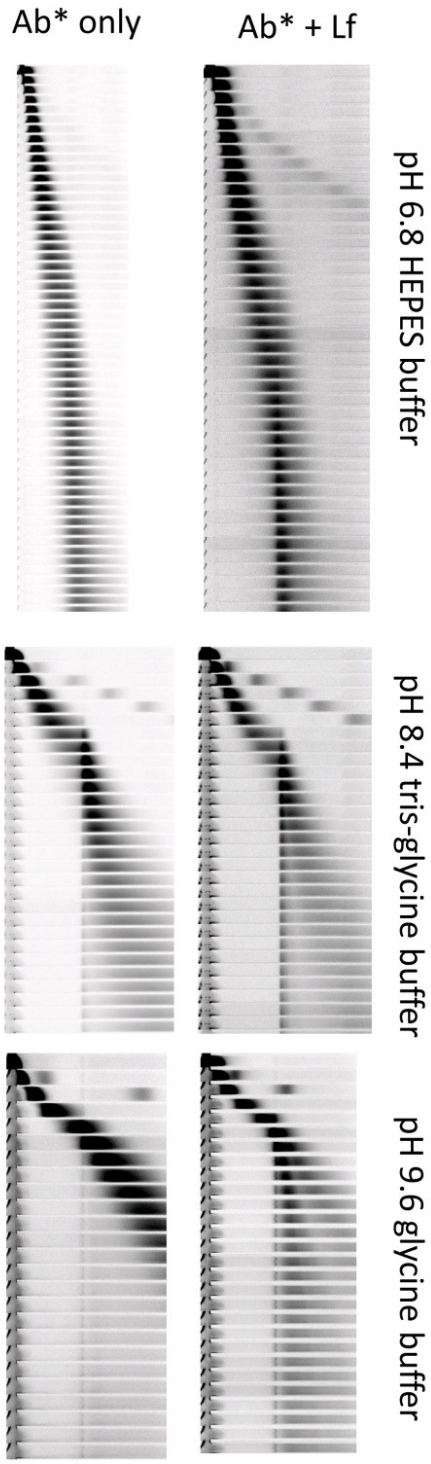

Figure 33. Comparison of Ab + Lf separation montages in pH 6.8 HEPES (top panel), pH 8.4 tris-glycine (middle panel), and pH 9.6 glycine (bottom panel) buffers. 3-5.5%T discontinuous gel, E = 102 V/cm, 2 seconds per frame. Gel fabricated with primary exposure of 6 mW for 5:15min followed by a 7 min flood exposure at 10.5mW/cm^2. DyLight488 labeled antibody used in all separations.*

Considering the amino acid pka values in Table 4, for the buffer range used in Figure 33 (pH 6.8-9.6), the only pKa threshold that was crossed was that of cysteine (pKa of 8.18). Previously, I had observed that when moving from a pH 8.4 to pH 9.75 buffer with an antibody labeled with amine-bound AlexaFluor 488 dye, there was a clear increase in the amount of complex that was able to migrate into the chip. This is likely attributed to the fact that moving up to a pH 9.75 buffer moves farther away from the cysteine pKa threshold of 8.18 and will cause the majority of cysteines to be negatively charged at this higher pH.

In contrast, the results in Figure 33 use the –SH-specific dye DyLight 488. With DyLight488, all the free –SH groups on cysteines should now be bound by –SH-specific DyLight dye. Therefore, these groups will not become de-proteinated in pH 9.6 and there will be a smaller net change in overall charge when I move from pH 8.4-9.6. To get a similar increase in net negative charge on the complex, I needed to cross the tyrosine, lysine and/or arginine pKa thresholds.

Thus, we selected a higher pH buffer: N-cyclohexyl-3-aminopropanesulfonic acid (CAPS) titrated to a measured pH of 11. This buffer was selected for its pKa of 10.5. Since a buffer has a maximal buffering capacity within 1 pH unit of its pKa,[162] CAPS is an effective buffer in a pH range of 9.5 to 11.5. Therefore, operating at a pH of 11 maintains buffering capacity in the system and minimizes the amount of positive residues left on protein analytes in the system since the buffer pH is above the pKas of all amino acids except for arginine. Thus, all residues will be negatively charged except for arginines. This should serve to impart a greater negative charge to the immune complex, leading to increased immune complex loading on-chip and fewer opportunities for weak non-specific electrostatic binding with the antibody. It is important to note that the amino acid sequence of the positively charged 50 residues at the N-terminus, which has been previously implicated in these electrostatic binding interactions with surrounding positive residues, is:

GRRRSVQWCTVSQPEATKCFQWQRNMRKVRGPPVSCIKRDSPIQCIQAIA

The last 11 amino acids of the N-terminus contain 4 arginines and 1 cysteine. Therefore, moving to a pH of 11 will not eliminate the positive charges contributed by the arginines. As a result, there may still be some non-specific binding that remains, despite the high pH. The trade-off in selecting buffer pH is the maintenance of biological activity. Moving to a buffer with pH 11 had the potential to cause denaturation of the protein or antibody and limit biological activity and immunospecificity. However, the separations did not reveal antibody denaturation, a noticeable reduction in the fluorescence signal, or altered mobility of the analytes at the high pH.

Figure 34 (left panel) shows a carton of Lf with positively charged residues at pH 8.4 (arginine, lysine and tyrosine) highlighted in blue. Figure 34 (right panel) shows the significantly reduced number of positively charged residues on Lf at pH 11 (arginine) highlighted in blue.

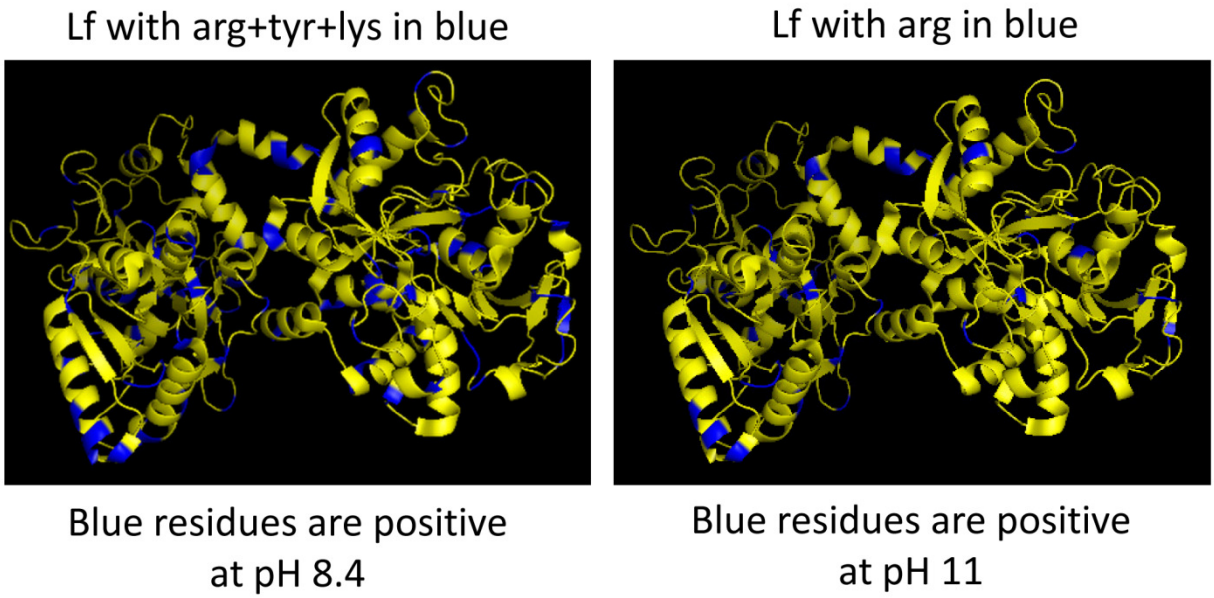

Figure 34. 3D structure of Lf with positively charged amino acids at pH 8.4 (left panel) and pH 11 (right panel) in blue. At pH 11, fewer positively charged amino acids are available to engage in non-specific electrostatic interactions with the antibody or surrounding assay structures. Structural information was obtained from the Protein Data Bank[127] and displayed using pymol. The original protein crystal structure is from Sun, et al., 1999[128]

Throughout assay development, we tracked three metrics to assess the impact of each condition (e.g., antibody or buffer choice) on non-specific interactions and overall assay performance. Firstly, the separation resolution (SR) of the specific and non-specific complex bands assesses the extent to which the peaks overlap. Fully resolved peaks have SR ≥1 and enable facile detection of the specific complex band. A key performance metric specific to the homogeneous electrophoretic immunoassay technique is minimization of complex peak dispersion. Secondly, the percent contribution of the specific complex peak to total complex dispersion [$\sigma_{specific}/(\sigma_{non\text{-}specific}+\sigma_{non\text{-}specific})$] was used to assess the degree of complex smearing which is mostly attributed to the non-specific peak. A 100% dispersion contribution by the specific complex peak indicates no contribution from the non-specific peak and negligible complex smearing. Thirdly, the fraction of the total complex signal arising from the specific complex area ($A_{specific}/(A_{non\text{-}specific}+A_{non\text{-}specific}$) evaluates how much the non-specific complex peak obscures the specific complex signal.

To assess the impact of alkaline separation buffer pH on assay performance, we compared the homogeneous electrophoretic immunoassays for recombinant Lf in the discontinuous sieving PA gel system using the CAPS buffer system. Full field fluorescence microscopy images in Figure 35A visually reports non-ideal separation performance characteristics for the pH 8.4 tris-glycine buffer system (anti-Lf antibody clone 1). In contrast, Figure 35B reports the performance of the same immunoassay (anti-Lf antibody clone 1), but now conducted in the pH 11.0 CAPS buffer.

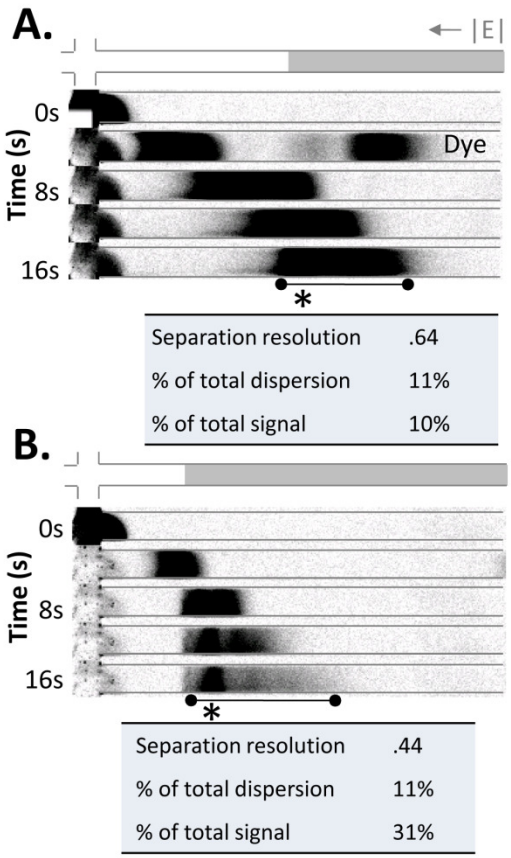

Figure 35. Buffer pH greatly impacts antibody migration, complex charge and overall assay performance. Separation montages of the same antibody clone (clone 1) combined with Lf in (a) pH 8.4 buffer and (b) pH 11 buffer show the improvement of assay performance by increasing buffer pH. We observe an increase in relative specific complex signal and reduction in complex precipitation and loading channel staining in pH 11 buffer. Complex peaks are confirmed by comparing separation with Ab-only montage and indicated with an asterisk. Free antibody is indicated, where detectable by 'Ab*'*

Comparison of Figure 35A and B shows the high pH separation buffer yields a fully resolved, non-dispersed complex peak (marked with "*") with a resultant increase in resolved complex signal (increase in percent of total signal contributed by specific complex band). This increase in immune complex signal is likely obtained by imparting all immune complexes with a net negative charge and allowing for loading of the entire complex population onto the device. Further, increasing the separation buffer pH from 8.4 to 11 minimized the positive charges on the Lf immune complex, resulting in an observed reduction in complex smearing within the PA gel and diminished loading channel gel staining and immune complex precipitation. By imparting additional negative charges to the immune complex, much faster sample loading times were also observed as evidenced by a 25% average increase in complex mobility in a 3%T

PA gel when moving from pH 8.4 to pH 11 buffer. Increasing buffer pH from 8.4 to 11 therefore appeared to minimize the positive charges on the Lf immune complex, resulting in an observed reduction in complex smearing within the PA gel and diminished loading channel gel staining.

Antibody, Dye and Electric Field Optimization

To optimize separation performance, numerous anti-Lf antibody clones were systematically tested, as is often necessary in other antibody-based analytical techniques (e.g., antibody microarrays, Western blotting).[163] We found antibody probe clone selection yielded a notable impact on assay performance. Even in highly alkaline conditions, antibody clones (even the same clone from different vendors) were found to be highly variable in charge, peak profile and degree of peak dispersion or smearing in the small pore-size regions of PA gels. Figure 36 shows the effect of antibody clone on non-specific antibody-antigen binding. Figure 36A-C reports full field fluorescence microscopy image sequences of Lf homogeneous electrophoretic immunoassays (CAPS buffer) operated under identical conditions (with purified Lf in pH 11 CAPS buffer), with the exception of antibody clone choice. Comparison of the Lf immunoassay at 16 s elapsed separation time shows a qualitatively wide variation in axial concentration distributions (peak profiles), charge, degree of peak dispersion (~17-fold variation among antibodies tested) and antibody-complex separation resolution. As a result, numerous anti-Lf antibody clones were systematically tested and assessed in their ability to form tight bands with minimal dispersion (Table 5). It was found that monoclonal antibody clones KT33 (Pierce) and 2B8 (Abcam) had a high degree of smearing; immune complexes formed with monoclonal antibody clones 1A1 (GeneTex) and 1C6 (Abcam) consistently precipitated out of solution; goat anti-human Lf polyclonal antibody (Bethyl labs) and monoclonal antibody clone B97 (Abcam) exhibited a low degree of labeling; monoclonal antibody clone CLB-13.17 yielded very low levels of detectable antibody; and rabbit anti-human Lf polyclonal antibody (Sigma) had numerous peaks suggesting an impure sample.

Monoclonal antibody clone 6 shown in Figure 36C was selected as having the best performance as we found no detectable non-specific complex peak, an appreciable amount of detectable antibody in solution, minimal complex smearing and minimal gel staining. This resulted in 100% of total dispersion and total area coming from the specific complex peak, maximizing the detectable signal.

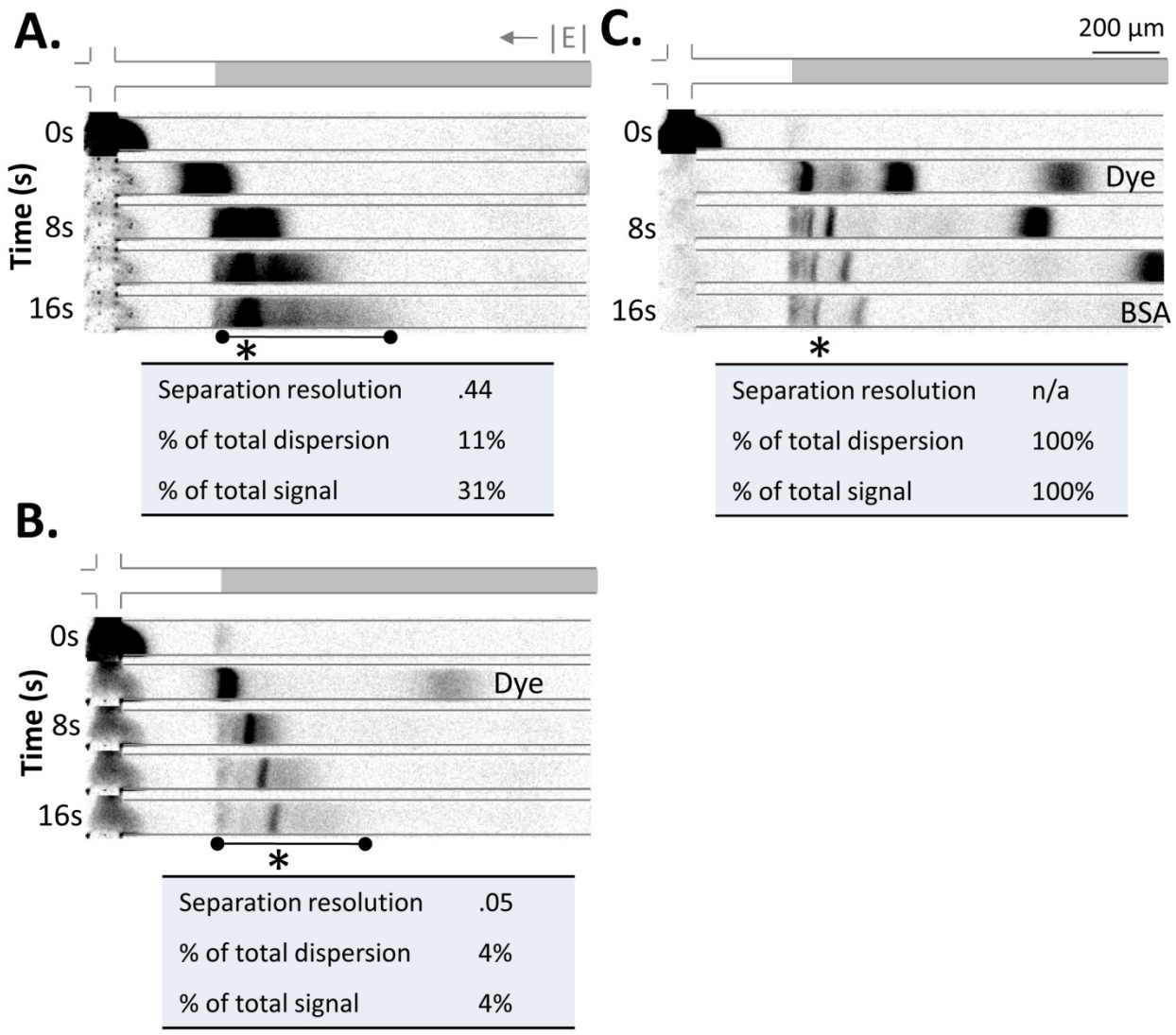

Figure 36. Antibody choice impacts degree of non-specific complex formation, antibody migration and overall assay performance. Monoclonal antibody clones (A) 1, (B) 5 and (C) 6 combined with Lf in pH 11 buffer show the importance of antibody clone on assay performance. Clone 6 was selected for the assay owing to minimal non-specific complex formation and minimal immune complex precipitation as seen in the loading channel. Specific complex peaks are confirmed by comparing separation with Ab-only montage and indicated with an asterisk. Non-specific complex peaks are indicated by a 'barbell'.*

Table 5. High observed variability in antibody performance in pH 11 buffer conditions. Reprinted with permission from Karns and Herr, Human Tear Protein Analysis Enabled by an Alkaline Microfluidic Homogeneous Immunoassay*, 2011, 83, 8115-8122. © 2011 American Chemical Society.*

Ab Clone	Result
Monoclonal	
1	Large complex dispersion (11% of total dispersion from specific complex)
2	Complex precipitated
3	Low degree of labeling
4	Low levels of detectable Ab
5	Large complex dispersion (4% of total dispersion from specific complex)
6	Minimal complex dispersion and non-specific complex-PA gel immobilization (100% of total dispersion from specific complex)
7	Complex precipitated
Polyclonal	
Goat anti-human Lf	Low degree of labeling
Rabbit anti-human Lf	Numerous peaks

Antibody samples were also found to degrade and change over time. Newly labeled antibody samples contained significantly more antibody as indicated by fluorescence signal when run on chip. Further, a native PAGE gel of two samples of the same antibody clone which had been stored for 0 and 8 weeks showed a significant difference in mobility and band dispersion (data not shown). As a result, only newly labeled antibodies (stored <1 month) were used for experimentation.

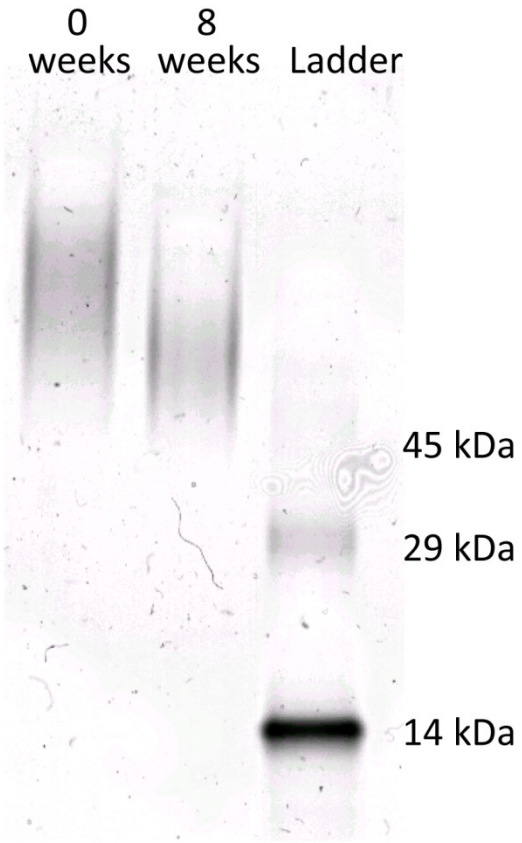

Figure 37. Native PAGE slab gel of anti-Lf antibody clone at 2B8 0 weeks (Lane A) and 8 weeks (Lane B) after purchasing and fluorescently labeling. Lane C is a molecular weight ladder. Reprinted with permission from Karns and Herr, Human Tear Protein Analysis Enabled by an Alkaline Microfluidic Homogeneous Immunoassay*, 2011, 83, 8115-8122. © 2011 American Chemical Society.*

Fluorophore choice also impacted the degree of non-specific binding and assay performance. Antibody charge appears to be impacted by the fluorophore used. In Figure 38, the antibody labeled with DyLight 488 migrates much slower, suggesting that the antibody is less negatively charged and that AF488 contributes a significant amount to the antibody charge and mobility. Further, the antibody band that is labeled with DyLight 488 has less observed post-discontinuity dispersion, suggesting that the heterogeneity in the antibody population may be minimized with the DyLight 488 dye. This increased negative charge on the antibody may augment the occurrence of weak electrostatic interactions between the positive residues on the Lf molecule and negatively charged groups on the antibody and increase the immune complex dispersion observed. As seen above, the AF488 dye appears to impart a significant amount of negative charge to the antibody which may cause the Lf to bind to it. This electrostatic interaction will be especially favored if the dye molecules are obscuring the antibody epitope in any way.

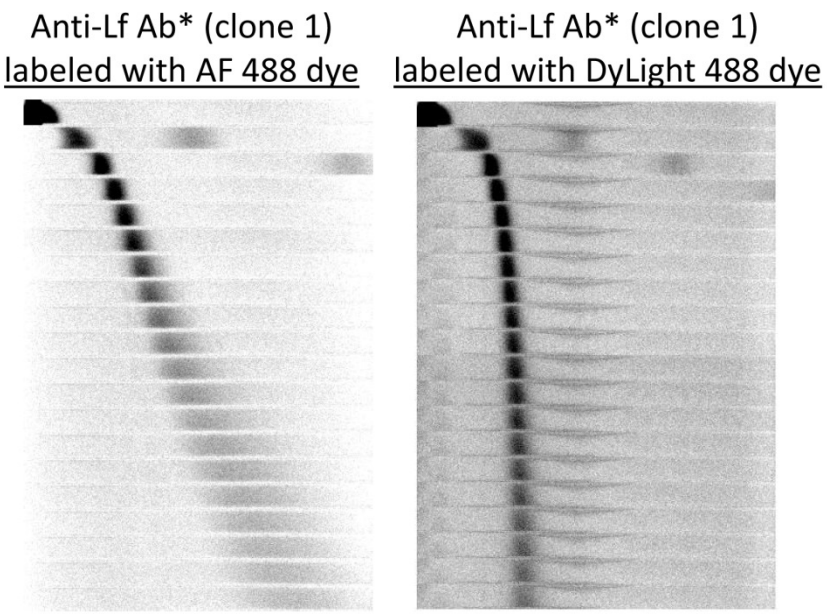

Figure 38. Separations of Anti-Lf Ab labeled with AF488 (left) and DyLight 488 (right). AF488 appears to add negative charge to the antibody as indicated by the faster observed mobility. 102 V/cm electric field. 3-6% discontinuous gelwith pH 9.75 glycine buffer fabricated with 4 min @ 7.2 mW/cm^2 followed by 15 min @ 11.7mW/cm^2. 2 seconds per frame.*

These observations can be explained when we look into the properties of different types of dyes. Cyanine dyes (Cy dyes) utilize a N-hydroxysuccinimidyl-ester (NHS) reactive group which forms covalent amide bond with epsilon amino group of lysine. In this binding reaction, a single positive charge on the Cy dye substitutes the single positive charge of a lysine and therefore leaves the pI and mobility of the labeled protein relatively unchanged. The NHS ester hydrolysis of this reaction only occurs above pH 9. Therefore, it is likely that this dye chemistry will be unstable in alkaline pH buffers.

Alexa Fluor dyes are modeled after Cy dyes and claim improvements in conjugate fluorescence and photostability. They utilize a carboxylic acid TFP ester reaction to react with free amines on the protein. TFP esters are less susceptible to spontaneous hydrolysis during conjugation and are more stable at basic pH. However, Alexa Fluor dyes are synthesized through sulfonation of other dyes, making them negatively charged and hydrophilic, and explaining the observed mobility increase of Alexa Fluor labeled antibodies.

In contrast, DyLight dyes are maleimide-activated dyes which react with reduced sulfhydryl groups (-SH) to form stable thioether bonds. Maleimides are specific for sulfhydryl groups in the pH range 6.5-7.5 and therefore the labeling reaction should be done at neutral pH. DyLight dyes do not contribute a negative charge to the protein. In contrast, sulfhydryls are not as numerous as primary amines on the surface of the protein; thus the degree of labeling is likely to be lower than that with Alexa Fluor dyes.

The effect of the dye on binding affinity and assay performance is also demonstrated in Figure 39 where a separation of labeled Lf and unlabeled anti-Lf Ab (clone 1) yielded a beautiful separation of Lf* and complex on a 3-6% discontinuous gel (fabrication conditions 4.5 min @ 7.1 mW/cm^2 followed by 17 min @ 12.3 mW/cm^2). Velocity pre- and post-discontinuity was linear for both the Lf* and complex peaks and the complex was able to freely migrate past the discontinuity with no smearing or gel staining. In addition, a fully resolved electropherogram was achieved. None of the non-ideal artifacts (e.g., complex precipitation, complex smearing, gel staining) were observed when Lf was labeled. This observation may be due to the fact that labeling the antibody can obscure the binding site on the antibody whereas labeling the Lf does not interfere with the binding site on this protein.

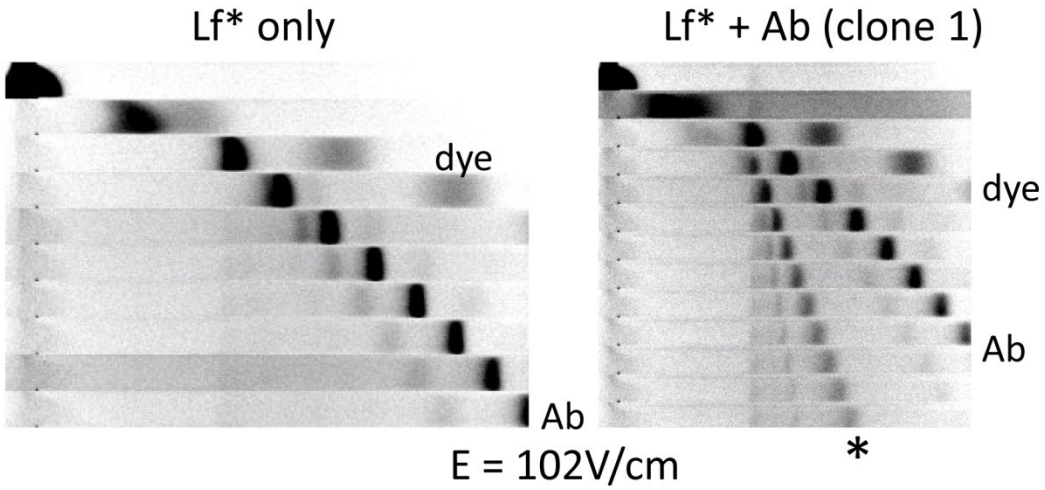

Figure 39. A separation of labeled Lf does not yield the same non-ideal separation performance as labeled Ab. Anti-Lf clone 1 used and amine-reactive Alexa Fluor dye. Each frame is 2 sec.

Therefore, we sought to select a set of antibody and dye conditions that would minimize the negative charge on the antibody capable of interacting with the positive residues on Lf and causing dispersion-inducing weak electrostatic interactions between the antibody probe and the alkaline Lf target. Dylight 488 dye was employed since Dylight 488 contributed minimal charge to the labeled antibody probe as compared to other commonly used fluorescent dyes (e.g. Alexa Fluor 488) as evidenced by a 3.8x reduction in antibody velocity in 5%T gel when DyLight dye was used instead of Alexa Fluor dye (Figure 38). Fluorescently-labeled antibody probes were labeled in-house with DyLight 488 fluorescent dye at 4°C overnight and purified to remove un-reacted dye using 10k MWCO Slide-A-Lyzer Dialysis Cassettes in PBS with 3 buffer exchanges overnight.

Because increased complex resonance time in the gel was observed to increase protein-gel interactions and non-specific immune complex-PA gel immobilization, the applied electric field was also optimized to the highest level that would allow for multiple (20-40) runs and was

determined to be 150V/cm for the first 5.5 seconds followed by 102V/cm.[142] The reductions in gel-analyte contact time afforded by increasing electric field strength improved assay performance by decreasing gel staining and complex smearing.

Carrier proteins (e.g., BSA or anti-CRP and CRP) were also observed to increase the signal of the immune complex. When a sample containing anti-CRP*and CRP was run after a sample that contained anti-Lf Ab* and Lf, all gel staining from the first run was washed away, suggesting that these carrier proteins shield the charge of the complex and allow it to migrate freely without electrostatic interactions in the gel. Adding a carrier protein was also shown to decrease immune complex peak dispersion, allowing for a tighter migrating band to be detected and a clearer electropherogram to be generated.

Pore Size Discontinuity Optimization

The PA gel pore size in the separation channel was tuned in order to enhance sensitivity and further minimize the observed complex peak dispersion. Sample stacking occurs at the pore discontinuity and is proportional to the extent of pore size change as given the equation below

$$\log\left(\frac{C_1}{C_2}\right) = -k_r(T_2 - T_1)$$

where C_1 and C_2 are the average plug concentrations before and after the discontinuity respectively, k_r is the retardation coefficient of the analyte and T_1 and T_2 are the total acrylamide concentrations before and after the discontinuity respectively. The change in total acrylamide concentration was therefore maximized to achieve the greatest possible sample stacking and enhanced sensitivity. A discontinuous gel architecture of 3-6%T was experimentally determined to allow for maximal sample stacking and resolution while still allowing for the migration of both free antibody and complex.

Summary of Assay Optimization

In summary, in order to minimize the observed issues of gel staining, complex smearing, and complex precipitation, we employed a pore-size discontinuity of 3-6%T in order to reduce the immune complex peak dispersion, a pH 11 CAPS buffer in order to minimize positive charge on the Lf molecule and the resultant non-specific binding, and added reagents in the following order in order to establish their charge before allowing them to interact: 1) Lf, 2) 1× pH 11 CAPS buffer, 3) tear matrix (if indicated), and 4) Ab*.

5.9 Effect of High pH CAPS Buffer on PA Gel Polymerization

In the alkaline buffer conditions, roughly 36% of as-fabricated chips were usable – which is a significant reduction in chip yield as compared to our previous assay buffer formats (neutral pH). The most common modes of chip failure were gel breakdown through void formation (and subsequent interrupted current path) and gel hydrolysis during prolonged chip storage resulting in an inability to load sample on-chip. The degree and rate of hydrolysis increases with decreasing acrylamide concentration (%T)[164] and therefore was most extensive in the loading

channel region where the majority of chip failures were observed. To mitigate these failure methods, two major quality checks were implemented: 1) chip storage time between fabrication and use did not to exceed 3 hours and 2) BSA was introduced as an internal velocity standard to track analyte velocity over time. Using the BSA mobility standard, a 30% reduction in starting velocity in the dilute tear matrix was set as a threshold for the minimum acceptable chip performance.

The chip failure modes arise from fabrication and operation of PA gel in high pH CAPS buffer. Full polymerization of all monomers in the precursor solution is critical as un-reacted acrylamide monomers can covalently bind to proteins at alkaline pH by reacting with the ε-amino group of lysine residues.[165] This monomer-analyte reaction has been shown to decrease the pI point of basic proteins and cause artifacts in basic PAGE such as streaking of proteins or band multiplication.[165] We therefore hypothesized that incomplete polymerization of all monomers in solution was a contributor to the smearing observed during immunoassay operation. Further, we observed frequent gel failures after short (10-30) runs, indicating a lower mechanical integrity of the resultant gel polymerized with the high pH CAPS buffer.

Introducing the CAPS molecule and moving to a high pH regime affects the polymerization reaction and overall gel integrity. Therefore, attention was paid to understand gel performance in this highly alkaline regime. Recalling that PA gels are formed by copolymerization of acrylamide and bis-acrylamide ("bis", N,N-methylene-bisacrylamide) in a vinyl addition polymerization reaction initiated by a free radical-generating photoinitiator[155] with a rate of polymerization given by the equation:[156]

$$R_p = k_p \left(\frac{\Phi \varepsilon I_0}{k_t}\right)^{1/2} [M][I]^{1/2}$$

Currie and co-workers determined that k_t and k_p decrease 16x and 4x respectively as pH is changed from 1 to 13 and initiation is kept constant, meaning that $k_p/(k_t^{1/2})$ remains relatively constant over a wide pH range.[166] These results suggest that, although the presence of highly alkaline buffers slows the propagation and termination steps significantly, the overall polymerization reaction would not be adversely affected by the high pH conditions needed for the immunoassays detailed here.

However, the introduction of the CAPS molecule has several effects on the polymerization rate. CAPS is a chain transfer agent that suppresses or retards polymerization by reacting with the initiating radical species and yielding radicals with low or no activity or capacity for further propagation.[167] When CAPS is present, a growing polymer chain abstracts a hydrogen atom off the sulfonic acid group of the CAPS molecule (Figure 40), giving a terminated polymer chain and new initiating radical on the solvent molecule which is unable to initiate or propagate additional polymer synthesis. This serves to increase the rate of termination, decreasing the polymerization rate, shortening the overall chain length and reducing the mechanical integrity of the gel.[168] The radical-scavenging activity of CAPS also serves to decrease initiator efficiency by competing with monomers in solution for free radical electrons, thereby reacting with free

radicals in solution and reducing their effective concentration. This decrease in radical efficiency or quantum yield also serves to decrease polymerization rate.

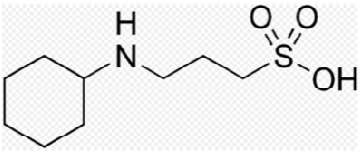

Figure 40. CAPS molecule. The hydrogen atom is abstracted from the sulfonic acid group by the growing polymer chain during polymerization, retarding polymerization.

Experimentally, we noted an increase in polymerization rate and gel mechanical integrity with increasing starting initiator concentration. This served to increase the effective free-radical concentration available for initiation and propagation and reduce the inhibiting effect of the CAPS solute. Employing the Henderson-Hasselbach equation to calculate the percentage of CAPS molecules that will be deprotonated at pH 11, 3.98x more unprotonated CAPS molecules will exist in solution than protonated CAPS molecules. These unprotonated CAPS molecules can act as electron acceptors, competing with the monomers in solution for free radical electrons and inhibiting initiation. However, no noticeable improvement in polymerization rate or qualitative assessment of mechanical integrity was noted when the relative concentrations of protonated or deprotonated forms of CAPS were altered by polymerizing at pH's below and above the pKa of CAPS respectively (i.e. 9% deprotonated versus 72% deprotonated molecules in solution).

These results suggest that, while the overall polymerization reaction is not adversely affected by the high pH conditions needed for the immunoassays detailed here, the presence of the CAPS molecule slows the propagation and termination steps significantly and irrespective of protonation state, and therefore higher concentrations of initiator are needed for complete polymerization.

As a result of the predicted and observed reduction in polymerization rate, 2× more VA-086 was used for all chips fabricated with CAPS buffer (0.4%) and polymerization time was increased dramatically in the optimized fabrication protocol to 18 minutes (220% longer time than polymerization in pH 8.4 tris-glycine buffer) for all gels used in experimentation. It was found that the longer exposure times allowed for more monomer uptake and an overall reduction in gel smearing (Figure 41).

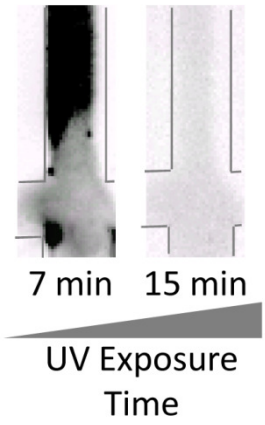

Figure 41. Increasing UV exposure time leads to a greater degree of polymerization and a resultant decrease in protein-monomer interactions (complex immobilization). Reprinted with permission from Karns and Herr, Human Tear Protein Analysis Enabled by an Alkaline Microfluidic Homogeneous Immunoassay*, 2011, 83, 8115-8122. © 2011 American Chemical Society.*

Since oxygen also has an inhibitory effect on acrylamide polymerization,[155,169] diffusion of oxygen into the precursor solution ultimately limits the possible reaction times and some reduction in PA chain length and gel integrity was retained despite the increase in exposure time. Further, even polymerization under optimal conditions yields approximately 96% monomer consumption,[170] leaving 50-60mM of un-reacted acrylamide monomers in a 10%T gel matrix.[165] These residual monomers likely contribute to the small degree of residual protein smearing that remains in this alkaline regime despite increased exposure times.

5.10 Alkaline Hydrolysis of Polymerized PA Gels

The reduction in gel integrity caused by shorter chain lengths was further augmented by rapid alkaline hydrolysis of the polymerized PA gel which yields random copolymers of acrylamide and acrylic acid.[164] The kinetics of the hydrolysis reaction have been studied extensively [164,171-173] are shown to have fast reaction rates at the initial stages followed by a quick rate decrease with increasing conversion. The rapid initial rate is accelerated by the ability of carboxylate groups formed in the hydrolysis reaction to hydrolyze neighboring amide groups.[164] The subsequent deceleration in hydrolysis rate is due to the accumulation of negative carboxylate charges on the polymeric chains which exert an electrostatic repulsion effect towards negative ions.[172,173] This build-up of negative charge serves to repel hydroxyl ions, slowing the rate of reaction and also increases the repulsive force between the gel and the negative analytes,[173] thus decreasing the ability to load negative analytes on-chip over time and resulting in an overall decrease in analyte mobility. Further, alkaline hydrolysis has been shown to cause a marked decrease in the molecular weight and chain length of PA gels over time, further contributing to short chip lifetimes.[173]

As a result of these combined effects, only 25% of fabricated chips were usable and chip storage time between fabrication and use had to be minimized to < 3 hours. The three most common modes of chip failure were fabrication inconsistencies owing to chip alignment during discontinuity fabrication, gel breakdown through bubble formation, and gel hydrolysis during prolonged chip storage resulting in an inability to load sample on-chip. The degree and rate of hydrolysis increases with decreasing acrylamide concentration (%T)[164] and therefore was most extensive in the loading channel region where the majority of chip failures were observed. To mitigate these failure methods, device lifetime was monitored using BSA as an internal velocity standard. A 30% reduction in BSA velocity was set as the threshold for the minimum acceptable chip performance. In the CAPS system, gel failures were observed after 10-30 electrophoretic runs, indicating a lower integrity of the resultant gel polymerized with the high pH CAPS buffer.

All devices reported in this work functioned within specifications for an average of 26 runs before dropping below the pre-defined mobility threshold or experiencing one of the two most common catastrophic failure mechanisms (e.g. bubble/void formation). Sample-to-sample loading variability due to changes in the well-loading channel gel interface over time, gel hydrolysis over time or small changes in sample conductivity as Lf concentration is increased was eliminated by normalizing complex peak areas by the BSA internal standard peak area.

5.11 Lactoferrin Immunoassay Device Performance & Characterization

The final optimized assay incorporates a 3-6%T PA gel pore-size discontinuity photolithographically fabricated *in situ* 0.33 mm downstream of the injection junction with pH 11 CAPS sample and gel buffers. As detailed earlier, the optimized antibody probe used DyLight 488 label on clone 1B8 (clone 6). Figure 42A shows full field microscopy images of the separations when recombinant Lf was spiked into Lf-depleted human tear matrix (377 nM, positive control) compared to Lf-depleted tear matrix (negative control). In both cases, Lf-depleted tear matrix was diluted 20x in pH 11 CAPS run buffer. Under these conditions, the assay is able to resolve free antibody and immune complex (SR ≥ 1) in <5 µL of dilute tear matrix and <5 seconds of assay run time. To our knowledge, this is the first demonstration of native PAGE at this high of a pH.

Comparison of immunoassay results from the positive and negative controls reveals resolution (SR = 1) of an immune complex peak (indicated with an asterisk) at 4 s and a separation length of 0.374 mm (defined as immune complex location at time of analysis). The immune complex peak has an observed mobility of $6 \times 10^{-5} \pm 1 \times 10^{-5}$ $cm^2/(V\ s)$. Quantitation of peak mobility allowed identification of the immune complex peak, even for the promiscuous Lf analyte. Importantly for tear analysis, the assay is capable of analyzing < 1 µL of tear fluid. The sparing consumption of sample material is critical to the study of tear samples from dry eye patients and biospecimen repositories where limited material is longitudinally collected for subsequent, retrospective analysis.

We also sought to demonstrate detection of endogenous Lf in <1 µL of the tear matrix of both healthy and SS patients. In Figure 42B, we see that healthy tear assays showed a distinct immune complex peak arising from endogenous Lf, with a mobility matched to that measured using recombinant Lf spiked into Lf-depleted tears (Figure 42A, positive control). Interestingly, the SS tear fluid exhibited numerous well defined, immune complex peaks having a range of mobilities. As Lf is known to complex promiscuously and dry eye tear fluid is anticipated to have lower volumes and thus higher concentrations of matrix components (as compared to healthy tear fluid), the multiple peaks are attributed to Lf binding with other analytes in the tear matrix and, thus, the formation of multiple immune complexes with distinct mobilities.[68]

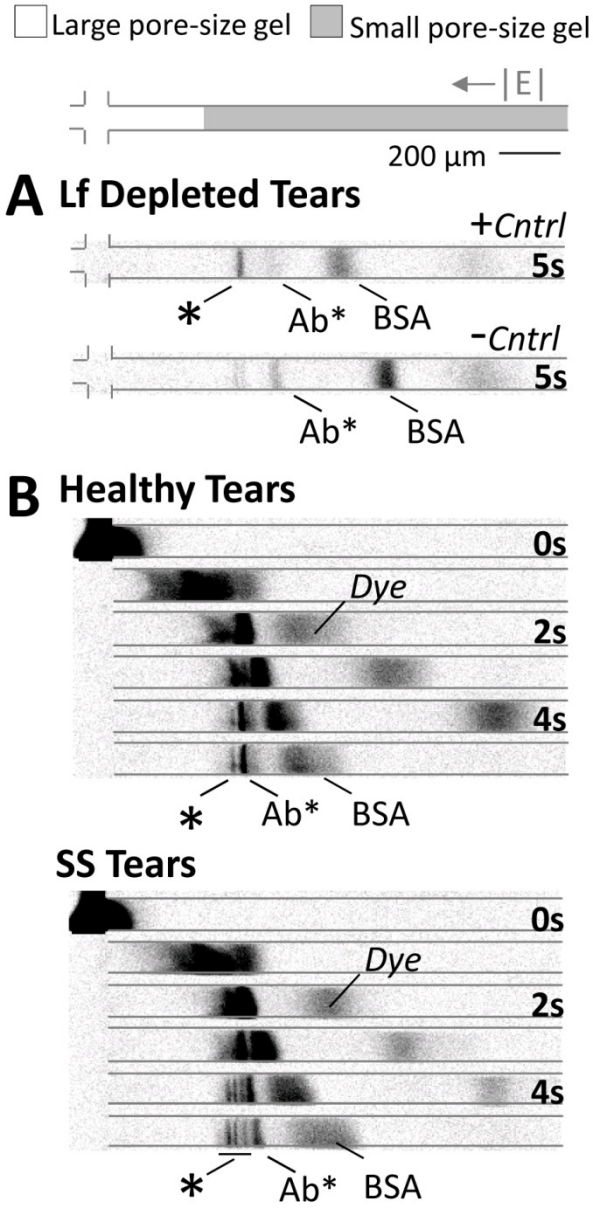

Figure 42. Optimized separation conditions enable detection of endogenous Lf in diluted human tears. (A) The immune complex peak is identified through mobility information and confirmed by comparing separations of positive (Ab and Lf in Lf-depleted tears) and negative (Ab* in Lf-depleted tears) controls. (B) Endogeneous Lf is detected in <1 µL of healthy and SS tears. Specific immune complex peaks are indicated with an asterisk. BSA internal standard was used in analytical normalization. Reprinted with permission from Karns and Herr,* Human Tear Protein Analysis Enabled by an Alkaline Microfluidic Homogeneous Immunoassay*, 2011, 83, 8115-8122. © 2011 American Chemical Society.*

Nevertheless, mobility information obtained from positive and negative controls (Figure 42A, positive control) enables the identification of one complex peak for direction comparison and quantification. The endogenous Lf assays reported endogenous Lf complexes in 5 s of elapsed separation time, on par with the time required for measurement of spiked Lf under the same assay conditions (Figure 42A). Figure 43 reports intensity profiles of the optimized homogeneous electrophoretic immunoassay for analysis of Ab* in dilute Lf-depleted tear matrix ([Ab* = 100 nM]) (Lf-, left panel) and analysis of Ab* in dilute Lf-depleted tear matrix, now with recombinant Lf protein (283 nM) present (Lf+, right panel). In both cases, the Lf-depleted tear matrix was diluted by 20x in CAPS.

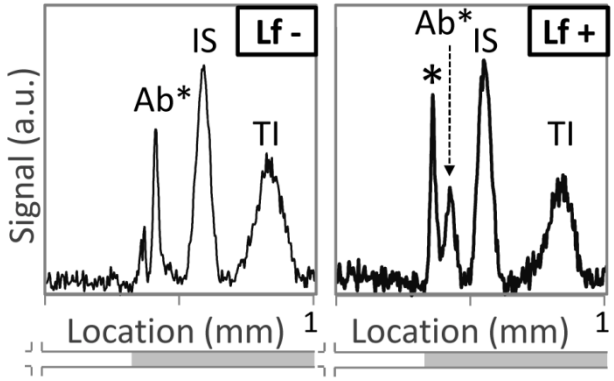

Figure 43. The assay can detect Lf in human tears. Intensity profile of microchannel at 4 s reveals quantifiable immune complex peak. Left panel shows separation of Ab in Lf-depleted tear matrix (Lf-). Right panel shows separation of Ab* and 283nM spiked Lf in Lf-depleted tear matrix (Lf+). TI indicates trypsin inhibitor internal standard and IS indicates BSA internal standard used in analytical normalization. Immune complex peak is indicated with an asterisk. Adapted with permission from Karns and Herr, Human Tear Protein Analysis Enabled by an Alkaline Microfluidic Homogeneous Immunoassay, 2011, 83, 8115-8122. © 2011 American Chemical Society.*

The quantitative capabilities and dynamic range of the assay are shown in Figure 44 where a calibration curve of known concentrations of recombinant Lf were spiked into dilute Lf-depleted tear matrix. The immune complex peak was positively identified by matching the mobility across the samples to enable direct comparison of like peaks. Here, a quantitative assessment of total Lf content in a sample is generated by plotting the measured normalized complex peak area against the expected concentrations for each sample. On-chip measurements of endogenous Lf concentration in SS and healthy patients (black circles) were calculated from a 4-parameter logistic fit model [y = B2 + (B1 - B2)/(1+(x/B3)^B4)] of the dose response curve (4P fit) and plotted against measured normalized immune complex peak area. The assay has a linear quantitative range of 40-400 nM Lf (10x quantitative range) and a detectable concentration range of 3-754 nM Lf which corresponds well with the desired

quantitative range of 13-390 nM Lf to be clinically relevant for SS diagnostics (including a 10x dilution factor in buffer).[30] The lower limit of detection (defined as SNR = 3) for the alkaline homogeneous electrophoretic immunoassay is 3 ± 2 nM Lf in tear matrix.

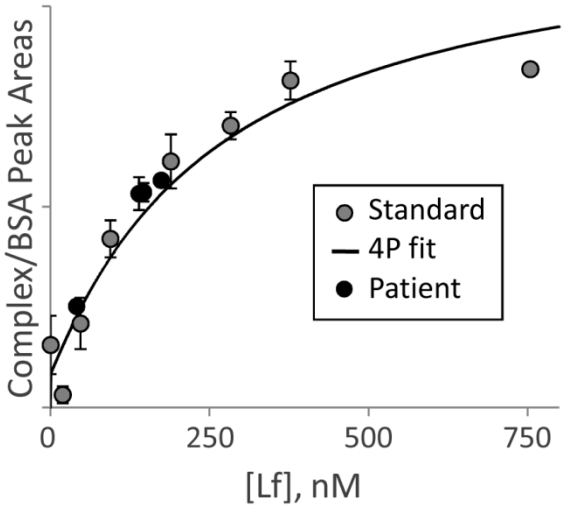

Figure 44. The assay is capable of quantifying Lf concentration in dilute tear matrix. Grey circles represent on-chip measurements of normalized immune complex peak area of a spiked Lf standard curve in dilute tear matrix. On-chip measurements of endogenous Lf concentration in SS and healthy patients (black circles) are shown. Error bars are calculated from replicate trials. Adapted with permission from Karns and Herr, Human Tear Protein Analysis Enabled by an Alkaline Microfluidic Homogeneous Immunoassay, 2011, 83, 8115-8122. © 2011 American Chemical Society.

The Lf concentration at which half of the maximum immune complex is formed is 262.4 ± 0.9 nM which represents a low binding affinity in the assay conditions when compared to ten previously characterized monoclonal antibodies to human Lf which had dissociation constants ranging from 0.5 nM to 18 nM.[174] As mentioned, when compared to measurements in the presence of saliva and serum, tear fluid has been shown to dramatically reduce the binding efficiency of immunoglobulins, especially in alkaline pH conditions.[48] Therefore, this low measured binding affinity may be weakened by remaining electrostatic binding interactions between the alkaline target and antibody, some denaturation of antibody or antigen in the high pH conditions, and/or the presence of these unidentified factors present in tear fluid which inhibit the binding efficiency of immunoglobulins.[48] Nevertheless, as demonstrated in the immunoassays presented here, the immune complex formation is sufficient for Lf quantitation on the time scales of the assay.

Having established a dose-response curve for Lf in depleted human tear matrix and characterized the impact of the sample processing on Lf concentration, analysis of both healthy and SS patient tear samples was conducted with the new on-chip format. Endogenous Lf in the

tears of four human volunteers was measured using the alkaline homogeneous immunoassays developed in this work (dark circles in Figure 44 and Figure 45A). Both healthy and SS human tears were assayed, after dilution to within the quantitative range of the assay (20× for healthy and 10× for SS tears). Qualitative comparison of the resulting electropherograms revealed down-regulated Lf levels in SS compared to healthy tears when normalized to an internal standard peak (Figure 45A). The measured normalized complex peak area was plotted against the expected concentrations. The three-parameter fit generated from the spiked dose-response study was used to determine the Lf concentration in the patient samples.

The assay precision (using ELISA as a gold-standard) was assessed by comparing the on-chip measurements of Lf concentration in the patient population with measurements made by ELISA (Table 6). As shown in Figure 45B, a linear regression shows a high degree of correlation between the two measurement techniques (r^2 = 0.9935). Table 6 demonstrates the assay precision to within 15% of ELISA and attests to the assay's ability to quantify Lf concentrations in tears.

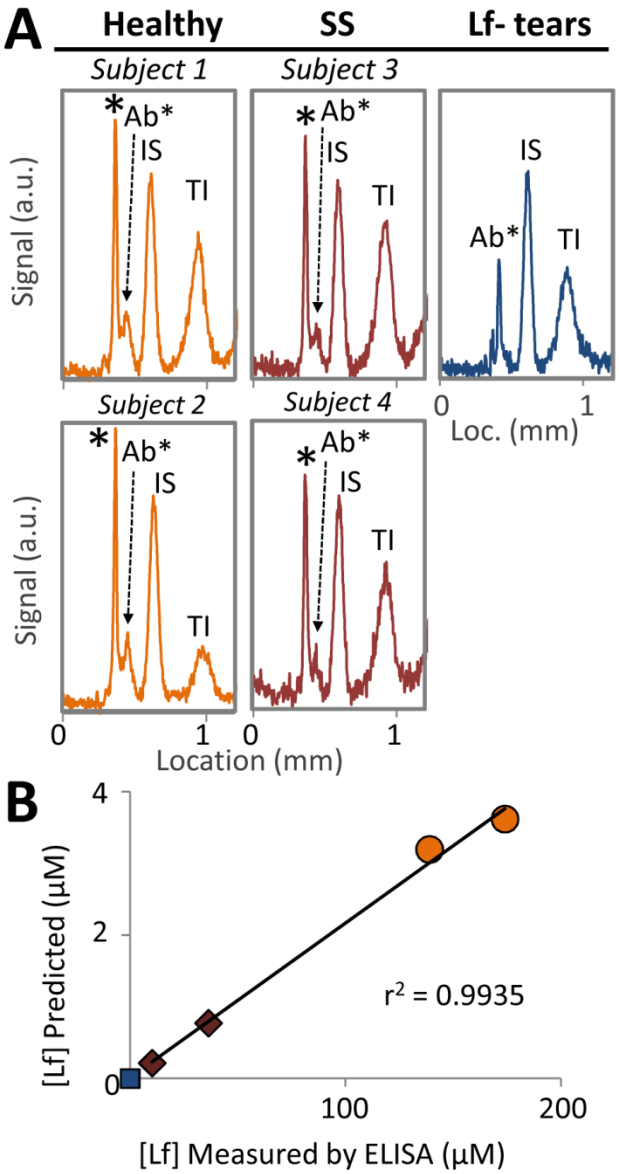

Figure 45. Endogenous Lf quantitation. (A) Endogenous detection of multiple patient samples reveals down-regulated Lf levels in SS tears compared to healthy controls when complex peak is normalized to an internal standard (IS). Complex is indicated with an ''. Intensity profiles taken 5.1 sec after injection. (B) The assay demonstrates a high degree of correlation between endogenous Lf measurements made on-chip and by ELISA (R^2 = 0.9935). Healthy patients (circles), SS patients (diamonds), Lf-depleted tears (square). Reprinted with permission from Karns and Herr, Human Tear Protein Analysis Enabled by an Alkaline Microfluidic Homogeneous Immunoassay, 2011, 83, 8115-8122. © 2011 American Chemical Society.*

Table 6. On-chip endogenous Lf measurements are accurate to within 15% of ELISA. Adapted with permission from Karns and Herr, Human Tear Protein Analysis Enabled by an Alkaline Microfluidic Homogeneous Immunoassay, 2011, 83, 8115-8122. © 2011 American Chemical Society.

Patient	On-chip [Lf], nM	ELISA [Lf], nM	% error
#75R Healthy	180.5	174	3.8%
#101 Healthy	159.4	139	14.7%
#63R SS	44.7	41	9.1%
#63L SS	161.5	146	10.6%

Although ELISA has been used extensively in tear fluid research and was chosen as a gold-standard for comparison, the reported interfering factors, high background signals, blooming and matrix effects, and cross-talk commonly found in micro-well arrays and immunoassays[33] led us to seek another method of validating assay accuracy. Using known concentrations of Lf spiked into dilute tear matrix to validate assay accuracy compared to absolute Lf concentrations, we obtained a distinct dose response curve. We systematically removed each known Lf concentration point, applied a three-parameter least squares curve fit of the form y = (B1*x)/(x+B2) + B3 to the remaining points, and determined the expected Lf concentration with the updated curve fit. The results show that the assay is predictive to within 30% in the concentration range 19nM – 377nM. Using the three dose response curves to assess chip-to-chip reproducibility showed an average measured B_1 of 0.27 $\pm$ 0.05 (17% variation), average B_2 = 220 $\pm$ 27 nM (12% variation) and an average B_3 = -0.01 $\pm$ 0.02 nM.

The comparable quantitative capabilities to ELISA combined with the 770x time savings, small sample volume requirements which eliminate the need to pool patient samples and enable measurements in single patient tears, and reduction in non-specific matrix effects owing to the highly alkaline pH conditions point to the utility of this assay in enabling more accurate protein measurements in tear fluid.

Tear Matrix Effects

The tear matrix has been shown to have an effect on measurements made using immunoassays.[49] We therefore sought to probe the effect of tear fluid on the Lf measurements made using our microfluidic immunoassay. The presence of dilute tear matrix had both positive and negative effects on assay performance. First, the high salt content and resultant conductivity of tears contributes to leading-edge dispersion of all sample bands and an overall reduction in assay performance. Fluid buffers used in electrokinetic systems must be conductive; however, the deleterious Joule heating caused by high conductivity buffers has precluded the use of some biological fluids.[175] In this case, continuous loading of tear-

containing sample fills the loading channel with higher conductivity sample and creates a discontinuity in buffer conductivity and thus applied electric field between the loading and separation channels. After injection of the higher conductivity sample plug into the separation channel, any molecules diffusing over the leading edge of the band will sample the lower conductivity buffer and be accelerated down the separation channel contributing to the leading-edge dispersion of the band and signal loss. Conversely, molecules that diffuse over the trailing edge of the band will be accelerated back into the sample plug. In sum, this effect leads to band dispersion. Figure 46 shows the increase in BSA velocity from runs 2 to 5 as tear fluid is added to the sample buffer. This increase in buffer conductivity accounts for the initial rise in BSA velocity. As the run number increases from there, there is a gradual decrease in BSA velocity which can be used as a proxy for degree of gel hydrolysis in high pH conditions and applied electric fields. All devices used in the work were able to run an average of 26 runs before dropping below the threshold or experiencing one of the three most common catastrophic failure mechanisms (e.g. bubble formation)

Figure 46 also shows the sample-to-sample loading variability. This variability may be accounted for due to changes in the well-loading channel gel interface over time, gel hydrolysis over time or small changes in sample conductivity as Lf concentration is increased. However, any variability in sample loading was removed by normalizing complex peak areas by the BSA internal standard peak area in analysis.

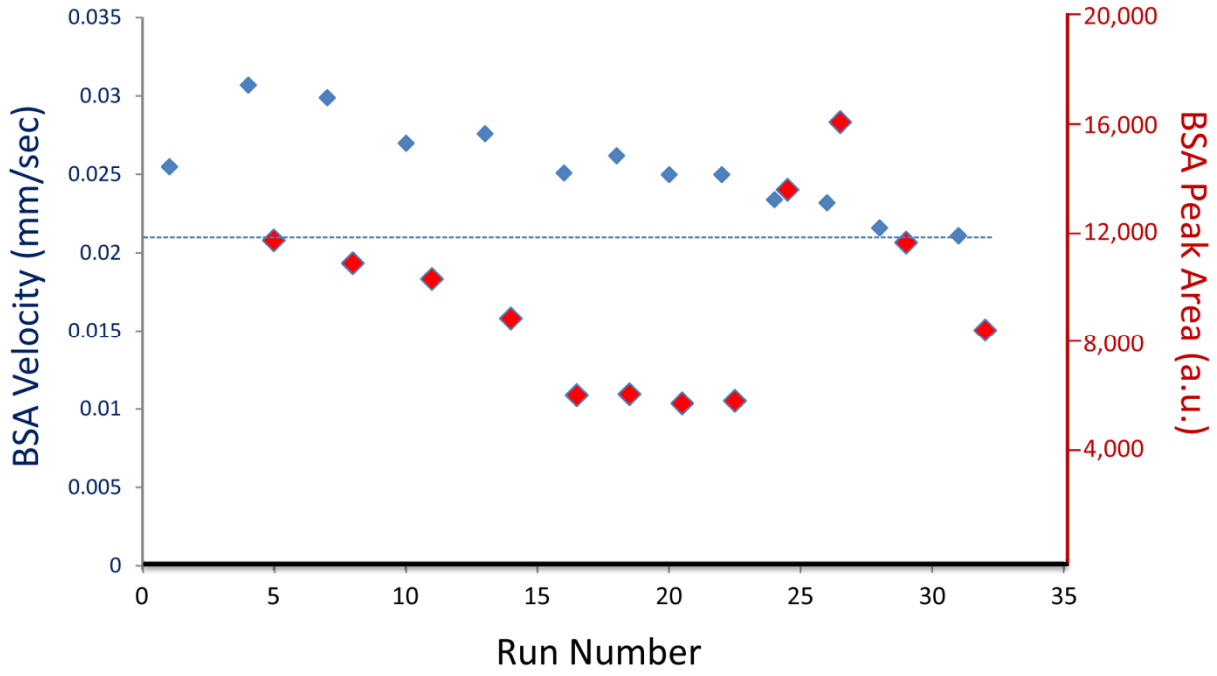

Figure 46. Chip lifetime is limited by PA gel hydrolysis under high pH buffer conditions and high currents owing to high tear conductivity. Velocity of a BSA internal standard was tracked over chip usage (blue diamonds). A 30% drop in BSA internal standard mobility was used as a threshold for chip failure (dashed blue line). Sample loading variability is shown with fluctuations in BSA peak area over run number (red diamonds), especially in the four endogeneous tear samples run at the end. Loading variability is accounted for in all quantitative calculations by normalizing all peaks to the BSA internal standard.

Secondly, Lf has been shown previously to bind to other matrix factors in the presence of tear fluid.[46] This observation in the literature was confirmed in experiments showing that increasing concentrations of tears causes increased complex formation when incubated with labeled Lf (Figure 47). This nonspecific complexing of Lf with other analytes in the tear matrix may result in charge shielding of Lf and contribute to the reduction in gel staining and complex smearing observed when tears are present. It also increases the overall complex size in the presence of tear fluid and increases the overall mobility shift between the free antibody and immune complex, thus improving separation resolution.

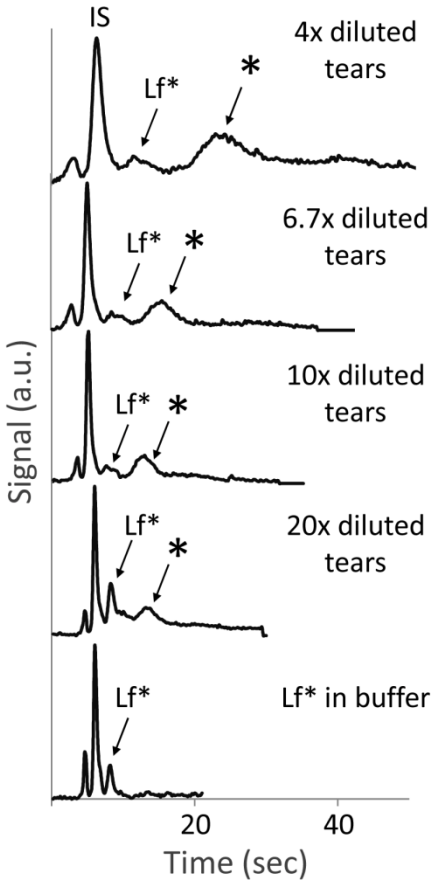

Figure 47. Evidence of non-specific Lf binding to analytes in tear matrix. A complex peak appears when labeled Lf (Lf) in buffer is compared with Lf* in the presence of healthy tear fluid. As tear concentration is increased, the complex peak increases and free Lf* peak decreases. 20x (healthy) and 4.75x (SS) dilution factors are used for all other analyses. Asterisk indicates complex peak, tris-glycine buffer conditions, detector located 1 mm downstream of injection junction, E = 102 V/cm for first 5.5 sec, then 150 V/cm. Reprinted with permission from Karns and Herr, Human Tear Protein Analysis Enabled by an Alkaline Microfluidic Homogeneous Immunoassay, 2011, 83, 8115-8122. © 2011 American Chemical Society*

Despite these matrix interactions, the antibody still appears to specifically bind to Lf in the sample as shown in Figure 48. Assay specificity was assessed by depleting a healthy and a SS tear sample of Lf to levels below the LLOD of the assay (3.18nM Lf remaining in healthy sample, 1.2nM remaining in SS sample) and comparing Ab* spiked in Lf depleted tears to that in non-depleted (Lf positive) tears. Figure 48A compares the separation montages of 40x diluted healthy Lf positive and Lf depleted tears and 20x diluted SS Lf positive and Lf depleted tears. There is a marked reduction in complex signal (indicated by an asterisk) in the depleted samples with a 6.8% residual signal in healthy tears and 14.5% residual signal in SS tears (10.7% average

non-specific signal, Figure 48B). This is likely due to some non-specific electrostatic interactions between the Ab* and other high abundant alkaline proteins found in tears.

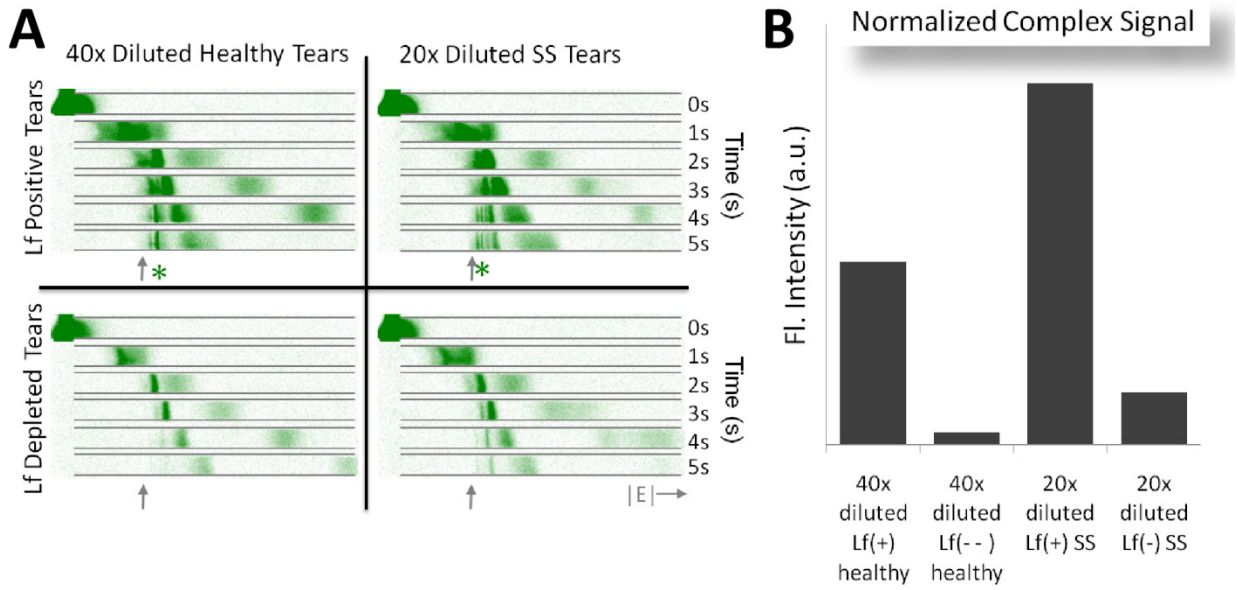

Figure 48. The assay is specific for endogenous Lf in human tears. (A) Immune complex peaks ('') appear in non-depleted (Lf+) healthy and SS tears but not in Lf-depleted tears. (B) A 6.8% residual signal is detectable in Lf-depleted (Lf-) healthy tears and 14.5% residual signal is detectable in Lf-depleted SS tears. All trials are in pH 11 CAPS buffer, antibody clone 6, E = 102 V/cm. Healthy tears were diluted 40x, SS tears were diluted 20x.*

5.12 Relevance to Real Ocular Concentration

It is known that tear protein concentration is highly dependent on sample preparation, yet no standard sample preparation methodology exists.[58,176] Schirmer strips have been shown to be effective collection methods for removing some of the unknown non-specific interfering factors found in tear fluid[33] and are the clinical *de facto* standard for tear collection and storage in large patient registries (e.g. UCSF). However, little attempt to date has been made to characterize specific tear fluid collection methodologies (e.g., Schirmer strips, microcapillaries) so as to relate disparate assay measurements back to the actual protein concentration in the eye. As a result, collection methodologies and tear protein measurements in the literature vary widely.[177,178,20,34]

Since assay reliability is only as good as upstream sample preparation, we therefore also endeavored to determine the exact Lf extraction efficiency from Schirmer strips using our elution protocol by loading 2.5 µL of 1 mg/mL purified Lf onto the bottom bulb of Schirmer strips, performing the same overnight elution protocol as for the human samples and measuring the Lf concentration in the eluate with ELISA. We found the average Lf extraction efficiency to be 37 ± 7%. Noting that the elution protocol dilutes the tears ~16x, we can

therefore determine that the amount of Lf in the eluate is 2.3 ± 0.5% that of the actual concentration in the eye using this protocol.

In combination with the *a priori* determined Schirmer strip elution efficiency, on-chip measured Lf concentrations in diluted tear matrix were employed to estimate the endogenous ocular Lf concentrations for the four patient samples analyzed (two classified as healthy, two classified as SS positive): 12.1 mg/mL and 10.7 mg/mL for the two healthy patients and 0.7 mg/mL and 2.7 mg/mL for the two SS patients (Table 7). The measured endogenous Lf down-regulation in SS tears compared to healthy tears was as expected from the literature[30] and validates the clinical relevance of the assay's quantitative capabilities. To our knowledge, this is the first attempt in the literature to standardize the collection method so as to arrive at a final measured concentration in the eye and advances our ability to make cross-study comparisons of tear protein levels.

Table 7. Sample preparation characterization allows for measured Lf concentration to be related back to the actual Lf concentration in the eye. The Lf elution efficiency from Schirmer strips using our reported reconstitution protocol was demonstrated to be 37 ±7%. Accounting for the 16x dilution factor introduced by the elution protocol, 2.3 ±0.5% of Lf concentration in the eye is therefore analyzed in the final tear eluate run on-chip. The actual concentration in the eye shows substantially higher Lf levels in healthy tears when compared to SS tears as expected.

Patient	Measured [Lf] in Schirmer strip-collected, diluted tear eluate, nM	Dilution factor introduced by assay	Actual concentration in the eye, µM	Actual concentration in the eye, mg/mL
#75R Healthy	180.5	20.0	157.0	12.1
#101 Healthy	159.4	20.0	138.6	10.7
#63R SS	44.7	5.0	9.7	0.7
#63L SS	161.5	5.0	35.1	2.7

5.13 Conclusions

Chapter 5 details the development, optimization and characterization of a highly alkaline microfluidic homogeneous immunoassay capable of rapidly quantifying endogenous human tear lactoferrin in <5µL of human tear fluid from both healthy and SS patients. This assay is the first demonstration of a tear-based immunoassay that could be used for systemic diagnosis

using tear fluid. In particular, we detailed device fabrication and discussed the implications of a highly alkaline buffer regime on the free-radical gel polymerization process and post-fabrication gel integrity. While the free-radical scavenging capabilities of buffer molecules, alkaline gel hydrolysis and protein-gel interactions enabled by the highly alkaline conditions have potentially deleterious effects on assay performance, careful monitoring of device integrity through use of a BSA internal standard, deliberate selection of the antibody probe, and optimized fabrication conditions enabled robust and repeatable analyte measurements to be made. The Lf immunoassay presented here demonstrates our ability to make biochemical measurements in tear fluid, in the process overcoming many challenges of tear analysis including the high conductivity of tears, interfering components, nonspecific interactions, and the high alkalinity of many tear proteins.

The quantitative capabilities of the device were demonstrated using Lf, a tear-specific biomarker for SS. Lf was quantified in a clinically relevant range for SS diagnostics and the assay was shown to accurately measure endogenous tear Lf to within 15% of ELISA and to be predictive to within 30% of spiked Lf measurements in tear fluid. The lower limit of detection was 3 ± 2 nM Lf in tear fluid. Tear matrix effects, including enhanced band dispersion caused by high tear matrix conductivity and non-specific complexing of Lf with other analytes in the tear matrix, were discussed and the assay was shown to be specific for Lf (<15% non-specific signal).

Finally, we characterized a useful and streamlined sample preparation protocol for reconstituting tear proteins from Schirmer strips, the clinical standard for tear collection and storage, which had 37 ± 7% protein extraction efficiency and resulted in tear eluate containing 2.3 ± 0.5% of total tear Lf concentration on the ocular surface. This work enabled us to relate the final assay measurement back to the expected Lf concentration in the tear fluid on the ocular surface for the first time in the literature.

Given the current challenges in making specific tear protein measurements and dearth of biochemical tear diagnostic tests in clinical use, we believe this work makes important steps toward enabling 1) specific quantification of tear proteins within the complexity of the tear matrix, 2) a more universal immunoassay that can separate analytes irrespective of their pI point and 3) a protein biomarker-based, non-invasive diagnostic test for SS. We believe that this work has the potential to revolutionize our understanding of ocular disease pathology, enable non-invasive diagnosis of systemic disease (where biomarkers are available) using tears, and may be used to stratify Sjögren's syndrome patients from those with other forms of dry eye. Taken in sum, this work has broad implications in the proteomic analysis of tear fluid and can be used in the advancement of both basic science and clinical medicine.

Chapter 6: Multiplexed Microfluidic Tear Biomarker Assay for Dry Eye Patient Stratification and Disease Severity Assessment

6.1 Tear Osmolarity as an Indicator of Dry Eye Disease Severity

Tear osmolarity has emerged as a validated biomarker for dry eye or keratoconjunctivitis sicca (KCS) diagnosis.[179,180] Further, recent studies have shown that tear osmolarity values increase with increasing disease severity.[181] In a 2010 study, Versura et al., measured tear osmolarity values of 296.5 $\pm$ 9.8 mOsm/L in healthy volunteers and increasing values as dry eye disease severity increased: 298.1 $\pm$ 10.6 mOsm/L in mild dry eye patients, 306.7 $\pm$ 9.5 mOsm/L in moderate dry eye patients, and 314.4 $\pm$ 10.1 mOsm/L in severe dry eye patients ($p < 0.05$).[181] A tear osmolarity value of 305 mOsm/L has been proposed as a threshold value to diagnose dry eye, 309 mOsm/L for moderate dry eye, and 318 mOsm/L for severe dry eye.[181]

Quantitative tools to assess dry eye severity are needed for many of the same reasons that quantitative tools capable of stratifying Sjögrens syndrome are needed. Treatment of dry eye is often adapted based on severity of symptoms, with more aggressive treatments being used in severe dry eye cases. As a result, tools capable of quantifying tear osmolarity would have real clinical benefit for patients.

Osmolality and osmolarity are often used interchangeably in English vernacular. However, osmolality is a measure of the total number of solute particles dissolved in one kilogram of solvent and does not take into account particle size, density, configuration, or electrical charge. Osmolality has units of mOsm/Kg.[182] Meanwhile, osmolarity is a measure of the total number of solute particles dissolved in one liter of solution. Osmolarity is typically equated with the osmotic pressure that a solution exerts across a semi-permeable membrane and depends on the number of particles in solution. Osmolarity has units of mOsm/L.[183]

The osmolarity and osmolality of the tear film are identical measures.[182] This is true for most biological systems because the density of water is 1 kg/L. However, there is a slight difference between the molality and molarity of plasma because of the presence of high concentrations of proteins and lipids which make up approximately 6% of the total volume. Thus, the molality of a molecule in serum is approximately 6% higher than its molarity. Since the concentration of protein in the tear film is 10% that of plasma,[21] the contribution of tear proteins to tear osmolality is minimal. As a result, the difference between tear osmolality and osmolarity is negligible and the terms are used interchangeably.

Several commercial tools have been developed or are in the process of being developed to measure tear osmolarity. Traditional osmometers use freezing point depression to measure the osmolality of a sample (mOsm/Kg) by freezing a small volume of the sample and measuring

the time for the volume to fully thaw. Older instruments such as the Clifton Tear Osmometer (Clifton Technical Physics, Hartford, NY) and the 3100 Tear Osmometer (Advanced Instruments) utilize freezing point depression to measure tear osmolarity and are considered the 'gold standard' tear osmometer.[184] The OcuSense TearLab osmometer (OcuSense, Inc, San Diego, CA) is currently being developed and utilizes electrical impedance "lab on a chip" nanoliter technology to measure osmolarity.[184] Both measurement techniques have been shown to be comparable.[184] However, difficulty in tear hyperosmolarity measurement has limited its utility in the clinic and development of new instruments could facilitate clinical uptake.[184]

As a result, tear osmolarity is an attractive biomarker target for a clinically useful point-of-care dry eye test. However, it is important to note that although osmolarity testing can be used as a diagnostic for dry eye, the only thing it tells you is that your patient has dry eye (with an indication to its severity). It cannot tell you the reason why the patient has dry eye and cannot differentiate between aqueous deficient dry eye or evaporative dry eye. Additional clinical tests and subjective patient questionnaires are still necessary to enable you to treat the patient's condition. Therefore, pairing this osmolality test with a measure of Lf would enable a measure of lacrimal gland function and enable differentiation of aqueous deficient and evaporative forms of dry eye for more appropriate treatment administration. A multiplexed device capable of stratifying Sjogren's syndrome from other forms of dry eye disease as well as assessing the general severity of dry eye symptoms would be useful in enabling more effect treatments targeted at both disease mechanism and disease severity.

6.2 Microfluidic Osmolarity Assay Design

Osmolarity is a measure of the number of osmoles of solute particles in solution and accounts for solute dissociation in solution. As a result, it measures the concentration of both charged ions and uncharged (non-dissociating) biomolecules as shown in the equation below.

$$osmolarity = c_{ions} + c_{\substack{uncharged \\ biomolecules}}$$

The tear film is composed of a trilaminar structure with the inner, aqueous layer being composed of a wide variety of small molecules, proteins and lipids. The major tear components which comprise 95% of tear molecules by weight are listed in Figure 3. Urea (14.55 mOsm/L) and glucose (4.2 mOsm/L) are the only uncharged molecules of the major tear molecules. As such, uncharged biomolecules represent only 2.2% of major molecules in tear fluid and approximately 98% of major tear molecules are ions in solution. Consequently, a tool capable of measuring the ion concentration of tear fluid will also measure tear osmolarity.

To derive an on-chip method of determining ion concentration in solution, we refer back to the Nernst-Planck equation which is a conservation of mass equation and describes the flux of ions under the influence of an ionic concentration gradient, electric field, and bulk fluid flow.

$$J = J_{\substack{concentration \\ gradient}} + J_{E-field} + J_{bulk\ fluid\ flow}$$

or

$$\frac{\partial c}{\partial t} = \nabla \cdot \left[D\nabla c - uc + \frac{Dze}{k_B T} c \left(\nabla \emptyset + \frac{\partial A}{\partial t} \right) \right]$$

where t is time, D is the diffusion coefficient, c is the concentration, u is the velocity of the fluid, z is the valence, e is the elementary charge, k_B is the Boltzmann constant, the applied electric field is represented by $-\nabla\emptyset - \frac{\partial A}{\partial t}$, and T is the temperature.

Here, the total flux is determined by the sum of the ion fluxes dictated by each of these forces. Since our channels contain polyacrylamide gels, no bulk fluid flow exists (u = 0). Further, by waiting until the loading channel is completely loaded with sample, we eliminate any concentration gradient that exists in the channels ($\nabla c = 0$). Therefore, in our system, total ion flux is dictated entirely by the applied electric field.

$$\frac{\partial c}{\partial t} = \frac{Dze}{k_B T} c_{ions} E$$

Substituting in for the ion flux (dc/dt), which is simply current per unit area, we can solve for ion concentration and see that it is directly proportional to current, I.

$$\frac{I}{xy} = \frac{Dze}{k_B T} c_{ions} E$$

and

$$c_{ions} \sim I$$

Now, using the definition of electrical conductivity, which is equal to the valence of ions (z), number of charges per mole of ions (F), mobility (μ), and ion concentration (c_{ions}), across all ions in solution, we can derive an equation that relates conductivity (σ), a measurable property in our system, to the measured current and applied electric field.

$$\sigma = \sum |z|F\mu|c_{ions}| = \frac{I}{xyE}$$

Therefore, we can see that electrical conductivity also scales with current.

$$\sigma \sim I$$

Therefore, we see that in our assay conditions, and assuming full loading of the channel, ion concentration is directly proportional to conductivity.

$$c_{ions} \sim I \sim \sigma$$

Since 98% of particles in tears by weight are ions in solution, conductivity can be tracked to quantify particle concentration, or tear osmolarity, on-chip.

On-chip conductivity measurements were integrated into the assay design during the loading step as shown in Figure 49. Current was monitored and conductivity calculated using the formula $\sigma = I/xyE$ after the sample had fully loaded into the loading channel.

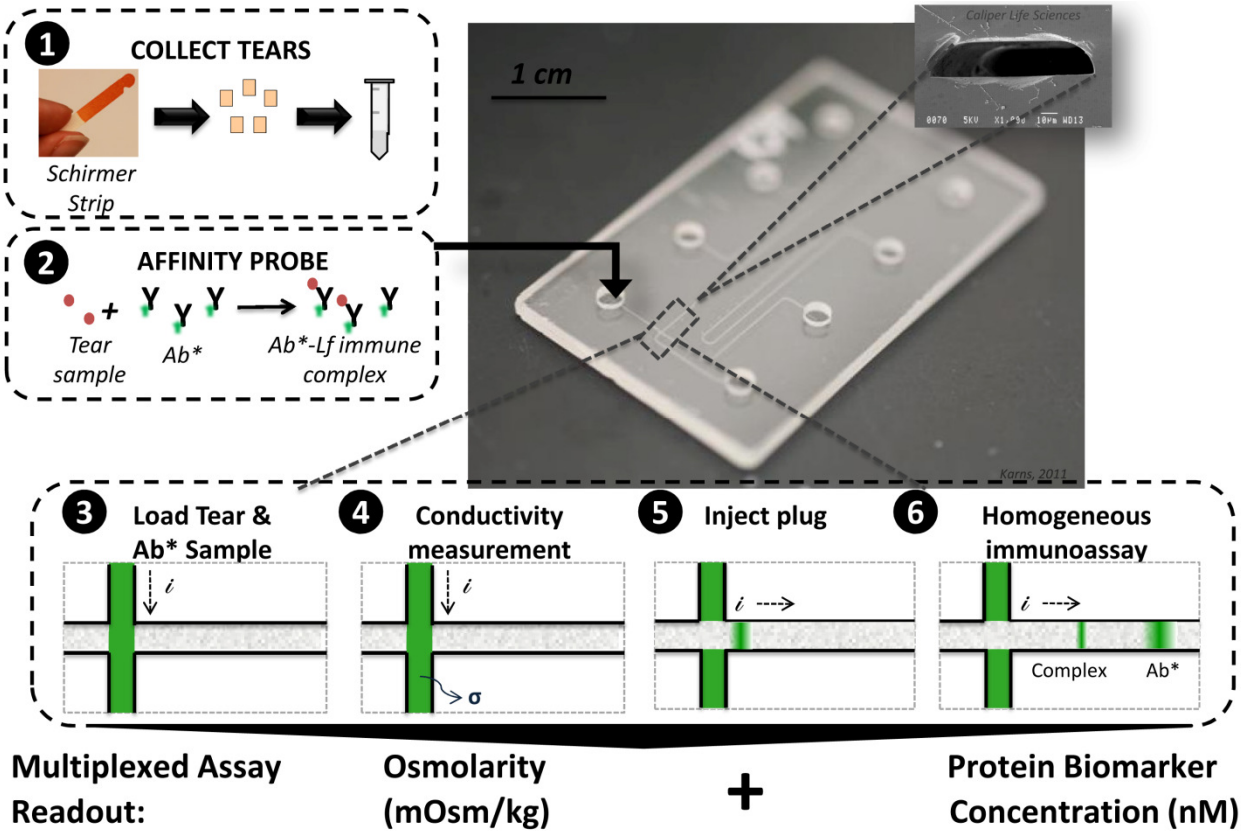

Figure 49. Multiplexed assay design concept measures both tear osmolarity and protein biomarker (Lf) concentration.

6.3 Microfluidic Osmolarity Detection

To verify this experimentally, I measured current in the loading channel as a 50 mOsm/kg osmolarity standard was electrophoretically loaded onto a buffer-containing chip (Figure 50). The plot shows two regimes: when the sample is loading and after loading is complete. In the regime where the sample was loading, the ion flux is dictated by both the electrophoretic force

and the concentration gradient. However, once the sample is fully loaded into the channel, the current reaches a steady state level where ion flux is dictated by the E-field contribution alone and the conductivity (σ) can be measured using the formula $\sigma = I/xyE$.

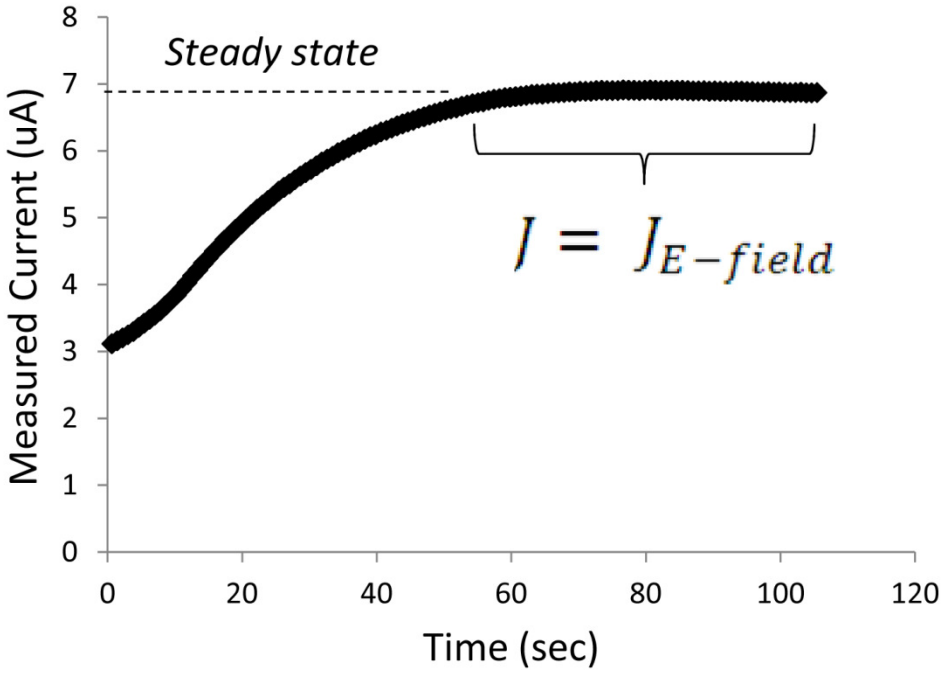

Figure 50. Current trace in the loading channel as 50 mOsm/kg sample loads

I then created a dilution series of NaCl samples (osmolality dilution series) and measured the conductivity of the samples on a gold standard conductivity meter to determine if the conductivities would increase linearly as the osmolality increased. The conductivity meter relies on the AC bipolar method to measure conductivity measuring. The osmolality dilution series was linear over the range of 50 to 2000 mOsm/kg.

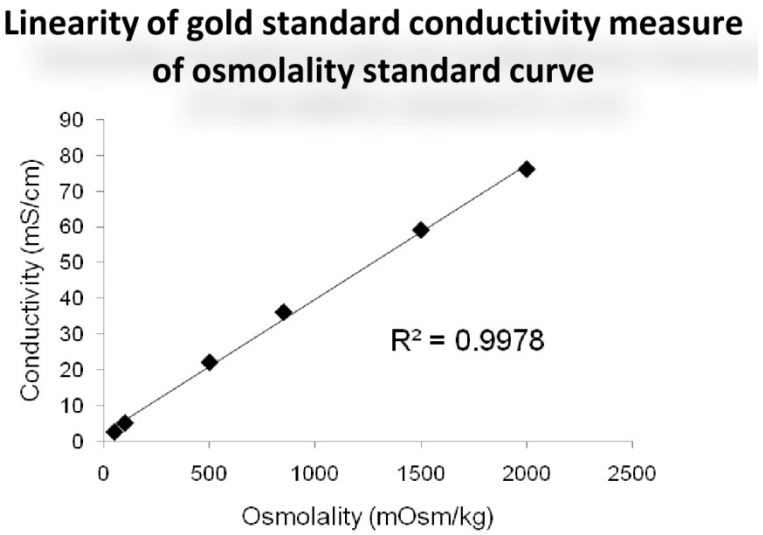

Figure 51. Measured conductivity for an osmolality dilution series on a gold-standard AC biopolar conductivity meter.

Taking this osmolality dilution series and running it on a gold standard Wescor vapor pressure osmometer (Marla Feller Lab), I next sought to demonstrate that a standard osmometer would also measure a linear increase in osmolality values for my standard curve. Figure 52 shows that the osmometer measures a linear dose response curve from 50-2000 mOsm/kg with less than 10% error above 100 mOsm/kg.

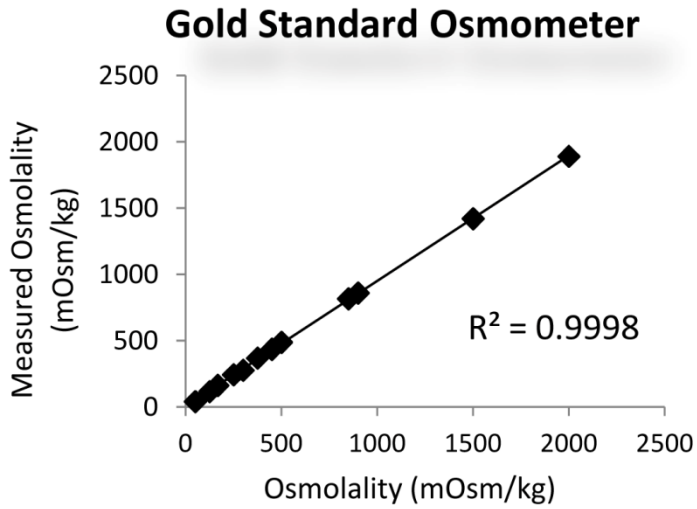

Figure 52. Measured osmolality for an osmolality dilution series on a vapor pressure osmometer

Using the same osmolality dilution series, I next ran it on an open microfluidic channel (with no PA gel) and plotted conductivity vs. osmolality to see if I could replicate this same linear response curve, but this time by measuring conductivity within the loading channel. Here, we

see a linear curve again from 50-2000 mOsm/kg (Figure 53). This demonstrates that measuring conductivity in the loading channel of a microfluidic chip is effective in measuring the osmolality of a sample.

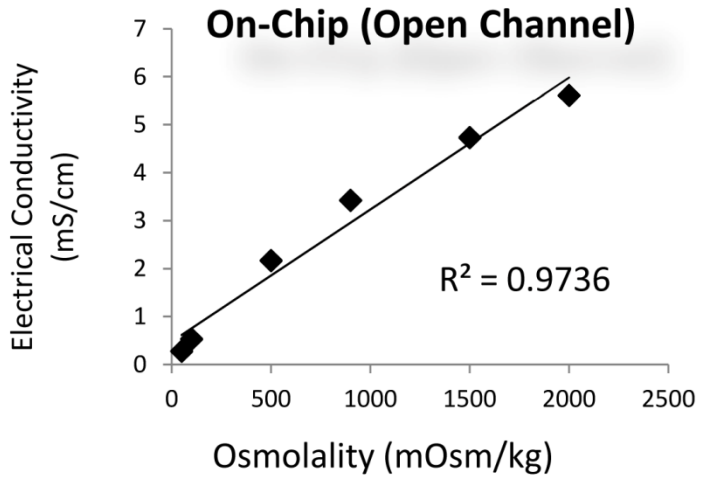

Figure 53. Measured conductivity for an osmolality dilution series in an open loading channel of a microfluidic chip.

Running the same osmolality dilution series again, but this time with the addition of 3%T PA gel in the loading channel of the microfluidic chip, the conductivity decreases owing to the resistance added by the gel as we would expect; however, I am still able to get a linear dose response curve with a clinically relevant range for human tear fluid (Figure 54). However, this data shows the ability to successfully quantify clinically relevant osmolality levels using a PA gel-containing microfluidic chip and conductivity tracking.

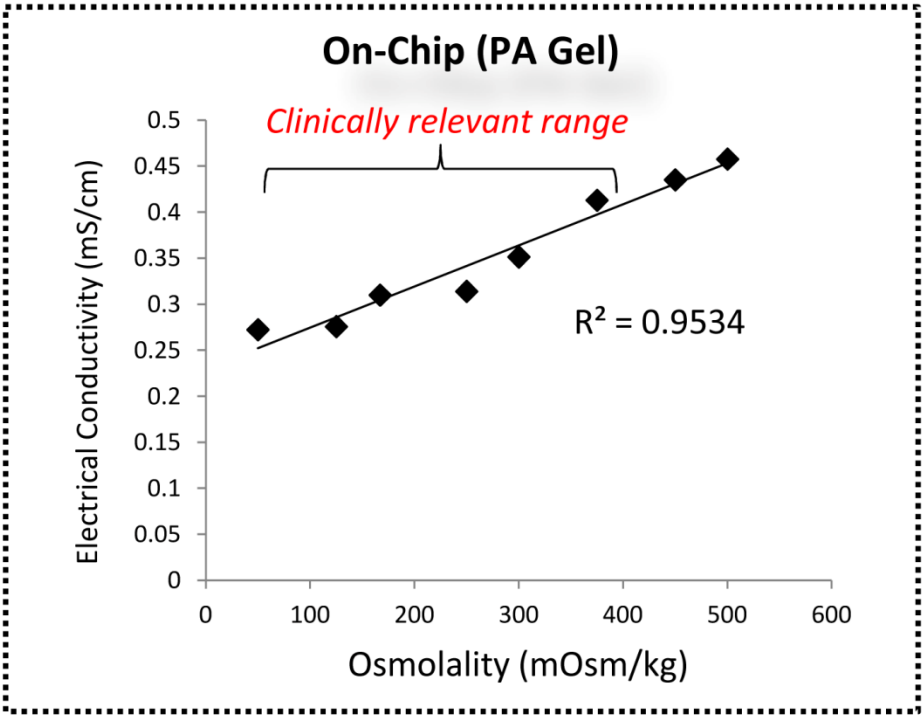

Figure 54. Measured conductivity for an osmolality dilution series in the loading channel of a microfluidic chip which contains 3%T PA gel.

Above ~500 mOsm/kg, we see saturation of the curve which is likely due to a gel-based polarization effect (Figure 55).

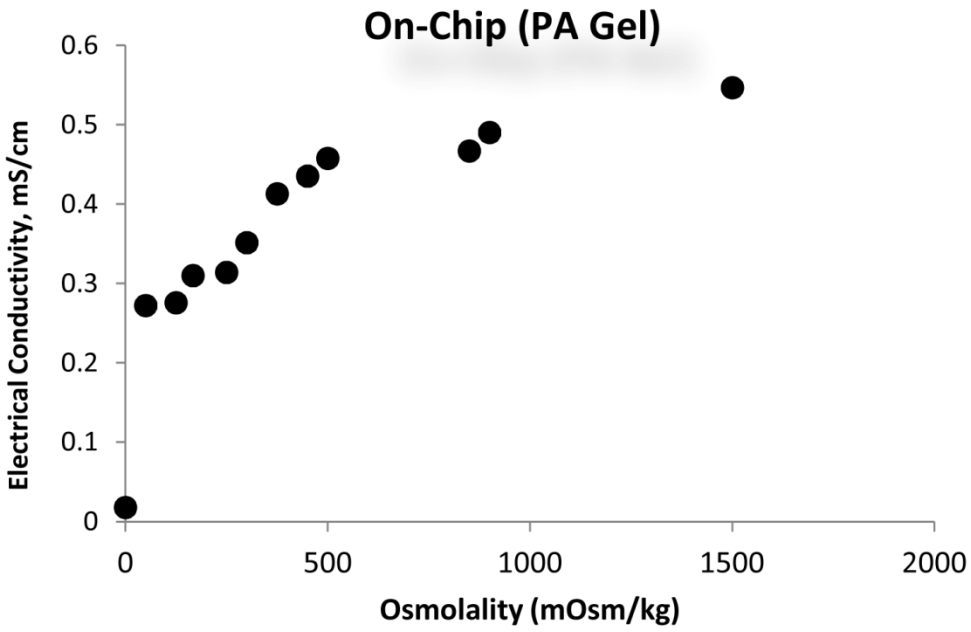

Figure 55. Saturation of the measured conductivity is observed above 500 mOsm/kg for an osmolality dilution series in the loading channel of a microfluidic chip which contains 3%T PA gel.

As a control, I also characterized the linearity of our high voltage power supply and current monitoring instrumentation and found them to be very linear in the voltage and current regimes we are working in (100 – 1000V or 3 – 30uA) (Figure 56).

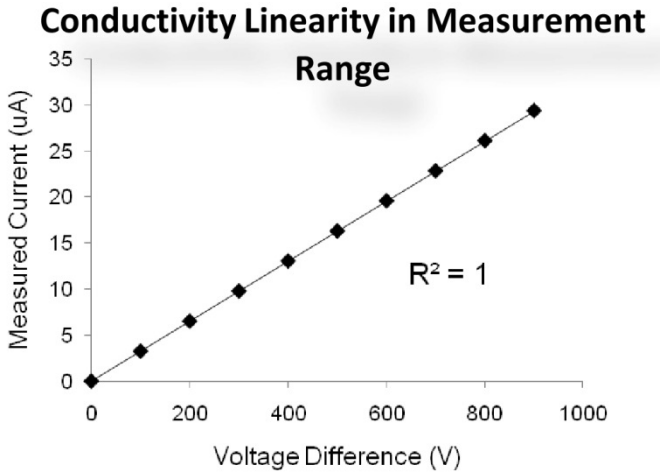

Figure 56. Measured currents for increasing applied voltages using a Caliper high voltage power supply.

I next sought to measure osmolality or osmolarity of tear fluid from real patient samples collected with Schirmer strips and provided by our collaborator. These samples are reconstituted in water and then diluted in 50 mM pH 11 CAPS buffer in order to conduct the

electrophoretic immunoassay described in Chapter 5. As such, the conductivity of the tear samples will be heavily influenced by the conductivity of the CAPS buffer ions.

Therefore, I validated a method for accounting for the osmolality contribution of the CAPS buffer by running known osmolality standards diluted by various degrees in CAPS buffer on the Wescor vapor pressure osmometer and calculating what the osmolality of the diluted sample should be (Table 8). I used the measured osmolality of 1x CAPS of 41 mOsm/kg and the equations below to solve for $Osm_{unknown\ sample}$. I found that the method is accurate to within ~8%.

If diluted 2x in CAPS: $(5\ \mu L)(Osm_{unknown\ sample}) + (5\ \mu L)(Osm_{1x\ CAPS}) = (10\ \mu L)(Osm_{measured})$

If diluted 5x in CAPS: $(2\ \mu L)(Osm_{unknown\ sample}) + (8\ \mu L)(Osm_{1x\ CAPS}) = (10\ \mu L)(Osm_{measured})$

Table 8. Dilution of four different osmolality standards 2x and 5x in CAPS buffer and the calculated osmolality with known osmolality of CAPS

Standard	Dilution factor in CAPS	Trial 1	Avg Osmolality	Predicted Sample Osm	Actual	% error
125 mOsm/kg	5	58	58	126	125	0.80%
125 mOsm/kg	2	79	79	117	125	-6.40%
250 mOsm/kg	5	79	79	231	250	-7.60%
250 mOsm/kg	2					
375 mOsm/kg	5	113	113	401	375	6.93%
375 mOsm/kg	2	222	222	403	375	7.47%
500 mOsm/kg	2	277	277	513	500	2.60%

I next validated my on-chip method of conductivity tracking to assess osmolality. Using 1x CAPS and 1x PBS samples as unknowns, my on-chip method predicts CAPS osmolality from the osmometer to within 6.8% and PBS osmolality from the osmometer to within 18.8%.

Next, I ran dilutions of patient samples (reconstituted in water) and diluted in 1x CAPS on the vapor pressure osmometer to understand the effect of CAPS dilution on the calculated tear sample osmolality. Dilution factors that I used include: no dilution, 1:2 dilution and 1:5 dilution. Averages of the dilution corrected osmolalities are given below in Figure 57, where the error bars are the standard deviation of the osmolalities across the three dilution factors. A large error is introduced by diluting the tear samples in CAPS buffer (up to 34%). This is likely due to the fact that a 5x dilution in CAPS means that the majority of the sample osmolality is accounted for by the CAPS buffer rather than the tear sample and thus, the errors confound as dilution increases. Also important to note is that when I use this method for accounting for sample dilution, there is no observed increase in osmolality for SS patients compared to healthy controls. To be sure, I would need to increase the number of patient samples I analyzed here, but I would expect there to be a significant increase in all SS patient samples regardless.

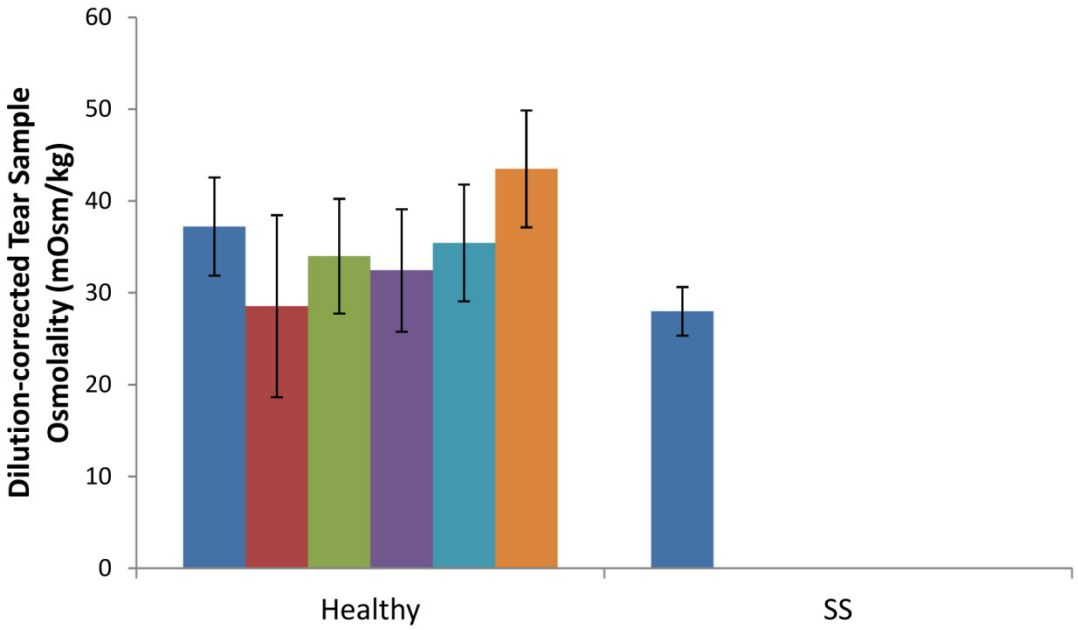

Figure 57. Patient samples reconstituted in dI water and diluted in CAPS buffer. Measured osmolality was conducted on a vapor pressure osmometer. Dilution in CAPS buffer was corrected.

Another control that must be accounted for is the effect of the reconstitution buffer on the sample osmolality. The results in Figure 57 were obtained from tear samples reconstituted in dI water, which theoretically would not contribute to the sample osmolality. However, other samples I had were reconstituted in 1x PBS buffer which would likely have an enormous effect on the calculated tear osmolality. Reconstituting the tear fluid from the Schirmer strips using PBS totally overwhelms any osmolality introduced by the tears. This is shown in Figure 58 by the ~5x increase in osmolality (y-axis) for the tear samples reconstituted in PBS compared to the measured osmolalities for samples reconstituted in water (Figure 57). It is practically very difficult to predict how much dilution of the tear sample occurs during reconstitution in each buffer and therefore it is almost impossible to compare calculated tear osmolality levels from different reconstitution buffers. As a result, all osmolality measurements must be made on samples that are reconstituted in dI water.

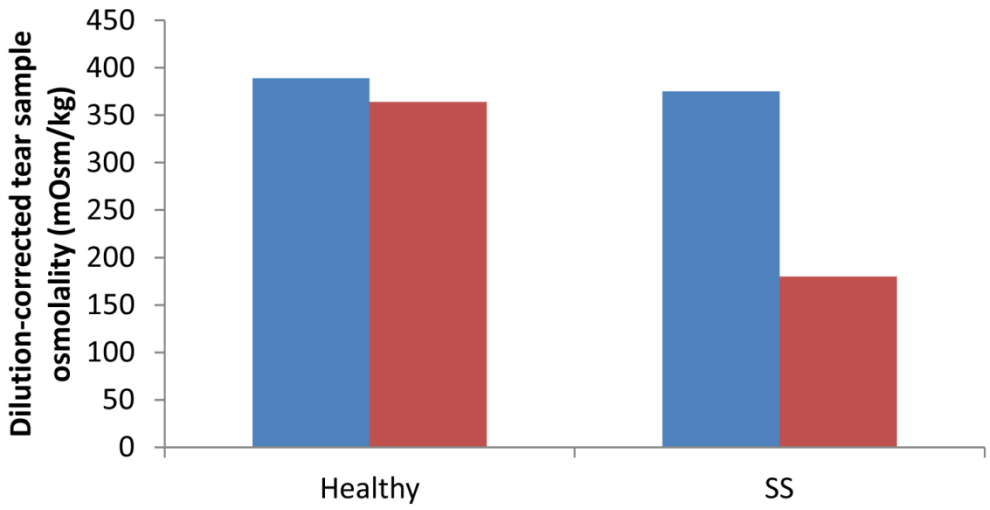

Figure 58. Patient samples reconstituted in PBS and diluted 5x in CAPS buffer. Measured osmolality was conducted on a vapor pressure osmometer. Dilution in CAPS buffer was corrected.

In order to proceed with this study, we need to obtain and measure the osmolality levels of more tear samples (both healthy and SS patients). However, before proceeding, we also sought to consider whether we should be using Schirmer strips as the collection medium for osmolality. The osmolality levels I measured for the samples reconstituted in dI water are much lower than the physiological levels should be, suggesting that the Schirmer strips may influence the osmolality and tear composition. As an alternative, microcapillaries may be a better collection method so as to eliminate the influence of collection on osmolality.

To investigate the effect of Schirmer strips on osmolality, I spiked known osmolality standards onto Schirmer strips, allowed them to dry, eluted off the samples overnight in water, pooled the eluate, and then ran it on a gold standard vapor pressure osmometer. There seems to be a linear trend for the measured osmolality in the eluate when comparing to the osmolality in the spiked sample. This provides a calibration curve that relates the measurable osmolality in the sample back to the original concentration in the eye (Figure 59).

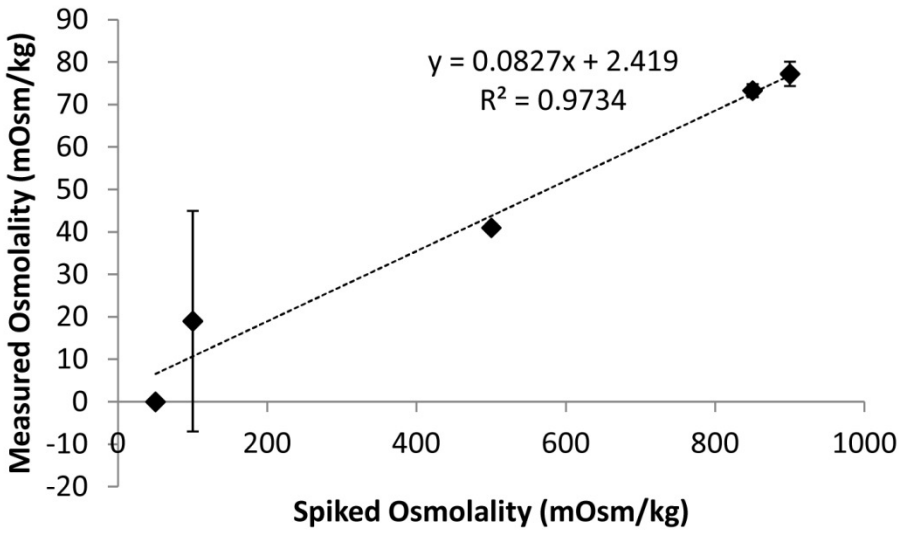

Figure 59. Calibration curve for osmolality elution showing the relationship between the original osmolality of the sample introduced onto the Schirmer strip and the osmolality of the sample that is eluted off.

It is also clear that there is quite a bit of error in the reading when samples with osmolalities less than about 200 mOsm/kg are introduced. The physiological levels in a healthy eye should be around 290 mOsm/kg; therefore, using this calibration curve to account for the difference in osmolality measured off of a Schirmer strip compared with that spiked onto the Schirmer strip, we can see much higher tear sample osmolalities that resemble physiological values (Figure 60). However, this does not solve the problem that the samples we have do not demonstrate any variation in the osmolality for SS patients compared to healthy controls. We need to obtain and run additional some more patient samples to continue with this effort and determine if higher osmolarity levels can be measured in SS patients.

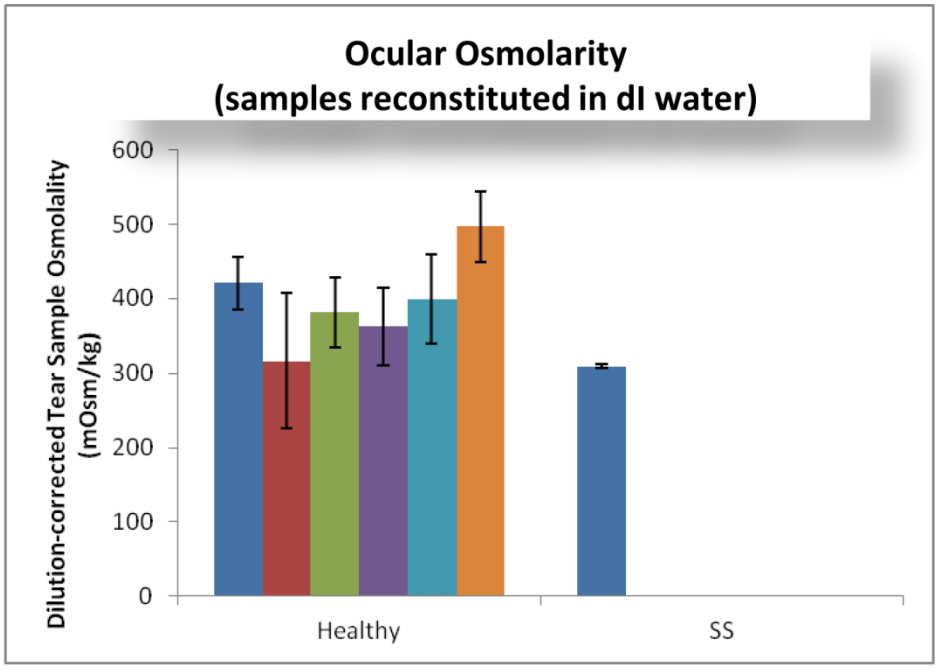

Figure 60. Measured patient sample osmolality after calibrating for effect of elution process on recoverable osmolality. Only patient samples reconstituted in dI water were used.

6.4 Other Applications for Multiplexed Tear Biomarker Assay

Looking forward, there are several other clinical applications for a multiplexed microfluidic assay capable of making biochemical measurements in human tear fluid. There are several other biomarkers of clinical relevance as well as questions about the properties of the eye that could open the door to new diagnostics and more effective therapies for ocular disease.

A protein biomarker target of interest for future study is small proline-rich protein 1B (SPRR1B), which is a putative biomarker for corneal squamous metaplasia in dry eye disease.[185] SPRR1B is found on the corneal surface in SS squamous metaplasian and therefore is also likely found in the tear film and may be collected by the Schirmer strip. SPRR1B is also alkaline with a theoretical pI of 8.85 and molecular weight of 15 kDa. There do not appear to be any unconjugated proteins that exist commercially, although a GST-conjugated form exists from Novus Bioogicals. Only one antibody exists commercially: a rabbit anti-human SPRR1B polyclonal antibody (unconjugated) from Abgent or Abcam which is reactive with the C terminal region of human SPRR1B.

Immunoglobulin isotyping in tear fluid may also be of interest. IgA, IgD, IgG, IgE, and IgM molecules exist in tear fluid. IgD, IgE, and IgG are monomers, while IgA exists in a dimer form in tears. The most interesting immunoglobulin isotypes in tear fluid diagnostics are IgG, IgA, IgM,

and IgE. IgG is mostly membrane bound in B cells and IgE binds to allergens. Detection of IgG may be an indication of B cell presence. Further altered IgE levels may point to allergic conjunctivitis. IgM is a secreted molecule that typically exists as a pentamer and acts to eliminate pathogens in the early stages of B cell mediated immunity before sufficient IgG levels are present. Serum IgA levels are normally elevated in autoimmune diseases and detecting tear IgA levels may give another indication of whether dry eye symptoms are due to an autoimmune mechanism (e.g., SS).

Detecting tear autoantibodies against nuclear antigens such as those detected now in blood for autoimmune diagnosis could be used for pre-symptomatic assessment of RA and other systemic autoimmune diseases (e.g., lupus, SS). Although other serum proteins have been shown to be able to pass into tear fluid, it is not well known whether autoantibodies from serum can pass into tear fluid. Therefore, it would be interesting to study what conditions (e.g., inflammation, stress, dilated vessels) allow serum proteins to pass into tear fluid for easier detection. It is known that autoantibodies predate the onset of systemic lupus with the most sensitive autoantibodies being ANA, Ro/SSA, and dsDNA. Anti-SSA and Anti-SSB are present in saliva and may also be present in tears. Further, there are other autoantibody biomarkers that continue to be identified for diseases such as SS.[186,187]

Mucins are also of interest owing to the difficulty of collecting and measuring them. Mucins are high molecular weight, heavily glycosylated proteins that are produced by epithelial cells on the surface of the eye. Their large size makes them very difficult to collect and measure. However, it is possible that mucins from the epithelial cells on the ocular surface would be collected with Schirmer strips but not with capillary tubes, making them analyzable with this technology. Of particular interest in the dry eye community is mucin 5AC (MUC5AC)[188] which has a molecular weight of 1503 kDa, a theoretical pI of 6.02, is found in tears in ~200 ug/mL concentrations, and may be down regulated in SS tears. There are several antibodies that exist commercially including mouse monoclonal anti-human MUC5AC clone 45M1 from Abcam which recognizes the peptide core of gastric mucin M1 (MUC5AC). There are fewer commercial options for the protein, but a MUC5AC analog 2 synthetic peptide does exist from Raybiotech.

Several cytokines are also of interest in learning about the role of inflammation in dry eye. In particular, IL-1B has been shown to increase in SS tears (concentration of approximately 13 pg/mL) and IL-23 is a putative diagnostic target for SS. Mean tear IL-17 concentration has also been shown to be significantly higher in moderate to severe KCS compared to mild KCS for both total SS and primary SS patients. Anti-annexin autoantibodies may also have a role as biomarkers for autoimmune diseases and aquaporins 4 and 5 are lower in the lacrimal gland of rabbit models of SS compared to healthy.[189]

Odorant binding protein 1a (OBP1a) is another potential biomarker of interest that is an autoantigen in the lacrimal gland which causes CD4 infiltration.[190] Autoantibodies present in the sera of aire-deficient mice recognize and react with proteins present in or around the ducts. Therefore, it may be of interest to probe for antibodies to OBP1a. OBP1a is 18 kDa, produced in the lacrimal gland, and in the lipocalin family, making it hydrophobic and closely related in

properties to Lf, making this particular assay well suited for OBP1a analysis. Further, OBP1a expression appears to be restricted mainly to the lacrimal gland, providing some evidence for tissue specificity of the autoimmune response and reinforcing the need to measure this molecule in tears rather than another biological fluid.[190]

α-fodrin is another protein target of potential interest. It has been identified as a potential autoantigen for SS in mouse models and in some human patients, although the relevance of this putative autoantigen remains controversial.[191-193] However, α-fodrin has poor solubility and may be difficult to analyze. Antibodies are commercially available through Abcam and the protein is approximately 240 kDa (full length) or 150 kDa if just the N-terminal fragment is used. Autoantibodies to α-fodrin have been demonstrated in a number of diseases including juvenile rheumatoid arthritis, lupus erythramatosus without secondary SS, multiple sclerosis, Moyamoya and glaucoma.[194]

Other potential protein biomarker targets include follistatin-like protein 1 (FSTL1) since serum FSTL1 levels in rheumatoid arthritis and secondary SS patients are substantially higher than those in other patients such as those with ulcerative colitis, systemic lupus erythematosus, systemic sclerosis and polymyositis/dermatomyositis.[195] Further, an assay capable of detecting autoantibodies to the Epstein-barr virus (EBV) may be able to determine if EBV infection is linked to the pathogenesis of SS, which remains an outstanding clinical question.[196]

Another clinical question that is of great interest deals with the properties that impart ocular surface sterility. It is poorly understood what enables the eye to be the only external surface of our bodies that remains sterile. Numerous proteins and peptides have been identified which play a roll.[197] We are interested in using this analytical tool to investigate what factors in tears contribute to these observed matrix effects and what also might impart surface sterility to the eye. This work could have implications in the development of novel anti-microbial materials for surgical, building, and food preparation applications.

Finally, a point-of-care test for diagnosing *Chlamydia trachomatis* (trachoma) would have real clinical benefit in the developing world. Trachoma is a widespread disease in the developing world and the number one cause of preventative blindness in those countries.[198] Trachoma is a WHO priority eye disease and is currently diagnosed by looking at conjunctival swabs or scrapings for chlamydial antigen, typically with a DNA-based test. The need for improved diagnostic tools is large.[199] Schirmer strips may be advantageous collection tools for tear samples as it will remove some of the conjuctival surface cells when taken off the surface of the eye. There are several possible antigens that have been published in the literature. Chlamydia trachomatis multipass membrane protein (MOMP) is found on the outer membrane of the Chlamydia bacterial cell and is an attractive (direct) target, if there are sufficient bacteria present and we are able to load them on-chip.[198] *C. trachomatis* specific secretory immunoglobulin A (s-IgA) has also been detected in patients with a positive result in cultures and direct immunofluorescence tests. *C. trachomatis* specific s-IgA is tear specific and has not been detected in serum and is thought to be present in chronic as well as acute cases.[200] Finally, species specific anti-Hsp60 IgGs have been discovered and it may be possible to probe

for them in tear fluid with recombinant Chlamydiaceae species-specific Hsp60 antibodies in tears for three species: *C. trachomatis, Chlamydophilia psittaci, and Chlamydophila pneumonia.*[201]

6.5 Conclusions and Implications

Microfluidic measurement of tear osmolarity measurements would compliment an assay that is capable of stratifying SS patients from other forms of KCS by enabling the simultaneous assessment of dry eye disease severity for appropriate treatment recommendations. In this chapter, I demonstrated the ability to successfully quantify clinically relevant osmolarity levels using a PA gel-containing microfluidic chip and conductivity tracking. I validated a method for accounting for the osmolality contribution of the CAPS sample buffer, investigated the effect of the sample reconstitution buffer and the Schirmer strip on measured sample osmolarity, and created a linear calibration curve to relate the measurable osmolality in the sample back to the original osmolality in the eye. These results show that all tear osmolarity measurements must be made on samples that are reconstituted in dI water and the effect of run buffer must be accounted for.

Looking forward, now that the method has been validated with osmolality standards, it will be important to obtain and run additional patient samples in order to continue with this effort and determine if higher osmolarity levels are measured in SS patients compared to healthy controls. We would also like to expand the multiplexing capabilities of the device to address some of the other interesting questions facing the tear fluid community.

Chapter 7: Path to Clinical Use for Tear Biomarker Diagnostic Test

7.1 FDA approval pathway

In order for a point-of-care diagnostic test to be used in the clinic, it must be approved by a governmental regulatory body, which is tasked with the job of protecting consumers by keeping unsafe and ineffective medical products out of the market. In the United States, this agency is called the Food and Drug Administration (FDA). In Europe, this agency is called the European Medicines Agency (EMA), previously known as the European Agency for the Evaluation of Medicinal Products (EMEA). Medical devices (e.g., diagnostic tests, implantable devices, surgical tools) go through a different pathway than therapeutic drugs or biologics. The pathway outlined in the legal regulatory mandates determines what steps product developer must take and what information must be proven to the regulatory agency in order to legally sell their product in that country.

In the United States, medical devices can be approved for use through one of two tracks: 1) the Clinical Laboratory Improvement Amendments (CLIA) track through the Center for Medicare & Medicaid Services (CMS), or the 510k/PMA track through the FDA.[202] The major difference between the pathways is that the FDA wants to know why device developers are measuring what they are measuring and wants cut-offs and thresholds that will be used to influence medical practice, whereas the LDT pathway does not require developers to provide this information.

The Clinical Laboratory Improvement Act was passed in 1988 and published in the Federal Register in 1992. CLIA strives to establish quality laboratory testing and to ensure the accuracy, reliability, and timeliness of test results regardless of where the test was performed.[203] CLIA requires that all entities that perform tests on "materials derived from the human body for the purpose of providing information for the diagnosis, prevention or treatment of any disease or impairment of, or the assessment of the health of, human beings" must meet certain federally mandated requirements.[204] If an entity performs clinical testing for these purposes, it is considered under the rules outlined in CLIA to be a laboratory and must register with the CLIA program.[204] It is important to note that CLIA does not regulate research laboratories and entities that perform tests for research use only. There are three types of CLIA-certified laboratories: high complexity (requiring high levels of staff training but allowing the interpretation of testing results), CLIA moderate laboratories, and CLIA waived laboratories (where tests can exist in an office or clinical setting). In the United States, CLIA regulations cover approximately 225,000 laboratory entities.[195]

If deciding to market this device for use in a lab (i.e., "Laboratory-Developed Tests" or LDTs), the developer would need to fulfill the requirements outlined in the CLIA pathway. The CLIA

pathway would be appropriate if the test would be used as a 'test-as-service' model, meaning that a manufacturer would set up its own CLIA-certified laboratory, develop a test kit, and then perform all testing within that lab. The CLIA pathway may not be appropriate for a test intended for use in a hospital or ophthalmologist's office where testing was to be performed at the 'point-of-care,' unless the test had been given 'waived' status.

There are five different types of CLIA certificates which are all valid for two years before re-certification is required. A Certificate of Waiver (COW) can be issued to a laboratory that only performs waived tests that do not fall under CLIA regulations.[203] There are some tests that are granted waived status under CLIA and can exist in an office or clinical setting. These include tests such as urine pregnancy tests by visual color comparison (CPT Code 81025) and blood counting through spun microhematocrit screens for anemia (CPT Code 85013).[205] However, a microfluidic immunoassay for SS diagnosis is unlikely to be waived owing to the interpretation involved in the assay read-out. A tear osmolarity test to assess dry eye severity may be considered a waived device as evidenced by the CLIA-waived status granted to in January 2012 to TearLab, which is marketing a tear osmolarity test.[206] A Certificate for Provider Performed Microscopy procedures can be issues to a laboratory in which a technician performs specific microscopy procedures during a patient's visit. A Certificate of Registration is issued to a laboratory to allow the laboratory to conduct non-waived (e.g, moderate and/or high complexity) testing until the laboratory can be inspected to determine compliance with CLIA regulations. A Certificate of Compliance is issued once a laboratory has been inspected by the State Department of Health to determine their compliance with all CLIA requirements. Finally, a Certificate of Accreditation is issued to laboratories if they are accredited by an accreditation organization approved by CMS.[203] Laboratories that handle LDTs must apply for a Certificate of Registration, then pursue either a Certificate of Compliance or Certificate of Accreditation.

CLIA requirements stipulate that laboratories must have in place numerous control measures to ensure the quality of their test results. Each laboratory must perform regular testing to ensure the tests they are running in the facility are accurate, precise, within the reportable range, and agree with reference ranges/intervals (normal values).[207] In particular, CLIA requirements include verification of testing methods to confirm that the test's performance in the laboratory is similar to the manufacturer's claims for accuracy, precision, and reportable range.[208] Further, calibration testing must be performed at least every six months and checked at a minimum of three levels that are within the reportable range of the test.[208] All directors of high complexity testing laboratories must also be certified by an approved board.[208] Quality control measures must be put in place according to the manufacturer's directions and at a minimum at least two levels of control materials must be performed each day that the test is performed.[208] Proficiency testing must be performed and laboratories must record and retain specimens for applicable time frames.[208]

In order to market a non CLIA-waived device for use outside of a laboratory (e.g., in a clinical or home setting), device developers must go through the FDA to obtain regulatory approval. The FDA is an agency within the Department of Health and Human Services and is headed by the office of the commissioner, Dr. Margaret A. Hamburg. The FDA is composed of several centers

including the Center for Food Safety and Applied Nutrition Organization (CFSAN), Center for Veterinary Medicine Organization (CVM), National Center for Toxicological Research Organization (NCTR), Center for Drug Evaluation and Research Organization (CDER), Center for Device and Radiological Health Organization (CDRH), Center for Biologics Evaluation & Research Organization (CBER), and Center for Tobacco Products (CTP).[209] CDER regulates small molecule therapeutics, CBER regulates biologics, and CDRH regulates medical devices including diagnostics (Figure 61).

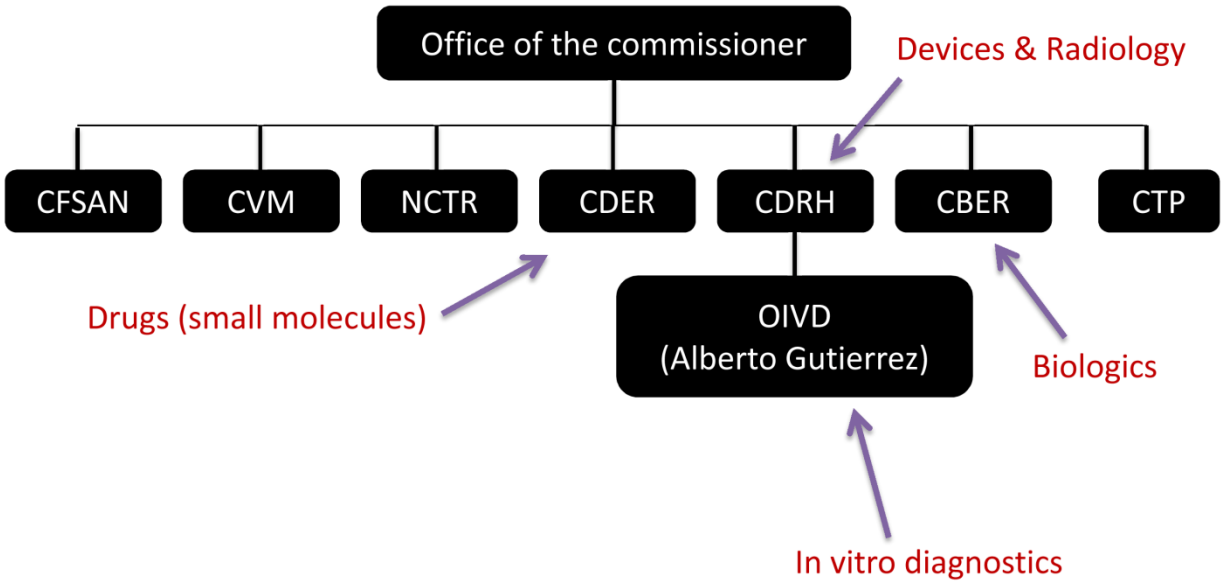

Figure 61. Organizational structure of the Food and Drug Administration (FDA)

CDRH is currently led by the center director, Jeffrey Shuren. Within CDRH lies the Office of In Vitro Diagnostic Device Evaluation and Safety (OVID), which is currently led by Alberto Gutierrez. OVID is composed of several groups including the Division of Radiological Devices, Division of Chemistry and Toxicology Devices, Division of Microbiology Devices, Division of Immunology and Hematology Devices, and Personalized Medicine group (Figure 62).[210]

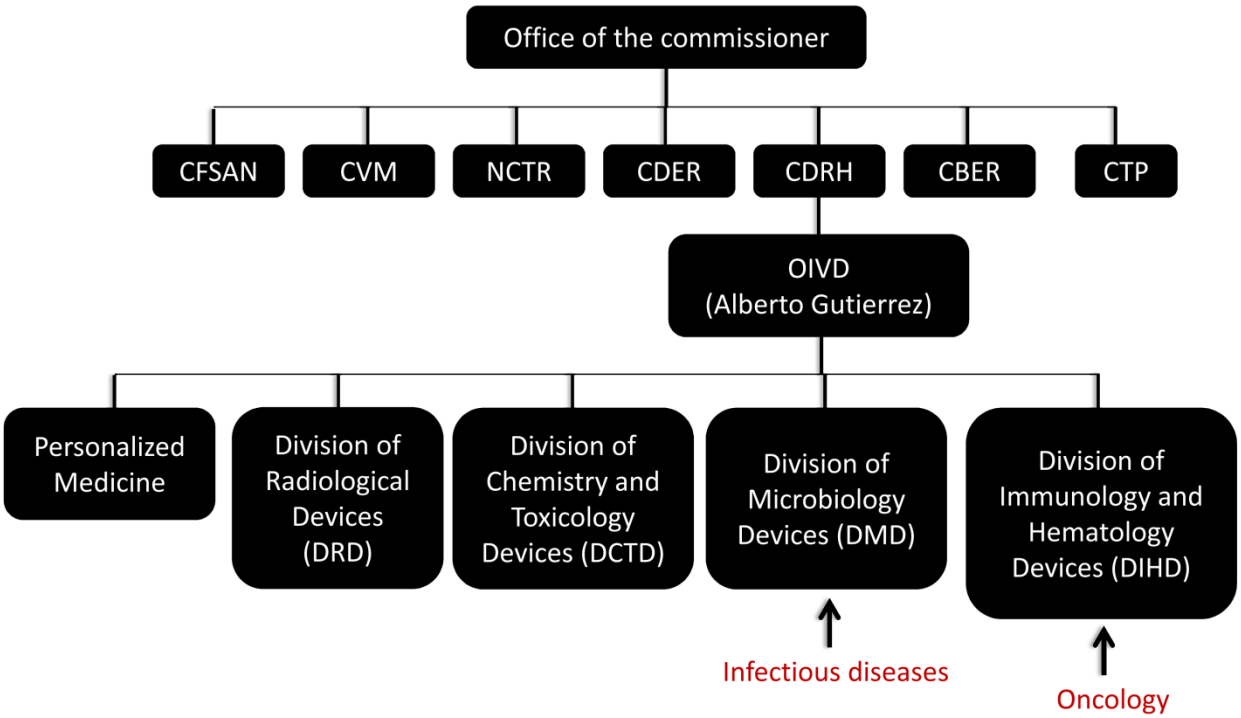

Figure 62. Organizational structure of the Office of In Vitro Diagnostics (OVID)

There are three device classification levels that each in vitro diagnostic (IVD) device is given which dictates the hurdles which must be met by the device developer. Class I IVD devices are common, low risk devices. To be given Class I status, developers must show 'substantial equivalence' to an already-marketed Class I device. If granted classification as a Class I device, the device is subject to general controls and is considered having 'waived status' or being exempt from needing to file a premarket submission. These devices can then be used in the 150,000+ doctor's offices and clinics in the US.[202]

Class 2 IVD devices have moderate risk to patients. Examples include devices that provide prognostic information or monitoring in already diagnosed cancer patients. To be classified as a Class 2 device, developers must show 'substantial equivalence' to a currently marketed Class 2 device. If granted classification as a Class 2 device, the device is subject to special controls and the developer must go through the 510(k) premarket notification process. If given 510(k) approval, the device can then be used in the clinic as well as the 35,000 laboratories with CLIA certification in the US.[202]

Class 3 IVD devices are the most complex and post the highest risk to patients. Therefore, all devices that are not classified as Class 1 or Class 2 devices must be given approval through the Pre-Market Approval (PMA) process. Here, device developers submit a PMA application and must show evidence of safety and effectiveness including impact on the patient, controlled clinical trials, and that the device stands on its own. Only when given pre-market approval can the device be used in the clinic as well as CLIA certified laboratories.

Clinical diagnostics can either be approved through the laboratory developed test/CLIA pathway or the in vitro diagnostic pathway through the FDA (Figure 63). In summary, the LDT pathway regulates the laboratory in which the test is performed and the developer is ultimately selling *results* to physicians and/or consumers rather than devices. The IVD pathway through the FDA office of in vitro diagnostics (OVID) regulates the actual diagnostic device itself and requires proof of clinical validity through clinical trial data. Ultimately, the IVD developer sells an FDA approved *product* to physicians and/or consumers.[202]

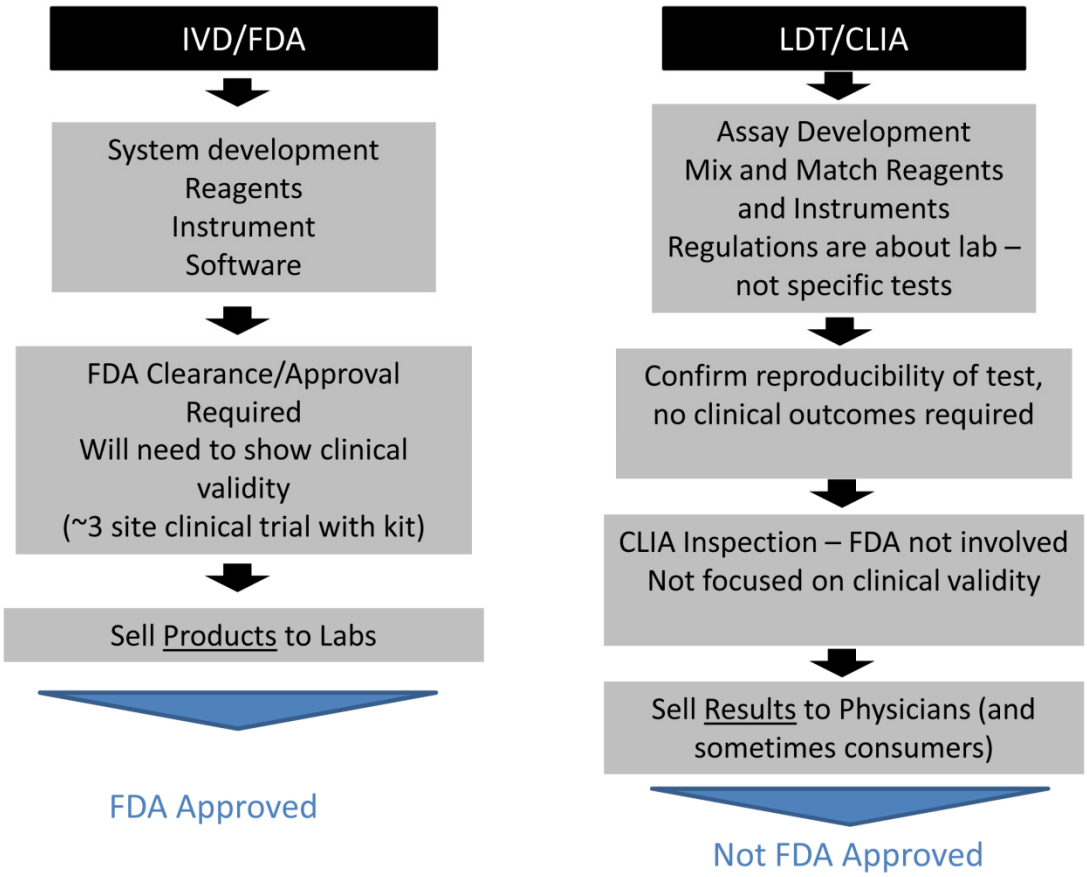

Figure 63. The two major pathways to clinical diagnostics are the laboratory developed test/CLIA pathway through CMS and the in vitro diagnostic pathway through the FDA

There are several advantages to pursuing a CLIA approval pathway rather than going through the FDA. First of all, it is typically much faster to get CLIA approval than FDA approval. This can have a big impact on small start-up medical device companies that have limited funding to get their product to market. Further, CLIA-approved devices can take advantage of the potentially expensive, highly specialized medical equipment available in CLIA-certified laboratories that might not be available in a physician's office or hospital. The evidence points to the benefit of the CLIA approval pathway as well since the vast majority of tests are approved through the CLIA route rather than the FDA.[202] As a result of the differences in regulatory approval

pathways, many device makers pursue a business structure that centers around a centralized CLIA-certified laboratory that accepts patient samples and returns the read-out. The 'test-as-a-service' model is generally preferable to distributed device sales. Few true point-of-care test that are marketed and approved for use in the clinic (that are not very simple and therefore given waived status) have been successful.[202]

Owing to the large number of medical devices that are approved through the CLIA pathway, the FDA is beginning to pay more attention to the CLIA approval process in recent years and is focusing on tests that do not show valid clinical utility. In June 2011, the FDA sent out a guidance to industry on the use of 'research use only' products. Most reagents that are used in LDT/CLIA products are 'research use only.' This will disallow manufactures to sell these reagents to companies using LDT kits for human diagnostics, in essence regulating LDT/CLIA devices through the reagents. This additional oversight could mean the closure of the test-as-a-service model for medical device companies and the requirement for all LDT manufacturers to seek out 510(k) or PMA approval.[202]

This has implications in the commercialization of a tear biomarker diagnostic test since point-of-care devices that impact serious clinical outcomes are difficult to get regulatory approval for (owing to the need to go down the IVD/FDA pathway). While confirmatory or other tests run in a centralized laboratory setting are much easier to get regulatory approval for, the CLIA approval pathway may be closing and all tests will be subject to additional scrutiny, making translation of IVDs even more challenging.

7.2 Commercialization Plan and Commercial Potential

The commercial potential for a dry eye diagnostic test is considerable, owing to the large size of the dry eye market. Collectively dry eye disease (KCS) affects 30-50 million Americans. Of the people with dry eye disorders, approximately 1-2 million have Sjögren's syndrome.[211] Seven to 10 million Americans self-medicate with artificial tear preparations at a cost of more than $100 million per year.[37] The cost of managing and treating dry eye patients in health care organizations is estimated at $700,000 per million patients,[37] resulting in estimated health care costs of more than $35 million per year in the US. The over $100 million per year that patients spend on artificial tears and palliative dry eye treatments provides an indication of demand and the unmet clinical need. Patients are willing to pay out of pocket to improve their symptoms. Furthermore, it is likely that the relatively low market size for current diagnostics is largely due to the fact that only rudimentary tests are currently available. These tests are very inexpensive to run (e.g., Schirmer strip test which costs a few cents and slit lamp examination which is a one-time fixed cost and used in other clinical applications). Therefore, a new test capable of stratifying SS patients from those with other forms of KCS and assessing dry eye severity would need to be inexpensive as well. The multiplexed assay presented here would need to be adapted to an inexpensive substrate (i.e., not glass), battery operated, and be able to utilize an inexpensive, off-the-shelf fluorescence detector.

The material used for the microfluidic chip format would need to be inexpensive but also conducive to fabrication of ~80 µm microfluidic channels in a scalable, batch process. In an effort to move this assay into a point-of-care setting, it will be important to adapt the materials used for scale-up. Microfluidic devices made of plastic would likely be the most attractive option since several companies exist that can fabricate < 100 µm channels in plastic. For example, ALine Inc has fabricated from cast acrylic and a silicone adhesive. To adapt the device to a plastic format, additional surface treatment chemistries may be required to allow gel fabrication and adherence to the channel walls.

Battery operation of the device, although not demonstrated here, should be possible owing to the short (<500 µm) separation distances demonstrated for the immunoassay. The short separation distances enable achievement of the same electric field (V/cm) required for the separation in a shorter channel despite a lower applied voltage difference. Protein separations have been demonstrated using 9-volt batteries by others in our group on 1.3 mm channels.[212]

Inexpensive, portable fluorescence detection can be achieved using off-the-shelf hardware components and several options exist for small, portable excitation sources. LED-based excitation is the least expensive method of fluorescent excitation. For example, Professor Daniel Fletcher and his group proved the ability to use LED for fluorescence microscopy in their CellScope device.[213] There are also several portable LIF systems that have been reported which use some form of diode including the µChemLab chip which uses a laser diode and photo-multiplier tube (PMT) detection set-up for on-chip electrophoretic protein separations.[214] The Backhouse group has also developed an inexpensive USB-powered solid-state laser-based photo-diode LIF system for protein electrophoresis that is suitable for point-of-care medical diagnostics.[215]

Inexpensive detection systems can include PMTs, although their size, cost, and vulnerability to physical shock limit their use in portable lab-on-a-chip applications. CCD cameras are good for low-light illumination but have lower speeds than PIN or PN photodiodes and are most commonly used for portable devices. Avalanche photodiodes (APDs) are very sensitive but require complex operating circuitry and are therefore quite expensive. As a result, photodiode-based detection, such as that used by the Backhouse group in their device,[215] presents itself as the most promising option. The Backhouse group uses these in their system.

It is also possible to integrate other read-out modalities besides fluorescence, which expand the range of possibilities for detection systems. These include amperometric, potentiometric and conductivity detection. The field is also moving toward on-chip integration of LIF-based and electrochemical detection methods. Although promising, it seems that this work may still be too early to be commercially available for integration into the presented device.

The intended use environment of this test is the ophthalmologist's clinic. This is because the burden of sending patient samples away to be diagnosed for SS is high in this disease area. An ophthalmologist will likely not want to wait for several days to get an assessment of the severity of a patient's dry eye symptoms. Further, the rapid assay times demonstrated here

would be rendered irrelevant if patient samples had to be shipped to the device before being analyzed. Therefore, this type of test is most appropriately suited for a point-of-care setting and therefore must go through the FDA/IVD regulatory pathway to approval. It is likely that the osmolarity measurement component for dry eye severity assessment would be classified as a Class 1 (waived) device. TearLab set this precedent very recently in 2012 when their similar device was given Class 1 designation. TearLab's test could also be used as a comparator in establishing substantial equivalence. However, the Lf immunoassay test would likely be classified as a Class 2 device by the FDA and be subject to the 510(k) approval process owing to the clinical diagnosis that would be given to differentiate SS from another form of KCS. This diagnosis would require diagnostic thresholds to be determined and clinical trials to be run in the 510(k) approval process.

A major challenge in the commercialization process would likely be around device distribution. Establishing market penetration and actually getting the device into ophthalmologist's office would likely either rely on establishing an in-house sales force, which can be very costly, or establishing a partnership with a strategic partner that has established distribution channels. The latter is most likely and companies like Becton Dickenson and Alcon would be likely targets.

7.3 Challenges in Clinical Biomarker Validation

It is important to note that there is a difference between device approval and biomarker validation and approval. The 510(k) approval process would allow for marketing of the device. However, validation of the Lf biomarker in clinical trials would also be required in order to establish diagnostic thresholds. These additional trials for biomarker validation will increase the development funds required to commercialize this device. The additional step of needing to validate the clinical significance of the biomarker also introduces several additional challenges to development.

Molecular biomarkers such as osmolarity and lactoferrin have the potential to change the face of medicine. It is increasingly important to identify patients who will respond to therapy, diagnose illness earlier and more accurately, and understand the underlying biochemical mechanisms of disease. Protein biomarkers in particular have tremendous predictive and prognostic value since they are the executers of molecular function and mediators of virtually every process that takes place in the body. However, while hundreds of thousands of articles have been published touting candidate biomarkers, the vast majority remain unvalidated, unapproved, and unrealized in the clinic.[216] Herein presents a tremendous challenge and important opportunity for bioanalytical science.[13]

There are several economic and commercial factors that contribute to disincentivizing the validation of even the most promising candidate biomarkers. Firstly, biomarker validation trials often require large prospective, randomized control trials. Targeted quantitation of candidate biomarkers must be made in thousands of patient samples.[217] These trials are expensive and have an inherently high risk of failure, while the potential economic reward tends to be lower than that of pharmaceutical drugs.

Looking at this problem from the perspective of pharmaceutical drug development, novel biomarkers are needed to provide more accurate clinical endpoints in pharmaceutical drug trials and give vitality to the concept of 'fail early, fail cheaply.' For example, the FDA estimates that a 10% improvement in the ability to predict drug failures before clinical trials could save US$100 million in developmental costs per drug.[218] Moreover, biomarkers are increasingly sought for use in companion diagnostic tests to identify patient populations that will benefit from a certain drug, thus shortening drug trials and accelerating the time to market. However, owing to the risk and expense of biomarker validation trials, there is usually a poor business case for investing in novel biomarkers. Likewise, the coordination of biomarker validation and FDA approvals in advance of drug trials can also be practically very difficult.[219] Finally, although the majority of biomarker discovery is currently done in academia,[216] academic institutions typically do not have a strong incentive to invest in expensive validation trials. Academia often is not interested in commercializing validated biomarkers and, thus, lacks the motivation and resources to pursue large, expensive biomarker validation studies.

Technologies that can reduce the economic barriers to pursuing biomarker validation studies may help to accelerate validation of the thousands of identified and unvalidated candidate biomarkers.[13] Traditionally, enzyme-linked immunosorbent assays (ELISAs) have been the gold standard for protein biomarker validation studies owing to their ability to selectively probe for tens of target analytes using automated robots to run the thousands of requisite patient samples. However, assaying costs in biomarker validation trials typically equal an estimated $80 per protein biomarker per patient,[220] which comprises only a few percent of the full cost of validation trials. The vast majority of validation trial costs stem from testing site fees which include investigator salaries, facility costs, and other sources of necessary overhead.

If we are to realize the extraordinary promise of personalized medicine, the expensive and time-consuming process of biomarker validation in its current form must be made cheaper and more streamlined by employing technologies that can achieve comparable sensitivity and quantitation to ELISA, while eliminating the need for expensive machinery and trained personnel. Technologies that can reduce both assaying costs and, perhaps more importantly, site fees would go far in reducing the economic disincentives to biomarker validation.[13] More specifically, tools that are capable of highly sensitive, targeted, quantitative, and multiplexed measurements while automating and integrating all assay steps including sample preparation, enrichment, measurement, and detection, may hold the key to reducing both technological and site fees by moving trials out of expensive hospital settings. Achieving large scale integration of all assay steps on one chip would eliminate the need for trained hospital personnel, reduce reagent volumes, and eliminate expensive robots and machinery, making validation trials more affordable for all stakeholders in the developmental process.

Therefore, in addition to needing to obtain regulatory approval of the device developed here, it would be important to also validate the clinical relevance and diagnostic power of the biomarkers used in diagnosing SS and informing treatment recommendations. Noting the many economic and technical challenges involved in running an additional biomarker validation trial, the multiplexed microfluidic tool presented here has the potential to speed up the validation

trial by offering integration, speed, and portability. However, while technologies such as these hold promise, additional work is required in order for this technology to be directly relevant in biomarker validation studies. Advances in the integration of assay steps on-chip and the expansion of multiplexed target detection are needed.

In order to validate a biomarker from within real patient samples, significant sample preparation is often required in order to address the huge dynamic range of protein biomarkers found in the body, separate out particulates or cells in a biological fluid, enrich a very dilute biomarker to within the detectable range of the assay, and/or introduce the targeted affinity probe. While there have been numerous reports demonstrating the integration of a single upstream sample manipulation (e.g. purification, enrichment, dilution, mixing), with on-chip measurement and detection, few studies have been able to demonstrate the on-chip integration of all assay steps needed to process and analyze a raw biological sample. For example, Herr, et. al. demonstrated the integration of in-line sample pre-treatment (filtering, enrichment, mixing) with electrophoretic homo-geneous immunoassays for MMP-8 in saliva.[221] Further, Chiem & Harrison[222] demonstrated the integration of on-chip mixing of the affinity probe with the sample, followed by separation and analysis. Qiu & Harrison[223] demonstrated the ability to control the ratio of mixed analytes for the on-chip generation of calibration curves. Yue, et. al.[224] demonstrated the integration of on-chip proteolysis with downstream homogeneous peptide detection by employing trypsin-immobilized agarose beads in a microfluidic channel. For the device presented here to be useful in a biomarker validation trial, it would be beneficial to achieve full integration of all assay steps in one streamlined device by integrating sample preparation on-chip. This would serve to reduce biomarker validation trial costs and achieve repeatability in the clinic.

Through integration, multiplexing, speed, and automation, the microfluidic assays presented here has the potential to create a paradigm shift in biomarker development and to accelerate the validation of the biomarkers used in this assay. By enabling the integration of novel biomarker measurements, a tool such as the multiplexed microfluidic homogeneous immunoassay presented here makes important steps toward achieving streamlined assay integration and lowers the hurdles to biomarker validation and development.

Chapter 8: Riboswitches: ancient genetic regulators

8.1 Background on Riboswitches

Molecular conformation is fundamental to gene expression. In particular, localized RNA conformational changes upon ligand binding are critical to riboswitch-mediated gene control. Riboswitches are *cis* acting RNA elements that undergo a conformational change in response to binding by a regulatory small molecule, resulting in modulation of gene expression.[225] Metabolite-binding riboswitches were established for the first time in 2002[226] as a new mechanism of gene regulation. For the first time, there was evidence that gene regulation could be accomplished in the absence of proteins, giving weight to the theory that the information of early life was first encoded in RNA (RNA world hypothesis). Since then, only a handful of riboswitches have been identified, warranting further discovery and characterization efforts. Riboswitches are composed of two parts including 1) an aptamer domain that binds a small molecule ligand and 2) an expression platform that adopts a different conformation in response to ligand binding and regulates gene expression.[227] Riboswitch aptamer domains are among the most highly conserved biopolymers in all of biology.[228] The riboswitch element itself is typically located in the 5' untranslated region (5' UTR), directly upstream of the start codon (e.g., AUG) and the gene coding region of RNA (Figure 64).

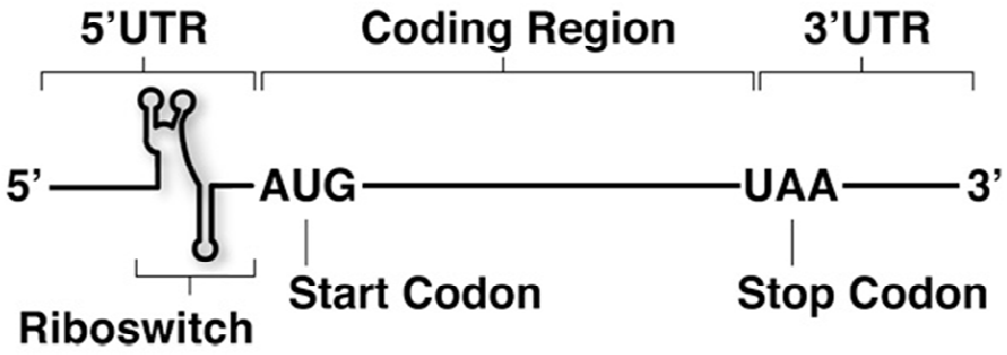

Figure 64. Typical riboswitches are found in the 5' untranslated region (5' UTR) and are directly upstream of the start codon (AUG) and the protein-coding region. Reprinted with permission from Edwards, A. L. & Batey, R. T. (2010) Riboswitches: A Common RNA Regulatory Element*. Nature Education 3(9):9*

Riboswitch function relies primarily on the ability of RNA to form different secondary structures. The most basic RNA secondary structure is a double-stranded helix (similar to DNA) where base pairs are formed to create a double-stranded nucleotide chain. A single strand of RNA can also fold back on itself to form a structure called a hairpin loop which is composed of a double-stranded helix and capped by a loop.[227] The conformation change that occurs after

ligand binding is typically due to a change in RNA secondary structure. Riboswitch conformation change confers gene regulation mainly by terminating transcription (e.g., through formation of a terminator hairpin which occludes RNA polymerase from the strand) or inhibiting translation initiation (e.g., through sequestration of the Shine-Dalgarno sequence).[225] Although some riboswitches have been discovered that regulate translation initiation, the majority of riboswitches have been shown to modulate transcription termination.

Figure 65 shows an example schematic of a riboswitch that regulates gene transcription. When metabolite is not bound (-M), the expression platform incorporates an antiterminator stem-loop (AT) that allows transcription to proceed through the gene-coding region of the mRNA. When metabolite is bound (+M), a switching sequence is triggered that incorporates part of the expression platform into the aptamer domain and a terminator stem loop (T) is formed, stopping transcription. In this way, the expression platform is able to directly modulate gene expression by switching between two different secondary structures upon ligand binding.[227]

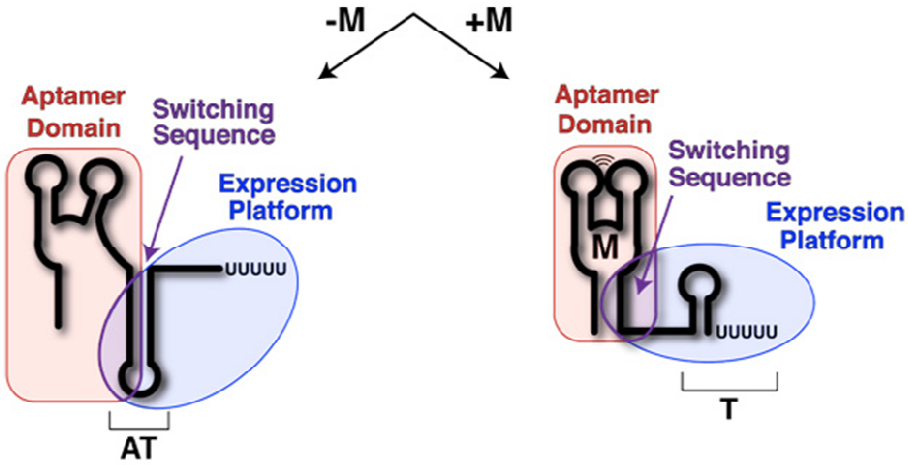

Figure 65. Schematic of a transcription-regulating riboswitch. The aptamer domain is shown in red, switching sequence in purple, and expression platform in blue. AT is antiterminator stem-loop and T is terminator stem loop. Reprinted with permission from Edwards, A. L. & Batey, R. T. (2010) Riboswitches: A Common RNA Regulatory Element*. Nature Education 3(9):9*

For a riboswitch to effectively regulate gene transcription or translation, the binding-induced conformational change intrinsic to riboswitch function must occur faster than the RNA polymerase can move past the expression platform and begin transcribing the RNA. In effect, riboswitch function is in a race with transcription.[227] The speed of genetic modulation is influenced by several processes including 1) the speed of riboswitch transcription (influenced by any 'pause sites' in the RNA structure that slow down the RNA polymerase molecule), 2) the rate of ligand binding (influenced by binding rate constant and the ligand concentration), and 3)

any secondary structure conformational changes.[227] When the ability to modulate gene expression is dictated by the inherent ligand affinity of a riboswitch, that riboswitch is thermodynamically controlled[227] and the speed of riboswitch function is dictated by equilibrium binding conditions.

However, recent studies of riboswitches *in vivo* have showed that many riboswitches require much higher ligand concentrations than what would be predicted by equilibrium binding equations to modulate gene expression.[229] In this case, if the rate of ligand binding is slow, a much higher concentration of ligand would be required for binding to happen in the same amount of time as a faster binding riboswitch-ligand pair. Therefore, the cellular ligand concentration would need to be much larger than the dissociation constant (K_d) of the binding pair in order for binding to be fast enough to beat the kinetics of transcription. In the case that the riboswitch and ligand do not reach equilibrium before genetic regulation occurs, the riboswitch is said to be kinetically controlled.[227]

Figure 66 shows a schematic of a kinetically controlled riboswitch. The observed rate of riboswitch function is dependent on the association constant (k_{on}) and the ligand concentration ([M]). After the aptamer is transcribed, if ligand concentration is high, the ligand binds and induces a change before the RNA polymerase (orange circle) can pass by, terminating transcription (top panel of Figure 66). When a pause site (purple star) is introduced or ligand concentration is reduced, the riboswitch may not change conformation before before RNA polymerase passes and transcription would continue to occur (bottom panel of Figure 66).

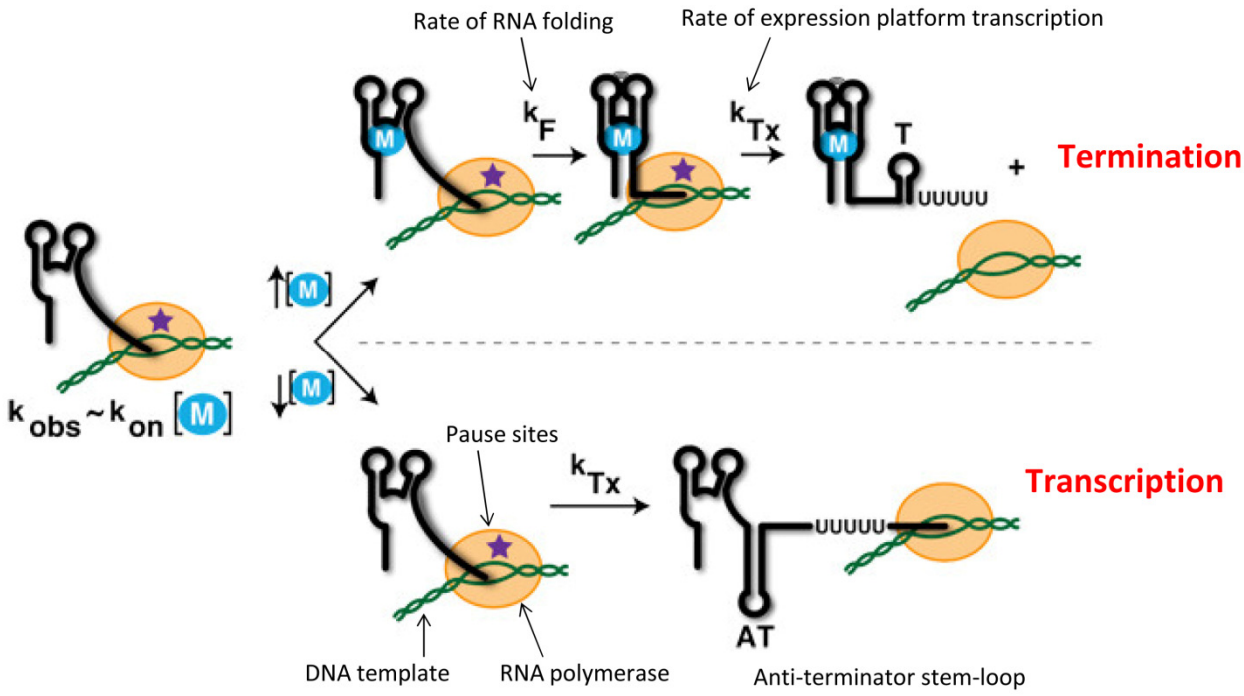

Figure 66. Schematic of a kinetically controlled riboswitch. When ligand concentration ([M]) is high, the ligand binds and induces a change before the RNA polymerase (orange circle) can pass by, transcription is terminated. When a pause site (purple star) is introduced or ligand concentration is reduced, the riboswitch cannot act before RNA polymerase passes and transcription occurs. Adapted with permission from Edwards, A. L. & Batey, R. T. (2010) Riboswitches: A Common RNA Regulatory Element. *Nature Education 3(9):9*

Riboswitches are categorized into families which recognize the ligand to which they bind. Subcategories of riboswitch families are riboswitch classes which include common sequence patterns of nucleotides in the ligand-binding pocket and secondary structure similarities. For example, the SAM riboswitch family, studied here, recognizes the compound S-adenosylmethionine (SAM). There are at least five known classes of SAM riboswitches including the SAM-I riboswitch class, studied here.[227]

Several different families of riboswitches have been discovered including eight coenzymes or coenzyme derivatives, three of the twenty standard amino acids, four purine nucleobases and their derivatives, and the essential amino sugar glucosamine-6-phosphate.[228] Specific examples include adenosylcobalamin (coenzyme B_{12}), thiamine pyrophosphate (TPP), S-adenosylmethionine (SAM), purine, flavin mononucleotide (FMN), lysine, and glycine riboswitches.[230] SAM riboswitches are a particularly well-studied riboswitch and play a role in regulating genes involved in sulfur metabolism, biosynthesis and transport of important metabolites like cysteine, methionine, and SAM.[230]

8.2 Conventional Technologies and Challenges in Riboswitch Research

A central goal of riboswitch research is to 1) identify new riboswitch candidates, 2) link these orphan riboswitches to ligand pairs, 3) experimentally validate the functionality of the riboswitch-ligand pair (e.g., detect ligand binding and a resultant conformational change), 4) characterize the binding interaction (e.g., measure binding strength), and 5) validate their possibly exotic role in genetic regulation.[228] The first riboswitch classes to be discovered were exceedingly widespread in bacteria and played a role in regulating prevalent and highly studied cellular metabolites. In fact, the known riboswitch ligands are a near perfect subset of molecules that are universal to modern life.[228] It was therefore thought that additional riboswitches must exist that bound and regulated many other, lesser studied cellular molecules.[230] As a result, bioinformatics algorithms were developed to look for additional evolutionarily conserved riboswitches.[231] These algorithms search for sequence similarity among intergenic regions of bacterial RNA and couple this information with predictions of the functions of the genes encoded downstream.[230]

With the development of these powerful bioinformatics tools (e.g., BLISS, mfold), thousands of *in silico* predicted riboswitch candidates have been computationally determined.[231-233] At least two of these candidates, glmS and gcvT, have subsequently been experimentally validated to function as riboswitches.[234,235] However, linking these orphan riboswitches to their ligand pairs and experimentally validating their functionality is laborious with current techniques, and in some cases impossible. In fact, at least two dozen orphan riboswitch classes exist to date which have no known ligand pair.

High throughput screening technologies for riboswitch validation, ligand identification, and the characterization of riboswitch-ligand binding interactions are needed. Experimental validation of putative *in silico* predicted riboswitch candidates relies on bench-top assays that determine ligand binding through various means, including observation of RNA conformational change via techniques such as in-line probing,[236] 2-aminopurine fluorescence,[237,238] and Förster resonance energy transfer (FRET);[239] change in heat of the reaction via isothermal calorimetry;[240] or ligand diffusion via equilibrium dialysis.[241]

While suitable for low-throughput biophysical measurements, these conventional riboswitch analytical tools have notable limitations, such as requiring lengthy incubation times, large sample sizes, or site-specific labeling of the ligand or the RNA, all of which slow down analytical throughput.

A binding assay that obviates the need for site-specific labeling of the ligand or the RNA is native polyacrylamide gel electrophoresis (PAGE). Native PAGE is extensively employed to study protein-protein,[11] protein-nucleotide,[242] and nucleotide-small molecule[237] interactions. In particular, slab gel mobility shift assays are a workhorse tool for the validation of riboswitch-ligand binding and conformational change. Slab gel native PAGE has been used to confirm protein-free riboswitch-metabolite binding and altered RNA conformation through an observed change in riboswitch aptamer electrophoretic mobility ('mobility shift').[243,244] The mobility shift

typically stems from the more compact structure of the ligand-bound riboswitch aptamer as compared to unbound RNA. Thus, the compact bound riboswitch exhibits a faster apparent electrophoretic mobility than the unbound RNA.

Mobility shift assays are used routinely to validate computationally predicted riboswitches within a known riboswitch class. Yet, of the thousands of candidate riboswitches with suspected ligand pairs, only a few have been experimentally validated. The workhorse native PAGE slab gel assay is unsuitable for the high throughput screens needed to experimentally validate candidate riboswitches and explore promising regions of the prediction space.

Ligand identification is also challenging to perform on slab gel native PAGE assays. In the case where a ligand target is not known, high throughput screens of large chemical libraries are needed to identify chemical ligands that bind to orphan riboswitches and induce a conformational change. However, broad library screens are difficult to perform with slab gel mobility shift assays owing to their labor intensive and time consuming nature. As a result, current efforts toward ligand discovery and orphan riboswitch validation have focused on downselecting which chemicals should be included in the screen by determining the function of the downstream regulated gene and running targeted screens with related compounds.[245] However, it is increasingly difficult to assign ligand specificity to riboswitch candidates owing to lack of information on gene function and the fact that the ligand may be currently unknown to science.[228] As a result several large orphan riboswitch classes remain that have no known ligand pair (e.g., yybP/ykoK motif, ydaO/yuaA motif, pfl motif, and ykkC/ykkD motif RNAs.[228]

Further, native PAGE slab gels often lack the resolving power required to separate molecular populations with small mobility shifts or those that differ in conformation rather than weight. Perhaps most important to riboswitch functional validation, slab gel native PAGE lacks the quantitation capacity essential to generate a robust, detailed understanding of riboswitch function and binding affinity.

A high throughput tool capable of rapidly validating candidate riboswitch functionality and challenging orphan riboswitches with large chemical libraries would accelerate riboswitch discovery and validation, advance ligand discovery and validation, and provide the quantitative capabilities required to make robust, detailed conclusions about riboswitch function.

8.3 Microfluidic Assays for Riboswitch Analysis

Our understanding of riboswitch regulatory function would be accelerated by a high throughput, quantitative screening tool capable of measuring riboswitch-ligand binding. In contrast to slab gel native PAGE assays, microfluidic electrophoretic assays offer run-to-run repeatability and a degree of precision not attainable with slab gel formats. While microfluidic integration and automation has begun to benefit drug screening,[246] developmental biology,[247,248] and cell sorting for cancer research,[249] neither the throughput nor precision of on-chip PAGE have been harnessed for quantitative characterization of riboswitch-ligand binding interactions.

In the following chapters, we present a microfluidic mobility shift assay (μMSA) that dramatically improves upon slab gel mobility shift assays by reporting ligand binding and riboswitch conformational change quickly (3 min) and quantitatively. We demonstrate the ability to use μMSA for streamlined validation of new riboswitch candidates and to facilitate rapid screening of possible ligand pairs and environmental conditions.

In particular, μMSA enables precise and rapid quantitation of ligand binding and subsequent riboswitch conformational change. These capabilities enable the use of μMSA in validation of riboswitch-ligand binding interactions and calculation of the statistical significance of an observed shift.

In 0.3% of the time required for bench top assays (3.2 min vs. 1020 min), we apply the riboswitch screening platform to functional analysis of five candidate SAM-I riboswitches isolated from thermophilic and cryophilic bacteria. These candidate riboswitches were computationally predicted, but previously unvalidated SAM-I riboswitches. Thus, we complete the screening process with unmatched precision, reproducibility, and sparing resource consumption. The format offers enhanced resolution of conformational change compared to slab gel formats, quantitation and repeatability for statistical assessment of the small mobility shifts inherent to conformational change differences, low reagent consumption, and riboswitch characterization without modification of the aptamer structure.

We demonstrate high sensitivity fluorescence-based detection that does not require *a priori* knowledge or modification of the riboswitch aptamer structure. This appreciable analytical sensitivity coupled with high resolution separation performance allows quantitation of equilibrium dissociation constants (K_d) for both rapidly and slowly interconverting riboswitch-ligand pairs as validated through experiments and modeling. A computational model relating the assay and kinetic timescales to these interconversion regimes validates the k_d measurement methods and enables conclusions to be drawn about the association, dissociation, and equilibrium binding timescales, giving insight into the kinetic versus thermodynamic control of riboswitch-regulated transcription for a given riboswitch. Conformational change, triplicate mobility shift measurements, and K_d are reported for both a known and a candidate SAM-I riboswitch with comparison to in-line probing assay results.

Finally, we demonstrate the utility of these tools for screening applications by screening Mg^{2+} and K^+ concentrations to assess their effect on SAM-I Bs riboswitch binding affinity and binding-induced conformational change.

8.4 Potential Implications of Microfluidic Screening Tools

The microfluidic screening tools introduced here have the potential to facilitate riboswitch discovery and validation of the thousands of *in silico* predicted riboswitches. Further, these tools may accelerate ligand discovery and the identification of ligand pairs for the over 24 candidate or orphan riboswitch classes for which no ligand has been discovered to date.[245] In addition, the quantitation and repeatability enabled by the rapid microfluidic format will allow

for the assessment of the statistical significance of the small mobility shifts inherent to conformational change differences.

Taken in sum, these tools will enable researchers to screen conditions (e.g., buffer composition, ligand libraries) to determine optimal conditions for riboswitch-ligand binding and selection, and open the possibility of screening riboswitch libraries for selection & validation of novel riboswitches. These tools may also enable the identification of orthogonal RNA-ligand pairs (synthetic ligands that bind with known natural riboswitches or vice versa) with broad applications in RNA-tagging in vivo, new genetic regulation control,[250] and for use as biosensors for metabolite sensing in vivo.[251] Riboswitches may also be used in the design of genetic circuitry for synthetic biology applications.[250]

Understanding and harnessing these ancient gene regulatory mechanisms also has implications in human health and the development of novel antibiotics based on newly identified drug targets.[252] No riboswitches have been identified to date in mammals so it is unlikely that drugs targeting riboswitches would act on mammalian mRNA. Since riboswitches control genes that are essential for bacterial survival, they may therefore be used for novel and bacteria-specific antibiotics. Further, a new class of antibiotics could be developed that are designed to interfere with riboswitch complex shape, the fundamental basis for riboswitch control of RNA transcription.

The microfluidic mobility shift assay establishes a scalable format for the study of riboswitch-ligand binding that will advance the discovery and selection of novel riboswitches and the development of antibiotics to target bacterial riboswitches.

Chapter 9: Microfluidic Riboswitch Mobility Shift Assays for Analysis of Riboswitch Function

9.1 Introduction

Riboswitch functionality is determined by detecting ligand-RNA binding and a resulting conformational change in the absence of accessory proteins.[2] Polyacrylamide gel electrophoresis (PAGE) slab gels are routinely used to confirm protein-free riboswitch-metabolite binding. An observed change in riboswitch mobility ('mobility shift') in the presence of ligand compared to no ligand conditions demonstrates both ligand binding and a resultant conformational change, often to a riboswitch structure that is more compact and with a faster apparent electrophoretic mobility. PAGE in microfluidic formats has been previously demonstrated by our group and others,[133,141,253] but has not been applied to riboswitch analysis to date.

To introduce a broadly relevant riboswitch screening tool, we sought to design a microfluidic native PAGE mobility shift assay capable of: (i) high-precision peak shift measurements appropriate for assessment of the small anticipated mobility shifts associated with RNA conformation change, (ii) repeatable operation to allow assessment of the statistical significance for observed mobility shifts, (iii) resource-sparing operation (material, time, handling) to afford assay scalability for screening uses, and (iv) quantifying K_d for a broad range of riboswitch-ligand binding kinetics. Here we detail salient design considerations for μMSA noting that while we focus attention on demonstrating the ability to screen for mobility shifts and measure K_d for the ligand *S*-adenosylmethionine (SAM) binding to a set of fluorescently labeled known or putative SAM-I riboswitch aptamers, the assay platform is conversely well-suited to screening of a single putative riboswitch against a library of ligands.

9.2 Materials and Methods

Our microfluidic mobility shift assay (μMSA) utilizes polyacrylamide gel photopatterned in 50 × 20 μm microfluidic channels that intersect in a 't' pattern (Figure 67). The riboswitch and ligand pair are incubated off-chip, pipetted into the sample well (S) and electrophoretically loaded through the loading channel to the sample waste well (SW). The electric field is then switched orthogonally so that a plug of sample is injected into the separation channel (B to BW) and the riboswitch and internal standards are allowed to migrate and resolve according to their electrophoretic mobilities.

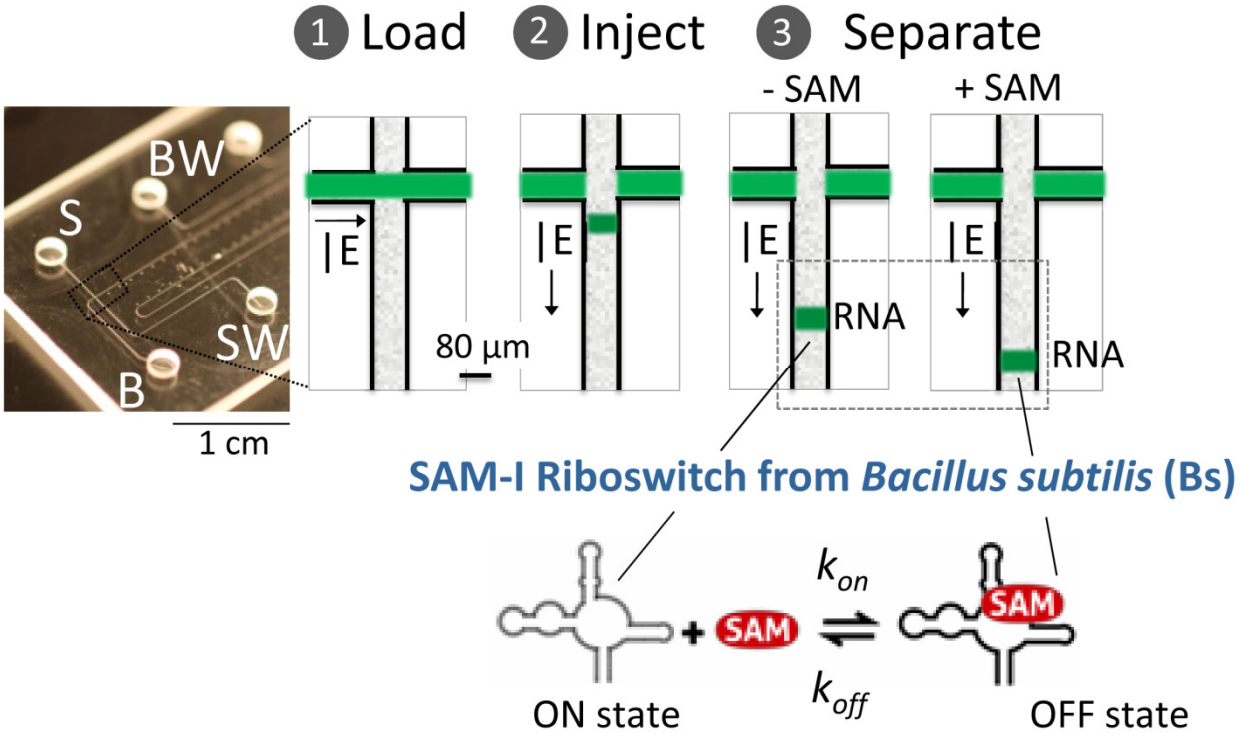

Figure 67. The microfluidic mobility shift assay (µMSA) detects ligand binding and riboswitch conformational change. Sample is electrophoretically loaded, injected, and separated on-chip. SAM ligand binding to SAM-I riboswitches induces a conformational change in the RNA molecule and faster electrophoretic mobility.

The excellent heat dissipation inherent to micro scale electrophoretic formats enables high electric field PAGE separations. High electric fields in turn yield fast separations which reduce the time for band broadening arising from molecular diffusion. Reductions in band dispersion also contribute to the speed of the separation since narrower peaks need less distance between them to be detectable.

In the field of separation science, this concept is known as separation resolution, which is the metric used to quantify the overlap of two peaks of interest. Separation resolution is defined as $R_s = \Delta a/(2\sigma_1 + 2\sigma_2)$, where σ is peak width, σ_0 is starting peak width, D is the diffusion coefficient, t is time, Δa is the distance between the peaks, and σ_1 and σ_2 are the bound and unbound peak widths, respectively. As the peak dispersion or peak widths decreases, separation resolution increases. In this work, when $R_s > 0.5$, the peaks were considered resolved, according to convention.[254]

Reagents and Oligonucleotides

10× tris-borate (TB) buffer was made by adding 900 mM tris base (Thermo Fisher Scientific, Waltham, MA), 890 mM boric acid (VWR, Radnor, PA), and $MgCl_2$ (EMD Millipore, Darmstadt,

Germany), and/or KCl (Sigma-Aldrich, St. Louis, MO), as indicated to 30 mL water and titrating to pH 8.5 with 1 M NaOH (Thermo Fisher Scientific).

Internal mobility standards included bovine-serum albumin (BSA, Sigma Alderich), phosphorylase B (PB, Sigma-Aldrich), α-lactalbumin (α-lact, Sigma-Aldrich), and trypsin inhibitor (TI, Life Technologies, Grand Island, NY). BSA, an inherently 'sticky' protein was found at times to influence the mobility of the riboswitches and was not used in all experiments. Non-specific interactions were not observed with PB, α-lact, or TI. Internal standards were labeled in-house with AlexaFluor 488 or 633 dyes (LIF system only) according to the manufacturer's instructions (Life Technologies). Protein concentration and the degree of labeling were measured using a NanoDrop (Thermo Fisher Scientific).

DNA oligonucleotides were purchased from ElimBio (Hayward, CA) or Integrated DNA Technologies (San Diego, CA). Sodium periodate, fluorescein-5-thiosemicarbazide and *S*-adenosylmethionine (SAM) were purchased from Sigma Aldrich. AlexaFluor 488 hydrazide sodium salt, and AlexaFluor 633 hydrazide bis(triethylammonium) salt were purchased from Invitrogen.

Preparation of DNA constructs used to make RNAs

DNA templates for the RNA constructs used in this work that correspond to computationally predicted wild-type riboswitch sequences from different organisms (*Bacillus subtilis*, *Polaribacter irgensii*, *Acidothermus cellulolíticus*, *Carboxydothermus hydrogenoformans*, *Polaribacter spp.*, and *Rubrobacter xylanophilus*) were either amplified by PCR from the genomic DNA or purchased from IDT as a single-stranded oligonucleotide and amplified by PCR. The resulting PCR products were cloned into TOPO vector (Invitrogen) and sequence confirmed. DNA templates for the P2 and M1 mutants used as negative controls were generated by PCR extension of overlapping primers containing the desired mutations, followed by cloning into TOPO vector and sequence confirmation. M1N and P2N were simply M1 and P2 mutants with additional natural flanking sequences (+27 nt upstream at the 5' end and +25 nt downstream at the 3' end). They were constructed by Quikchange mutagenesis using WTN as the template (124 yitJ+natural flanks).

Sequences of DNA constructs

The sequences of all the DNA templates used in this study are provided below and sequences for the primers are provided in Table 9. The extended T7 promoter sequence is shown in lower caps. Additional G nucleotides to enhance transcription initiation are bolded. Mutations are shown in red. The natural flanking sequences are underlined.

<u>*Bacillus subtilis* 124 yitJ SAM-I aptamer domain (Bs):</u>

Wild type[255]

ccaagtaatacgactcactata**GG**GTTCTTATCAAGAGAAGCAGAGGGACTGGCCCGACGAAGCTTCAGCAAC
CGGTGTAATGGCGATCAGCCATGACCAAGGTGCTAAATCCAGCAAGCTCGAACAGCTTGGAAGATAAG
AAGAG

P2 (a mutation at P2 stem has been shown to disrupt pseudoknot formation)[244]
ccaagtaatacgactcactata**GG**GTTCTTATCAAGAGAAGCAGAGGGACTCCCCCGACGAAGCTTCAGCAACC
GGTGTAATGGCGATCAGCCATGACCAAGGTGCTAAATCCAGCAAGCTCGAACAGCTTGGAAGATAAGA
AGAG

M1 (a mutation at P1/P2 junction has been shown to disrupt ligand binding but not folding)[255]
ccaagtaatacgactcactata**GG**GTTCTTATCAGAAGAAGCAGAGGGACTGGCCCGACGAAGCTTCAGCAAC
CGGTGTAATGGCGATCAGCCATGACCAAGGTGCTAAATCCAGCAAGCTCGAACAGCTTGGAAGATAAG
AAGAG

P2N
ccaagtaatacgactcactata**GG**ACTTCCTGACACGAAAATTTCATATCCGTTCTTATCAAGAGAAGCAGAG
GGACTCCCCCGACGAAGCTTCAGCAACCGGTGTAATGGCGATCAGCCATGACCAAGGTGCTAAATC
CAGCAAGCTCGAACAGCTTGGAAGATAAGAAGAGACAAAATCACTGACAAAGTCTTCTT

M1N
ccaagtaatacgactcactata**GG**ACTTCCTGACACGAAAATTTCATATCCGTTCTTATCAGAAGAAGCAGAG
GGACTGGCCCGACGAAGCTTCAGCAACCGGTGTAATGGCGATCAGCCATGACCAAGGTGCTAAATC
CAGCAAGCTCGAACAGCTTGGAAGATAAGAAGAGACAAAATCACTGACAAAGTCTTCTT

Polaribacter irgensii 23-P SAM-I aptamer domain (Pi):
Genbank accession AAOG01000001.1, nucleotides 142961..142846
ccaagtaatacgactcactata**GG**GAAATGTTATCAAGAAAGGCGGAGGGATTAGACCCATTGAAGCCTTAGC
AACCCTTTAGTAATAAAGAAGGTGCTAAATTCTACTCAATTATTCGTAATTGGATAGATAACAAAAA

Rubrobacter xylanophilus DSM 9941 SAM-I aptamer domain (Rx):
Genbank genome accession CP000386.1, nucleotides 882034..882017
ccaagtaatacgactcactata**GG**GGGCGCTCATCGAGAGCGGTGGAGGGACGGGCCCTGCGAAGCCGCGGC
AACCGGCGGGCGGCGGACGCCCGCGCCAGGTGCCAATTCCCGCGGAGGAGACTCCGAGAGATGAGCC
GGC

Acidothermus cellulolitícus 11B SAM-I aptamer domain (Ac):
Genbank genome accession CP000481.1, nucleotides 103255..103416
ccaagtaatacgactcactata**GG**CCGCTCATCGAGAGGGGCTGAGGGACCGGCCCGGTGAAGCCCCGGCAAC
CGTCACGGCGGTGTGGACGCCGAAGAGGCGCTGGAGTTGCGGCGCCAACGCGAGGCCACGTCGTGAT
CGGTGCCAAATCCGGCCTGCGGAAGGTCCGCGGGGAAGATGAGGAG

Carboxydothermus hydrogenoformans Z-2901 SAM-I aptamer domain (Ch):
Genbank genome accession CP000141.1, nucleotides 2169981..2169871

ccaagtaatacgactcactata**GG**CGCCTCTTATCAAGAGTGGCGGAGGGACTGGCCCAATGAAGCCCGGCAA
CCGGCCATATTTTTGGCAATGGTGCCAATTCCTGCGGATTAAATTCCGGGAGATAAGAGGAG

<u>*Polaribacter sp.* MED152 SAM-I aptamer domain (Ps):</u>
NCBI reference sequence NZ_CH902588.1, nucleotides 1408674..1408551
ccaagtaatacgactcactata**GG**GAAATGTTATCAAGAAAGGTGGAGGGATTAGACCCATTGAAGCCTTAGC
AACCCTTTAGAAATAAAGAAGGTGCTAAATTCTACTCTTTTAAATTGTTTAATTTAAAAGGATAGATAACA
AAAG

Table 9. Primer sequences used to create riboswitch aptamers used in this work

EXPERIMENT		**NOTES**
NAME		
	Bs SAM-I WT	
SH19	ccaagtaatacgactcactata**GG**GTTCTTATCAAGAGAAGCAGAGGG	For
SH20	CTCTTCTTATCTTCCAAGCTGTTCGAG	Rev
	Bs SAM-I M1	
SH21	ccaagtaatacgactcactata**GG**GTTCTTATCAAGAGAAGCAGAGGGA CTCCCCCGACGAAGCTTCAGCAACCGGTGTAATGGCGATCAGCCA TGACCAAGGTGCTAAATCCAGCAAGCTCGAACAGCTTGGA AGATAAGAAGAG	For (Primer extension)
SH19	See above	For (Template amplification)
SH20	See above	Rev
	Bs SAM-I P2	
SH22	ccaagtaatacgactcactata**GG**GTTCTTATCAGAAGAAGCAGAGGGA CTGGCCCGACGAAGCTTCAGCAACCGGTGTAATGGCGATCAGCC ATGACCAAGGTGCTAAATCCAGCAAGCTCGAACAGCTTGGAAGAT AAGAAGAG	For (Primer extension)
SH23	ccaagtaatacgactcactata**GG**GTTCTTATCAGAAGAAGCAGAGGG	For (Template amplification)
SH20	See above	Rev
	Bs SAM-I M1N	
QQ45	TGACACGAAAATTTCATATCCGTTCTTATCAGAAGAAGCAGAGGG ACTG	For (Quikchange)
QQ46	CAGTCCCTCTGCTTCTTCTGATAAGAACGGATATGAAATTTTCGTG TCA	Rev (Quikchange)
	Bs SAM-I P2N	
QQ43	CAAGAGAAGCAGAGGGACTCCCCGACGAAG	For (Quikchange)
QQ44	CTTCGTCGGGGGAGTCCCTCTGCTTCTCTTG	Rev (Quikchange)
	Pi SAM-I	
SCW13	ccaagtaatacgactcactata**GG**GAAATGTTATCAAGAAAGGCGGA	For

SCW14	TTTTTGTTATCTATCCAATTACGAATAATTG	Rev
	Rx SAM-I	
SCW7	ccaagtaatacgactcactata**GG**GGGCGCTCATCGAGAG	For
SCW8	GCCGGCTCATCTCTCG	Rev
	Ac SAM-I	
SCW3	ccaagtaatacgactcactata**GG**CCGCTCATCGAGAGGG	For
SCW4	CTCCTCATCTTCCCCGC	Rev
	Ch SAM-I	
SCW1	ccaagtaatacgactcactata**GG**CGCCTCTTATCAAGAGTGG	For
SCW2	CTCCTCTTATCTCCCGGAA	Rev
	Ps SAM-I	
SCW11	ccaagtaatacgactcactata**GG**GAAATGTTATCAAGAAAGGTGGAG	For
SCW12	CTTTTGTTATCTATCCTTTTAAATTAAACAA	Rev

Creation of RNA molecules using DNA templates

RNAs were transcribed *in vitro* using standard protocols[256] from DNA templates containing the extended T7 promoter sequence generated by PCR. Briefly, the transcription reactions were performed using 2 µg DNA template and T7 RNA polymerase (expressed from pT7-911 plasmid in BL21 Star and purified using Ni-NTA by QB3 MacroLab Facility, UC Berkeley) at 37 °C for 2-3 h. RNAs were then purified by separating them on a 6% denaturing PAGE gel, extracting the RNA from gel slices using crush-soak buffer (10 mM Tris, pH 7.5, 200 mM NaCl, 1 mM EDTA, pH 8.0), and precipitating the RNA molecules out in ethanol at -20 °C. After decanting the ethanol, RNAs were air-dried and redissolved in water. RNA concentrations were measured by the absorbance at 260 nm using a micro-volume UV-Vis spectrophotometer (Nanodrop ND-8000), in accordance with the standard methods in the field.

The RNA concentration was also determined using a new thermal hydrolysis method that measures the absorbance of degraded, rather than intact, RNA in order to account for the loss of absorbance encountered when RNA is base paired in secondary structures. This RNA concentration method was used to calculate the degree of labeling as described below. However, the absorbance readings of intact RNA obtained on the Nanodrop were determined empirically to be a more reliable method owing to the fact that the expected band pattern for a given RNA:SAM ratio was only observed when the intact RNA concentration was used. Additional effort will likely be required to create and confirm a more reliable method of determining RNA concentration going forward.

Fluorescently Labeling RNAs

All fluorescently labeled RNAs were labeled on the 3’ end of the molecule. Fluorophore dyes including fluorescein, AlexaFluor 488, or AlexaFluor 633 were conjugated to the RNAs following standard procedures for 3’ end labeling.[257] Briefly, the dialdehyde of the 3’ end ribose sugar was generated by oxidation of the RNAs (0.1-1 nmol) using freshly prepared 2.5 mM sodium

periodate in 100 mM sodium acetate buffer, pH 5.0 at 0 °C for 50 min. The oxidation reaction was quenched by addition of excess ethanol to precipitate the RNA dialdehydes at -20 °C. After removal of the ethanol and air-drying, RNAs were immediately dissolved in 100 mM sodium acetate buffer, pH 5.0 and incubated with excess reactive fluorophore reagent (fluorescein-5-thiosemicarbazide, AlexaFluor 488 hydrazide, or AlexaFluor 633 hydrazide) at 1 mM concentration at 0 °C overnight in the dark. The RNAs were recovered by ethanol precipitation followed by gel purification as described above.

The labeling efficiency for each fluorophore dye was determined using absorbance. The absorbance at the fluorophore excitation wavelength (494 nm for fluorescein, 633 nm for AlexaFluor 633) was measured and this value was divided by the appropriate extinction coefficient (68,000 M^{-1} cm^{-1} for fluorescein[258], 160,000 M^{-1} cm^{-1} for AlexaFluor 633[259], and 71,000 M^{-1} cm^{-1} for AlexaFluor 488[260]) to yield the fluorophore dye concentration. The RNA concentration was determined by measurement of the UV absorbance at 260 nm after thermal hydrolysis to yield the nucleotide monophosphates and employing Beer's law and the extinction coefficient of the nucleotide monophosphates to calculate the concentration of the known RNA sequence. The labeling efficiency was calculated as moles of fluorophore dye per moles of RNA by taking the ratio of the concentrations. The average RNA labeling efficiency for molecules used in this work was 75% using fluorescein-5-thiosemicarbazide (5 independent samples) and 30% using AlexaFluor 633 hydrazide bis(triethylammonium) salt (7 independent samples).

Microfluidic Device Fabrication

Optical white soda lime glass microfluidic chips were fabricated with standard wet etch processing by Caliper Life Sciences (Hopkinton, MA). Photopatterning of polymer structures and sieving matrixes in the glass channels was conducted in-house. Open channels were washed and silanized using 3-(trimethoxysilyl)-propyl methacrylate (98%) (Sigma Aldrich, St. Louis, MO) as described previously.[68] 3-10%T discontinuous polyacrylamide gel architectures were utilized in all mobility shift assays to match the conditions typically used in slab gel formats. 3-12%T discontinuous polyacrylamide gel architectures were utilized in all microfluidic K_d measurement experiments to increase the stacking effect and maximize assay sensitivity. The stacking interface has also been shown to increase resolving power,[11] as is important for detection of small conformation differences such as in riboswitch analysis.

Gel precursor solutions were prepared by diluting 30% (w/v) acrylamide/bis-acrylamide (Sigma Aldrich, St. Louis, MO) with the appropriate 10× TB buffer and water to achieve the desired total acrylamide concentration (3%T, 10%T or 12%T) in 1× TB buffer with 0.2% (w/v) water-soluble photoinitiator 2,2-azobis[2-methyl-N-(2-hydroxyethyl) propionamide] (VA-086, Wako Chemicals, Richmond, VA). Precursor solutions were degassed using sonication (~5 min) before use. The small pore size precursor solution was introduced into the channels using capillary action and the chip was aligned over a transparency mask with a 4 mm x 500 µm opening (designed in-house and fabricated by Fineline Imaging, Colorado Springs, CO) so that the region of the separation channel directly downstream of the injection junction was exposed. The

masked device was seated on an inverted Nikon Diaphot 200 microscope (Melville, NY), drops of viscous 5% (w/v) 2-hydroxyethyl cellulose (HEC) (Sigma Aldrich, St. Louis, MO) were applied to each well to suppress bulk fluid flow, and the device was allowed to equilibrate for 5 min. UV light from a Hamamatsu LightningCure LC5 UV light source (Hamamatsu City, Japan) was directed into the light path of the microscope and through a UV transmission objective lens (UPLANS-APO 4x, Olympus, Center Valley, PA). The masked chip was exposed to UV light for 270 sec at a beam intensity of ~1.65 mW/cm^2 (measured with a UV513AB Digital Light Meter, General Tools, New York, NY). Unpolymerized precursor solution was replaced with 3%T precursor solution by sequentially applying vacuum to wells S, SW, and B (Figure 67). The entire chip was then flood exposed for 8 min at ~8.5 mW/cm^2 on a 100 W filtered mercury UV lamp (UVP B100-AP, Upland, CA) a distance of 5 in from the chip. Bubble formation throughout the 10%T region of the separation channel was sometimes observed. In this case, longer degassing of the precursor solution and lower flood exposure intensities should be used.

Sample Preparation for μMSA Analysis

Riboswitch-ligand binding reactions were performed off-chip. Samples for μMSA were prepared by adding RNA, SAM ligand (as indicated), 2× TB buffer (with the indicated Mg^{2+} and/or K^+ concentration), and dI water in a LoBind eppendorf tube at the indicated concentrations. A LoBind eppendorf tube was important as significant sample loss was observed when the sample was allowed to interact with non-functionalized surfaces, leading to loss of assay sensitivity. The sample was then heated at 70°C for 3 min and cooled for 10 min to avoid denaturing the internal standard(s). The internal standard(s) were then added and the sample was allowed to equilibrate at room temperature for 1 hour in the dark before running on-chip.

μMSA Operation

The μMSA utilizes polyacrylamide gel photopatterned in 80 × 20 μm microfluidic channels that intersect in a 't' pattern.[133,253] PA gel-containing glass chips were secured in a custom-built Delrin manifold to expand the reservoirs for each well and minimize external light which would raise the background signal and reduce assay sensitivity. A practical advantage of the Delrin manifold over pipette tips which are also commonly used is that the manifold screws into place and is much more stable and robust than the pipette tips which may fall out during the course of an experiment.

The riboswitch and ligand pair were incubated off-chip and 2 μL of sample were pipetted into the sample well (S, Figure 67). All other wells were filled with 50 μL of 1× TB buffer with the appropriate Mg^{2+} and K^+ concentration. Voltage and current monitoring and control at each well was accomplished using a custom built, eight channel high voltage power supply with current/voltage feedback control. Platinum electrodes were inserted into each well. Electrophoretic sample loading was accomplished by applying -3 μA to S, 0 μA to buffer (B) and buffer waste (BW), and grounding well sample waste (SW) for ~ 1 min (E ~ 130 V/cm loading). Electrophoretic separation was initiated by switching the electric field orthogonally to apply -5

μA or -7 μA to well B, 0 μA to S and SW, and grounding well BW (E ~ 240 - 530 V/cm in separation channel). In this step, a plug of sample is injected into the separation channel (B to BW) and the riboswitch and internal standards are allowed to migrate and resolve according to their electrophoretic mobilities. The chip was cleared between runs by applying -3 μA to well BW, 0 μA to S and B, and grounding well SW, which moved the analyzed plug out of the separation channel into well SW.

Epi-Fluorescent Microscope Set-up and Image Processing

Migration and concentration distributions of separating fluorescent analytes were measured via an IX-70 inverted epi-fluorescent microscope equipped with a 100 W mercury arc lamp (Olympus, Center Valley, PA), 10× objective (UPlanFL, NA 0.3, Olympus, Center Valley, PA), 0.63× demagnifier (Diagnostic Instruments Inc., Sterling Heights, MI), and a filter cube optimized for GFP (XF100-3, Omega Optical, Brattleboro, VT). Sequential full-field image capture was performed using a 1392×1030 Peltier-cooled charge-coupled device (CCD) camera (CoolSNAP HQ2, Roper Scientific, Trenton, NJ), 75 msec exposure time, and 4×4 pixel binning. Image stacks were saved as .stk files in order to preserve the exact time stamps of image collection and enable precise mobility calculations to be made.

Full-field image post-processing was done with ImageJ (National Institutes of Health). .stk files were read into ImageJ with a plug-in that also imports the time stamp data directly from the stack. Intensity profiles of the separation channel were generated using a standardized ROI along the length of the separation channel. FITC-labeled SAM-I Bs RNA was used at 12 nM and 158 nM Alexa fluor 488-labeled BSA was used as an internal standard (Figure 69A).

On-chip gel shifts were assessed by extracting electropherograms 2 mm downstream of the injection junction, aligning the internal standard peaks for all runs for a given sample, and fitting a nonlinear Gaussian peak fitting algorithm (GaussAmp) using OriginPro 8.5 (OriginLab, Northampton, MA) in order to measure the peak center. RNA peak mobility was calculated as peak velocity ÷ applied electric field. Statistical significance was determined for triplicate runs using a two-tailed t-test with $p < 0.05$. Percent mobility increase was calculated as $(\mu_{shifted} - \mu_{unshifted})/\mu_{unshifted}$.

μMSA Screening of Mg^{2+} and K^{+} Concentrations

All buffer screening experiments were done with 3-12%T microfluidic gel architectures fabricated in the appropriate buffer as indicated. Full field imaging was done on the IX-70 inverted epi-fluorescence microscope set-up as described above. 1× TB buffer with 1 mM Mg^{2+}, 3 mM M^{2+}, 10 mM Mg^{2+}, 1 mM Mg^{2+} and 10 mM K^{+}, 3 mM Mg^{2+} and 10 mM K^{+}, 10 mM Mg^{2+} and 10 mM K^{+}, and 10 mM Mg^{2+} and 25 mM K^{+} concentrations were screened. The buffer screening studies utilized 93 nM of FITC-labeled SAM-I Bs RNA and 400 nM Alexa Fluor 488-labeled TI and 424 nM Alexa Fluor 488-labeled PB as internal standards (Figure 73). Statistical significance of a mobility shift was assessed using a two tailed t-test ($p < 0.05$, $n = 3$).

μMSA Screening of Candidate Riboswitch Functionality

Ligand binding and the resultant conformational change of candidate SAM-I riboswitches Rx, Ac, Ch, Bs, Pi, and Ps were assessed on-chip using full-field imaging on the inverted epi-fluorescence IX-70 microscope. M1 and P2 are single point-mutated derivations of the Bs SAM-I riboswitch and have been shown previously to lack function.[244,261] M1 and P2 aptamers were also run on slab gel PAGE assays and µMSA and confirmed that they do not exhibit a shift (Figure 68). Fluorescein-labeled SAM-I mutant riboswitches M1 and P2 (on-chip) and M1N and P2N (slab gel) were run as negative controls.

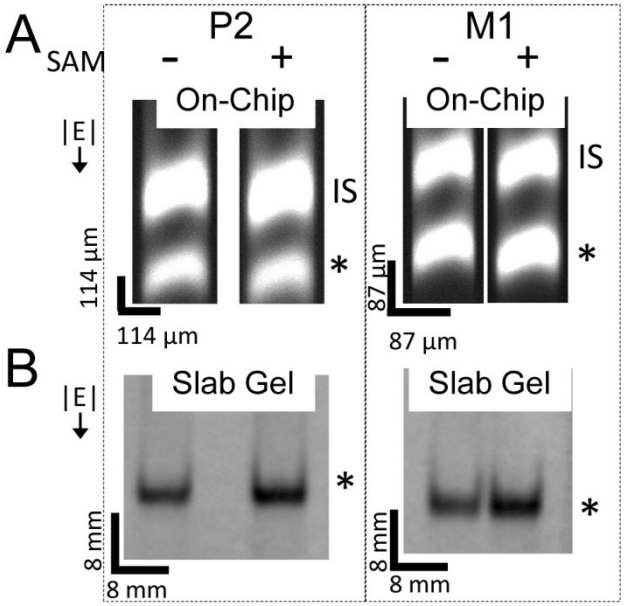

*Figure 68. No shift is observed for M1 or P2 mutants on-chip **(A)** or on a slab gel format **(B)**. RNA mutants are indicated with '*' and IS indicates BSA internal standard. TBM10 used in gel and run buffers. RNA is labeled with AF488 (A) and FITC (B).*

The mobility shift of candidate riboswitch-ligand pairs was assessed by comparing riboswitch mobility in no ligand and saturating ligand (7.1 µM) conditions. The statistical significance of the mobility shift was assessed using a two tailed t-test ($p < 0.05$, $n = 3$). A 3-10%T gel architecture was used and TBM10 buffer was used in the sample, gel, and run buffers. 400 nM Alexa Fluor 488-labeled TI and 424 nM Alexa Fluor 488-labeled PB were used as internal standards. FITC-labeled SAM-I Rx, Ac, and Ch riboswitches were at 150 nM. FITC-labeled SAM-I Pi and Ps riboswitches were at 412 nM and 260 nM, respectively. M1 and P2 mutants were run on-chip at 304 nM and 360 nM concentrations, respectively. Slab gels were run with no internal controls and M1N and P2N mutant riboswitches as negative controls.

Sample Preparation for Slab Gel PAGE Analysis

While protected from light, 1-3 pmol of fluorescently labeled RNA in 20 µL of TBM10 buffer (90 mM Tris, 89 mM Boric acid, 10 mM $MgCl_2$, pH 8.5) was renatured by heating to 70 °C on a heat

block for 3 min followed by a quick table-top centrifugation and slow cooling to room temperature for 1 h. This process was identical to that used to prepare samples for μMSA. Renaturation of the RNA was performed either in the presence (500 nM or 5 μM) or absence of SAM. Glycerol was added the sample in order to increase sample density and help with band stacking at the well-gel interface. Glycerol was added to 5-10% v/v prior to loading onto a 10% acrylamide/bisacrylamide (29:1) gel made with TBM10 buffer, which had been pre-equilibrated with TBM10 buffer for at least 1 h.

Slab Gel Native PAGE to Analyze RNA-ligand Interactions

The 10%T gel was run with recirculating TBM10 buffer at 4 °C at 200 V (electric field of 8 V/cm) for 17-20 h in the dark. After drying the gel at 70 °C for 30 min using the Bio-Rad model 583 gel dryer connected to a Welch DryFast vacuum pump, the gel was scanned using the Typhoon laser-based scanning system (GE Healthcare) at the excitation and emission wavelength settings appropriate to the fluorophore dye used (ex/em 532/526SP nm for fluorescein, either 532/526SP or 488/520BP AlexaFluor 488, and 633/670 nm for AlexaFluor 633). Internal standards (used as indicated) were diluted to match the fluorescence intensity of the labeled RNA and added immediately prior to sample loading. AlexaFluor 488-labeled bovine serum albumin (BSA) or trypsin inhibitor (TI) were used as internal standards for slab gel PAGE assays and exhibited slower and faster mobility, respectively, than the RNA or RNA-ligand complex.

For experiments performed at 1 mM Mg^{2+}, TBM1 buffer was used in the sample reaction, in the gel, and as the running buffer. For experiments performed at different RNA to ligand ratios, the concentration of RNA was kept constant (120 nM for fluorescein-labeled *B. subtilis* SAM-I riboswitch and 120 nM for fluorescein-labeled *P. irgensii* SAM-I riboswitch) and the concentration of the SAM ligand was added in the ratios indicated.

9.3 Microfluidic Mobility Shift Assay (μMSA) Demonstration

To demonstrate the ability to implement a riboswitch mobility shift assay in a microfluidic format and study the time savings achieved, an electrophoretic separation of the SAM-I riboswitch from *Bacillus subtilis* (Bs) in the presence and absence of SAM were compared. A 3-10%T discontinuous polyacrylamide gel was fabricated in the separation channel as described previously[142] and utilized in this work to match the conditions typically used in slab gel formats. We detected a 9.4% increase in SAM-I Bs riboswitch mobility with the addition of SAM ligand in a total analysis time of 3.2 min (Figure 69A). A comparable 10.8% mobility shift took 17 hrs to run on a slab gel plus an additional hour to dry the gel before imaging (Figure 69B). Percent mobility increase was calculated as $(\mu_{shifted} - \mu_{unshifted})/\mu_{unshifted}$. Total time to results for the microfluidic format includes 12.3 sec for each run to complete, a 20 sec load time for each run, a control and ligand sample, and triplicate runs for both samples in order to assess the statistical significance of the shift. The time savings achieved with the microfluidic format translates to a 316x reduction in analysis time. Additionally, the microfluidic format requires

reduced reagent and buffer volumes (µL) and eliminates the need for recycling and cooling of buffer over the duration of the assay run.

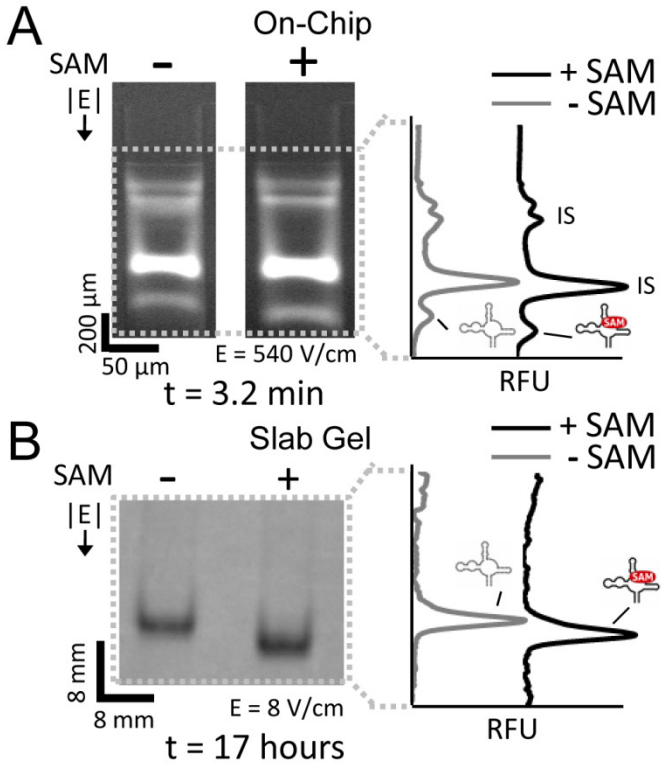

*Figure 69. µMSA detects Bs SAM-I riboswitch shift in the presence of SAM ligand in 3.2 minutes **(A)** compared to 17 hours on a conventional slab gel **(B)**. Riboswitch schematic indicates Bs SAM-I riboswitch peak. IS indicates BSA internal standard. TBM10 used in gel and run buffers. RNA is labeled with AF488 (A) and FITC (B).*

9.4 Improved Mobility Resolution in Microfluidic Formats

The repeatability and precision gained by moving to the microscale enables quantitative measurements of small differences in RNA peak mobility. The microscale also allows for improved resolution of mobility differences as compared to slab gel formats. As a result, the microscale offers a theoretical advantage in discriminating between bands with small mobility differences, such as those arising from molecular conformation changes rather than larger size or weight differences.

These theoretical improvements arise from the shorter assay timescales enabled by high electric field separations. Diffusion scales with the square root of assay time. Therefore, the rapid separation timescales of microfluidic formats (µMSA completes in 12.3 sec compared to

17 hours on a slab gel) lead to reduced diffusion and peak dispersion and enhanced signal to noise ratios. Since $\sigma^2 = \sigma_0^2 + 4Dt$ and separation resolution (R_s) is defined as $R_s = \Delta a/(2\sigma_1 + 2\sigma_2)$, where σ is peak width, σ_0 is starting peak width, D is the diffusion coefficient, t is time, Δa is the distance between the peaks, and σ_1 and σ_2 are the bound and unbound peak widths, respectively, we can derive the relationship between separation resolution, peak width, and time:

$$R_s = \frac{\Delta a}{2(\sqrt{\sigma_0^2 + 4D_1 t} + \sqrt{\sigma_0^2 + 4D_2 t})}$$

The initial starting plug width on a slab gel can be estimated to be around 100 μm. Similarly, the initial starting plug width on μMSA is defined by the injection junction dimensions and is also approximately 100 μm. Further, the diffusion coefficient is dependent on the analyte in the system and the gel pore sizes which are the same both in the μMSA and slab gel formats. Therefore, assuming that σ_0 and D are the same on the slab gel and μMSA (here assumed to be 100 μm and 1E-6 cm^2/sec, respectively), and given the measured assay times of 12 sec on-chip and 17 hours on a slab gel, we can see that for $R_s = 1$, Δa is 0.048859 cm on-chip and 1.979495 cm on a slab gel. 40-fold smaller differences in peak location (Δa) can be detected on-chip compared to a slab gel for the same peak R_s. This increased mobility resolution arises due to a reduction in diffusive peak dispersion with faster assay times.

Mobility (μ) is defined as u/E where u is velocity and E is the applied electric field. Therefore, μ is x/tE where x is the location of a band at time t. A mobility shift (Δμ) can then be calculated as Δx/tE where Δx is the difference in the band locations, or Δa. In comparing the band positions as the SAM ligand concentration changes, we can therefore determine a ligand-induced mobility shift according to this equation.

This scaling analysis shows us that, in addition to the improvements in repeatability and speed, moving to the microscale should provide a 40-fold improvement in the mobility resolution, or the ability to discriminate between differences in peak mobility. This increased mobility resolution arises due to a reduction in diffusive peak dispersion with faster assay times. Importantly for drawing conclusions on populations that have small differences between them, quantitative measurement of RNA peak mobility and assay repeatability also allows for the assessment of the statistical significance of a conformational change-induced mobility shift.

9.5 Benefits and Assay Characterization

As is important for screening large numbers of riboswitches or ligands, the total time to results using μMSA was notably shorter than the 17 hr required for slab gel analysis. A single run on μMSA took 12 seconds and full analysis of a mobility shift using μMSA required 3.2 min including sample loading and triplicate runs for both samples in order to assess the statistical significance of any observed shift. Thus, the time savings achieved with μMSA translates to a 316-fold reduction – critical for high throughput experimental validation of computationally predicted riboswitch-ligand interactions.

Other common, yet important, advantages of μMSA gained by moving to a microfluidic format are that μMSA requires reduced reagent (attomol compared to pmol) and buffer volumes (μL compared to L). Further, μMSA is performed at room temperature, making it easily translatable in a laboratory environment. In contrast, cooling to less than or equal to 10 °C is often required in native PAGE slab gel formats in order to limit diffusion and prevent RNA degradation during the long duration assay runs.[262] In a practical but important point, the μMSA screening platform also allows repeated use of a single PAGE channel for multiple assays that, with proper intermediate wash steps and controls that are demonstrated here, limit platform preparation time and effort while enabling excellent run-to-run reproducibility.

9.6 μMSA Screening for Candidate Riboswitch Functionality

Tools for efficient riboswitch discovery and validation are one of the unmet needs in the field of riboswitch research. As such, efficient screening of computationally predicted riboswitches for functionality is critical for increasing the number of known riboswitch-ligand pairs. Almost three thousand putative SAM-I riboswitches have been identified in a wide variety of bacteria, yet the SAM-I riboswitch from *Bacillus subtilis* has been the most well studied system. This tremendous phylogenetic diversity may provide a ready source of riboswitches with exploitable functionalities. Therefore, a diverse set of 5 previously uncharacterized, putative SAM-I riboswitches were transcribed, labeled, and characterized using μMSA.

We thus, compared the separations of five computationally predicted but previously unvalidated SAM-I riboswitches in the presence and absence of SAM ligand on μMSA. These novel SAM-I riboswitches were isolated from *Rubrobacter xylanophilus* (Rx), *Acidothermus cellulolyticus* (Ac), *Carboxydothermus hydrogenoformans* (Ch), *Polaribacter irgensii* (Pi), and *Polaribacter sp.* (Ps). The computationally predicted riboswitches were selected for their varying properties (e.g., GC content, length), while all being suspected of binding SAM ligand. The specific properties of each suspected SAM-I riboswitch are shown in Figure 70 below.

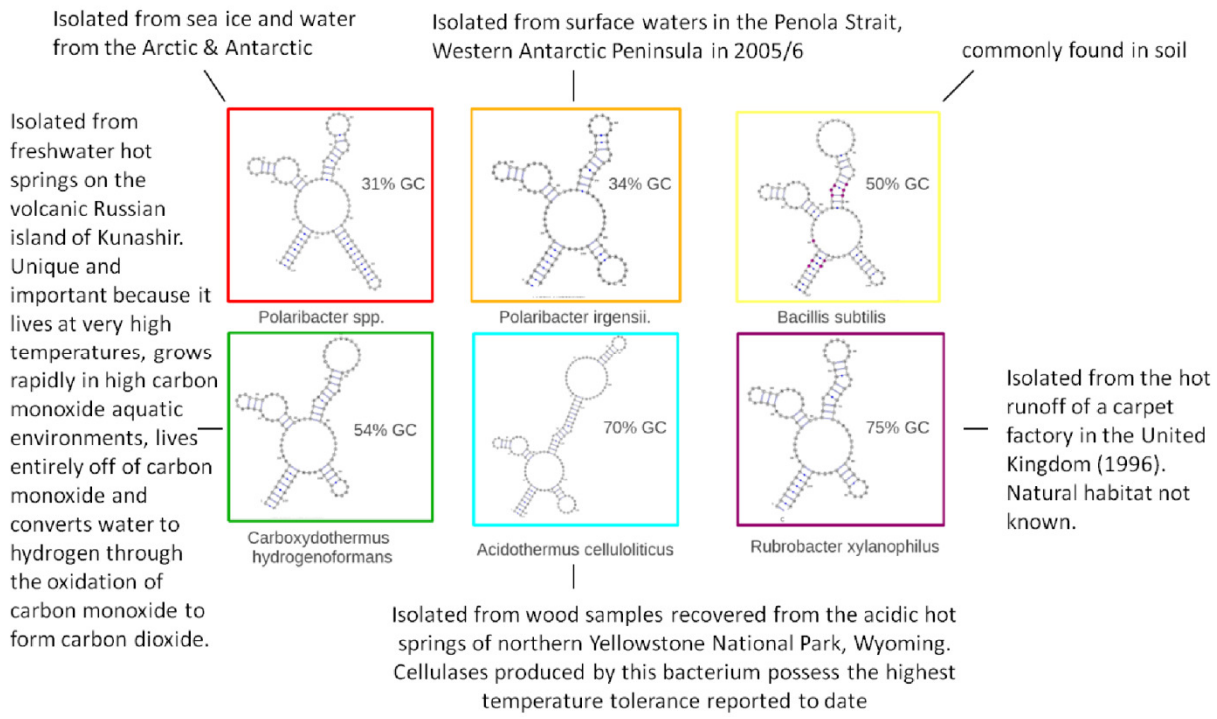

Figure 70. Thermophilic and cryophilic riboswitch structures, GC content, and history. Structures courtesy of Jonathan McMurray (Hammond Lab, UC Berkeley).[263-266]

A statistically significant mobility shift was shown on the microfluidic assay for all five putative SAM-I riboswitches from Rx, Ac, Ch, Pi, and Ps (indicated with a '*' in Figure 71). Statistical significance ($p < 0.05$) was assessed using a two tailed t-test ($n = 3$). The well-studied SAM-I riboswitch from *Bacillus subtilis* (Bs) was included as a positive control and demonstrated a statistically significant mobility shift, as expected. Mutant SAM-I riboswitches M1 and P2 (on-chip) and M1N and P2N (slab gel) were included as negative controls and demonstrated no statistically significant mobility shift in equally powered experiments, as expected.

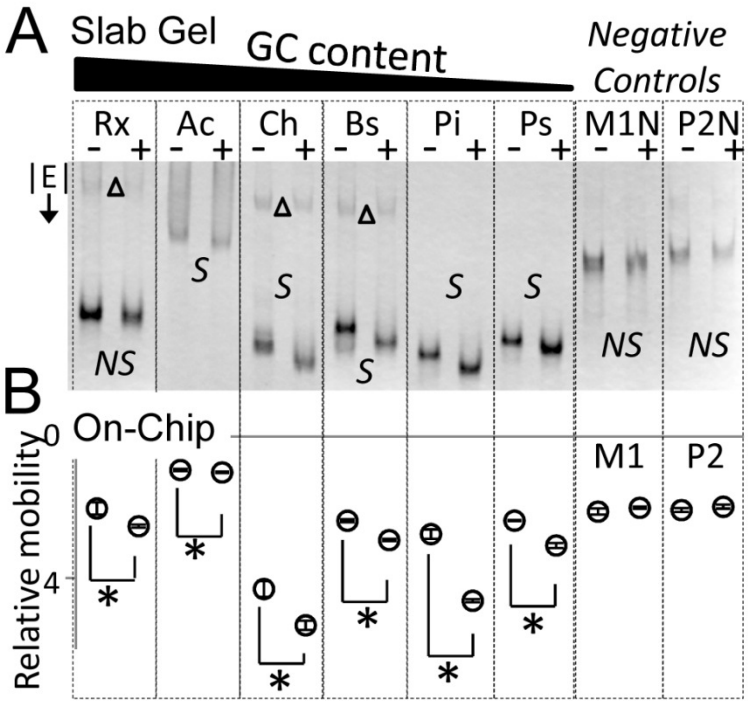

Figure 71. µMSA screen of candidate riboswitches. Microfluidic precision enables mobility shift as metric for screening candidate riboswitch function. The improved resolution of the microfluidic mobility shift assay over conventional slab gel mobility shift assays allows detection of GC-rich putative SAM-I riboswitches. ***(A)*** *'S' indicates a shift and 'NS' indicates no shift.* ***(B)*** *All on-chip mobility shifts are statistically significant using a two tailed t-test ($p<0.05$) and indicated by '*'. Error bars represent standard deviation of triplicate runs. M1, M1N, P2 and P2N mutants do not demonstrate a shift, as expected. See Figure S1 for slab gel data on M1 and P2 mutants. Upper bands in slab gel ('Δ') appear to be non-binding RNA conformers. Slab gel E = 8 V/cm, on-chip E = 240 V/cm. 1× TB + 10 mM Mg^{2+} in gel and run buffers. Relative mobility values are ×10^{-3} cm^2/Vs.*

The resolving power of the microfluidic mobility shift assay was assessed by comparing the mobility shifts measured on-chip with those measured using a conventional slab gel. Figure 71 shows that the microfluidic mobility shift assay is able to detect a mobility shift for Rx, Ac, Ch, Bs, Pi, and Ps SAM-I riboswitches (indicated with 'S' in Figure 71), whereas mobility shifts cannot be detected for Rx riboswitch on a slab gel ('NS' in Figure 71). These results support our theoretical calculation of the improved mobility resolution afforded by moving to a microfluidic format. µMSA enables detection of a mobility shift for smaller conformational changes, including conformationally 'locked' riboswitches with high GC content (e.g., Rx – 75% GC) and riboswitches with long chain lengths which result in a smaller shift relative to the total size of the molecule (e.g., Ac – 162 nt).

The resolution power of the slab gel can be improved by increasing the size of the sample wells, likely owing to increased sample stacking at the well-gel interface. Figure 72 shows that a mobility shift can be detected for Rx on a slab gel with larger sample wells. However, from a practical perspective, increasing the well sizes ultimately hurts analytical throughput, a critical consideration when designing a screening assay and a major motivation for the development of μMSA.

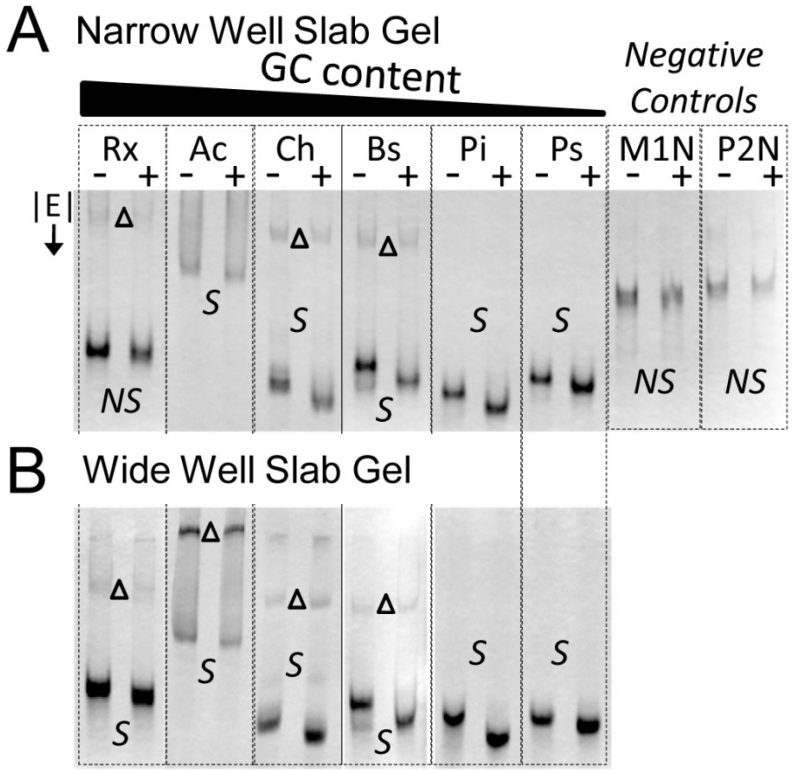

*Figure 72. Mobility shift resolution on a slab gel is dependent on well size. No mobility shift is detected for Rx when narrow sample wells are used **(A)**, while a mobility shift is detected for Rx when well size is increased **(B)**. Narrower sample loading wells allow for increased parallelization of sample runs, but sacrifice resolution of mobility shifts by increasing injection band dispersion. 'S' indicates a shift and 'NS' indicates no shift. M1N and P2N mutants do not demonstrate a shift, as expected. Upper bands in slab gel ('Δ') appear to be non-binding RNA conformers. Slab gel E = 8 V/cm, on-chip E = 240 V/cm. 1× TB + 10 mM Mg^{2+} in gel and run buffers.*

The total time to screen these five novel riboswitches, one positive control and two negative controls on-chip was 58 min. The time savings and repeatability attained with the microfluidic format enabled repeat trials to be run and the statistical significance of an observed shift to be calculated, an endeavor that is laborious and not typically done with conventional slab gels.

9.7 Effect of Mg^{2+} and K^+ Concentration on Riboswitch Mobility Shift

Mg^{2+} has been shown to improve riboswitch stability and facilitate riboswitch-ligand binding.[243,267] To probe the effect of Mg^{2+} and K^+ on the extent of the riboswitch mobility shift and further demonstrate the screening capabilities of the microfluidic assay, we screened the SAM-I Bs riboswitch in varying buffer compositions and extracted riboswitch mobility and the percentage mobility change with SAM present (Figure 73). A statistically significant shift was observed for Bs in all buffer conditions tested when saturating concentrations of SAM ligand were introduced ($p < 0.05$ using two tailed t-test). Interestingly, the concentration of Mg^{2+} and K^+ did not impact relative RNA mobility or the relative mobility change in a consistent manner. These observations suggest that changing ion concentrations affect not only the RNA-ligand interaction but also the RNA fold and the RNA interaction with electrolyte (run buffer) in the gel matrix.[262] This information should prove useful for informing the design of selection assays. In selection assays, the extent of the shift cannot be used as a proxy for selecting tighter binding pairs. Further, the mobility shift cannot be augmented by altering the buffer composition.

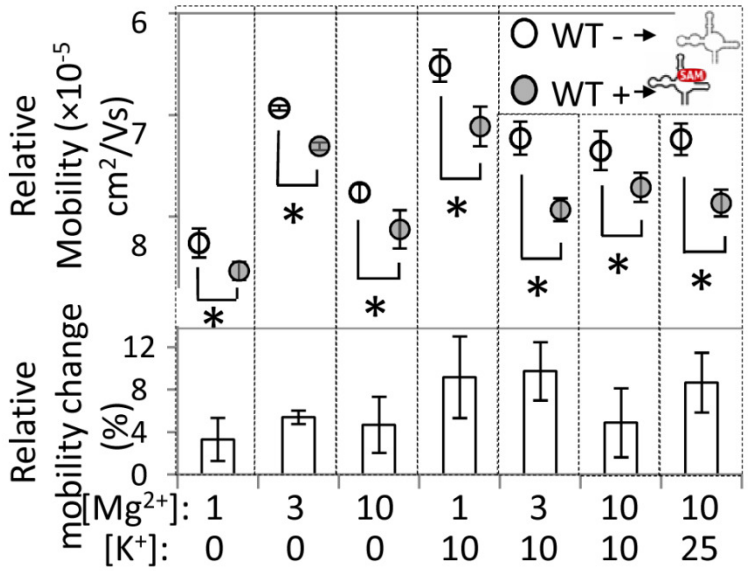

Figure 73. Screening for the effect of Mg^{2+} and K^+ concentration on Bs SAM-I riboswitch mobility and the extent of the mobility shift in the presence of SAM ligand. All on-chip mobility shifts are statistically significant using a two tailed t-test ($p<0.05$) and indicated by ''. Relative mobility change is the % increase in RNA mobility in the presence of SAM. WT- and WT+ indicate the absence and presence of SAM ligand, respectively. Error bars are standard deviation of triplicate runs. All runs were done in 1× TB buffer with salt concentrations as indicated in mM.*

Chapter 10: Microfluidic Equilibrium Dissociation Constant Assays for Characterization of Riboswitch-Ligand Binding

10.1 Theory and Computational Model of Riboswitch-Ligand Binding Kinetics

Affinity constants such as dissociation constant (K_d) and binding constant (K_b) are quantitative representations of the strength with which two molecules interact. Therefore, measuring the binding affinity of two molecules can give insight into the mechanisms by which they interact.[3]

Once an orphan riboswitch has been linked with a ligand and experimentally validated, it is often desirable to characterize the binding interaction by measuring the binding strength of the pair. Measurement of riboswitch-ligand equilibrium dissociation constant (K_d) enables the characterization of the binding affinity of newly discovered riboswitches and riboswitch classes,[268] comparison of the binding strength of engineered ligand-riboswitch pairs to native counterparts, insight into the concentrations of ligand needed in the cell to induce genetic regulation for thermodynamically controlled riboswitches, an understanding of the effect of environmental conditions on riboswitch folding states,[269] and some knowledge of the binding (t_{on}) and dissociation (t_{off}) timescales and how they relate to transcriptional timescales. Riboswitch k_d is typically determined using laborious in-line probing assays which are not suitable for screening applications as they rely on the natural tendency of RNA to differentially degrade based on its structure and employ a 40 hour incubation of RNA and ligand followed by separation on a denaturing urea slab gel for 2-4 hours.[236]

To derive a theoretical method by which to measure K_d for both slowly and rapidly interconverting riboswitch pairs in a microfluidic format, we modeled the mass transport for an unbound riboswitch (A) binding to ligand (L) to form a bound form of the riboswitch (B) according to the equation:

$$A + L \underset{K2}{\overset{K1}{\leftrightarrow}} B$$

Then, modeling the mass transport for an electrophoretic separation of these components in a microfluidic format, the relevant transport mechanisms are binding reaction, diffusion, and electrophoretic migration. Assuming first order Langmuir binding, the concentration distributions of free riboswitch (c_A), bound riboswitch (c_B), and free ligand (c_L) during electrophoretic separation can be expressed as a system of partial differential equations:

$$\frac{\partial c_A}{\partial t} = D_a \frac{\partial^2 c_A}{\partial x^2} - \mu_A E \frac{\partial c_A}{\partial x} - k_1 c_L c_A + k_2 c_B$$

$$\frac{\partial c_B}{\partial t} = D_B \frac{\partial^2 c_B}{\partial x^2} - \mu_B E \frac{\partial c_B}{\partial x} + k_1 c_L c_A - k_2 c_B$$

$$\frac{\partial c_L}{\partial t} = D_L \frac{\partial^2 c_L}{\partial x^2} - \mu_L E \frac{\partial c_L}{\partial x} - k_1 c_L c_A + k_2 c_B$$

where t is time, D_i is the characteristic diffusivity for each analyte, E is the applied electric field, and μ is analyte mobility.

We can then non-dimensionalize the equations by defining dimensionless parameters. We can non-dimensionalize x by dividing by the characteristic length scale of the separation (L) to yield $\bar{x}$:

$$\bar{x} = \frac{x}{L}$$

We can non-dimensionalize D by dividing by the characteristic diffusion coefficient (D_0) to yield $\overline{D_i}$:

$$\overline{D} = \frac{D_i}{D_0}$$

We can non-dimensionalize t by dividing by the time it takes for the unbound riboswitch (A) to reach te end of the channel, L, to yield $\bar{t}$:

$$\bar{t} = \frac{t}{t_0}$$

where

$$t_0 = \frac{L}{\mu_A E}$$

so

$$\bar{t} = \frac{t}{L/\mu_A E}$$

and

$$\bar{t} = \frac{t\mu_A E}{L}$$

We can then plug these non-dimensionless parameters into the differential equations and simplify them to get the following system of non-dimensionalized equations:

$$\frac{\partial c_A}{\partial \bar{t}} = \frac{\overline{D_A}\mathrm{D_0}}{E\mu_A L}\frac{\partial^2 c_A}{\partial \bar{x}^2} - \overline{\mu_A}\frac{\partial c_A}{\partial \bar{x}} - \frac{\mathrm{k_1 L}}{\mathrm{E\mu_A}}\mathrm{c_L}c_A + \frac{\mathrm{k_2 L}}{\mathrm{E\mu_A}}c_B$$

$$\frac{\partial c_B}{\partial \bar{t}} = \frac{\overline{D_\mathrm{B}}\mathrm{D_0}}{E\mu_A L}\frac{\partial^2 c_B}{\partial \bar{x}^2} - \overline{\mu_B}\frac{\partial c_B}{\partial \bar{x}} + \frac{\mathrm{k_1 L}}{\mathrm{E\mu_A}}c_A - \frac{\mathrm{k_2 L}}{\mathrm{E\mu_A}}c_B$$

$$\frac{\partial c_L}{\partial \bar{t}} = \frac{\overline{D_\mathrm{L}}\mathrm{D_0}}{E\mu_A L}\frac{\partial^2 c_L}{\partial \bar{x}^2} - \overline{\mu_L}\frac{\partial c_L}{\partial \bar{x}} - \frac{\mathrm{k_1 L}}{\mathrm{E\mu_A}}c_A + \frac{\mathrm{k_2 L}}{\mathrm{E\mu_A}}c_B$$

Following convention, we can then define non-dimensional ratios including the Peclet number, Pe, which gives the ratio of the electromigration timescale to the diffusion timescale and is defined as $E\mu_A L/D_o$. We can also define two Damkohler numbers, Da_{on} and Da_{off}, which give the ratio of the migration timescale to the reaction timescale and are defined as $Da_{on} = k_1 L c_L/E\mu_A$ and $Da_{off} = k_2 L/E\mu_A$ where k_1 and k_2 are the association and dissociation rate constants, respectively. A large Damkohler number indicates the reaction is happening faster than electromigration along the channel (Da_{on} and $Da_{off} > 1$).

Substituting in Pe, Da_{on} and Da_{off}, we get the following, non-dimensionalized system of equations:

$$\frac{\partial c_A}{\partial \bar{t}} = \frac{\overline{D_A}}{Pe}\frac{\partial^2 c_A}{\partial \bar{x}^2} - \overline{\mu_A}\frac{\partial c_A}{\partial \bar{x}} - Da_{on}c_A + Da_{off}c_B$$

$$\frac{\partial c_B}{\partial \bar{t}} = \frac{\overline{D_B}}{Pe}\frac{\partial^2 c_B}{\partial \bar{x}^2} - \overline{\mu_B}\frac{\partial c_B}{\partial \bar{x}} + Da_{on}c_A - Da_{off}c_B$$

$$\frac{\partial c_L}{\partial \bar{t}} = \frac{\overline{D_L}}{Pe}\frac{\partial^2 c_L}{\partial \bar{x}^2} - \overline{\mu_L}\frac{\partial c_L}{\partial \bar{x}} - Da_{on}c_A + Da_{off}c_B$$

where $\bar{t} = t\mu_A E/L$, $\bar{x} = x/L$, $\overline{D} = D_i/D_o$, $\bar{\mu} = \mu_i/\mu_A$, L is the separation length, E is the applied electric field, μ is analyte mobility, t is time, and D_o is the characteristic diffusivity. Experimentally, $c_A + c_B$ is equal to the initial concentration of riboswitch added to the system and $c_L + c_B$ is equal to the initial concentration of ligand added to the system, assuming a 1:1 riboswitch-ligand binding ratio. The question to solve is therefore: what is $c_A + c_B$ at the end of separation (at $\bar{x}$ = 1 and $\bar{t}$ = 1)?

Using a numerical initial-boundary value partial differential equation solver in Matlab, we solved these equations simultaneously for a given set of parameter values. Initial analyte concentrations (u_0) were assumed to be overlapping equilibrium Gaussian peaks at the beginning of the separation channel with 200 μm peak widths according to the equations:

$$u_0 = \begin{pmatrix} c_A e^{-\frac{\bar{x}^2}{2\bar{\sigma}_0^2}} \\ c_B e^{-\frac{\bar{x}^2}{2\bar{\sigma}_0^2}} \\ c_L e^{-\frac{\bar{x}^2}{2\bar{\sigma}_0^2}} \end{pmatrix}$$

Since $4\sigma_0$ represents the initial peak width of 200 µm, we can normalize by L (assumed to be 4 mm) to get $\frac{1}{2\bar{\sigma}_0^2} = 3200$. Substituting this in, we get non-dimensionalized initial conditions of:

$$\overline{u_0} = \begin{pmatrix} c_A e^{-3200\bar{x}^2} \\ c_B e^{-3200\bar{x}^2} \\ c_L e^{-3200\bar{x}^2} \end{pmatrix}$$

where cA, cB, and cL are solved according to equilibrium binding conditions, knowing that $c_A + c_B$ is equal to the initial concentration of riboswitch added to the system and $c_L + c_B$ is equal to the initial concentration of ligand added to the system.

Total RNA concentration ($c_A + c_B$) was assumed to be 1 µM and ligand concentration (c_L) was 1 µM. Peak mobilities of 1.06338E-5 cm^2/Vs, 1.18E-5 cm^2/Vs, and 1.2E-5 cm^2/Vs, a separation length of 4 mm, and an applied electric field of 500 V/cm was assumed to match experimental conditions. For separations where either peak had a measured concentration < 0.01 µM at L, only one peak was assumed and R_s was undefined. In these regimes, all RNA was either bound or unbound. The Peclet number (Pe = LµE/D) is ~500 for all µMSA simulations and data and ~800 for all slab gel data.

Modeling the mass transport for varying association and dissociation rate constants (k_{on} and k_{off} values), we could computationally extract bound and unbound riboswitch concentration profiles along the channel and calculate bound and unbound riboswitch peak separation resolution (R_s) which reports the ability to resolve shifted riboswitch populations (i.e., ligand-bound) using PAGE. Calculation of the two Da metrics also allowed us to compare the migration to the reaction timescales. This allowed us the ability to rationally choose the assay parameters to use during system operation and also understand the performance improvements gained by moving to a microfluidic format by comparing the Da_{on} and Da_{off} values that are accessible to slab gels and microfluidic formats for given association and dissociation rates.

The absolute R_s value extracted from the computational model is dependent on the difference in absolute mobility values given for the bound and unbound riboswitch peaks, electric field and separation time.[254] Thus, these values needed to be carefully chosen. The proof for this is given by the following equations which describe peaks as illustrated in Figure 74:

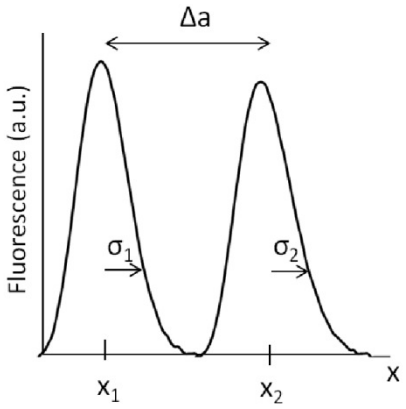

Figure 74. Schematic of the fluorescence signal of two resolved RNA bands. σ positions in the figure are approximate.

Separation resolution, Rs, is defined as:[254]

$$R_s = \frac{\Delta a}{4\sigma}$$

Since $u = \mu E$ and u = x/t where u is peak velocity, μ is peak mobility, x is peak position, t is time, and E is the applied electric field,

$$\mu = \frac{x}{tE} \quad \text{and} \quad \Delta\mu = \frac{\Delta x}{tE}$$

Since Δx = Δa as shown in the figure above,

$$R_s = \frac{\Delta\mu tE}{4\sigma}$$

Therefore, the absolute separation resolution extracted from the model is dependent on the values of these variables as entered into the model. To match the model to separation conditions measured on-chip, peak mobilities of 1.06338E-5 cm^2/Vs, 1.18E-5 cm^2/Vs, and 1.2E-5 cm^2/Vs, a separation length of 4 mm, and an applied electric field of 500 V/cm was assumed. A characteristic diffusion coefficient (which will impact σ) was assumed to be 1E-6 cm^2/s (measured value for GFP protein in a 4%T polyacrylamide gel) and then weighted by the relative mobility of the bound and unbound peaks to give 0.169272E-6 cm^2/sec and 1E-6 cm^2/s for unbound and bound peaks, respectively. With these values, the model gives a maximum R_s of 0.6 at 4 mm separation distance, which matches experimental values.

Figure 75 shows that R_s is dependent on both Da_{on} and Da_{off}. The heat map in Figure 75 shows the calculated R_s values for the bound and unbound riboswitch peaks across a biologically relevant range of electrophoretic and reactive transport conditions. R_s values are calculated between the bound and unbound riboswitch peaks after the peaks have traveled 1 mm on the microfluidic chip for varying Da_{on} and Da_{off} values. In Figure 75, undefined R_s regimes (where either no bound or no unbound riboswitches were detected) were represented as R_s of 0 (black

regions). Since $\frac{Da_{off}}{Da_{on}} = \frac{K_D}{c_L} = \frac{c_A}{c_B} = \frac{k_{off}}{k_{on}c_L}$, peak overlap, measured by R_s, is determined by the magnitudes of Da_{on} and Da_{off}, while peak height depends on the ratio of Da_{off}/Da_{on}.

Figure 75 illustrates the various regimes that exist for differing association, dissociation, and electromigration timescales. The two Da metrics allow us to compare the migration to the reaction timescales. A large Damkohler number indicates the reaction is happening faster than electromigration along the channel (Da_{on} and $Da_{off} > 1$). In the case when $Da_{on} > 1$ and $Da_{off} < 1$ or $Log(Da_{on}) > 0$ and $Log(Da_{off}) < 0$, k_{on} is high and the timescale for binding is very fast, while k_{off} is low and the timescale for dissociation is very slow relative to the electromigration timescale. In Figure S2, this regime is in the upper right hand corner and we see that the peaks are well resolved with a maximum R_s. In this case, there is minimal interconversion between bound and unbound forms of the riboswitch owing to the rapid binding and slow dissociation times – bound RNA remains bound during the separation. In this regime, two peaks are resolved from each other which represent the bound and unbound populations and the K_d can be extracted by tracking the amount of bound RNA as ligand concentration is increased.

In the case when $Da_{on} > 1$ and $Da_{off} > 1$ or $Log(Da_{on}) > 0$ and $Log(Da_{off}) > 0$, k_{on} is high and the timescale for binding is very fast. Meanwhile k_{off} is also high and the timescale for dissociation is also very fast relative to the electromigration timescale. In Figure 75, this regime is in the lower right hand corner and we see that the peaks are poorly resolved with a minimum R_s (while still retaining both bound and unbound forms in the system). In this case, there is rapid interconversion between bound and unbound forms of the riboswitch during the separation owing to the rapid binding and dissociation times relative to the electromigration times. Here, ligand that is dissociated during the separation is quickly rebound by free RNA in the plug. In this regime, the two peaks are predicted to overlap, yielding a single riboswitch peak which represents the fraction bound and the K_d can be extracted by tracking the mobility of the single peak as ligand concentration is increased. In both regimes, free ligand will move with a fast electrophoretic mobility, owing to its small size, but the observed interconversion regimes will occur independent of ligand mobility.

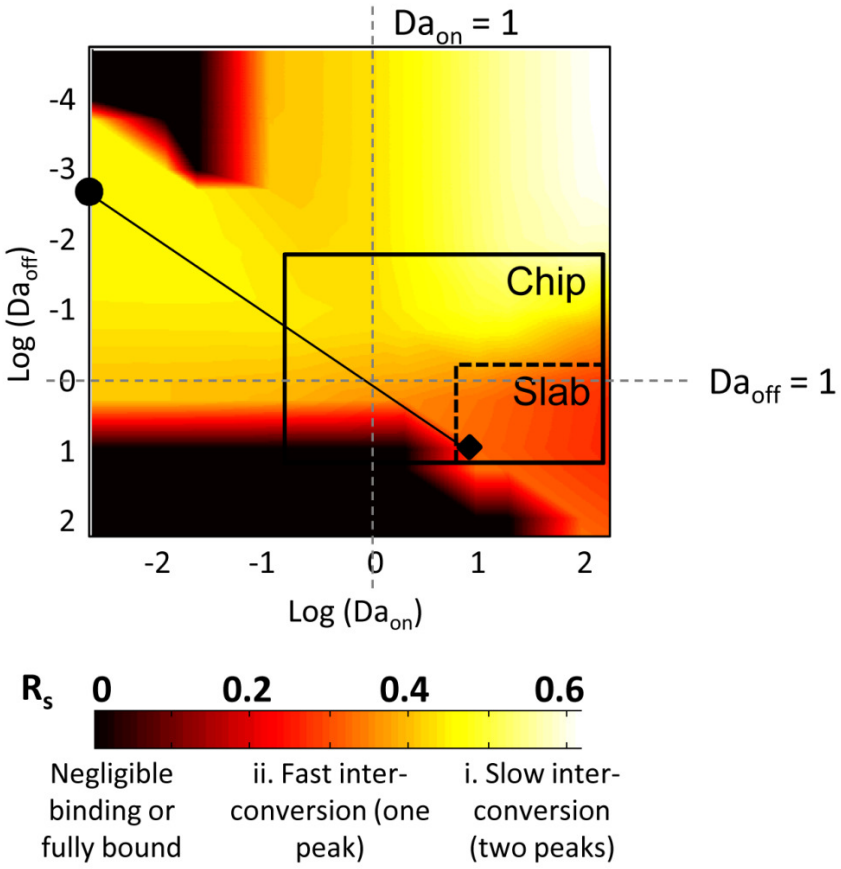

Figure 75. Separation resolution of bound and unbound riboswitch populations is dependent on Da. Tuning assay conditions such as applied voltage and ligand concentration allows the microfluidic format to access a wider range of Da_{on} and Da_{off} values. Compare the microfluidic performance space (solid box) to that of the conventional slab gel (dashed box), here for a riboswitch-ligand pair with k_{on} = 1.5E-3 /µMsec (similar to k_{on} of 2AP and 70 pbuE riboswitch[270]) and k_{off} =1.5E-5 /sec (similar to FMN + 165 ribD riboswitch[229]). The microfluidic format allows assay operation at $Da_{on} < 1$ and $Da_{off} < 1$, and therefore allows two peaks to be resolved for a given riboswitch-ligand pair (dark circle where k_{on} = 1.5E-4/µMsec and k_{off} = 1.5E-4/sec) where they could not be in a slab gel format (dark diamond for the same k_{on} and k_{off} values).

Third and fourth regimes also exist where 1) binding is so slow that only unbound RNA exists and 2) dissociation is so slow that only bound forms of the riboswitch exist; however, these regimes are not observed here.

To understand the performance improvements gained by moving to a microfluidic format, we compared the Da_{on} and Da_{off} values that are accessible to slab gels and microfluidic formats for a given association and dissociation rate. Because of the higher electric field strengths that can be applied in a microfluidic channel (~800 V/cm maximum on-chip vs. ~20V/cm on a slab gel),

microfluidic electrophoretic separations allow access to 40× lower Da_{on} and Da_{off} values compared to slab gels for a given riboswitch-ligand pair. Thus, improved separation resolution is expected between unbound and bound riboswitch peaks on a microfluidic format compared to a slab gel. For example, given k_{on} = 1.5E-3/μMsec and k_{off} =1.5E-5/sec, a typical 17 hour slab gel with a 10 cm separation and 1 μM ligand concentration can access log(Da_{on}) values of 0.9 to 2.2 and log(Da_{off}) values of -0.12 to 1.2 (dashed box in Figure 75). With the same conditions on-chip, the microfluidic format can access log(Da_{on}) values of -0.727 to 2.2 and log(Da_{off}) values of -1.7 to 1.2 (solid box in Figure 75). Access to a wider range of Da_{on} and Da_{off} values enables optimization of microfluidic assay conditions (e.g., electric field and ligand concentration) so as to improve separation resolution between two resolved peaks or move more solidly into the single peak regime.

Further, for a given riboswitch-ligand pair, the microfluidic format can allow assay operation at $Da_{on} < 1$ and $Da_{off} < 1$, and therefore allow two peaks to be resolved where they could not be on a slab gel format. Figure 75 shows that a riboswitch-ligand pair with k_{on} = 1.5E-4/μMsec and k_{off} = 1.5E-4/sec would operate at log(Da_{on}) = 1 and log(Da_{off}) = 1, where the migration timescale is 10x faster than both the on-rate and off-rate of reaction, if run with typical slab gel conditions (dark diamond in Figure 75) and would be detected as a single peak. However, if detected at a 1 mm separation distance on-chip, it would appear as log(Da_{on}) = -2.5 and log(Da_{off}) = -2.5 and two peaks could be resolved (solid box in Figure 75).

10.2 Computational Model for Microfluidic K_d Measurement of Rapidly and Slowly Interconverting Riboswitches

The observation in Figure 75 that R_s is dependent on both Da_{on} and Da_{off} is important because in experiments, we observed that at ligand:RNA ratios of less than one, we sometimes saw the appearance of two bands as we would expect in an antibody-antigen immunoassay, but other riboswitches would reveal the appearance of a single band with a mobility that was proportional to the ligand:RNA ratio. We hypothesized that this was due to differences in interconversion rates of the riboswitch pairs.

Thus, we next sought to design electrophoretic separations capable of probing riboswitch-ligand binding interactions spanning rapidly to slowly interconverting systems (i.e., interconversion between bound and unbound forms). The speed of interconversion is important, as the regime informs method selection for K_d determination using electrophoresis. Since K_d is a ratio of the rates of dissociation and association, binding pairs with similar K_d values can be either fast or slow interconverting species. We consider both cases here.

A large Damkohler number indicates the reaction is happening faster than electromigration along the channel (Da_{on} and $Da_{off} > 1$). For association and dissociation timescales where riboswitch interconversion is occurring rapidly compared to the timescale of the assay (Da_{on} and $Da_{off} > 1$), Figure 75 shows that the SR is low, indicating that bound and unbound peaks overlap yielding a single riboswitch peak. The lowest SR is found in the regime where Da_{on} and $Da_{off} > 1$ and the association and dissociation timescales are similar. In this regime, the

observed band has a weight-averaged mobility[271] which represents the fraction of bound RNA. The fraction of bound riboswitches increases as ligand concentration increases, increasing the peak mobility until all the RNA molecules are bound and the peak is fully shifted. It was therefore hypothesized that, for rapidly interconverting riboswitch-ligand pairs, riboswitch peak mobility could be tracked for increasing ligand concentration and a 3-parameter logistic fit binding equation of the form $y = \beta_1 \times [SAM]/(k_d+[SAM])+\beta_3$ could be used to extract K_d. This method was first computationally predicted by Cann[271] and later experimentally validated by Woodson.[262] This technique relies on the ability to resolve small increases in riboswitch mobility as ligand concentration is increased and therefore is well-suited for the increased resolving power and small electrophoretic timescales demonstrated by the microfluidic format employed here. A similar method has been used to determine the dependence of Mg^{2+} concentration on RNA binding and conformation.[269].

In the rapid interconversion regime (Da_{on}, $Da_{off} > 1$), bound and unbound populations are predicted to overlap ($R_s < 0.5$), yielding a single riboswitch peak via native PAGE analysis. Our simulation results confirm this hypothesis. When association and dissociation rates are chosen so that riboswitch interconversion is rapid compared to assay timescales, simulation results show the appearance of a single mobility-shifted RNA peak (Figure 76). Thus, the mobility of this single peak corresponds to the population-average of bound riboswitches.[262,271]. In Figure 76, k_{on} is 4.55 $s^{-1}\mu M^{-1}$ and k_{off} is 0.455 s^{-1} or $\log(Da_{on}) = 2$ and $\log(Da_{off}) = 1$. This translates to $t_{binding}$ ~ 0.2 sec (with 1µM ligand), $t_{dissociation}$ ~ 2 sec, and $t_{separation}$ ~ 10 sec.

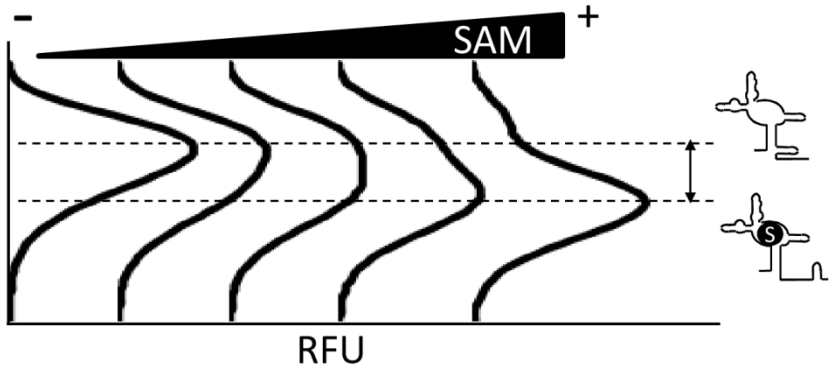

Figure 76. A single mobility-shifting peak is observed in simulations of rapidly interconverting riboswitch-ligand pairs.

Simulation results also confirm the ability to track peak mobility, which should represent the fraction of bound RNA, for increasing ligand concentration to extract K_d. Figure 77 shows that, for the same rapidly interconverting rate constants used in Figure 76 above, peak mobility at each ligand concentration can be plotted vs. ligand concentration to get a dose response curve. A 3-parameter curve fit of the form $y = \beta_1 \times [SAM]/(k_d+[SAM])+\beta_3$ can then be used to extract a K_d of 100 nM.

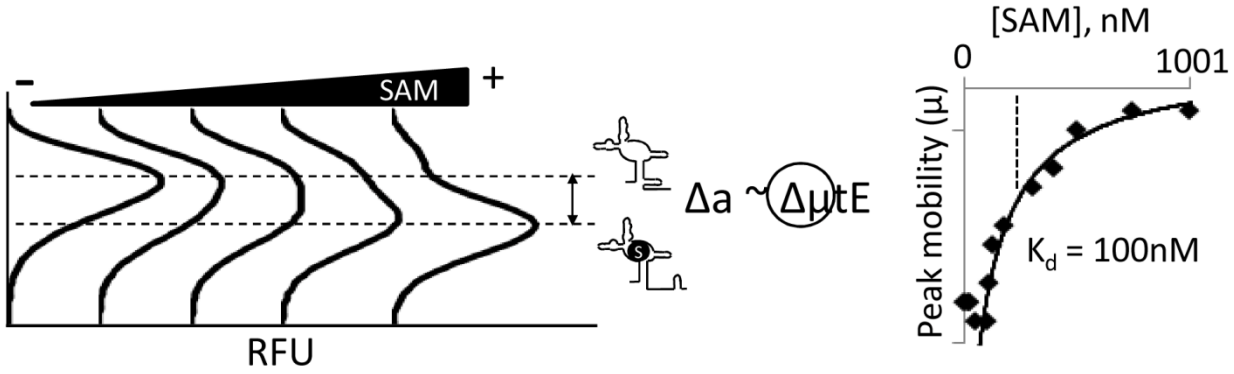

Figure 77. Mobility can be tracked as ligand concentration is increased to extract K_d for rapidly interconverting riboswitch pairs

In contrast, for association and dissociation timescales where binding occurs rapidly and dissociation is slow compared to the timescale of the assay, interconversion is negligible (e.g., $Da_{on} > 1$ and $Da_{off} < 1$).[262,271] In this regime, bound and unbound riboswitch peaks should be resolved during the separation and the fluorescent signal of the bound peak can be tracked for increasing ligand concentration. Our simulation results confirm this observation. When association and dissociation rates are chosen so that riboswitch interconversion is slow compared to assay timescales, and therefore assumed to be negligible, simulation results show the appearance of two resolved ($R_s > 0.5$) riboswitch bands representing bound and unbound riboswitches (Figure 78). The two populations are resolvable, as riboswitch-ligand association is rapid while dissociation is slow in this regime – meaning that bound species stay bound throughout the characteristic electrophoresis time.[262,271] In Figure 78, k_{on} is 2.22 $s^{-1}\mu M^{-1}$ and k_{off} is 2E-6 s^{-1} or $\log(Da_{on}) = 2$ and $\log(Da_{off}) = -4$. This translates to $t_{binding}$ ~ 0.5 sec (with 1μM ligand), $t_{dissociation}$ ~ 138 hours, and $t_{separation}$ ~ 10 sec.

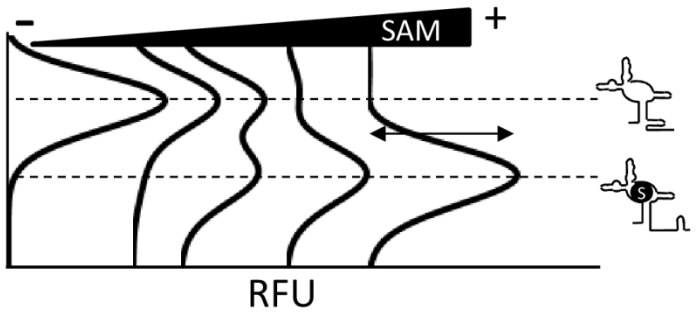

Figure 78. Two riboswitch peaks representing bound and unbound populations are observed in simulations of slowly interconverting riboswitch-ligand pairs.

Simulation results also confirm the ability to track the peak height of the bound riboswitch population, which represents the fraction of bound RNA, for increasing ligand concentration to extract K_d. Here, the fluorescent intensity of the bound peak increases as ligand concentration

increases until all RNA molecules in the system are in the bound state and the curve saturates. The same 3-parameter logistic binding equation can be used to extract K_d (Figure 79). In Figure 79, bound peak height is plotted vs. ligand concentration and a 3-parameter curve fit of the form $y = \beta_1 \times [SAM]/(k_d+[SAM])+\beta_3$ can then be used to extract a K_d of 60 nM. A similar method has been used to measure antibody-antigen K_d on-chip.[68]

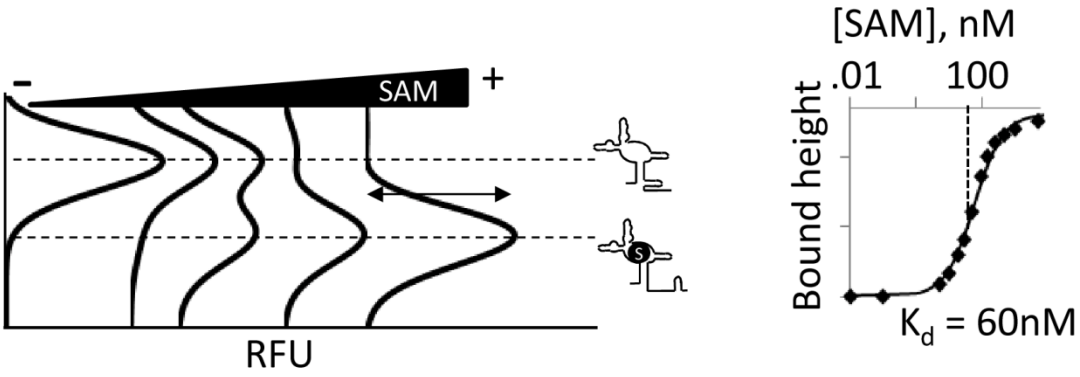

Figure 79. Peak height of the bound riboswitch population can be tracked as ligand concentration is increased to extract K_d for slowly interconverting riboswitch pairs

Riboswitch K_d therefore can be measured in a microfluidic format using these two methods for both slowly and rapidly interconverting riboswitch-ligand pairs. In the experiments described here, a threshold Rs value of 0.5 was chosen as a critical threshold for determining when riboswitch bands were resolved. Figure 75 confirms this threshold choice for the assay and analyte conditions measured here. Above R_s of 0.5, two peaks are observed and slow interconversion is apparent. Below R_s of 0.5, a single peak is observable and rapid interconversion is apparent.

With these transport and reaction considerations in mind, we describe development of µMSA for K_d determination of a rapidly interconverting riboswitch-ligand binding pair (a validated SAM-I riboswitch from *Bacillus subtilis*), then of a slowly interconverting pair (a putative SAM-I riboswitch from *Polaribacter irgensii*).

10.3 High Sensitivity Laser-Induced-Fluorescence Detection System

In addition to the importance of Da_{on} and Da_{off} in determining a method to measure K_d, analyte concentration must also be carefully chosen.

Again, for a bimolecular binding reaction, the equation is:

$$A + B \underset{K_{off}}{\overset{K_{on}}{\Longleftrightarrow}} AB$$

The total concentration of A ($[A]_T$) is split between free A and A taken up in the bound AB complex so that:

$$[A_T] = [A] + [AB] \quad \text{or} \quad [A] = [A_T] - [AB]$$

At equilibrium, the dissociation constant is:

$$K_d = \frac{k_{off}}{k_{on}} = \frac{[A][B]}{[AB]}$$

Rearranging this, we see that:

$$K_d[AB] = [A][B]$$

Substituting in for [A], we get the equation:

$$K_d[AB] = [A_T][B] - [AB][B]$$

Rearranging, we get:

$$[AB](K_D + [B]) = [A_T][B]$$

Or:

$$\frac{[AB]}{[A]_{TOTAL}} = \frac{[B]}{[B] + K_D}$$

Here, $[AB]/[A]_{TOTAL}$ represents the fraction of A that is bound. [B] is the concentration of free [B] in solution. Therefore, measuring K_D can be done by keeping the concentration of A in the reaction constant and varying the amount of B added. At each concentration of B, the concentrations of the AB complex and free B are measured.[3] In theory, any concentration of A can be used in this experiment. However, in practice, it is often difficult to measure free B. Since the total concentration of B in a reaction (easily known since it is the amount of ligand added), is equal to the sum of the concentrations of free and bound B, when $[A]_{TOTAL} << K_D$ at all concentrations of B that are added to the solution, the amount of B bound in the AB complex will be only a very small fraction of the total B. Therefore free [B] is approximately equal to $[B]_{TOTAL}$. Therefore, if $[A]_{TOTAL} << K_D$, the total concentration of B added to each reaction can be plotted on the x-axis instead of free [B] and the K_D can be determined using the equation above.[3]

In seeking to introduce a riboswitch functional screening assay optimized for measurement of K_d, we noted that, for K_d determination, the RNA concentration typically must be significantly less than the expected K_d value,[3] making analytical sensitivity an important design specification for this screening assay. To meet this specification, we combined sensitive laser induced fluorescence (LIF) detection with fast microfluidic PAGE separations.

A LIF microscopy set-up was designed, built and optimized to enable high sensitivity RNA detection. Laser excitation was selected over a mercury arc lamp the owing to the higher power of the laser which would enable additional sensitivity. The LIF system was built using a 25 LHP 991-249 HeNe laser (Melles Griot, Carlsbad, CA) and IX70 inverted epi-fluorescence microscope (Olympus, Center Valley, PA) (Figure 80). Helium-Neon (HeNe) lasers produce a beam at 633 nm wavelengths. The laser light was passed through a 15× beam expander (BE 15M, Thorlabs, Newton, NJ) before passing into the back of the epi-fluorescence microscope and through XF2022 dichroic and XF3030 emission filters (Omega Optical, Brattleboro, VT). The filter sets were chosen to not contain an excitation filter; thus allowing 100% of excitation signal to pass to the sample and 75% of Alexa Fluor 633 dye emission signal to be collected (Figure 81). The fluorescence signal from separating peaks was collected by a D-104 photomultiplier tube (Photon Technology International, Birmingham, NJ) and integrated with the computer with a SCB-68 shielded I/O connector block and DAQ device (National Instruments, Austin, TX). LabView (National Instruments) was used to collect voltage data. A clip-on goose neck lamp was used as brightfield illumination for chip alignment. Laser safety glasses effective at 633 nm were worn at all times while operating the LIF system.

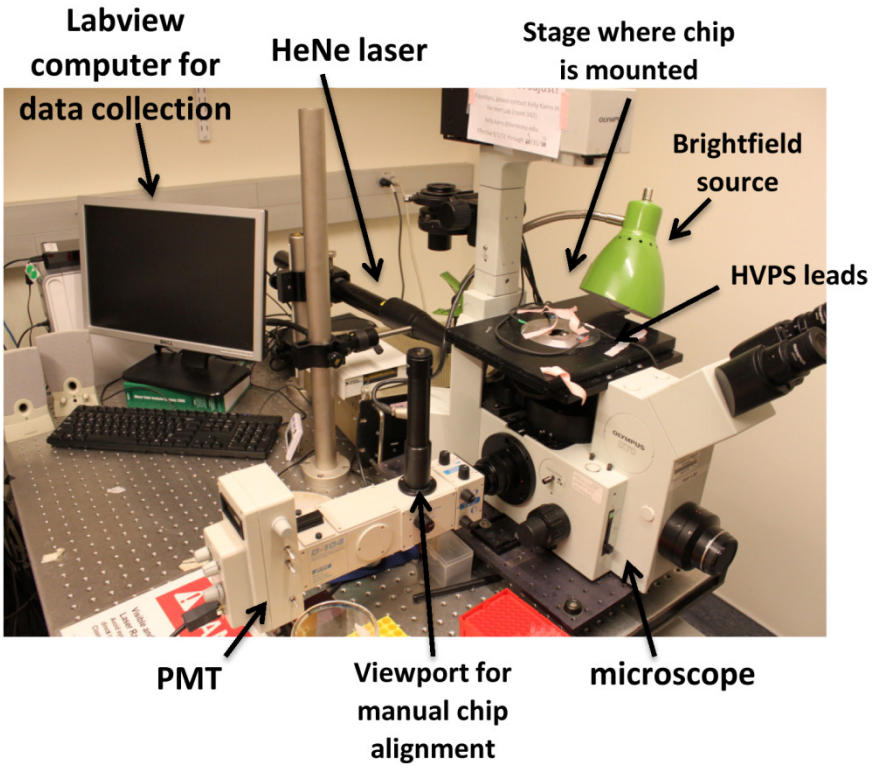

Figure 80. LIF set-up including inverted epi-fluorescence microscope, PMT detector, computer, brightfield source for chip alignment, and HeNe laser

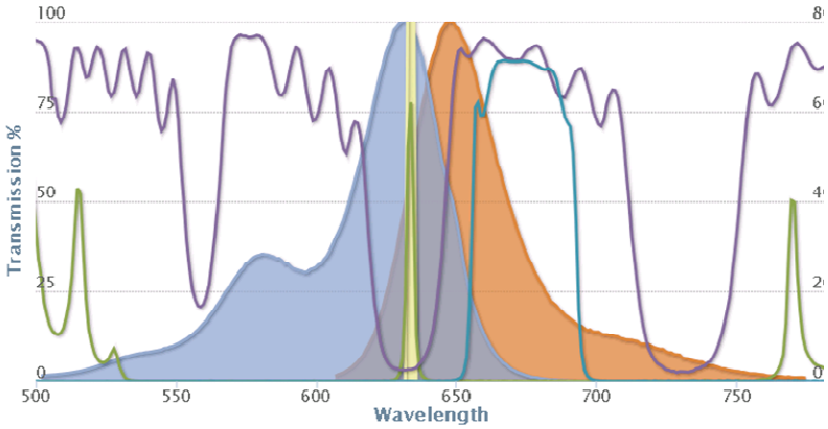

Figure 81. Filter Cube XF46 paired with AF633 dye allows detection of ~75% of emission signal and approximately 75% excitation with the excitation filter. Since we are using a filter cube without an excitation filter, we get 100% excitation. Blue shading represents excitation spectrum for AF633 dye, orange shading represents emission spectrum of AF633 dye, yellow band represents beam from HeNe laser, Purple line is dichroic and light blue line is emission filter. Light green line is for the excitation filter but is not present in the LIF system used in this work.[272]

Only AF633 labeled RNA can be used on the LIF system owing to the narrow excitation wavelength of the HeNe laser. To assess the sensitivity of the LIF system, we titrated the concentration of SAM-I Bs riboswitch and determined the lower limit of detection (LLOD) for a separation detected at 1 mm. μMSA lower limit of detection (LLOD) was 870 pM of RNA in 1 μL of sample detected using laser-induced-fluorescence (signal to noise ratio = 5.3, labeling efficiency of 0.45 AlexaFluor-633 dye molecules per RNA molecule, detection at 1 mm separation distance, 3-12%T PA gel). This translates to 391.5 attomol of fluorescently-labeled RNA. Since end-labeled RNA has a maximum theoretical labeling efficiency of 1, compared to up to ~20 for antibodies and other proteins, it is important to note that a LLOD of 870 pM for RNA with 0.45 dye molecules per RNA molecule means that some RNA molecules were not labeled. As a result, it is likely that the LLOD of the LIF system is much higher for proteins or antibodies with higher degrees of labeling.

To compare the LIF sensitivity to that used with slab gels, we used a laser-induced-fluorescence scanner to determine the LLOD for the slab gel format to be approximately 0.75 pmol for fluorescently labeled RNA (labeling efficiency of 0.75 fluorophore dye molecules per RNA molecule). Typical slab gel LLOD is 4.8 femtomol of radiolabeled RNA.[273] The μMSA platform thus yields a 1916-fold sensitivity improvement over a slab gel format for fluorescently labeled RNA and comparable sensitivity to radiolabeled RNA, which is commonly employed for in-line probing assays. Importantly, since μMSA LLOD is ~870 pM using LIF detection, it is likely that μMSA can be used to rapidly measure K_d values as low as 1 nM using fluorescence detection

and does not require modification of the riboswitch aptamer structure or the ligand, unlike 2AP fluorescence or FRET experiments.[274-276]

10.4 Materials and Methods

Microfluidic Kd measurements

All microfluidic K_d measurements were performed using the inverted laser-induced fluorescence (LIF) microscope. PA gel-containing glass chips were seated on the LIF microscope stage and pipette tips were fitted into the reservoir access holes to augment sample wells. Sample and buffer were pipetted on-chip and the assay was run as before. All microfluidic K_d measurements were collected at 1 mm separation distance on 3-12%T separation gels. SAM-I Bs riboswitch K_d was measured in TBM1 buffer (90 mM Tris, 89 mM Boric acid, 1 mM $MgCl_2$, pH 8.5) using 1 nM Alexa Fluor 633-labeled SAM-I Bs RNA, 6.3 nM PB, and varying SAM ligand concentrations. SAM-I Bs riboswitch K_d was measured in TBM10 buffer (90 mM Tris, 89 mM Boric acid, 10 mM $MgCl_2$, pH 8.5) using 870 pM Alexa Fluor 633-labeled SAM-I Bs RNA, BSA, 22.4 nM α-lact, and varying SAM ligand concentrations. SAM-I Pi riboswitch K_d was measured in TBM10 buffer (90 mM Tris, 89 mM Boric acid, 10 mM $MgCl_2$, pH 8.5) using 970 pM Alexa Fluor 633-labeled SAM-I Pi RNA (51% degree of labeling), phosphorylase B as an internal standard, and varying SAM ligand concentrations. In non-K_d measuring experiments, the inverted epi-fluorescent IX70 microscope was used and FITC-labeled SAM-I Bs RNA was used at 12 nM and 158 nM Alexa fluor 488-labeled BSA was used as an internal standard (Figure 82). In the SAM-I Pi mobility shifting experiments, 374 nM FITC-labeled SAM-I Pi riboswitch was used with 400 nM Alexa Fluor 488-labeled TI and 424 nM Alexa Fluor 488-labeled PB as internal standards (Figure 88A).

Imaging and Data Analysis

The separation resolution (R_s) metric reports the ability to resolve riboswitch populations using PAGE. When $R_s < 0.5$ and two peaks were expected owing to the presence of ligand, peaks were deemed un-resolved and rapid interconversion was assumed. Relative RNA mobility was used for the calculation of K_d for rapidly interconverting riboswitch-ligand pairs as derived above by fitting a 3-parameter logistic fit binding equation of the form $y = \beta_1 \times [SAM]/(K_d+[SAM])+\beta_3$ to a relative mobility (μ_{rel}) dose response curve. Relative RNA mobility was calculated as the difference in RNA and internal standard mobility at each ligand concentration tested. Electropherograms of fluorescent intensity over time were created 1 mm downstream of the injection junction using ImageJ and a Gaussian peak was fitted using OriginPro 8.5 in order to measure the time for the center of each peak to reach 1 mm. For rapidly interconverting riboswitch ligand pairs in TBM1 buffer, relative mobility = $\Delta\mu = (x/E)/(t_{RNA} - t_{IS})$ where IS is phosphorylase B internal standard, x is 1 mm separation distance, E is the measured applied E-field, and t is the measured time for the center of each band to travel 1 mm. In TBM10 buffer, relative mobility = maximum $\Delta\mu$ - $(x/E)/(t_{RNA} - t_{IS})$ where IS is BSA internal standard. Because BSA travels faster than SAM-I Bs RNA, $\Delta\mu$ was subtracted from the maximum $\Delta\mu$ in order to see an increasing trend similar to that of TBM1 buffer. Fitted variables for the SAM-I Bs riboswitch were β_1 = 5.9161E-6, β_3 = 34934E-6, K_d = 25.3 nM in TBM1 buffer

and β_1 = 4.3337E-6, β_3 = 1.9674E-6, K_d = 3.14123 nM in TBM10 buffer. Fitted variables for the SAM-I Pi riboswitch were β_1 = 0.18408 $\pm$ 0.02589, β_3 = 0.0735 $\pm$ 0.01447, K_d = 1.0 $\pm$ 0.2 nM in TBM10 buffer.

When R_s > 0.5, peaks were deemed resolved and slow interconversion was assumed. Peak height was used for the calculation of K_d for slowly interconverting riboswitch-ligand pairs as described above. Riboswitch K_d was calculated by fitting a 3-parameter logistic fit binding equation to the bound peak height dose response curve. Peak height measurements were extracted with a nonlinear Gaussian peak fitting algorithm (GaussAmp) using OriginPro 8.5 (OriginLab, Northampton, MA). Peak height was used to quantify the detectable signal from the bound Pi riboswitch peak. Peak height is often used as a proxy for bound peak area in the creation of dose response curves for antibody-antigen binding pairs.[277,278] Since separated RNA peaks are represented by a Gaussian curve owing to diffusive dispersion, the equation for a Gaussian curve is:

$$f(x) = he^{\frac{-(x-b)^2}{2\sigma^2}}$$

where h is peak height, b is the position of the peak center, and σ is peak variance. The total concentration is therefore the area under the Gaussian curve, or the integral of f(x). This is equal to:

$$concentration = h\sigma\sqrt{2\pi}$$

Therefore, assuming that the peak width (σ) does not change appreciably between runs, the concentration is proportional to peak height, h. This is a valid assumption because the peaks are analyzed at the same separation time in creating the dose response curve and therefore have experienced approximately equal diffusive dispersion (since diffusion scales with $\sqrt{time}$).

We used bound peak height in the computational model (Figure 79) to demonstrate our ability to extract K_d for slowly interconverting riboswitches. To maintain consistency and also because of the reasons outlined in the proof above, we also used peak height for the experimental data to extract K_d for Pi SAM-I riboswitch.

Analysis of RNA-ligand binding affinity using in-line probing assays

Ligand binding analysis was performed following standard in-line probing procedures as described by Regulski, et al.[236] Modifications were made to the buffer conditions to match the conditions used for native PAGE. Briefly, 5'-^{32}P radiolabeled RNAs were incubated in TBM10 or TBM1 buffer with 0-5 μM of SAM ligand for the *B. subtilis* SAM-I riboswitch or 0-500 nM of SAM ligand for the *P. irgensii* SAM-I riboswitch. After 43 h at room temperature, the reaction samples were loaded onto a 10% urea-PAGE gel made with TBE buffer (90 mM Tris, 90 mM Boric acid, 1 mM EDTA, pH 8.3) and the gel was run at constant 40 W for 2-3 h at room

temperature. After drying at 80 °C for 2 h, the gel was scanned using the Typhoon laser-scanning system (GE Healthcare) on the phosphorimager setting.

To determine K_D, sites were identified whose pattern of spontaneous cleavage changed upon ligand binding. For each of these sites of modulation, the signal intensity was normalized to the observed value at the highest ligand concentration. The fraction of RNA cleaved at each ligand concentration, which corresponds to the fraction of unbound RNA, was taken as the average of the data analyzed for several sites of modulation. The dissociation constant was determined by fitting the experimental data to a best-fit curve for a 1:1 RNA-ligand complex.

10.5 Quantitative Analysis of Rapidly Interconverting Riboswitch States: A Validated SAM-I Riboswitch from *Bacillus subtilis* (Bs)

To demonstrate our ability to use the microfluidic assay to measure K_d for rapidly interconverting riboswitches, we studied the mobility shift of and assessed the K_d for a previously confirmed 124 yitJ SAM-I riboswitch aptamer isolated from B. subtilis (Bs) that rapidly interconverts between bound and free states.[261] The mobility shift of the single peak was measured for increasing concentrations of SAM ligand with both μMSA and slab gel mobility shift formats. At a ligand:riboswitch ratio of 0.69, the microfluidic mobility shift assay detected a single peak with a mobility that was 30% of the maximum mobility when binding is saturated (Figure 82). At the same ligand:riboswitch ratio, a slab gel mobility shift assay reported a single Bs SAM-I riboswitch band with a mobility that was equal to the mobility in saturating ligand conditions (Figure 83). Consistent with our model for rapidly interconverting binding pairs, a single band was observed in both formats; however, the favorable scaling relationships of microfluidic formats and inclusion of internal standard peaks enable detection of smaller differences in peak mobility on μMSA compared to slab gels. Unlike the slab gel, μMSA's ability to resolve intermediate peak mobilities suggests the microfluidic assay is capable of determining riboswitch-ligand equilibrium dissociation constant (K_d). This lack of resolving power on a slab gel format also was observed for native PAGE analysis of the SAM-II riboswitch at intermediate ligand concentrations.[243]

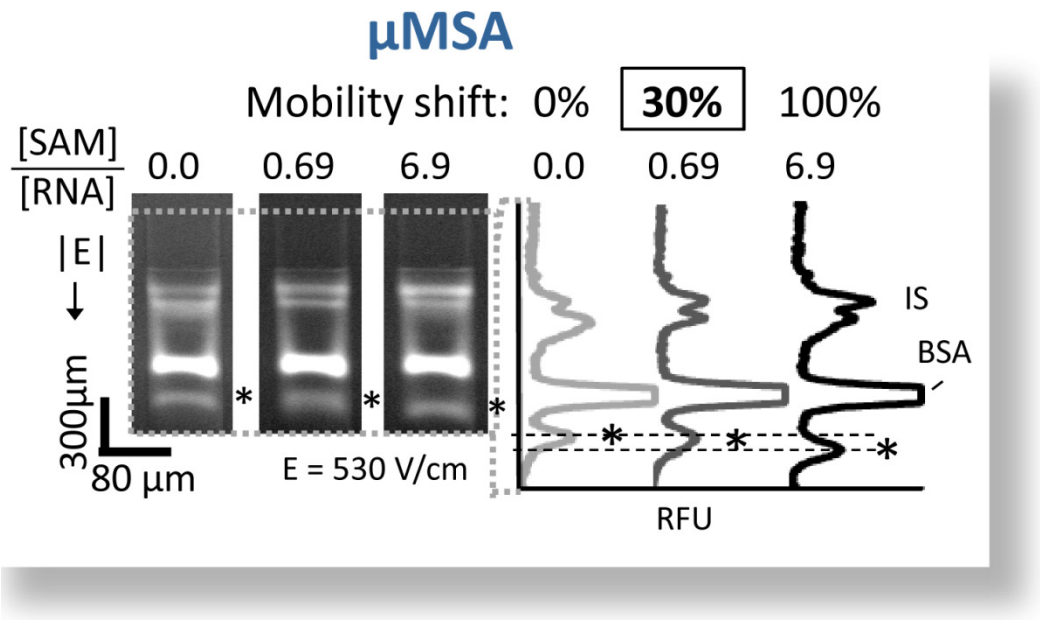

Figure 82. The microfluidic assay resolves a single mobility-shifted riboswitch peak in response to increasing ligand concentration. At a ligand:RNA ratio of 0.69, µMSA detects the SAM-I Bs riboswitch band at 30% of maximum mobility. BSA , TI and IS are internal standard peaks. '' corresponds to the SAM-I Bs riboswitch band. Dashed lines correspond to minimally (0%) and maximally (100%) shifted RNA peak locations. 1× TB + 10 mM Mg^{2+} in gel and run buffers. RNA is labeled with AF488*

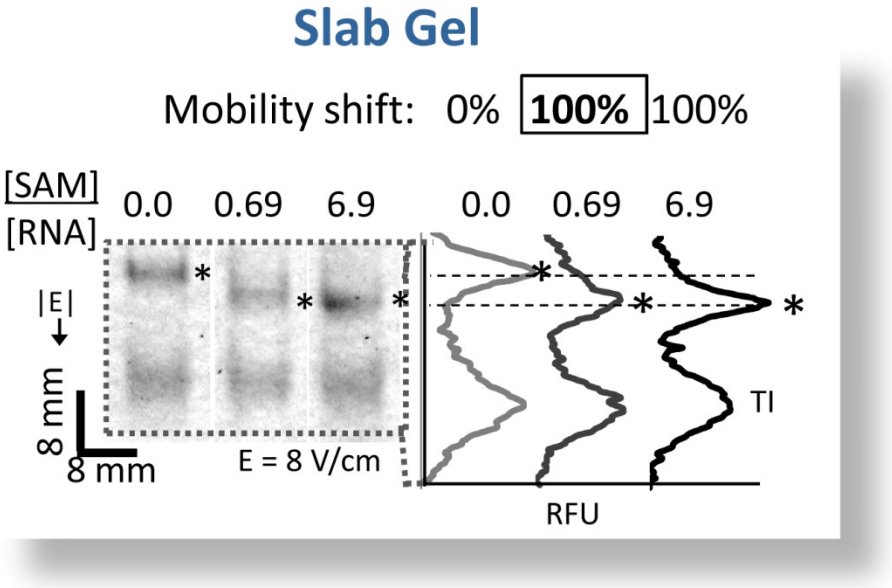

Figure 83. A slab gel mobility shift assay cannot resolve a single mobility-shifted riboswitch peak in response to increasing ligand concentration. At a ligand:RNA ratio of 0.69, μMSA detects a fully shifted SAM-I Bs riboswitch band instead of a band that is proportaional to the percent bound. BSA , TI and IS are internal standard peaks. '' corresponds to the SAM-I Bs riboswitch band. Dashed lines correspond to minimally (0%) and maximally (100%) shifted RNA peak locations. 1× TB + 10 mM Mg^{2+} in gel and run buffers. RNA is labeled with FITC*

We next determined K_d for the *Bs* SAM-I riboswitch using μMSA and compared our results against those from a conventional in-line probing assay. To extract K_d for this rapidly interconverting riboswitch-ligand pair, we plotted the relative riboswitch peak mobility (normalized to an internal standard) against different SAM ligand concentrations to generate a dose response curve. In this regime the band mobility represents the fraction of bound RNA to total RNA.[271] μMSA-determined K_d values were 25.226 ± 0.004 nM in tris-borate (TB) buffer with 1 mM Mg^{2+} (TBM1 buffer) (n = 4) (Figure 84) and 3.14123 ± 0.00005 nM in TB buffer with 10 mM Mg^{2+} (TBM10 buffer) (n = 4) (Figure 85). Both μMSA values agree well with results from the in-line probing assays performed using identical buffer conditions: 25 nM K_d and 3 nM K_d, respectively (Figure 86 and Figure 87). The observed improvement in ligand binding affinity at 10 mM Mg^{2+} is consistent with biophysical studies that have shown Mg^{2+} facilitates folding of the SAM-I and other riboswitches.[243,279,280]

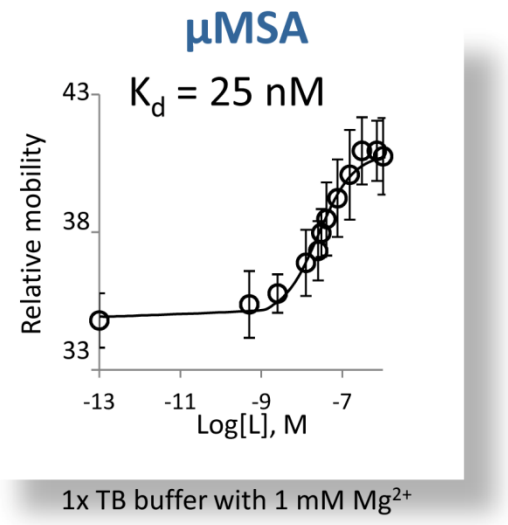

Figure 84. µMSA K_d measurement for rapidly interconverting riboswitch in TBM1 buffer. Riboswitch mobility can be used to extract K_d values that are equivalent to those measured by traditional in-line probing assays. TB buffer + 1 mM Mg^{2+}. On-chip RNA mobility values (relative to internal standard) are given as × 10^{-5} cm^2/Vs. Solid traces are best-fit curves at the K_d shown. Error bars are standard deviation of quadruplicate runs.

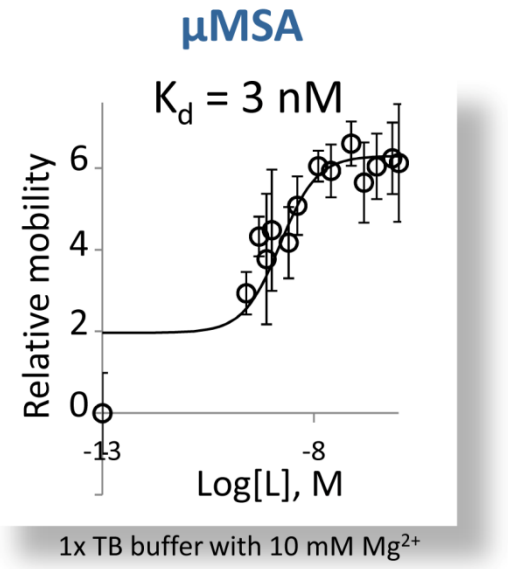

Figure 85. µMSA K_d measurement for rapidly interconverting riboswitch in TBM10 buffer. Riboswitch mobility can be used to extract K_d values that are equivalent to those measured by traditional in-line probing assays. TB buffer + 10 mM Mg^{2+}. On-chip RNA mobility values (relative to internal standard) are given as × 10^{-6} cm^2/Vs. Solid traces are best-fit curves at the K_d shown. Error bars are standard deviation of quadruplicate runs.

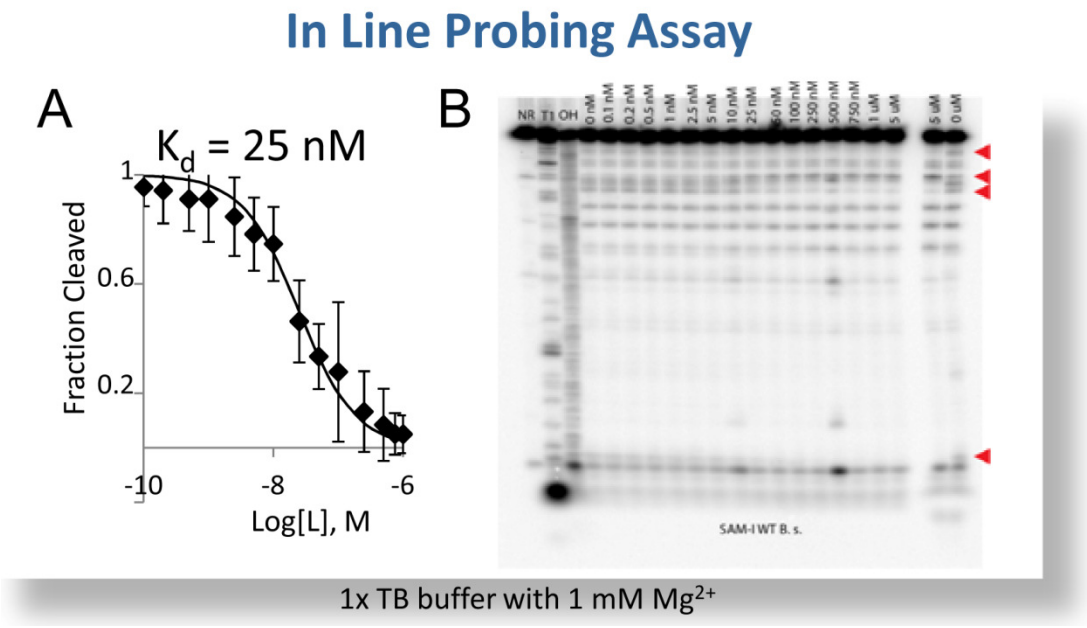

*Figure 86. In-line probing assays confirm on-chip K_d measurements for rapidly interconverting riboswitch-ligand pairs in TBM1 buffer. (**A**) Dose response curve from slab gel results for the SAM-I Bs riboswitch aptamer with TB buffer + 1 mM Mg^{2+}. Solid trace is best-fit curve at the K_d shown. Error bars for in-line probing assay is the standard deviation of values for the sites of modulation analyzed from a single slab gel. (**B**) Phosphorimager scan of in-line probing gel for Bs SAM-I riboswitch in 1x TB buffer with 1 mM Mg^{2+} shows the pattern of spontaneous cleavage. Sites of modulation that were analyzed are marked as red triangles. NR = no reaction, T1 = partial digest with RNase T1, -OH = partial digest with alkali. Control samples using standard in-line buffer (50 mM Tris-HCl, 20 mM $MgCl_2$, 100 mM KCl, pH 8.3) show the same modulation pattern.*

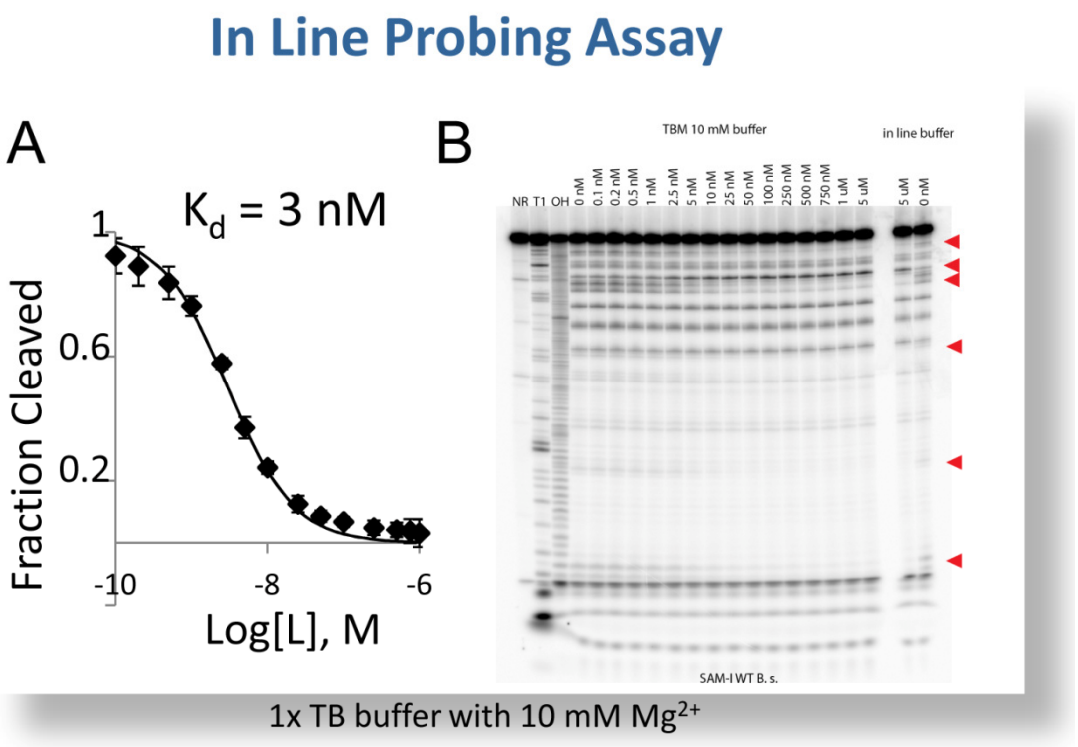

*Figure 87. In-line probing assays confirm on-chip K_d measurements for rapidly interconverting riboswitch-ligand pairs in TBM10 buffer. (**A**) Dose response curve from slab gel results for the SAM-I Bs riboswitch aptamer with TB buffer + 10 mM Mg^{2+}. Solid trace is best-fit curve at the K_d shown. Error bars for in-line probing assay is the standard deviation of values for the sites of modulation analyzed from a single slab gel. (**B**) Phosphorimager scan of in-line probing gel for Bs SAM-I riboswitch in 1x TB buffer with 10 mM Mg^{2+} shows the pattern of spontaneous cleavage. Sites of modulation that were analyzed are marked as red triangles. NR = no reaction, T1 = partial digest with RNase T1, -OH = partial digest with alkali. Control samples using standard in-line buffer (50 mM Tris-HCl, 20 mM $MgCl_2$, 100 mM KCl, pH 8.3) show the same modulation pattern.*

10.6 Quantitative Analysis of Slowly Interconverting Riboswitch States: A Putative SAM-I Riboswitch from Polaribacter irgensii (Pi)

To validate the model and demonstrate our ability to use the microfluidic assay to measure K_d for a riboswitch that slowly interconverts between bound and free states, we studied the mobility shift of a putative SAM-I riboswitch isolated from *Polaribacter irgensii* (Pi). Using µMSA, we monitored the band pattern of Pi for increasing concentrations of SAM ligand. Following a similar work flow as the microfluidic mobility shift assay, riboswitch and increasing concentrations of ligand were incubated off chip for 1 hour, pipetted into the sample well, electrophoretically loaded, injected, and separated. Figure 88 shows two Pi riboswitch peaks

are resolved at ligand:riboswitch ratios of less than 1 in both on-chip (R_s = 0.66) and slab gel formats (R_s = 0.16). For ligand:riboswitch ratios of less than 1, riboswitch molecules are present in excess over ligand molecules and two riboswitch populations are present: bound and unbound riboswitches (assuming a riboswitch-ligand binding ratio of 1:1). Resolution of two peaks at ligand:riboswitch ratios of less than 1 demonstrate that negligible interconversion is occurring between Pi and SAM ligand during the timescales of the microfluidic and slab gel separations; bound and unbound riboswitch populations are resolved in both cases. Consistent with our model for slowly interconverting binding pairs, two bands were observed in both formats. The lower Da_{on} and Da_{off} of the microfluidic format likely contribute to the higher observed R_s on the microfluidic format (4× increase).

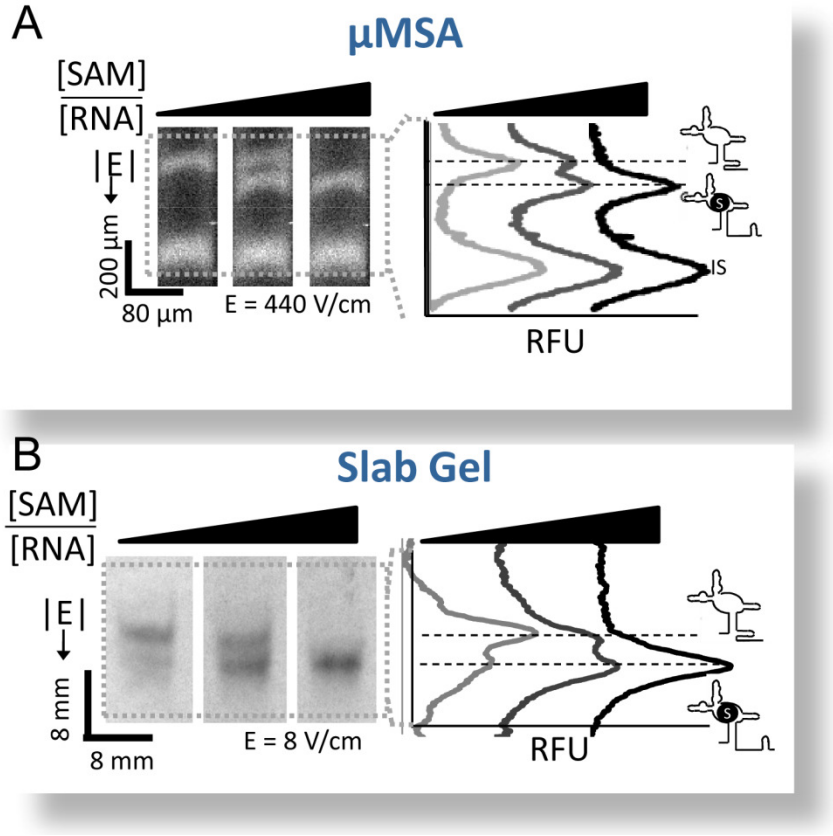

*Figure 88. Both µMSA **(A)** and slab gel **(B)** mobility shift formats resolve two peaks representing bound and unbound populations of slowly interconverting riboswitches. The amount of the bound form of the SAM-I Pi riboswitch increases as SAM concentration increases. Phosphorylase B internal standard (IS) peak is at 1.6 mm separation distance on-chip. 1× TB + 10 mM Mg^{2+} in gel and run buffers.*

We next determined K_d for the *Pi* SAM-I riboswitch using µMSA and compared our results against those from a conventional in-line probing assay. To extract K_d for this slowly interconverting riboswitch-ligand pair, we plotted the peak height of the bound riboswitch

population against different SAM ligand concentrations to generate a dose response curve. In this system, the ligand-bound riboswitch population increases with ligand concentration until all RNA molecules are in the bound state, as predicted. We used the μMSA to generate a dose-response curve then fit that experimental data with a 3-parameter logistic model to yield K_d. Figure 89 shows a dose response curve of bound riboswitch peak height (normalized to the internal standard peak to account for loading variability) at different SAM ligand concentrations. With this approach, the K_d of Pi was measured as 1 ± 0.2 nM using μMSA (n = 4) which is comparable to the 3 nM value measured using a conventional in-line probing assay (Figure 90). Deviation between the two methods may arise from the steep response curve slope. Figure 91 shows the sequence and secondary structure of the putative SAM-I *Pi* riboswitch derived from the in-line probing assay. Previous to these experiments, the Pi riboswitch had not been validated and the structure was not known.

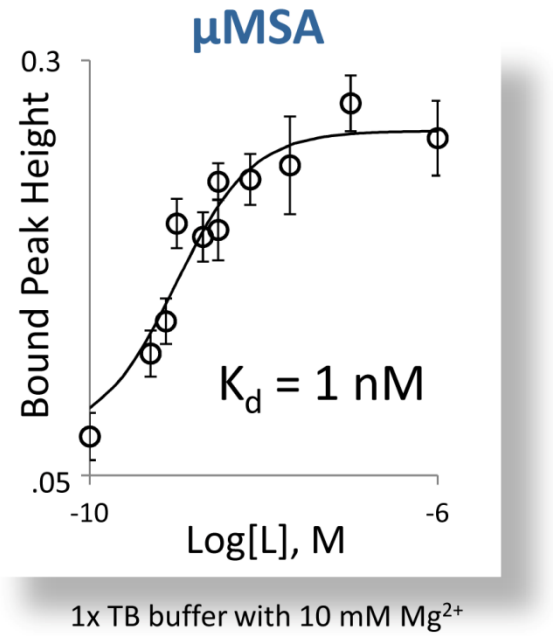

Figure 89. Bound riboswitch peak height measured with μMSA can be used to extract K_d values for slowly interconverting riboswitches (Pi) that are equivalent to those measured by traditional in-line probing assays. On-chip error bars represent the standard deviation of quadruplicate runs. 0 nM SAM sample was plotted at 0.1 nM to allow for logarithmic axis. 1× TB + 10 mM Mg^{2+} in gel and run buffers.

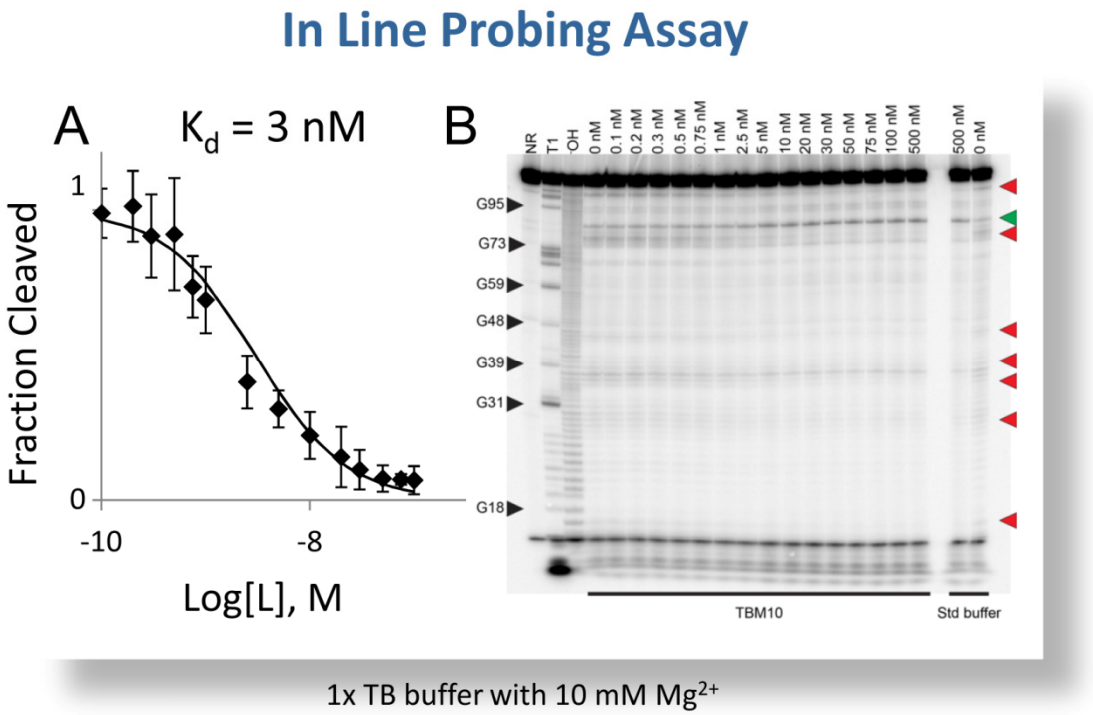

*Figure 90. In-line probing assays confirm on-chip K_d measurements for slowly interconverting riboswitch-ligand pairs in TBM10 buffer. (A) Dose response curve from slab gel results for the SAM-I Pi riboswitch aptamer with TB buffer + 10 mM Mg^{2+}. Solid trace is best-fit curve at the K_d shown. Error bars for in-line probing assay are the standard deviation of values for the sites of modulation analyzed from a single slab gel. 1× TB + 10 mM Mg^{2+} in gel and run buffers. (**B**) Phosphorimager scan of in-line probing gel for Pi SAM-I riboswitch in 1x TB buffer with 10 mM Mg^{2+} shows the pattern of spontaneous cleavage. Sites of modulation that were analyzed are marked as red triangles (increased scission). NR = no reaction, T1 = partial digest with RNase T1, -OH = partial digest with alkali. Control samples using standard in-line buffer (50 mM Tris-HCl, 20 mM $MgCl_2$, 100 mM KCl, pH 8.3) show the same modulation pattern.*

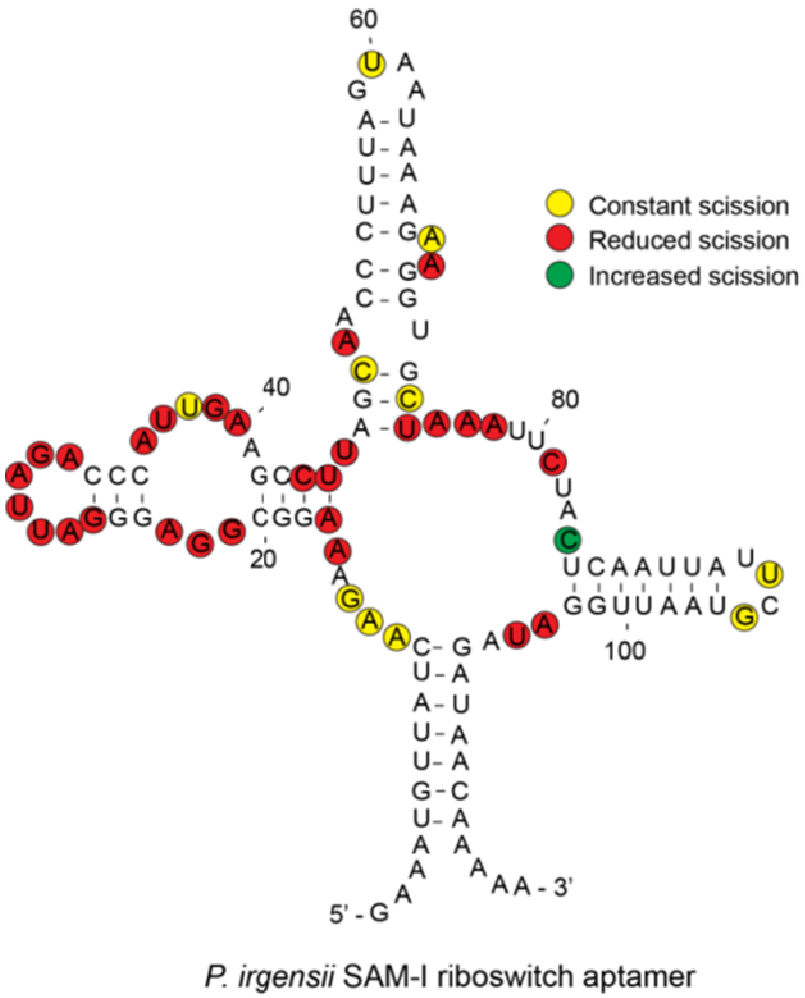

Figure 91. Sequence and secondary structure model for P. irgensii SAM-I mapped with the in-line probing pattern.

10.7 Benefits and Assay Characterization

To investigate the time savings achieved by measuring riboswitch K_d using a microfluidic format, we compared the time-to-results using the on-chip method with that for an in-line probing assay. Following a 1 hour sample incubation, riboswitch K_d measurement using μMSA required 52 minutes to run 12 samples on-chip in quadruplicate. This analysis time includes 12.3 sec runs, 30 sec loading times for each run, and 2 min channel washes between each sample. Meanwhile the in-line method required a 40 hour sample incubation, followed by a 2-4 hour denaturing PAGE slab gel run and an additional two hours to dry the gel, and several hours to overnight and image the gel using a phosphorimager cassette. Thus, as is critical to an efficient mobility shift screening platform, measurement of riboswitch-ligand K_d for one riboswitch-ligand pair required 1.87 hours for μMSA versus 44+ hours using the in-line probing assay. Use of μMSA resulted in (at a minimum) a 24-fold reduction in the time-to-results.

The short μMSA analysis times mitigate diffusive band broadening found in long-duration slab gel native PAGE[262] and enable resolution of smaller differences in peak mobility as detailed in Chapter 9.4. Quantifying the amount of material in each conformational state should thus benefit from native PAGE in microfluidic formats. Importantly, the microfluidic format does not require radiolabeling or internal chemical modification of the riboswitch which has the potential to alter apparent k_d. Riboswitch functionality is preserved, making it possible to collect the sample after analysis for subsequent testing.

10.8 Implications for Understanding the Kinetic or Thermodynamic Control of Riboswitch Genetic Regulation

Several riboswitches have been shown to be kinetically rather than thermodynamically driven[229,281] and an understanding of association and dissociation binding timescales can be important to understand the physiological function of a riboswitch-ligand pair. For kinetically driven riboswitches, information on k_{on} and k_{off} rates, rather than the equilibrium dissociation constant (k_d), is important because the concentration of metabolite required to trigger riboswitch function is based on the kinetics of ligand binding and the speed of RNA transcription, rather than equilibrium binding affinity. Armed with knowledge of typical intracellular concentrations of the target ligand, slab gel and on-chip mobility shift assays can reveal information on whether a given riboswitch is thermodynamically or kinetically controlled.

A characteristic of kinetic control of riboswitch function is that the time to equilibrium binding (t_{eq}) is greater than the time Δt_{RNAP} between completion of aptamer transcription by RNA polymerase and its progression to the termination decision point.[270] Thermodynamic control is defined when $t_{eq} < \Delta t_{RNAP.}$[270] Equilibrium times can be calculated with knowledge of k_{on}, k_{off}, and the intracellular ligand concentration. Δt_{RNAP} is dependent on intracellular ligand concentration as well as the speed at which RNA polymerase synthesizes the mRNA. This speed is dependent on the concentration of nucleotide triphosphates, Mg^{2+} ions, and any pertinent transcription factor(s),[281] as well as the sequence of the DNA template which can include pause sites that retard transcription. With the ability to differentiate between rapidly and slowly interconverting regimes on-chip and on slab gel formats, we can utilize the different assay timescales (seconds for on-chip and hours for slab gel formats) to pull out information on k_{on} and k_{off} values, depending on which regime is observed. As a result, both formats yield information on riboswitch equilibrium time.

Utilizing our knowledge of the timescales of the slab gel and on-chip assays, we can determine that a SAM-I riboswitch is thermodynamically controlled if a single peak is observed on a slab gel or on-chip format (e.g., Bs SAM-I riboswitch studied here). Noting the timescale of separation on-chip is 10.5 sec, if a single peak is observed on-chip with 1 μM SAM concentration, then $k_{off} > 0.095$/sec ($Da_{off} > 1$). Since the on-chip measured *Bs* SAM-I riboswitch k_d is 4 nM and the typical concentration of SAM in a cell is 180 μM,[282] we therefore can deduce that the association timescale is < 14.6 sec, dissociation timescale is < 10.5 sec, and the resulting equilibrium timescale is < 6.12 sec. Since typical RNA polymerase elongation times are

on the order of 10s of seconds (e.g., FMN riboswitch[229]), $t_{eq} < \Delta t_{RNAP}$ and the Bs SAM-I riboswitch is likely controlled thermodynamically, depending on the timescale of transcription. If we observe a single peak on a slab gel (e.g., *Bs* SAM-I riboswitch studied here), we can determine more definitively that the SAM-I riboswitch is thermodynamically controlled. Noting the timescale of separation on a slab gel is 17 hours, if a single peak is observed on a slab gel which utilizes 1 µM SAM assay concentrations, $k_{off} > 1.64E\text{-}5$/sec. Since the slab gel-measured Bs SAM-I riboswitch k_d is 3 nM and the typical concentration of SAM in a cell is 180 µM,[282] we therefore can deduce that the association timescale is < 1 sec, dissociation timescale is < 17 hours, equilibrium timescale is < 1 sec, and $t_{eq} < \Delta t_{RNAP}$. The Bs SAM-I riboswitch is likely controlled thermodynamically.

If we observe two peaks on a slab gel or on-chip format (e.g., *Pi* SAM-I riboswitch studied here), we can determine ranges for k_{on}, k_{off}, and t_{eq} values. An observation of two resolved Pi SAM-I riboswitch peaks on-chip indicates that association timescales are > 0.48 msec, dissociation timescales are > 10.5 sec, and equilibrium timescales are > 0.48 msec. Two resolved Pi SAM-I riboswitch peaks on a slab gel indicate association timescales of > 980 msec, dissociation timescales of > 43.4 hours, and equilibrium timescales of > 1.02 sec. Depending on the timescale of transcription and folding, the Pi SAM-I riboswitch may be either thermodynamically or kinetically controlled. Because the dissociation rate for the metabolite-RNA complex is so slow (> 43.4 hours), SAM binding to the Pi riboswitch essentially commits the mRNA to transcription termination. In the case of kinetically controlled riboswitches, equilibrium is not reached before the regulatory decision is made and therefore, the k_{on} and k_{off} rates are more important for understanding riboswitch function than the k_d.[229] Kinetically driven riboswitches are triggered only when ligand concentration in the cell is substantially higher than the k_d value determined by their aptamer domains.[229]

10.9 Effect of Mg^{2+} Concentration on SAM-I Bs Riboswitch K_d

In an effort to demonstrate the screening capabilities of the microfluidic assay and more precisely elucidate the effect of Mg^{2+} concentration on riboswitch-ligand binding affinity, we utilized the microfluidic K_d measurement assay to screen Mg^{2+} concentrations and note the effect on SAM-I Bs riboswitch K_d. Mg^{2+} has been shown to improve riboswitch stability and facilitate riboswitch-ligand binding as evidenced by increased observed mobility of folded *Tetrahymena* ribozyme RNA.[269] We measured the Bs SAM-I riboswitch K_d to be 3 nM in 10 mM Mg^{2+} and 25 nM in 1 mM Mg^{2+} (Figure 84 and Figure 85). This ~8x lower measured K_d in 10 mM Mg^{2+} confirms that Mg^{2+} is important to facilitate riboswitch ligand binding.[267] This has been confirmed for the guanine riboswitch.[283]

10.10 Conclusions and Implications to Riboswitch Research

In Chapters 8, 9 and 10, we present microfluidic screening technologies that dramatically improve upon conventional analytical methods to enable streamlined validation of new riboswitch candidates, efficiently characterize riboswitch-ligand dissociation constants (K_d), and facilitate rapid screening of possible ligand pairs and environmental conditions. Namely, we

introduce a rapid microfluidic mobility shift assay (μMSA) which improves upon the conventional slab gel mobility shift assay by demonstrating ligand binding & riboswitch conformational change in 3 minutes. The format offers enhanced resolution of conformational change compared to slab gel formats, quantitation and repeatability for statistical assessment of small mobility shifts, low reagent consumption, and riboswitch characterization without modification of the aptamer structure. We use μMSA to screen five putative SAM-I riboswitches isolated from thermophilic and cryophilic bacteria and validate their functionality in rapid, protein-free binding assays.

Combined with LIF, the rapid assay yields high signal to noise ratios (> 3) even for picomolar RNA concentrations. The demonstrated rapid assay times, high sensitivity detection, and precise quantitative capabilities of μMSA enable screening of the mobility resolution required to measure K_d for both slowly and rapidly interconverting riboswitch-ligand pairs. This microfluidic K_d measurement assay replaces the need to use in-line assays to make K_d measurements of riboswitch-ligand binding pairs. We measure a 9 nM K_d of the previously uncharacterized SAM-I riboswitch isolated from *Polaribacter irgensii* using both on-chip and in-line assays. Finally, we demonstrate the ability of these microfluidic assays to rapidly screen environmental conditions by using the microfluidic K_d measurement assay to assess the impact of Mg^{2+} concentration on SAM-I Bs riboswitch-ligand affinity.

Taken together, the μMSA format introduced here has wide-ranging potential to alleviate some of the most pressing bottle-necks in riboswitch research. Taking advantage of the device functionality demonstrated here, future work may include: facilitating the identification of ligand pairs for the over 24 candidate or orphan riboswitch classes for which no ligand has been discovered to date,[245] enabling researchers to screen conditions (e.g., buffer composition, ligand libraries) to determine optimal conditions for riboswitch-ligand binding and selection, and opening the possibility of screening riboswitch libraries for selection and validation of novel riboswitches. More efficient measurement of riboswitch-ligand K_d may also facilitate characterization of the binding affinity of newly discovered riboswitches and riboswitch classes,[268] comparison of the binding strength of engineered ligand-riboswitch pairs to native counterparts, and insight into the concentrations of ligand needed in the cell to induce genetic regulation for thermodynamically controlled riboswitches. These tools may also enable the identification of orthogonal RNA-ligand pairs (synthetic ligands that bind with known natural riboswitches or vice versa) with broad applications in antibiotic development,[252] RNA-tagging *in vivo*, new genetic regulation control,[250] and for use as biosensors for metabolite sensing *in vivo*.[251]

Chapter 11: Conclusions and Future Directions

Binding interactions underpin all biological processes. As a result, understanding binding interactions has implications in the development of novel diagnostics as well as advancing our understanding of biological processes and the molecular mechanisms of human disease.

Electrophoresis is a workhorse technology that is prevalent in many biological laboratories and is used to separate complex samples into more simplified fractions. The technique is used throughout studies of molecular binding interactions. Microfluidic assays have emerged as powerful tools that can be used to study and detect binding interactions between many of the major classes of biological macromolecules. Performing electrophoresis on the microscale enables the application of higher electric fields which in turn speeds up separations and enables increased resolution of analyte fractions.

In particular, microfluidic immunoassays can be used to study binding interactions between proteins. Immunoassays can also be used to study molecular binding affinity and to measure affinity constants. Both heterogeneous and homogeneous microfluidic immunoassays can be used as sensors. By harnessing the specificity of antibody-ligand binding reactions, electrophoretic immunoassays can also be used to probe for disease specific protein biomarkers.

In this work, we developed and presented a first-in-kind microfluidic homogeneous immunoassay that is able to probe for protein biomarkers in human tear fluid. In the process, we overcame the challenges of working with tear fluid proteins including the high alkalinity of many tear proteins, the occurrence of non-specific binding interactions between tear analytes which complicate specific detection of disease biomarkers, and the low solubility of immune complexes at physiological pH.

Mobility-based electrophoretic separations also allow for detection of binding interactions that, instead of creating a larger immune complex that can be separated from the smaller (unbound) components, induce a conformational change that alter the effective radius of a molecule. The rapid separation speeds of the microfluidic format reduce diffusive dispersion and enhance the resolution of separated analyte fractions. This enables detection of small mobility differences, such as those created by conformational differences.

In this work, we developed and presented a first-in-kind microfluidic mobility shift assay for riboswitch screening applications. We used it to demonstrate the ability to detect riboswitch binding to a small molecule ligand and the induced conformational change. We then screened five putative riboswitches and demonstrated their functionality for the first time in the literature. We also demonstrated the ability to utilize the fine mobility resolution of microfluidic formats to be able to study the binding affinity of both fast and slow interconverting riboswitch pairs.

Building on this work, future studies may focus on adaptation of the hardware components surrounding the assay itself to facilitate the use of the tear analysis device in point-of-care clinical settings and the translation of the riboswitch screening device into other laboratories for use in riboswitch analytical studies. This may include adapting the imaging components to facilitate inexpensive, portable fluorescence detection or other types of detection that are amenable for use in point-of-care settings. This may also include the demonstration of battery operation in order to eliminate the need for a custom high voltage power supply. Finally, future work may include the adaptation of the chip substrates to enable fabrication of gels in plastic or another inexpensive alternative to glass. Future work may also focus on validating the method of on-chip osmolarity measurements in real patient samples and expanding the multiplexing capabilities of the tear analysis device to address some of the other interesting questions facing the tear fluid community. Finally, exciting future work may include application of the riboswitch screening assay toward riboswitch discovery and validation of putative riboswitches, ligand discovery for orphan riboswitches, and characterization of the binding affinity for known or newly discovered riboswitch pairs in order to gain insight into the biological role of the genetic switch. Riboswitch selection assays and library screening efforts may also advance riboswitch discovery and sensing applications. It is also likely that the types of binding interactions studied with microfluidic mobility shift assays can be expanded to include another important class of biological macromolecules beyond the protein and RNA binding interactions studied here.

In sum, this work makes important contributions toward creating robust analytical tools capable of probing the binding interactions that underpin all of biology. By harnessing the speed, resolution, and portability of electrophoresis on the microscale, this work has the potential to enable these powerful analytical techniques to increasingly be used both at the bench and the bedside.

Chapter 12: Appendices

12.1 Protocol for Fabrication of Mobility Shift Assay

Wash

- Wash out channels with NaOH (let sit 10 minutes then pipette in water 2x to wash any residue acid or gel after ashing procedure).

Silane Solution

- Add the following in a 1.5 mL eppendorf tube:
    - 50 µL 3-(trimethoxysilyl)-propyl methacrylate (98%) silane (use needle/syringe)
    - 75 µL acetic acid
    - 125 µL DI water
- Poke hole in top of eppendorf tube with syringe
- Connect the vacuum hose to the top of the eppendorf tube and thoroughly agitate and degas while sonicating (4-5 min). Tap the tube on the bottom of the sonicator to ensure no trapped bubbles. Make sure water level is above the level of the silane solution in the eppendorf tube.
- After degassing, pipette solution onto chip. Pipette into the sample well first and wait for the solution to pass into the channels through capillary motion. Then put drops onto the other wells and allow precursor to enter other channels.
- Cover the chip and let it sit for 30 minutes. This step functionalizes the surface so that the PA gel is linked to the glass surface
- Remove the silane solution with vacuum
- Wipe surface of the chip clean with a kim wipe
- Using a pipette tip attached to the vacuum, vacuum out the channels. Then take off the pipette tip and put the vacuum tube on the sample well for a few minutes until all channels are white (empty).
- Wash with alternating methanol and water (three times each): Introduce methanol into channels. This clears unreacted silane. Remove the methanol with vacuum. Introduce water. Remove the water with vacuum. Repeat two more times.

Polyacrylamide Gel Fabrication

- Make precursor solution: take 30% acrylamide/bis-acrylamide bottle out of fridge to warm up beforehand so that less oxygen is dissolved and it is easier to degas
- Check microfluidic channels under the Olympus Diaphot (Emerald) microscope to be sure there is no residue silane. If residue is observed, you will see droplets. If observed, do another methanol/water wash and vacuum for ~5 min.

- Prepare precursor solution: Measure out ~1 mg of VA-086 (photoinitiator) into 1.5 mL eppendorf tube. Acrylamides are neurotoxins so use caution! Do not silane/acrylamides down the drain. Instead, use the waste container in the hood. The higher the acrylamide concentration, the smaller the pore size and the higher resolution of separated populations. (%T = percent monomer concentration).
- Prepare pipette tips for each well: Cut off 200 µL pipette tips just below last marking before the tip. Stick one in each well while twisting to ensure solid integration. These provide a reservoir for excess precursor during UV exposures.
- Calculate the volumes of reagents required for the desired %T. Multiply volumes (in Table 10) by the mass of VA-086 measured previously. Add the correct volumes of 30% acrylamide/bis stock, dI water and 10× buffer.

Table 10. Reagent concentrations for gel fabrication.

30% acrylamide/bis stock (29:1) (uL)	H20 (ul)	10X Buffer	n%T
100/mg of VA-086	350/mg of VA-086	50/mg VA-086	6
59.5/mg of VA-086	405.5/mg of VA-086	45/mg VA-086	3.5
133/mg of VA-086	339.3/mg of VA-086	37.7/mg of VA-086	8

- Vortex precursor gently to mix
- Degas precursor: Poke hole in top of eppendorf tube with syringe (*degassing is really important here!). Connect the vacuum hose to the top of the eppendorf tube and thoroughly agitate and degas while sonicating (4-5 min). Tap the tube on the bottom of the sonicator to ensure no trapped bubbles. Make sure water level is above the level of the precursor solution in the eppendorf tube.

Polymerize Discontinuous Gel

- Turn on the UV lamp on Emerald microscope. Let warm up beforehand.
- Use a UV meter to measure the maximum intensity of the UV light. This will require moving the stage to ensure you measure the maximum.
- Tape the mask on the stage and align the chip on top. The chip should be aligned so that the loading channel + ~80 um is exposed (Figure 92).

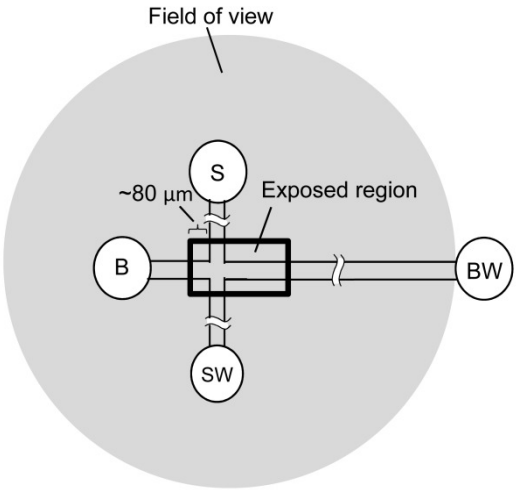

Figure 92. Chip alignment for discontinuous PA gel fabrication

- Load the precursor solution and drop 5% HEC on each well to suppress bulk fluid flow. Let the device equilibrate for 5 min.
- Expose with UV light for the optimized intensity and time.
- Turn on air for UV lamp. This cools the system so only driving force is UV light, not heat. Turn on the lab and let it heat up for ~5 minutes before use. It is best to introduce the precursor solution just before polymerization so you want lamp to be ready beforehand.
- Exchange the precursor solution in wells SW, S and B with the larger pore size precursor. Apply vacuum to each well in sequence to replace the precursor solutions in the channels.
- Tape the chip to a microscope plate, which acts as a holder. Pipette ~3 µL precursor solution into each well. Introduce into one well first and allow it to enter the channels before adding to the other wells. The fluid level should be approximately level with the well top. Put cut pipette tips into each well. Pipette an additional 7 µL more precursor solution into each pipette tip.
- Look at the chip under the microscope for bubbles. If bubbles are present, flush with methanol/water and start again.
- Place the chip on the UV lamp and allow to polymerize for 7-8 minutes at ~ 10 mW/cm^2. Wear a face mask to block the UV light! The intensity and exposure time must be optimized for each set of conditions.
- Remove the chip and inspect for bubbles under the microscope.
- Leave the lamp air on for 5 minutes after the lamp is turned off so the system can cool
- Remove pipette tips, noting the extent of polymerization of the gel plugs
- Store in buffer in 50mL eppendorf tube in the same buffer as that used for the gel
- Store in fridge

12.2 Matlab Code for Modeling of On-Chip Riboswitch Separations with Varying Binding and Dissociation Rates

```
%%%%riboswitchbinding3.m
%% Model of riboswitch binding with varying Kon and Koff

%% equations & definitions
%A = riboswitch (unbound)
%B = riboswitch (bound)
%L = ligand (SAM)
%       K1
% A + L <---> B
%       K2
clear all;
clc;
close all;
clc;
m = 0;
%% ADJUST THESE MESH SIZES FOR NON-DIMENSTIONALIZED X & T
x_bar = [linspace(0,1,400)];% x (non-dimensionlized)
t_bar = [linspace(0,1,1001)]; %time (non-dimensionalized)
sol = pdepe(m,@pdefun3,@icfun5,@bcfun3,x_bar,t_bar);

% Extract the first solution component as u.
u1 = sol(:,:,1); %unbound riboswitch concentration (t_bar, x_bar)
u2 = sol(:,:,2); %bound riboswitch concentration (t_bar, x_bar)
u3 = sol(:,:,3); %free ligand concentration (t_bar, x_bar)

%% display the results:
% calculate C_unbound + C_bound
c_total = u1+u2;
L = 0.4; %cm; separation length of 4mm
E = 500; %V/cm
mu = [1.06338e-5;1.18e-5;1.2e-5];
mu_bar = mu./mu(1); %non-dimensionalized mobility
x = x_bar*L; %units: cm
t = t_bar*L/(E*mu(1)); %units: sec

% %A surface plot is often a good way to study a solution.
figure;
surf(x*10,t,c_total,'FaceColor', 'interp','EdgeColor','none','FaceLighting','phong')
colormap default
colorbar
view(2)
ylim([0 75]);
set(gca,'Ydir','reverse');
```

```
xlabel('Distance x, mm');
ylabel('Time t, sec');
title('bound & unbound riboswitch');

figure;
surf(x*10,t,u1,'FaceColor', 'interp','EdgeColor','none','FaceLighting','phong')
colormap default
colorbar
view(2)
set(gca,'Ydir','reverse');
xlabel('Distance x, mm');
ylabel('Time t, sec');
title('unbound riboswitch');

figure;
surf(x*10,t,u2,'FaceColor', 'interp','EdgeColor','none','FaceLighting','phong')
colormap default
colorbar
view(2)
set(gca,'Ydir','reverse');
xlabel('Distance x, mm');
ylabel('Time t, sec');
title('bound riboswitch');

figure;
surf(x*10,t,u3,'FaceColor', 'interp','EdgeColor','none','FaceLighting','phong')
colormap default
colorbar
view(2)
set(gca,'Ydir','reverse');
xlabel('Distance, mm');
ylabel('Time t, sec');
title('Free SAM Ligand');

%% Define & plot SR
%SR = delta L / 4sigma
figure
for i = 1:11,
hold on;
 unbound = u1((i-1)*100+1,:);  %u1(t_bar,x_bar) where t_bar value = (t_bar row # - 1)/1000
 bound = u2((i-1)*100+1,:); %u2(t_bar,x_bar)
 %define initial conditions: ADJUST THESE
 t_row = (i-1)*100+1;
 t_bar_value = (t_row-1)/1000;
 x_bar_unbound = mu_bar(1)*t_bar_value; %x-bar value at the time (non-dimensionalized) at which the
intensity is fitted
```

```
 x_bar_bound = mu_bar(2)*t_bar_value; %x-bar value at the time (non-dimensionalized) at which the
intensity is fitted

 IC1_unbound = [(0.5/i) x_bar_unbound 0.1 0]; %[c1 peak height   %c2 migration distance  %c3 variance
%c4 offset]
 IC1_bound = [0.5 x_bar_bound 0.1 0]; %[c1 peak height   %c2 migration distance  %c3 variance  %c4
offset]
 c_unbound = lsqcurvefit(@gaussian, IC1_unbound, x_bar, unbound);
 c_bound = lsqcurvefit(@gaussian, IC1_bound, x_bar, bound);

 SR = (c_bound(2) - c_unbound(2))/(2*c_unbound(3)+2*c_bound(3));

 time_points(i) = t_bar_value;
 SR_matrix(i) = SR;
end

SR_matrix_column = SR_matrix';
plot(time_points, SR_matrix_column, 'bo');
title('Separation Resolution over Time')
xlabel('time (t/t0)')
ylabel('SR')
%SR_at_t_bar_zeropointthree = SR_matrix_column(4)
SR_at_t_bar_zeropointsix = SR_matrix_column(7)

%% Define & plot Peak intensity
figure
for i = 7:7,
hold on;
 unbound = u1((i-1)*100+1,:);  %u1(t_bar,x_bar) where t_bar value = (t_bar row # - 1)/1000
 bound = u2((i-1)*100+1,:); %u2(t_bar,x_bar)
 %define initial conditions
 t_row = (i-1)*100+1;
 t_bar_value = (t_row-1)/1000;
 x_bar_unbound = mu_bar(1)*t_bar_value; %x-bar value at the time (non-dimensionalized) at which the
intensity is fitted
 x_bar_bound = mu_bar(2)*t_bar_value; %x-bar value at the time (non-dimensionalized) at which the
intensity is fitted
 IC1_unbound = [(0.5/i) x_bar_unbound 0.1 0]; %[c1 peak height   %c2 migration distance  %c3 variance
%c4 offset]
 IC1_bound = [0.5 x_bar_bound 0.1 0]; %[c1 peak height   %c2 migration distance  %c3 variance  %c4
offset]

 %do a gaussian curve fit to the data
 c_unbound = lsqcurvefit(@gaussian, IC1_unbound, x_bar, unbound);
 c_bound = lsqcurvefit(@gaussian, IC1_bound, x_bar, bound);
```

```
 %plot(x_bar, unbound-sum(c_unbound(:,4)), 'bo', x_bar, gaussian(c_unbound, x_bar)-
sum(c_unbound(4)), 'rx-')

 peak_intensity_unbound(i) = c_unbound(1);
 peak_intensity_bound(i) = c_bound(1);
 time_points(i) = t_bar_value;
 peak_location_unbound(i) = c_unbound(2);
 peak_location_bound(i) = c_bound(2);
end

peak_intensity_unbound_matrix = peak_intensity_unbound';
peak_intensity_bound_matrix = peak_intensity_bound';
peak_location_unbound_matrix = peak_location_unbound';
peak_location_bound_matrix = peak_location_bound';

Bound_peak_intensity = peak_intensity_bound_matrix(7)
Unbound_peak_intensity = peak_intensity_unbound_matrix(7)
Bound_peak_location = peak_location_bound_matrix(7)
Unbound_peak_location = peak_location_unbound_matrix(7)

ub = unbound';
b = bound';
c = c_total(601,:);
c = c';

%% Figure out time for the C1+C2 peak at the end of the separation to see
%% if speed changes based on Kon, Koff or Kd
figure
% i = 11
for i = 7:7,
 hold on;
 unbound = u1((i-1)*100+1,:);  %u1(t_bar,x_bar) where t_bar value = (t_bar row # - 1)/1000
 bound = u2((i-1)*100+1,:); %u2(t_bar,x_bar)
 combined = unbound+bound;
 %define initial conditions: ADJUST THESE
 t_row = (i-1)*100+1;
 t_bar_value = (t_row-1)/1000;
 x_bar_unbound = mu_bar(1)*t_bar_value; %x-bar value at the time (non-dimensionalized) at which the
intensity is fitted
 x_bar_bound = mu_bar(2)*t_bar_value; %x-bar value at the time (non-dimensionalized) at which the
intensity is fitted

 IC1_unbound = [(0.5/i) x_bar_unbound 0.1 0]; %[c1 peak height   %c2 migration distance  %c3 variance
%c4 offset]
 IC1_bound = [(0.5/i) x_bar_bound 0.1 0]; %[c1 peak height   %c2 migration distance  %c3 variance  %c4
offset]
 IC1_combined = [(0.5/i) x_bar_bound 0.1 0];
```

```
 c_unbound = lsqcurvefit(@gaussian, IC1_unbound, x_bar, unbound);
 c_bound = lsqcurvefit(@gaussian, IC1_bound, x_bar, bound);
 c_combined = lsqcurvefit(@gaussian, IC1_combined, x_bar, combined);

 plot(x_bar, combined-sum(c_combined(:,4)), 'bo', x_bar, gaussian(c_combined,x_bar)-
sum(c_combined(4)), 'rx-')

 combined_peak_location(i) = c_combined(2);
%  combined_peak_location = c_combined(2)
 time_points(i) = t_bar_value;
end


%%%%pdefun3.m
function [c,f,s] = pdefun3(x_bar,t_bar,u,DuDx)
% matrices are: [Unbound; Bound; Ligand]
%% input the values for the system:
L = 0.4; %cm; separation length of 4mm
E = 500; %V/cm
 mu = [1.06338e-5;1.18e-5;1.2e-5];
mu_bar = mu./mu(1); %non-dimensionalized mobility
Do = 1e-6; %units = cm2/s  (characteristic diffusion coefficient)
   muRatio_A_B = mu(1)/mu(2);
   muRatio_L_B = mu(3)/mu(2);
D = [muRatio_A_B*1e-6; 1e-6; muRatio_L_B*1e-6]; %diffusion coeffients based on mobility ratios. units
= cm2/sec
D_bar = D/Do; %non-dimensionalized diffusion coefficient
Pe = E*mu(1)*L/Do;


%% VARY THESE VALUES TO SEE EFFECT ON OUTPUT!!
K1 = 2.22; %unit 1/(uM*s)  Kon
K2 = 2e-6; %units 1/s  Koff
%%
Da_on = K1*L/(E*mu(1));
Da_off = K2*L/(E*mu(1));
y = -Da_on*u(1)*u(3)+ Da_off*u(2);
c = [1;1;1];
f = (D_bar./Pe).*DuDx;
s = [(-mu_bar(1)*DuDx(1)+y);(-mu_bar(2)*DuDx(2)-y); (-mu_bar(3)*DuDx(3)+y)];

%%%%icfun5.m
function u0 = icfun3(x_bar)

%% Initial conditions: what the concentrations are at t = 0
% assume:
% 1) sample starts at equilibrium with overlapping peaks with a gaussian distribution
```

```
% 2) concentrations are equilibrium concentrations

%% CHANGE THESE INITIAL CONCENTRATION VALUES TO SEE EFFECT ON MOBILITY!
conc_riboswitch_total = 1; %units: uM
conc_ligand_total = 0; %units: uM

K1 = 2.22; %unit 1/(uM*s)  Kon
K2 = 2e-6; %units 1/s  Koff

%find concentration of complex:
a = K2/K1;
b = -(K2/K1)*conc_riboswitch_total -(K2/K1)*conc_ligand_total - 1;
c = K2/K1*conc_riboswitch_total*conc_ligand_total;
Complex_equilib_conc = (-b-sqrt(b^2-2*a*c))/(2*a);

%use the complex equilibrium concentration to plug back in for the free
%riboswitch and free ligand concentrations:
Ribo_free_equilib_conc = conc_riboswitch_total - Complex_equilib_conc;
Ligand_free_equilib_conc = conc_ligand_total - Complex_equilib_conc;
if Ribo_free_equilib_conc < 0
   Complex_equilib_conc = (-b+sqrt(b^2-2*a*c))/(2*a);
   Ribo_free_equilib_conc = conc_riboswitch_total - Complex_equilib_conc;
   Ligand_free_equilib_conc = conc_ligand_total - Complex_equilib_conc;
end

if Ligand_free_equilib_conc < 0
   Complex_equilib_conc = (-b+sqrt(b^2-2*a*c))/(2*a);
   Ribo_free_equilib_conc = conc_riboswitch_total - Complex_equilib_conc;
   Ligand_free_equilib_conc = conc_ligand_total - Complex_equilib_conc;
end

%Now define the initial plugs as overlaid gaussian peaks with 4*sigma (peak width) = 200um and heights
equal
%to the equilibrium concentrations we just found
A1 = Ribo_free_equilib_conc*exp(-(3200)*(x_bar).^2);
B1 = Complex_equilib_conc*exp(-(3200)*(x_bar).^2);
C1 = Ligand_free_equilib_conc*exp(-(3200)*(x_bar).^2);

u0 = [A1; B1; C1];

%%%%bcfun3.m
function [pl,ql,pr,qr] = bcfun3(xl,ul,xr,ur,t)

%% boundary conditions are what the concentrations are at x = 0 and x = 1
% or at the beginning and end of the separation
pl = [ul(1); ul(2); ul(3)];
ql = [0;0;0];
```

```
pr = [ur(1); ur(2); ur(3)];
qr = [0;0;0];
```

12.3 Perchloric Ashing Protocol for Chip Reuse

In order to enable glass microfluidic chips to be reused after experimentation, a protocol for removing the gels from within the channels was optimized both for efficacy as well as safety. A Standard Operating Procedure (SOP) safety information and disposal instructions for the perchloric acid/hydrogen peroxide solution used to acid ash glass microfluidic chips filled with polyacrylamide gels is included here. The developed SOP was intended to be used to train new users and be a reference for trained users and was approved by the Environmental Health and Safety Department at UC Berkeley. As detailed below, the primary hazards are the potential for injury resulting from the handling of a potent oxidizing mixture that contains highly corrosive acid. The container may become pressurized from reaction of the chemicals.

Background

Acid ashing of microfluidic chips is done to remove acrylamide gel from the microfluidic channel interior and allow for chip re-use. It was determined that this could be done by incubating chips at 75°C in a mixture of two reactive stock chemicals: perchloric acid ($\leq$70% concentration) and hydrogen peroxide (~30% concentration). These chemicals by themselves represent both chemical/physical and health hazards to potential users and to other laboratory personnel who may be in the vicinity where these solutions are being prepared, actively used or stored as hazardous waste. Both chemicals, individually or combined, must always be regarded as capable of causing great bodily harm in multiple ways, particularly at elevated temperatures as they are used in this procedure

Perchloric acid ($HClO_4$) is a strong, colorless, odorless mineral acid that acts as an extremely strong oxidizer. It is a highly corrosive substance and causes severe burns upon contact with the eyes, skin and mucous membranes.[284] Perchloric acid is a superacid, one of the strongest Bronsted-Lowry acids with a pKa of -10.[285] Its oxidizing strength dramatically increases when heated or at concentrations at or above 73%.[286] Perchloric vapors can create perchlorate crystals which are shock sensitive and can explode.

Hydrogen peroxide (H_2O_2) is a weak acid with strong oxidizing and bleaching properties. It is considered a highly reactive oxygen species and decomposes exothermically into water and oxygen gas spontaneously. Low concentrations (3%) are widely available and often used for medical purposes. Higher concentrations are hazardous and act as aggressive oxidizers that present a high corrosion hazard. In the presence of a reducing agent (i.e. *any* organic material), high concentrations will react violently.[287]

Mixing perchloric acid and hydrogen peroxide to create the necessary acid ashing solution yields a solution that is volatile, corrosive, oxidative and exothermal in nature. The combined solution is a very powerful oxidizer that can cause organic materials to ignite spontaneously, as

well as cause severe burns that are slow to heal. Care must also be exercised in disposal so that this solution poses a minimum/negligible risk to hazardous waste operations and personnel. Ashing reaction generates gases that, if confined, will increase pressure and may rupture the reaction vessel. Always cap containers loosely to avoid unwanted pressure buildup, or use a vented cap Never fill the waste containers but leave significant head space (>50%) so pressure will not rupture the bottle and spray contents.

Personnel and Documentation

Authorized Personnel: Acid ashing may only be performed by authorized personnel who are fully cognizant of all safety issues involved in the procedure by completing the "Approvals Required" steps outlined below. These personnel are to ensure that the procedure is only performed in the manner laid out in this document. Any changes requested to the SOP must be made in writing using the SOP approval procedure outlined by the laboratory.

Required Documentation: The lab member responsible for ashing for the month is also required to initial and date a mandatory perchloric acid safety checklist every time he or she performs a step in the ashing procedure (i.e. 3x per week) in order to track user compliance. This checklist is posted near the ashing hood at all times.

Unauthorized Personnel: No unauthorized personnel may handle or transport acids unless accompanied by an authorized user.

Super-users: Kelly Karns and Mei He, then Kelly Karns and Robert Lin.

Approvals Required

To become an authorized user, one must:

1. Read and understand perchloric acid MSDS, hydrogen peroxide MSDS and this SOP
2. Receive in-person/hands-on training on the procedure by an authorized super-user
3. Sign and date the authorized user sheet to affirm that the above steps have been completed
4. All users must annually complete the Hazardous Materials Spill Response Training online at:

   http://ehs.berkeley.edu/trainnonemploy/hazmaterialspill/index.html

   Training takes approximately 15 minutes and must be completed by September 1 of each year or upon initial training for new users. A new authorized user sheet should be signed every year and hung next to the hood to confirm training completion by all users.

Hazards

Perchloric Acid (70% in stock solution, 49% in final ashing mixture)

1. Highly corrosive substance that causes severe burns on contact with the eyes, skin, and mucous membranes
2. Unstable at ordinary temperature and pressure and can undergo explosive decomposition, especially at elevated temperatures or if allowed to dehydrate.
3. May emit toxic chloride fumes when heated to decomposition.
4. Vapors may also contaminate work surfaces or ventilation equipment with perchlorate residues, which form highly unstable compounds, such as metallic perchlorates which may ignite or detonate
5. If allowed to become anhydrous (dehydrated), perchloric acid may react violently with many organic materials posing a serious explosion hazard
6. Concentrated solutions can react violently with many oxidizable substances, such as paper and wood, and can detonate.
7. Powerful oxidizer that will destroy organic materials rapidly, often with liberation of large amounts of heat and the distinct possibility of a fire
8. Other material incompatibilities that elicit a violent response include:

Acetic anhydride, **Acetic acid, Alcohols,** Aniline, Benzene, Bismuth, Calcium hydride, **Cellulosic materials such as wood, paper and cotton,** Charcoal, **Combustible materials, Ethanol, Hydrochloric acid, Plastics (most common types), Reducing agents, Rubber (including rubber stoppers, tubes, or stopcocks),** Strong dehydrating agents (i.e. sulfuric acid), Sulfur, **Sulfuric acid,** Olefins, **Organic chemicals and materials, Oxidizing agents**

** Materials in bold are highlighted as commonly used in the Herr Lab and therefore pose an especially high risk.

Hydrogen Peroxide (30% in stock solution, 10% in ashing mixture)

1. Exposure to radiant heat, sources of ignition (such as heat or open flame), and physical or mechanical disturbances can create a potential fire or explosion hazard
2. Tremendous explosions can be caused by unstable mixtures with concentrated mineral acids such as perchloric acid.
3. Contact between hydrogen peroxide and certain materials (listed below) can cause immediate spontaneous ignition or combustion and violent explosions
4. Will release gaseous materials (primarily oxygen) that can pressurize a container where no pressure relief is possible (i.e. a closed bottle, regardless of the bottle's materials of construction).
5. Material incompatibilities include:

Aldehydes, and their anhydrides, **Cellulose materials such as wood, paper and cotton, Combustible materials, Glycerol, Metals including iron, copper, chromium, lead, silver, manganese, sodium, potassium, magnesium, nickel, gold and platinum,** Metal alloys such as,

brass or bronze, Metal oxides such as lead oxides, mercury oxides, or manganese dioxide, Metal salts, like potassium permanganate or sodium iodate, **Mineral acids include perchloric acid in high concentrations, Organic materials such as alcohols, acetone, and other ketones**

** Materials in bold are highlighted as commonly used in the Herr Lab and therefore pose an especially high risk.

Additional Hazards for Perchloric Acid/Hydrogen Peroxide Acid Ashing Solution

1. Solution spills on the outside of the container will cause the exterior to become slippery when handled with a gloved human hand
2. When mixed, acid solution self-heats. Be sure any container you are using can sustain heat and that care is taken when handled.
3. Gas build-up and overpressure concerns require the use of either vented caps or loosened caps to allow gas exchange so no pressure builds up in container.

Designated Use Areas and Maintenance

Hood use

All procedures should be performed in the designated hood for acid ashing use in Stanley Hall room 146 (in the BNC). Do not use perchloric acid in non-designated ashing hoods, unless approved by EH&S. The hood sash can act as additional personnel protection against explosion; lower the sash as much as possible to provide the greatest protection. Position a safety sash to further limit spray when hood sash is raised. When users are not present, cover the hotplate/beaker set-up with the designated plastic box to contain the acid should an accident occur. Cover the bottom interior of the hood with PIG Acid Encapsulating Neutralizing Mats to absorb any fumes that may be produced. Be sure not to cover the grating in the front of the hood (closest to the user) as this will block the air flow that contains fumes inside the hood. If there will be significant amounts of perchloric acid vapors the work must be done in a special perchloric acid hood. There is one designated perchloric acid hood in the Hearst Mining Building.

Hood maintenance

The crystalline form of perchloric acid, which is explosive and shock sensitive, can precipitate on hood surfaces, hood ductwork or fan. If pH of hood interior surfaces begins to drop, the hood interior should be washed regularly to return any crystalline form to solution and eliminate the explosion hazard. Various surfaces within the hood should be checked regularly for perchloric acid build-up using the methylene blue or diphenylamine tests described below:

Diphenylamine Test: Dissolve one gram of diphenylamine in 10 ml of "1 to 1" (18 normal) sulfuric acid to form a diphenylamine sulfate solution. Using a medicine dropper apply this solution to the test surface. The liquid turns black upon contact with perchlorate. The solution also reacts with nitrates, but turns blue.

Methylene Blue Test: Use 0.4% solution of methylene blue in water. Add a few drops of indicator solution to about 25 ml of trial solution, such as water used to test rinse from a length of potentially contaminated duct. Perchlorates will produce a violet precipitate.

Eyewash

The eyewash is located in the BNC corridor, immediately outside of room 146. The eyewash must be flushed at least monthly to verify proper function. Eyewash must be used if the ashing solution is sprayed in eyes. In case of eye exposure, hold eyelids open and flush with water for 15 minutes, then seek medical attention.

Safety Shower

The safety shower is located in the BNC corridor, immediately outside of room 146. Use the safety shower if body and/or face are contaminated. All users must know what to use, for various spill scenarios. Other lab mates must be prepared to assist.

Proper Handling Procedures

General Considerations

All operations should be performed in the hood, on chemically resistant surfaces and using compatible materials (see Section 5 for a list of incompatible materials). Pyrex or Teflon secondary containment trays with PIG Acid Encapsulating Neutralizing Mats in the bottom should be used at all times for 1) heating (on hot plate), 2) chemical transfer (pouring acid from stock bottles to ashing containers or acid waste from ashing containers to waste bottles), 3) transferring chips from water bath to acid bath and 4) ashing solution storage until EH&S pick-up. When no chips are being ashed, the hot plate should be turned off.

Specifics for Chip Transfer

Place water bath glass beaker, person's acid bath glass beakers and person's eppendorf tube chip storage container in Pyrex or Teflon secondary containment trays with PIG Acid Encapsulating Neutralizing Mats in the bottom. Transfer ashed chips from acid bath to water bath to person's eppendorf tube over this Pyrex or Teflon secondary containment tray with PIG Acid Encapsulating Neutralizing Mats in the bottom. Transfer new (unashed) chips from person's eppendorf tube to acid bath to over this Pyrex or Teflon secondary containment tray with PIG Acid Encapsulating Neutralizing Mats in the bottom.

Specifics for Heating

Heating should be done in Pyrex or Teflon secondary containment trays with PIG Acid Encapsulating Neutralizing Mats in the bottom (tray should be placed on top of hot plate). When handling beakers of hot acid use properly designed tongs or other remote-handling devices (see Section 5 for a list of incompatible materials). Secure all beakers of acid on a hot plate which incorporates a temperature sensor with auto-shutoff to prevent overheating and a

temperature controller that will shut off the unit when the controller is not in liquid contact to prevent the acid solution from drying out. The Corning PC-600D is recommended. Do not heat past 75°C.

Specifics for Replacement of Ashing Solution

Pour ashing solution from ashing container to waste bottle over Pyrex or Teflon secondary containment trays with PIG Acid Encapsulating Neutralizing Mats in the bottom. Pour perchloric acid and hydrogen peroxide from stock bottles into ashing containers over Pyrex or Teflon secondary containment trays with PIG Acid Encapsulating Neutralizing Mats in the bottom. Always add hydrogen peroxide to perchloric acid, not the other way around.

Waste Handling and Storage

Solutions of perchloric acid and hydrogen peroxide (especially waste) must be kept only in vented containers so that pressure does not build up. Allow >50% of container volume as headspace (i.e., only fill container half full with liquid). Allow waste material to fully react before sealing and sending waste to EH&S. After filling to 50% of total volume, set waste vented container aside (within secondary containment, in the hood) to react for 30 days before pickup. Close vented cap immediately prior to EH&S transport.

Proper User Attire

Closed toed non-mesh upper shoes must be worn when working with acid ashing solutions, regardless of its temperature. No exposed jewelry, including necklaces, rings, metallic bracelets or hair bands should be worn at any time. Long sleeved shirt and full length pants are highly recommended.

Additional Personal Protective Equipment (PPE) Requirements

1. Face-shield
2. Lowered hood sash, and/or portable safety shield.
3. Impact-resistant chemical safety goggles (vented)
4. Acid-resistant lab apron at least knee length and/or within 18 inches of the floor and the bottom of the apron
5. Lab coat
6. Appropriate gloves (e.g., nitrile only – long gauntlet suggested)

Storage Requirements

Perchloric Acid: Perchloric acid should be stored in its original container within compatible secondary containment, preferably glass or porcelain, which has a greater capacity than the container. (note: you may also use Teflon). Glass trays should be wiped periodically and wiped debris should be placed in a thick-gauge transparent/colorless poly bag that is held within a rigid outer container and is closed at the conclusion of the operations. Do not use paper towels for wipe down as they may ignite. The perchloric acid stock bottle should be stored separate

from other chemicals, but may be stored with other inorganic acids, preferably in a metal cabinet designed for acid/corrosive storage. It must, however, be stored away from organic chemicals, flammable or combustible materials and strong dehydrating agents such as sulfuric acid and anhydrous phosphorus pentoxide. If a bottle containing perchloric acid has turned dark and has crystals forming around the bottom of the bottle, there is a potential explosion hazard. Do NOT move the bottle, and contact EH&S Only the minimum amount of perchloric acid necessary for work should be kept in the lab. The maximum advised volume of perchloric acid to store is one 450g (1lb) bottle. Electrical wiring, etc., in storage areas must be watertight to protect against corrosive action of vapors. Containers may be hazardous when empty since they retain product residues (vapors, liquid). Do not store perchloric acid near any incompatible material or other acids.

Hydrogen Peroxide: Containers of hydrogen peroxide should be kept shock-free, covered and properly vented. Hydrogen peroxide should be stored in a cool, dry, well-ventilated area in tightly sealed containers that are labeled.

Ashing Solution Waste: Solutions of perchloric acid and hydrogen peroxide (especially waste) must be kept only in vented containers so that pressure does not build up. Allow >50% of container volume as headspace (i.e., only fill container half full with liquid). Allow waste material to fully react before sealing and sending waste to EH&S. After filling to 50% of total volume, set waste vented container aside (within secondary containment, in the hood) to react for 30 days before pickup. Close vented cap immediately prior to EH&S transport.

Emergency Procedures

In the event of a SERIOUS EMERGENCY involving perchloric acid/hydrogen peroxide solutions (significant human exposure, release of significant amount of solution, fire, interaction with flammable or combustible materials, any combination of these events), perform the following actions:

1. Immediately STOP what you are doing and begin emergency procedures
2. Use the safety shower and eyewash located in the lab to decontaminate yourself or assist with decontamination of those around you who may have been exposed
3. Call 911 from a land line or 510-642-3333 from a cell phone if medical attention is required
4. Call EH&S at 642-3073 (business hours) or UCPD Dispatch at 642-6760 (after hours) to report chemical spill
5. Do not attempt to clean up large spills by yourself
6. Vacate the lab
7. Contact QB3 Facilities 510-326-0496 (24/7)
8. Report incident to Amy Herr 510-666-3396 (office) 510-676-5805 (home)

Fire: Water spray can be used to extinguish fires and cool fire-exposed containers.

Inhalation: Remove to fresh air. If not breathing, give artificial respiration. If breathing is difficult, give oxygen. Call a physician.

Ingestion: If swallowed, DO NOT INDUCE VOMITING. Give large quantities of water. Never give anything by mouth to an unconscious person. Get medical attention immediately.

Skin Contact: Immediately flush skin with plenty of water for at least 15 minutes while removing contaminated clothing and shoes. Call a physician, immediately. Wash clothing before reuse.

Eye Contact: Immediately flush eyes with plenty of water in eyewash for at least 15 minutes, lifting lower and upper eyelids occasionally. Get medical attention immediately.

Minor Spill Incident and Accident Procedures

CLEAN UP SPILLS OF PERCHLORIC ACID ONLY IF YOU HAVE BEEN TRAINED TO DO SO AND THE APPROPRIATE EQUIPMENT IS AVAILABLE!

In the event of a minor spill (spill volume is less than 10 ml) and no human exposure, perform the following actions:

1. Notify those in your vicinity that there has been a minor spill of perchloric acid/hydrogen peroxide acid ashing solution. Do not panic.
2. Working with a lab partner, use a colorimetric neutralizing solution/kit (found in chemical spill crash cart located at 354 Stanley Hall) to treat the spill. Neutrasorb Acid Neutralizer with Bromocresol purple indicator dye is recommended (available in 354 Stanley and Lab 342 fumehood). It contains a dye that will turn purple when exposed to perchloric acid.
3. Soak up the neutralized spill with Neutrasorb Acid Neutralizer. *Do not use rags, paper towels, or sawdust and then put them aside to dry out, as such materials may spontaneously ignite*.
4. A second neutralization and rinsing of the affected area is recommended. Sodium bicarbonate can be sprinkled or wiped around the spill area.
5. Confirm proper clean-up with pH paper testing at several locations at the perimeter of the spill. A pH of 7.0 is considered neutralized. An acceptable range for normal disposal is pH = 6.0-9.0.
6. Keep others away from the spill location until it has been neutralized
7. Label all waste as flammable, corrosive hazardous waste and dispose in blue bins at the back (north side) of lab, or inside fume hood. If significant waste is produced, contact EH&S for pick-up.
8. Notify Superusers so that they can follow up with Thom Opal and Paul Lum for any additional requirements they request.

Waste Handling and Disposal

Waste should be stored in a glass bottle with *vented* replacement bottle cap. Date & initial all new waste containers when materials are first placed inside and for each addition of waste. Waste container should also have secondary containment with PIG Acid Encapsulating Neutralizing Mats in the bottom and be in fume hood at all times. Use waste generation notebook (affixed to outside of hood) with date,

name of user and approximate quantity being disposed to keep track of approximate total volume of waste in each waste container. Maximum waste volume is no more than the half of the container total volume and the maximum total waste collected in one container is no more than 500 mL.

When maximum level is reached:

1. Label container as "No Additional Waste Accepted", Today's Date, Date of Anticipated Pick-up (1 month from now) & Your Name and set aside with loose or vented cap in secondary containment with PIG Acid Encapsulating Neutralizing Mats in the bottom and in the fume hood for 30 days so that reaction/gas release can complete.
2. At 30 day mark, go online to request a waste pick-up using the EH&S electronic database schedule as follows:

- Go to http://mpl.ehs.berkeley.edu/
- Click "eMPL's"
- Fill in organization code: 11452
- Select Herr lab chartstring
- Click "Make a new Materials Packing List"
- Fill out "Materials Packing List", print, sign and attached to bagged waste
- Be sure to identify the contents of the bottle as 'perchloric acid & hydrogen peroxide mixture' (using this exact language so that EH&S can track this waste stream)

3. Close loose lid or replace vented lid with non-vented, tightened lid
4. Check outside of bottle for any signs of liquid (wipe off and neutralize with damp cloth if need be)
5. Attach necessary labels: all listed in Required Labeling section below and orange/yellow 'unwanted hazardous materials' label from chemical disposal/storage room of BNC (next to ashing room)
6. Enclose bottle in a polyethylene bag and place the bagged bottle into a sturdy cardboard box right before EH&S pick-up (place directly below hood for pick-up)

Starting a new waste bottle:

1. Obtain a new perchloric acid waste bottle (available from Paul Lum in BNC or use empty stock perchloric acid bottle)
2. Label with proper label
3. Store in hood in secondary containment with PIG Acid Encapsulating Neutralizing Mat in the bottom
4. Secondary containment of waste solution containers must be used and should be made of a compatible material such as glass.
5. Inspect storage containers frequently for signs of damage, elevated temperature, or crystalline build-up. If you see any of these indications, do not attempt to deal with this potentially dangerous situation for yourself – call EH&S (642-3073) for assistance!
6. Call to initiate waste disposal of any container that exhibits salt build-up on its exterior, particularly near the cap-bottle interface

Required Labeling

The following label must be clearly displayed on all formulations of acid ashing solution:

1. Date of preparation start
2. Name of person preparing solution
3. Quantities and concentrations of perchloric acid and hydrogen peroxide used
4. Hazards: oxidizer, corrosive, and pressure-release

The following label must be placed on waste container at all times:

DANGER! STRONG OXIDIZER. CONTACT WITH OTHER MATERIAL MAY CAUSE FIRE OR EXPLOSION. POTENTIAL PRESSURE-RELEASE HAZARD. CORROSIVE. CAUSES BURNS TO EVERY AREA OF CONTACT. HARMFUL IF SWALLOWED OR INHALED.

Engineering, Ventilation and Administrative Controls

Engineering and Ventilation Controls

Always handle in a specially designated or designed perchloric acid fume hood that is operating properly (minimum of 100 lfpm). Keep the fume hood sash at minimum height to optimize its draw and minimize both the liquid and vapor exposure potential to users. Do not place any solid objects in front of fume hood draw points that will compromise the designed operation of the fume hood. Do not store incompatible materials or equipment inside the fume hood. Incompatible materials are listed in Section 5 and include paper, cloth or rubber materials and other acids that could come into contact with emitted vapors. A hot plate that incorporates over-temperature protection to prevent overheating should be used and placed directly in the hood. Volumes and concentrations of acids used and stored should be minimized When users are not present, cover the experimental set-up with the designated plastic box to contain acid in the event of an accident and protect other room-users.

Administrative controls

Before working with acid ashing solution, read the Material Safety Data Sheets (MSDS) for perchloric acid and hydrogen peroxide. All users must be trained in proper lab technique and approved for use before handling acids. Solutions of perchloric acid above a 70% concentration are not authorized. Working alone with acids is strongly discouraged. Maintenance and visual inspection of storage and working area should be performed weekly by the lab manager on duty that week. Copies of relevant MSDS and this document are available on bspace and a hardcopy posted near the hood for easy access. Signage should be posted on the hood and room door which includes 1) chemicals used, 2) major hazards, 3) safety response and 4) EH&S contact information. Any and all questions should be directed to super-users. If in doubt, ask!

Perchloric Acid/Hydrogen Peroxide Acid Ashing Solution Training

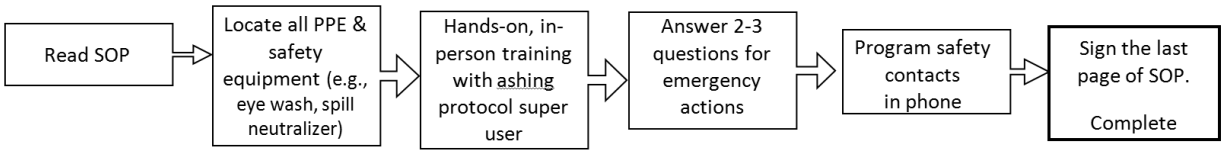

Figure 93. Training Flow Chart

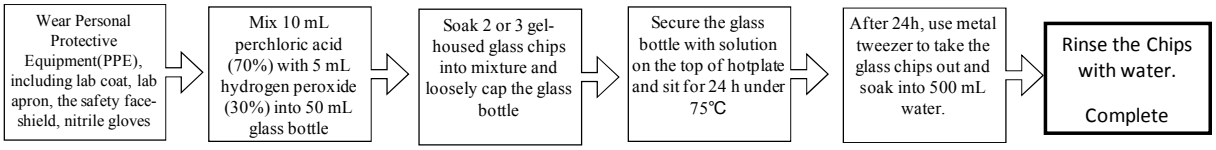

Figure 94. Gel Dissolution Flow Chart

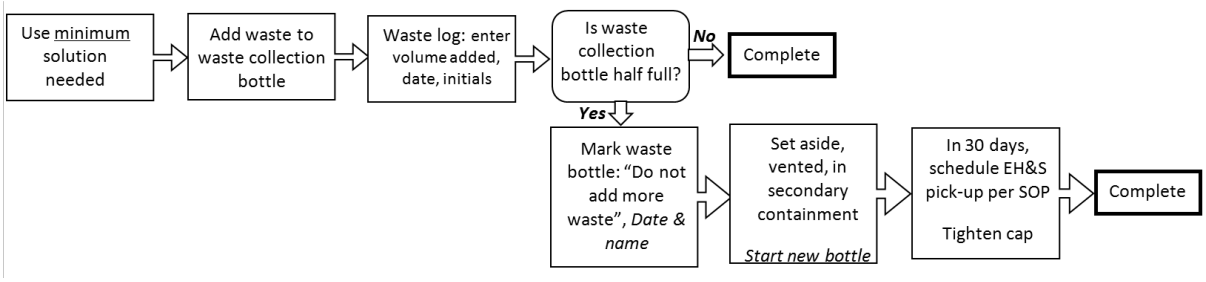

Figure 95. Waste Collection Flow Chart

12.4 Alternative Ashing Experiments with Piranha

Ashing with Piranha solution (sulfuric acid and hydrogen peroxide) was also tested as an alternative to the more unstable perchloric acid, hydrogen peroxide mixture. However, Piranha was found to not be viable for complete ashing of PA gels from within glass chips. The results are below. These results are without heating so it is possible that heating the Piranha, stirring it, and/or adding higher concentrations of hydrogen peroxide (until clear bubbling is observed) could yield higher ashing efficiencies.

Overview: Head to head trial of perchloric acid and piranha ashing protocols

Chips: NS12A chips filled with 3-10%T discontinuous gel in 1x TB + 10 mM Mg2+ buffer. Chips are < 4-5 months old and therefore will likely be challenging to ash, even in the Piranha solution.

Ashing conditions:

- 70% sulfuric acid/30% hydrogen peroxide (200 mL sulfuric, 100 mL H2O2)
- No heating, no stirring

Results:

At 2 days, there is approximately 1mm penetration of Piranha acid into the channels. Ashing is far from complete.

Buffer waste well – channel interface

Sample waste well – channel interface

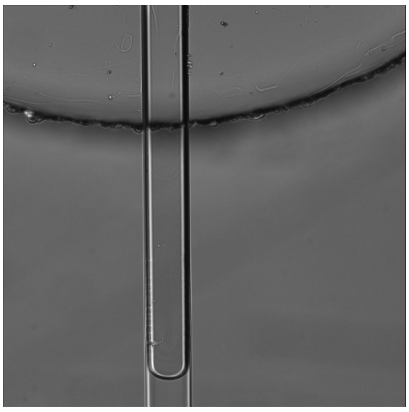

Sample well – channel interface

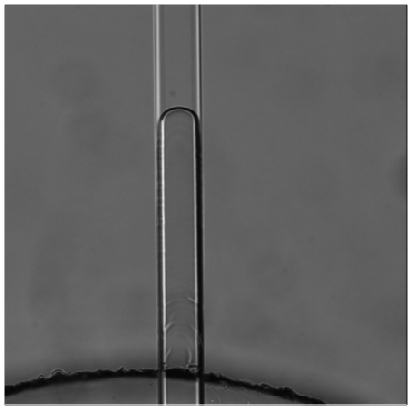

Separation channel and well interface

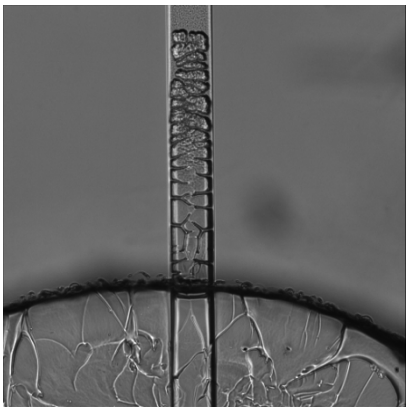

Comparing the normal perchloric acid process (70/30 ratio with heat) after 2 days of ashing, we see that the gel has been dissolved to a much greater degree, although the ashing is not fully complete.

Mostly ashed at 1mm in separation channel

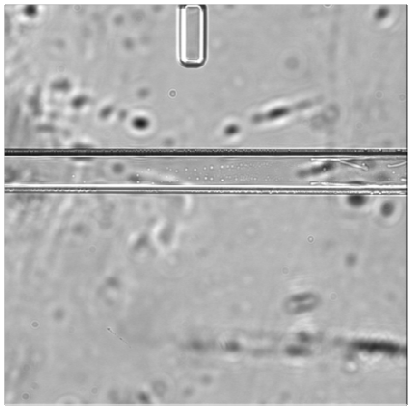

Gel remaining at separation channel well interface

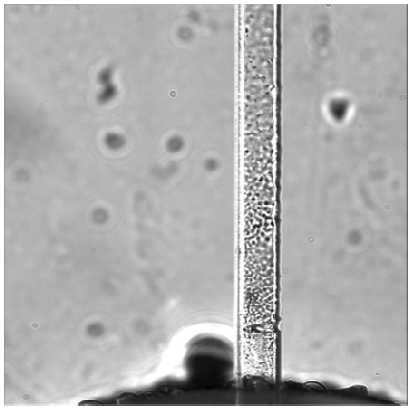

Some residue at injection junction

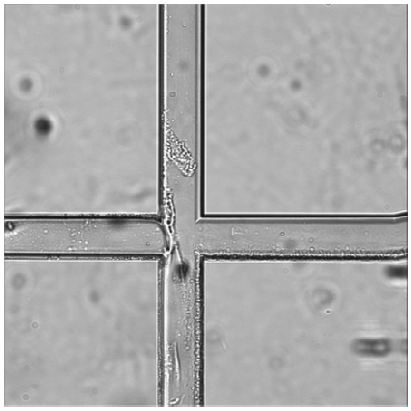

Some residue at sample well channel interface

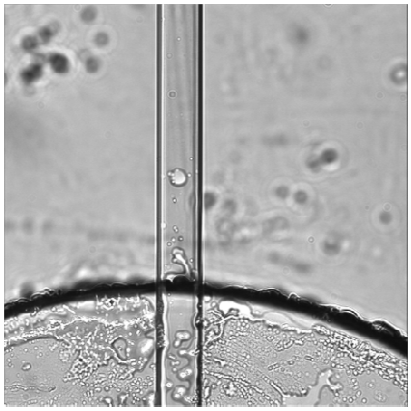

<u>5 days</u>

After 5 days of ashing, there has been little progress in the Piranha chip. Meanwhile, there is still residue in the perchloric acid chip. The extent of ashing remains similar to the day 2 results for both chips.

Piranha chips:

Ashing into sample waste well- channel interface

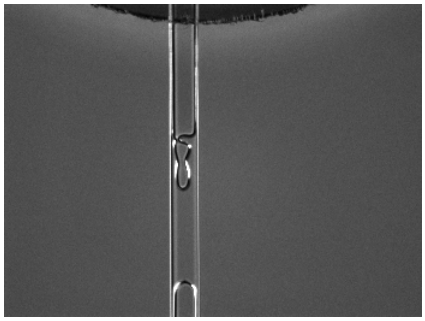

Gel all the way to the buffer well

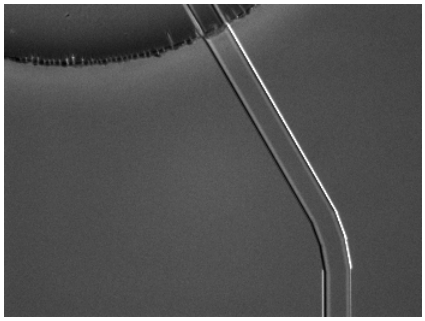

Gel still found throughout injection junction

some ashing at sample well inlet but not much more than day 2

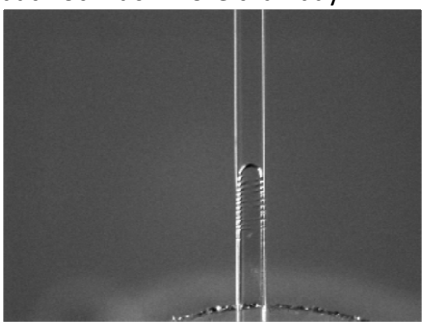

Perchloric chips:

Gel remains at buffer well-channel interface

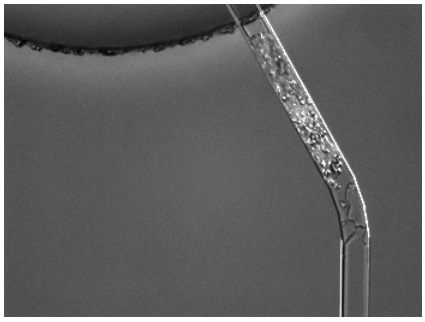

Good ashing at sample inlet

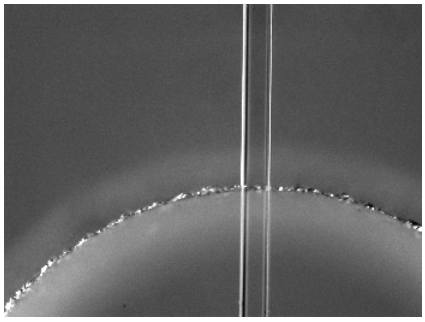

Incomplete ashing at injection junction

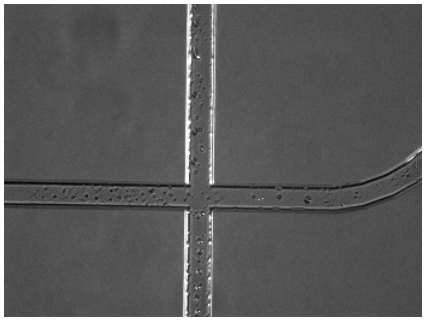

Some gel remains in separation channel

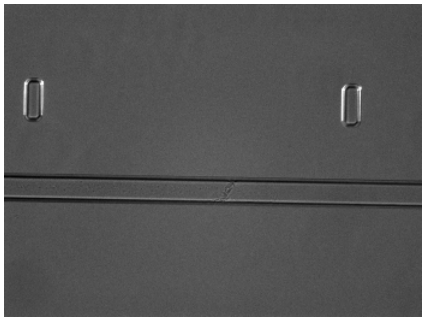

<u>7/8 days</u>

After 8 days of ashing, there has been little additional progress in the Piranha chip. Meanwhile, after 7 days of ashing there is still residue in the perchloric acid chip. The extent of ashing remains similar to the day 2 results for both chips.

Piranha chips:

Buffer well-channel interface

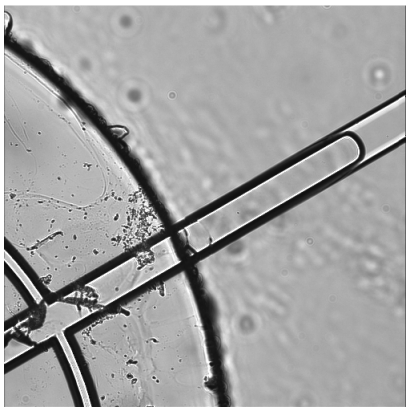

Gel in injection junction

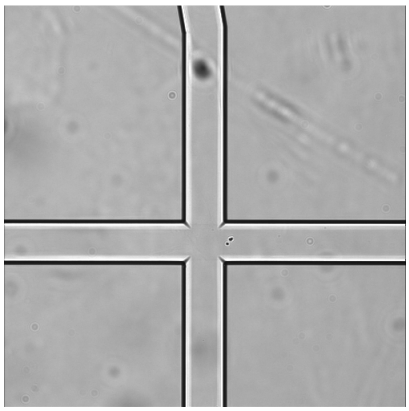

Sample waste well-channel interface

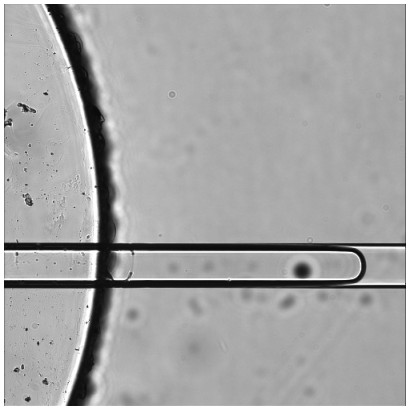

Sample well-channel interface

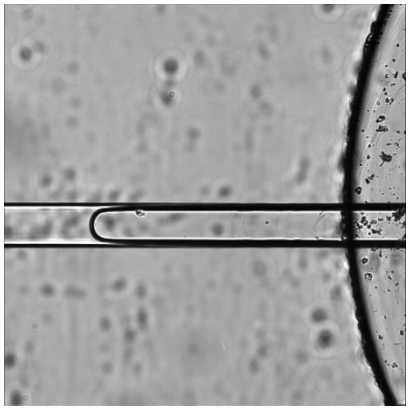

Separation channel-well interface

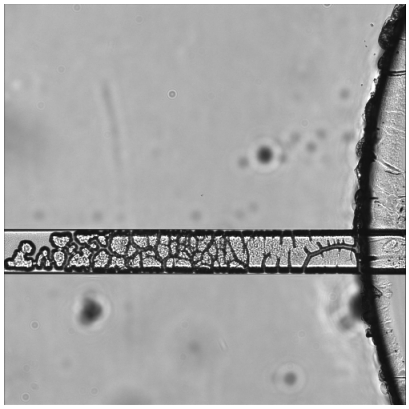

Perchloric chips:

Full ashing at sample well-channel interface

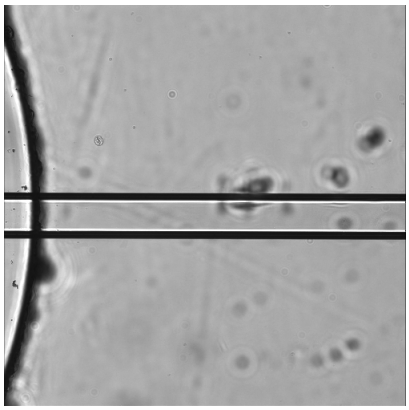

Some residue in channels

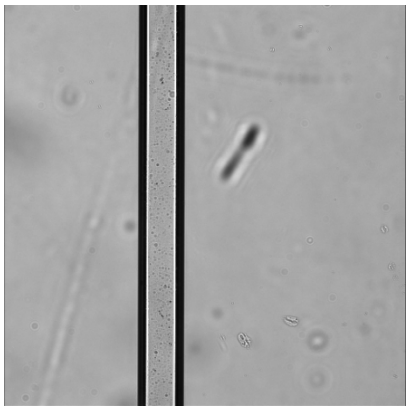

Some residue in injection junction

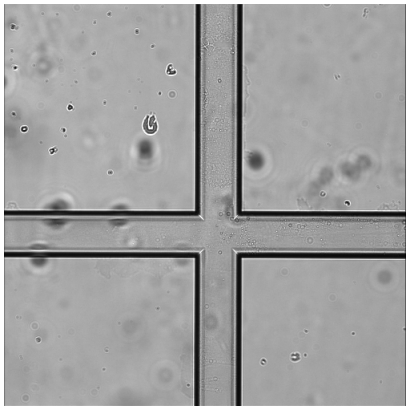

Next, I tried the following conditions:

Ashing conditions:

- 40% sulfuric acid/60% hydrogen peroxide (200 mL sulfuric, 300 mL H2O2) (new solution)
- No heating, no stirring

Results:

After a full day, there is approximately 500 µm penetration into the channels from the well but very little ashing overall. The same build-up is observed in the separation channel-well interface, which is interesting and unexplained. There were more bubbles on the chip and in the solution when we went down to get the chip.

Using the same chip, I then tried the following conditions:

Ashing conditions:

- 40% sulfuric acid/60% hydrogen peroxide (200 mL sulfuric, 300 mL H2O2) (new solution)
- With stirring
- No heat

Results:

After 3 days (over the weekend), there was no additional ashing observed. Acid penetration into the channels remained approximately 500 µm.

Using the same chip, I then tried the following conditions:

Ashing conditions:

- 40% sulfuric acid/60% hydrogen peroxide (200 mL sulfuric, 300 mL H2O2) (new solution)
- With stirring
- With heat (hot plate temperature set at 60°C)

Results:

After 1 day there was some ashing that occurred so we returned the chip to the beaker with new acid at 40% sulfuric acid/60% hydrogen peroxide) and ashed for another day at a higher heat (hot plate temperature set at 80°C).

By day 2, there was more ashing that occurred.

Full ashing had occurred in the sample channel originating off of the buffer well:

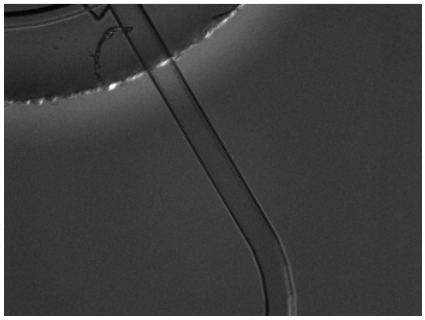

Full ashing had occurred in buffer and waste wells:

Ashing had occurred all the way to the junction from the buffer and sample waste wells:

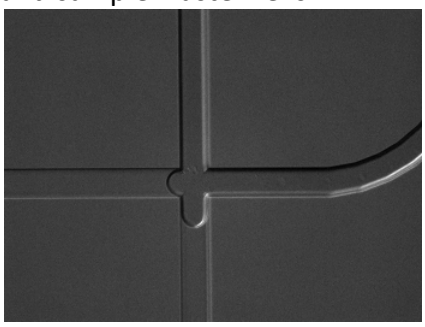

The interior of the gel also appeared to be breaking down since bubbles were visible in the separation channel:

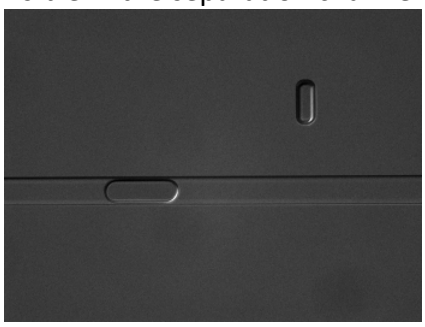

The end of the separation channel was still not fully ashed, but better than previously observed:

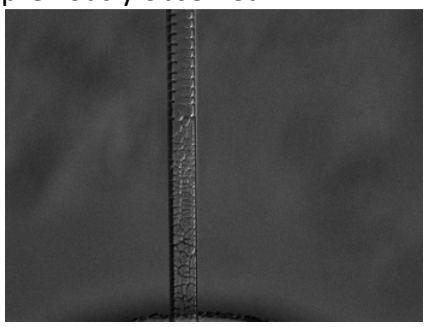

Ashing had also occurred further into the separation channel from the buffer waste well:

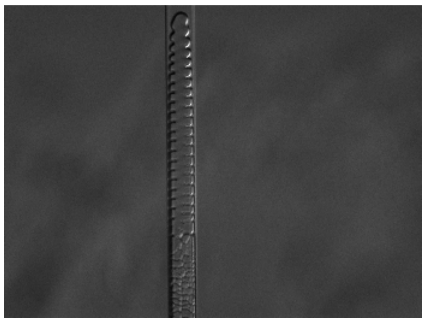

We then returned this chip to the solution and increased the temperature to 110°C for 3 more days and there appeared to be nearly complete ashing since fluid could be vacuumed through the channels.

Conclusions and Next steps:

It appears that piranha ashing with heat and stirring has potential as an alternative method to perchloric acid ashing with heat. Further study is needed to optimize the time and temperature conditions needed to fully ash the gel. In addition, it would be useful to verify the functionality of a chip after piranha ashing by actually fabricating a standard gel and running a standard assay. Once the time and temperature conditions are established, I would recommend replacing the perchloric acid ashing process with piranha in order to avoid having to control for the explosive nature of perchloric acid crystals.

Chapter 13: Bibliography

1 Nelson, D. L. & Cox, M. M. *Lehninger Principles of Biochemistry*. 5 edn, (W.H. Freeman and Company, 2008).

2 Winkler, W., Nahvi, A. & Breaker, R. R. Thiamine derivatives bind messenger RNAs directly to regulate bacterial gene expression. *Nature* **419**, 952-956 (2002).

3 Goodrich, J. A. & Kugel, J. F. *Binding and Kinetics for Molecular Biologists*. (Cold Spring Harbor Laboratory Press, 2007).

4 Laemmli, U. K. Cleavage of structural proteins during the assembly of the head of bacteriophage T4. *Nature* **227**, 680-685 (1970).

5 Chiem, N. & Harrison, D. J. Microchip-based capillary electrophoresis for immunoassays: analysis of monoclonal antibodies and theophylline. *Analytical Chemistry* **69**, 373-378 (1997).

6 Guzman, N. A. Determination of immunoreactive gonadotropin-releasing hormone in serum and urine by on-line immunoaffinity capillary electrophoresis coupled to mass spectrometry. *Journal of Chromatography B: Biomedical Sciences and Applications* **749**, 197-213 (2000).

7 Rifai, N., Gillette, M. A. & Carr, S. A. Protein biomarker discovery and validation: the long and uncertain path to clinical utility. *Nature Biotechnology* **24**, 971-983 (2006).

8 Chiem, N. & Harrison, D. J. Microchip-based capillary electrophoresis for immunoassays: analysis of monoclonal antibodies and theophylline. *Analytical Chemistry* **69**, 373-378 (1997).

9 Kawabata, T., Watanabe, M., Nakamura, K. & Satomura, S. Liquid-phase binding assay of α-fetoprotein using DNA-coupled antibody and capillary chip electrophoresis. *Analytical Chemistry* **77**, 5579-5582 (2005).

10 Wang, J., Ibáñez, A., Chatrathi, M. P. & Escarpa, A. Electrochemical enzyme immunoassays on microchip platforms. *Analytical Chemistry* **73**, 5323-5327 (2001).

11 Hou, C. & Herr, A. E. Ultrashort separation length homogeneous electrophoretic immunoassays using on-chip discontinuous polyacrylamide gels. *Analytical Chemistry* **82**, 3343-3351 (2010).

12 Phillips, T. M. Rapid analysis of inflammatory cytokines in cerebrospinal fluid using chip based immunoaffinity electrophoresis. *Electrophoresis* **25**, 1652-1659 (2004).

13 Karns, K. & Herr, A. E. Microfluidic homo-and hetero-geneous immunoassays: a tool to accelerate protein biomarker development. *Bioanalysis* **3**, 2161-2165 (2011).

14 Zichi, D., Eaton, B., Singer, B. & Gold, L. Proteomics and diagnostics: let's get specific, again. *Current Opinion in Chemical Biology* **12**, 78-85 (2008).

15 Brody, E. N., Gold, L., Lawn, R. M., Walker, J. J. & Zichi, D. High-content affinity-based proteomics: unlocking protein biomarker discovery. *Expert Review of Molecular Diagnostics* **10**, 1013-1022 (2010).

16 Koutny, L. B., Schmalzing, D., Taylor, T. A. & Fuchs, M. Microchip electrophoretic immunoassay for serum cortisol. *Analytical Chemistry* **68**, 18-22 (1996).
17 Bromberg, A. & Mathies, R. A. Multichannel homogeneous immunoassay for detection of 2, 4, 6 trinitrotoluene (TNT) using a microfabricated capillary array electrophoresis chip. *Electrophoresis* **25**, 1895-1900 (2004).
18 Berta, A. A polyacrylamide-gel electrophoretic study of human tear proteins. *Graefe's Archive for Clinical and Experimental Ophthalmology* **219**, 95-99, doi:10.1007/bf02173448 (1982).
19 Zhou, L. *et al.* Characterisation of human tear proteins using high-resolution mass spectrometry. *Annals Academy of Medicine Singapore* **35**, 7 (2006).
20 Wu, K. & Zhang, Y. Clinical application of tear proteomics: Present and future prospects. *PROTEOMICS - Clinical Applications* **1**, 972-982, doi:10.1002/prca.200700125 (2007).
21 Sariri, R. & Ghafoori, H. Tear proteins in health, disease, and contact lens wear. *Biochemistry (Mosc)* **73**, 381-392 (2008).
22 Flanagan, J. L. & Willcox, M. D. Role of lactoferrin in the tear film. *Biochimie* **91**, 35-43 (2009).
23 Korb, D. R. *et al. The tear film: structure, function and clinical examination*. Illustrated edn, (Butterworth-Heinemann, 2002).
24 Mishima, S., Gasset, A., Klyce, S. D., Jr. & Baum, J. L. Determination of tear volume and tear flow. *Investigative Ophthalmology* **5**, 264-276 (1966).
25 Prasad, S. *Dry Eyes*, <http://www.sight2020.co.uk/eye-conditions/dry-eyes> (2010).
26 Daum, K. M. & Hill, R. M. Human tear glucose. *Investigative Ophthalmology & Visual Science* **22**, 509-514 (1982).
27 Agarwal, S., Agarwal, A., Apple, D. J. & Buratto, L. *Textbook of Ophthalmology*. 1st edn, (Jaypee Brothers Medical Publishers, 2002).
28 Fung, K., Morris, C. & Duncan, M. Mass spectrometric techniques applied to the analysis of human tears: a focus on the peptide and protein constituents. *Advances in Experimental Medicine and Biology* **506**, 601-605 (2002).
29 de Souza, G. A., Godoy, L. M. & Mann, M. Identification of 491 proteins in the tear fluid proteome reveals a large number of proteases and protease inhibitors. *Genome Biology* **7**, R72 (2006).
30 Ohashi, Y. *et al.* Abnormal protein profiles in tears with dry eye syndrome. *American Journal of Ophthalmology* **136**, 291-299 (2003).
31 Sack, R. *et al.* Antibody array characterization of inflammatory mediators in allergic and normal tears in the open and closed eye environments. *Experimental Eye Research* **85**, 528-538 (2007).
32 Abe, T., Nakajima, A., Matsunaga, M., Sakuragi, S. & Komatsu, M. Decreased tear lactoferrin concentration in patients with chronic hepatitis C. *British Journal of Ophthalmology* **83**, 684-687 (1999).
33 Li, S. *et al.* Antibody protein array analysis of the tear film cytokines. *Optometry & Vision Science* **85**, 653-660 (2008).

34 Green-Church, K. B., Nichols, K. K., Kleinholz, N. M., Zhang, L. & Nichols, J. J. Investigation of the human tear film proteome using multiple proteomic approaches. *Molecular Vision* **14**, 456-470 (2008).
35 Bjerrum, K. Primary Sjogren's Syndrome and Keratoconjunctivitis Sicca: diagnostic methods, frequency and social disease aspects. *Acta Ophthalmologica Scandinavica* **78**, 3-37 (2000).
36 Lemp, M. A. *The Dry Eye: A Comprehensive Guide* (Springer-Verlag, 1992).
37 Asbell, P. A. & Lemp, M. A. *Dry Eye Disease: The Clinician's Guide to Diagnosis and Treatment*. (Thieme, 2006).
38 Farris, R. L., Gilbard, J. P., Stuchell, R. N. & Mandel, I. D. Diagnostic tests in keratoconjunctivitis sicca. *Eye & Contact Lens* **9**, 23 (1983).
39 Molloy, M. P. *et al.* Establishment of the human reflex tear two-dimensional polyacrylamide gel electrophoresis reference map: New proteins of potential diagnostic value. *Electrophoresis* **18**, 2811-2815 (2005).
40 Venkata Saijyothi, A. *et al.* Two dimensional electrophoretic analysis of human tears: Collection method in dry eye syndrome. *PROTEOMICS-Clinical Applications* **5**, 206-206 (2011).
41 Kuizenga, A., Van Haeringen, N. & Kijlstra, A. SDS-Minigel electrophoresis of human tears. Effect of sample treatment on protein patterns. *Investigative Ophthalmology & Visual Science* **32**, 381-386 (1991).
42 Versura, P. *et al.* Tear proteomics in evaporative dry eye disease. *Eye* **24**, 1396-1402 (2010).
43 Zhou, L. *et al.* Identification of tear fluid biomarkers in dry eye syndrome using iTRAQ quantitative proteomics. *Journal of Proteome Research* **8**, 4889-4905 (2009).
44 Teng, P., Bateman, N. W., Hood, B. L. & Conrads, T. Advances in proximal fluid proteomics for disease biomarker discovery. *Journal of Proteome Research* (2010).
45 Gasteiger, E. *et al. ExPASy: the proteomics server for in-depth protein knowledge and analysis*, <http://ca.expasy.org/tools/pi_tool.html> (2003).
46 Hekman, A. Association of lactoferrin with other proteins, as demonstrated by changes in electrophoretic mobility. *Biochimica et Biophysica Acta* **251**, 380-387 (1971).
47 Kuizenga, A., van Haeringen, N. J., Meijer, F. & Kijlstra, A. Analysis of human tear fluid components, inhibiting protein adhesion to plastic surfaces. *Experimental Eye Research* **63**, 319-328 (1996).
48 Poethke, R. *et al.* A putative enzyme from various secretions specifically inhibits antibody-antigen interactions. *Journal of Immunological Methods* **191**, 149-157 (1996).
49 Boonstra, A., Vanhaeringen, N. & Kijlstra, A. Human tears inhibit the coating of proteins to solid-phase surfaces. *Current Eye Research* **4**, 1137-1144 (1985).
50 Sack, R. A. *et al.* Membrane array characterization of 80 chemokines, cytokines, and growth factors in open- and closed-eye tears: Angiogenin and other defense system constituents. *Investigative Ophthalmology & Visual Science* **46**, 1228-1238, doi:Doi 10.1167/Iovs.04-0760 (2005).
51 Burton, M. J. Trachoma: an overview. *British Medical Bulletin* **84**, 99-116 (2007).

52 Caffery, B. *et al.* Tear lipocalin and lysozyme in Sjogren and non-Sjogren dry eye. *Optometry & Vision Science* **85**, 661 (2008).
53 An, H. J. *et al.* Glycomics analyses of tear fluid for the diagnostic detection of ocular rosacea. *Journal of Proteome Research* **4**, 1981-1987 (2005).
54 Tomosugi, N., Kitagawa, K., Takahashi, N., Sugai, S. & Ishikawa, I. Diagnostic potential of tear proteomic patterns in Sjögren's syndrome. *Journal of Proteome Research* **4**, 820-825 (2005).
55 Bjerrum, K. The ratio of albumin to lactoferrin in tear fluid as a diagnostic tool in primary Sjogren's syndrome. *Acta Ophthalmologica Scandinavica* **75**, 507-511 (1997).
56 Haeckel, R. & Hänecke, P. in *Annales de Biologie Clinique.* 903.
57 BiorepositoriesAndBiospecimenResearchBranch. in *http://biospecimens.cancer.gov/about/overview.asp* (ed National Cancer Institute) (2012).
58 Stuchell, R. N., Feldman, J. J., Farris, R. L. & Mandel, I. D. The effect of collection technique on tear composition. *Investigative Ophthalmology & Visual Science* **25**, 374-377 (1984).
59 Li, K., Chen, Z., Duan, F., Liang, J. & Wu, K. Quantification of tear proteins by SDS-PAGE with an internal standard protein: a new method with special reference to small volume tears. *Graefe's Archive for Clinical and Experimental Ophthalmology* **248**, 853-862 (2010).
60 Choy, C. K. M., Cho, P., Chung, W. Y. & Benzie, I. F. F. Water-soluble antioxidants in human tears: effect of the collection method. *Investigative Ophthalmology & Visual Science* **42**, 3130-3134 (2001).
61 Hemsley, S., Cole, N., Canfield, P. & Willcox, M. Protein microanalysis of animal tears. *Research in Veterinary Science* **68**, 207-209 (2000).
62 Tervo, T., Van Setten, G., Joutsimo, L. & Tarkkanen, A. Recommendations on the collection of tear fluid for investigations of the fibrinolytic system. *Experimental Eye Research* **53**, 809 (1991).
63 Tuft, S. & Dart, J. The measurement of IgE in tear fluid: a comparison of collection by sponge or capillary. *Acta Ophthalmologica* **67**, 301-305 (1989).
64 Hubel, A., Aksan, A., Skubitz, A. P. N., Wendt, C. & Zhong, X. State of the art in preservation of fluid biospecimens. *Biopreservation and Biobanking* **9**, 237-244 (2011).
65 Green-Church, K., Zhang, L. & Nichols, K. in *ARVO 2010 Annual Meeting, Dry Eye Session.*
66 VanDerMeid, K. R., Su, S. P., Krenzer, K. L., Ward, K. W. & Zhang, J. Z. A method to extract cytokines and matrix metalloproteinases from Schirmer strips and analyze using Luminex. *Molecular Vision* **17**, 1056 (2011).
67 Kijlstra, A., Jeurissen, S. & Koning, K. Lactoferrin levels in normal human tears. *British Journal of Ophthalmology* **67**, 199-202 (1983).
68 Karns, K. & Herr, A. E. Human tear protein analysis enabled by an alkaline microfluidic homogeneous immunoassay. *Analytical Chemistry* **83**, 8115-8122 (2011).
69 Kramann, C. *et al.* Effect of contact lenses on the protein composition in tear film: a ProteinChip study. *Graefe's Archive for Clinical and Experimental Ophthalmology* **249**, 233-243 (2011).

70 Wong, T. T. *et al.* Proteomic profiling of inflammatory signaling molecules in the tears of patients on chronic glaucoma medication. *Investigative Ophthalmology & Visual Science* **52**, 7385-7391 (2011).
71 Paulett, C. L. *Comparison of symptoms, signs, composition, and tear film dynamics in Sjögrens vs. Non-Sjögrens subjects* Master of Science thesis, The Ohio State University, (2010).
72 Chong, R. S. *et al.* Tear cytokine profile in medicated glaucoma patients: effect of monocyte chemoattractant protein 1 on early posttrabeculectomy outcome. *Ophthalmology* **117**, 2353-2358 (2010).
73 Li, K., Liu, X., Chen, Z., Huang, Q. & Wu, K. Quantification of tear proteins and sPLA2-IIa alteration in patients with allergic conjunctivitis. *Molecular Vision* **16**, 2084 (2010).
74 Remington, S. G., Crow, J. M. & Nelson, J. D. Antibodies to endogenous tear protein in normal human tears. *Current Eye Research* **34**, 819-823 (2009).
75 Inada, N., Shoji, J., Hoshino, M. & Sawa, M. Evaluation of total and allergen-specific secretory IgA in tears of allergic conjunctival disease patients. *Japanese Journal of Ophthalmology* **51**, 338-342 (2007).
76 Peral, A., Carracedo, G., Acosta, M. C., Gallar, J. & Pintor, J. Increased levels of diadenosine polyphosphates in dry eye. *Investigative Ophthalmology & Visual Science* **47**, 4053-4058 (2006).
77 Chisholm, D. M. & Mason, D. K. Labial salivary gland biopsy in Sjogren's disease. *Journal of Clinical Pathology* **21**, 656-660 (1968).
78 Hoshino, M., Shoji, J., Inada, N., Sawa, M. & Kato, H. Clinical evaluation of a measurement method for secretory IgA in tears. *Nippon Ganka Gakkai Zasshi* **110**, 276 (2006).
79 Grus, F. H. *et al.* SELDI-TOF-MS ProteinChip array profiling of tears from patients with dry eye. *Investigative Ophthalmology & Visual Science* **46**, 863-876 (2005).
80 Shoji, J., Kato, H., Kitazawa, M., Inada, N. & Sawa, M. Evaluation of staphylococcal enterotoxin-specific IgE antibody in tears in allergic keratoconjunctival disorders. *Japanese Journal of Ophthalmology* **47**, 609-611 (2003).
81 Pintor, J., Carracedo, G., Alonso, C. M., Bautista, A. & Peral, A. Presence of diadenosine polyphosphates in human tears. *Pflügers Archiv European Journal of Physiology* **443**, 432-436 (2002).
82 Shoji, J. *et al.* Efficacy of tear eosinophil cationic protein level measurement using filter paper for diagnosing allergic conjunctival disorders. *Japanese Journal of Ophthalmology* **47**, 64-68 (2003).
83 Shoji, J., Inada, N. & Sawa, M. Antibody array-generated cytokine profiles of tears of patients with vernal keratoconjunctivitis or giant papillary conjunctivitis. *Japanese Journal of Ophthalmology* **50**, 195-204 (2006).
84 Zhao, H., Jumblatt, J. E., Wood, T. O. & Jumblatt, M. M. Quantification of MUC5AC protein in human tears. *Cornea* **20**, 873 (2001).
85 Jumblatt, M. M., McKenzie, R. W. & Jumblatt, J. E. MUC5AC mucin is a component of the human precorneal tear film. *Investigative Ophthalmology & Visual Science* **40**, 43-49 (1999).

86 Barka, T., Asbell, P. A., van der Noen, H. & Prasad, A. Cystatins in human tear fluid. *Current Eye Research* **10**, 25-34 (1991).
87 Farris, R. L., Stuchell, R. N. & Mandel, I. Tear osmolarity variation in the dry eye. *Transactions of the American Ophthalmological Society* **84**, 250 (1986).
88 Boonstra, A. *et al.* Factors influencing the quantitative determination of tear proteins by high performance liquid chromatography. *Current Eye Research* **7**, 893-901 (1988).
89 Kitaoka, M., Nakazawa, M. & Hayasaka, S. Lysosomal enzymes in human tear fluid collected by filter paper strips. *Experimental Eye Research* **41**, 259-265 (1985).
90 Truskey, G. A., Yuan, F. & Katz, D. F. *Transport Phenomena in Biological Systems*. Vol. 82 (Pearson Prentice Hall 2004).
91 Wimpenny, J. W. T. *CRC Handbook of Laboratory Model Systems for Microbial Ecosystems*. Vol. 2 (CRC, 1988).
92 Culbertson, C. T., Jacobson, S. C. & Michael Ramsey, J. Diffusion coefficient measurements in microfluidic devices. *Talanta* **56**, 365-373 (2002).
93 Querinjean, P., Masson, P. L. & Heremans, J. F. Molecular weight, single-chain structure and amino acid composition of human lactoferrin. *European Journal of Biochemistry* **20**, 420-425 (1971).
94 RCSB_Protein_Data_Bank_(PDB). (http://www.rcsb.org/pdb/home/home.do).
95 SWISS-MODEL_Repository. (http://swissmodel.expasy.org/repository/).
96 Street, T. O., Bolen, D. W. & Rose, G. D. A molecular mechanism for osmolyte-induced protein stability. *Proceedings of the National Academy of Sciences of the United States of America* **103**, 13997-14002 (2006).
97 Tragoulias, S. T., Anderton, P. J., Dennis, G. R., Miano, F. & Millar, T. J. Surface pressure measurements of human tears and individual tear film components indicate that proteins are major contributors to the surface pressure. *Cornea* **24**, 189-200 (2005).
98 Glantz, S. A. *Primer of Biostatistics*. Vol. 309 (McGraw-Hill 1992).
99 Denisin, A. K., Karns, K. & Herr, A. Post-collection processing of Schirmer strip-collected human tear fluid impacts protein content. *Analyst* **137**, 5088-5096 (2012).
100 Dixit, C. K., Vashist, S. K., MacCraith, B. D. & O'Kennedy, R. Evaluation of apparent non-specific protein loss due to adsorption on sample tube surfaces and/or altered immunogenicity. *Analyst* **136**, 1406-1411 (2011).
101 Kang, J. S., Shim, J. K., Huh, H. & Lee, Y. M. Colloidal adsorption of bovine serum albumin on porous polypropylene-g-poly (2-hydroxyethyl methacrylate) membrane. *Langmuir* **17**, 4352-4359 (2001).
102 He, X. C. *et al.* Reducing protein fouling of a polypropylene microporous membrane by CO2 plasma surface modification. *Desalination* **244**, 80-89 (2009).
103 Andrade, J. & Hlady, V. Protein adsorption and materials biocompatibility: a tutorial review and suggested hypotheses. *Biopolymers/Non-Exclusion HPLC* **79**, 1-63 (1986).
104 Gin, J. & Wong, V. G. (Google Patents, 1991).
105 Baum, J. L., Isenberg, S. J. & Apt, L. Basal vs reflex lacrimation. *Archives of Ophthalmology* **117**, 141 (1999).
106 Lam, D. K. T., Wong, V. W. Y., Chow, V. W. S. & Chi, S. C. C. Epidemiology of dry eye syndrome in Hong Kong: a cross-sectional population-based study. *Surgery* **15**, 58-62.

107 Salas, C., Rojas, O. J., Lucia, L. A., Hubbe, M. A. & Genzer, J. Adsorption of glycinin and β-conglycinin on silica and cellulose: surface interactions as a function of denaturation, pH, and electrolytes. *Biomacromolecules* **13**, 387-396 (2012).
108 Song, J., Yamagushi, T., Silva, D. J., Hubbe, M. A. & Rojas, O. J. Effect of charge asymmetry on adsorption and phase separation of polyampholytes on silica and cellulose surfaces. *The Journal of Physical Chemistry B* **114**, 719-727 (2009).
109 Caldwell, K. D., Axén, R., Wall, M. B. & Porath, J. Immobilization of enzymes based on hydrophobic interaction. I. Preparation and properties of a β-amylase adsorbate. *Biotechnology and Bioengineering* **18**, 1573-1588 (2004).
110 Lemp, A. Report of the National Eye Institute/Industry workshop on clinical trials in dry eyes. *Eye & Contact Lens* **21**, 221-232 (1995).
111 Lemp, M. A. The definition and classification of dry eye disease: report of the Definition and Classification Subcommittee of the International Dry Eye WorkShop (2007). *The Ocular Surface* **5**, 75-92 (2007).
112 De Paiva, C. S. *et al.* Corticosteroid and doxycycline suppress MMP-9 and inflammatory cytokine expression, MAPK activation in the corneal epithelium in experimental dry eye. *Experimental Eye Research* **83**, 526 (2006).
113 Graham, J. E. *et al.* Attitudes towards diagnostic tests and therapies for dry eye disease. *Ophthalmic Research* **43**, 11-17 (2010).
114 Foulks, G. N. & Borchman, D. Meibomian gland dysfunction: The past, present, and future. *Eye & Contact Lens* **36**, 249 (2010).
115 Daniels, T. E. Sjogren's syndrome: clinical spectrum and current diagnostic controversies. *Advances in Dental Research* **10**, 3-8 (1996).
116 Zierhut, M., Dana, M. R., Stern, M. E. & Sullivan, D. A. Immunology of the lacrimal gland and ocular tear film. *Trends in Immunology* **23**, 333-335 (2002).
117 Fox, R. & Saito, I. in *Autoimmune Diseases of the Skin* 261-289 (Springer, 2005).
118 Fox, R. I., Robinson, C. A., Curd, J. G., Kozin, F. & Howelly, F. V. Sjögren's syndrome. Proposed criteria for classification. *Arthritis & Rheumatism* **29**, 577-585 (1986).
119 Vitali, C. *et al.* Classification criteria for Sjögren's syndrome: a revised version of the European criteria proposed by the American-European Consensus Group. *Annals of the Rheumatic Diseases* **61**, 554-558 (2002).
120 Daniels, T. & Fox, P. Salivary and oral components of Sjogren's syndrome. *Rheumatic Diseases Clinics of North America* **18**, 571 (1992).
121 Small, D. *Sjögren's FAQs* <http://www.sjogrens.org/home/about-sjogrens-syndrome/sjoegrens-faqs> (2009).
122 Fujihara, T., Nagano, T., Nakamura, M. & Shirasawa, E. Lactoferrin suppresses loss of corneal epithelial integrity in a rabbit short-term dry eye model. *Journal of Ocular Pharmacology and Therapeutics* **14**, 99-107 (1998).
123 Adlerova, L., Bartoskova, A. & Faldyna, M. Lactoferrin: a review. *Veterinarni Medicina* **53**, 457-468 (2008).
124 Noble, B. A. *et al.* Comparison of autologous serum eye drops with conventional therapy in a randomised controlled crossover trial for ocular surface disease. *British Journal of Ophthalmology* **88**, 647-652 (2004).

125 Tsubota, K. *et al.* Treatment of dry eye by autologous serum application in Sjögren's syndrome. *British Journal of Ophthalmology* **83**, 390-395 (1999).
126 Steijns, J. M. & van Hooijdonk, A. C. Occurrence, structure, biochemical properties and technological characteristics of lactoferrin. *British Journal of Nutrition* **84 Suppl 1**, S11-17 (2000).
127 Sun, X. L., Baker, H. M., Shewry, S. C., Jameson, G. B. & Baker, E. N. in *Acta Crystallographica Section D* Vol. 55 403-407 (Protein Data Bank, 1999).
128 Sun, X. L., Baker, H. M., Shewry, S. C., Jameson, G. B. & Baker, E. N. Structure of recombinant human lactoferrin expressed in Aspergillus awamori. *Acta Crystallographica Section D: Biological Crystallography* **55**, 403-407 (1999).
129 Janssen, P. T. & Vanbijsterveld, O. P. A simple test for lacrimal gland-function - a tear lactoferrin assay by radial immunodiffusion. *Graefe's Archive for Clinical and Experimental Ophthalmology* **220**, 171-174 (1983).
130 Mccollum, C. J. *et al.* Rapid assay of lactoferrin in keratoconjunctivitis sicca. *Cornea* **13**, 505-508 (1994).
131 el-Rakhawy, K. E., Zayed, A. I. & van Bijsterveld, O. P. Tear function in relation to the World Health Organization classification of cicatrization in trachoma. *International Ophthalmology* **12**, 31-35 (1988).
132 Herr, A. E. *et al.* Microfluidic immunoassays as rapid saliva-based clinical diagnostics. *Proceedings of the National Academy of Sciences of the United States of America* **104**, 5268-5273 (2007).
133 Colyer, C. L., Mangru, S. D. & Harrison, D. J. Microchip-based capillary electrophoresis of human serum proteins. *Journal of Chromatography A* **781**, 271-276 (1997).
134 Herr, A. E., Throckmorton, D. J., Davenport, A. A. & Singh, A. K. On-chip native gel electrophoresis-based immunoassays for tetanus antibody and toxin. *Analytical Chemistry* **77**, 585-590 (2005).
135 Schmalzing, D., Koutny, L. B., Taylor, T. A., Nashabeh, W. & Fuchs, M. Immunoassay for thyroxine (T4) in serum using capillary electrophoresis and micromachined devices. *Journal of Chromatography B: Biomedical Sciences and Applications* **697**, 175-180 (1997).
136 Phillips, T. M. & Wellner, E. F. Measurement of naproxen in human plasma by chip-based immunoaffinity capillary electrophoresis. *Biomedical Chromatography* **20**, 662-667 (2006).
137 Phillips, T. M. Rapid analysis of inflammatory cytokines in cerebrospinal fluid using chip-based immunoaffinity electrophoresis. *Electrophoresis* **25**, 1652-1659 (2004).
138 Cheng, S. B. *et al.* Development of a multichannel microfluidic analysis system employing affinity capillary electrophoresis for immunoassay. *Analytical Chemistry* **73**, 1472-1479 (2001).
139 Kagebayashi, C. *et al.* Automated immunoassay system for AFP-L3% using on-chip electrokinetic reaction and separation by affinity electrophoresis. *Analytical Biochemistry* **388**, 306-311 (2009).

140 Kawabata, T., Wada, H. G., Watanabe, M. & Satomura, S. "Electrokinetic Analyte Transport Assay" for alpha-fetoprotein immunoassay integrates mixing, reaction and separation on-chip. *Electrophoresis* **29**, 1399-1406 (2008).
141 Apori, A. A. & Herr, A. E. Homogeneous immunosubtraction integrated with sample preparation enabled by a microfluidic format. *Analytical Chemistry* **83**, 2691-2698 (2011).
142 Hou, C. L. & Herr, A. E. Ultrashort Separation Length Homogeneous Electrophoretic Immunoassays Using On-Chip Discontinuous Polyacrylamide Gels. *Analytical Chemistry* **82**, 3343-3351, doi:Doi 10.1021/Ac100182j (2010).
143 Colyer, C. L., Mangru, S. D. & Harrison, D. J. Microchip-based capillary electrophoresis of human serum proteins. *J Chromatogr A* **781**, 271-276 (1997).
144 Herr, A. E. *et al.* Integrated microfluidic platform for oral diagnostics. *Annals of the New York Academy of Sciences* **1098**, 362-374 (2007).
145 He, M. & Herr, A. E. Microfluidic polyacrylamide gel electrophoresis with in situ immunoblotting for native protein analysis. *Analytical Chemistry* **81**, 8177-8184 (2009).
146 Meagher, R. J., Hatch, A. V., Renzi, R. F. & Singh, A. K. An integrated microfluidic platform for sensitive and rapid detection of biological toxins. *Lab on a Chip* **8**, 2046-2053 (2008).
147 Unknown. *Tear Wallpaper*, <http://wallpaperswide.com/tear-wallpapers.html > (2012).
148 Su, C., Wang, F., Ciolek, D. & Pan, Y. C. E. Electrophoresis of proteins and protein-protein complexes in native polyacrylamide gels using a horizontal gel apparatus. *Analytical Biochemistry* **223**, 93-98 (1994).
149 Good, N. E. *et al.* Hydrogen ion buffers for biological research. *Biochemistry* **5**, 467-477 (1966).
150 Zais, D. P. & Roberts, R. C. System for simplified discontinuous-gradient polyacrylamide-gel electrophoresis. *Clinical Chemistry* **23**, 590-592 (1977).
151 Kaltschmidt, E. & Wittmann, H. G. Ribosomal proteins, XII. Number of proteins in small and large ribosomal subunits of Escherichia coli as determined by two-dimensional gel electrophoresis. *Proceedings of the National Academy of Sciences of the United States of America* **67**, 1276-1282 (1970).
152 Whitcher, J. P. *et al.* A simplified quantitative method for assessing keratoconjunctivitis sicca From the Sjögren's syndrome international registry. *American Journal of Ophthalmology* **149**, 405-415 (2010).
153 Klaeger, A. J., Whitcher, J. P. & Daniels, T. E. Tear lysozyme activity in frozen Schirmer strips and salivary gland biopsy as parameters of lacrimal gland function. *Ocular Immunology and Inflammation* **7**, 3-6 (1999).
154 Sitaramamma, T., Shivaji, S. & Rao, G. N. Effect of storage on protein concentration of tear samples. *Current Eye Research* **17**, 1027-1035 (1998).
155 Menter, P. *Acrylamide Polymerization — A Practical Approach*, <http://www.biocompare.com/Articles/ApplicationNote/1089/Acrylamide-Polymerization-%E2%80%94-A-Practical-Approach.html> (2000).
156 Young, R. J. & Lovell, P. A. *Introduction to Polymers*. Second Edition edn, (CRC Press, 1991).

157 Wako-Chemicals. in *http://www.wako-chem.co.jp/specialty/waterazo/VA-086.htm* (ed Wako Pure Chemical Industries) (2006).
158 Johnson, I. & Spence, M. T. Z. *Alexa Fluor dyes spanning the visible and infrared spectrum*, <http://www.invitrogen.com/site/us/en/home/References/Molecular-Probes-The-Handbook/Fluorophores-and-Their-Amine-Reactive-Derivatives/Alexa-Fluor-Dyes-Spanning-the-Visible-and-Infrared-Spectrum.html#head8> (
159 Shimazaki, K. *et al.* Analysis of human and bovine milk lactoferrins by Rotofor and chromatofocusing. *International Journal of Biochemistry* **25**, 1653-1658 (1993).
160 van Berkel, P. H. C. *Struture-function Studies of Human Lactoferrin*, University of Leiden, (1998).
161 Kijlstra, A., Kuizenga, A., Vandervelde, M. & Vanhaeringen, N. J. Gel-electrophoresis of human tears reveals various forms of tear lactoferrin. *Current Eye Research* **8**, 581-588 (1989).
162 Persat, A., Chambers, R. D. & Santiago, J. G. Basic principles of electrolyte chemistry for microfluidic electrokinetics. Part I: Acid-base equilibria and pH buffers. *Lab on a Chip* **9**, 2437-2453 (2009).
163 Taipa, M. A. Immunoassays: biological tools for high throughput screening and characterisation of combinatorial libraries. *Comb Chem High Throughput Screen* **11**, 325-335 (2008).
164 Kurenkov, V. F., Hartan, H. G. & Lobanov, F. I. Alkaline hydrolysis of polyacrylamide. *Russian Journal of Applied Chemistry* **74**, 543-554 (2001).
165 Geisthardt, D. & Kruppa, J. Polyacrylamide gel electrophoresis: reaction of acrylamide at alkaline pH with buffer components and proteins. *Analytical Biochemistry* **160**, 184-191 (1987).
166 Currie, D. J., Dainton, F. S. & Watt, W. S. The effect of pH on the polymerization of acrylamide in water. *Polymer* **6**, 451-453 (1965).
167 Cowie, J. M. G. & Arrighi, V. *Polymers: Chemistry and Physics of Modern Materials*. Third Edition edn, (CRC Press, Taylor & Francis Group, 2008).
168 Valdebenito, A. & Encinas, M. V. Chain transfer agents in vinyl polymerizations photoinduced by bimolecular photoinitiators. *Journal of Photochemistry & Photobiology A* **194**, 206-211 (2008).
169 Olabisi, O. *Handbook of Thermoplastics*. 1053 (CRC Press, 1997).
170 Bosisio, A. B., Loeherlein, C., Snyder, R. S. & Righetti, P. G. Titration curves of proteins by combined isoelectric focusing-electrophoresis in highly porous polyacrylamide matrices. *Journal of Chromatography A* **189**, 317-330 (1980).
171 St. Kenyeres, J. & Ursu, V. Polyacrylamide .1. Polymer Content and Hydrolysis Level Determination by Potentiometric Titration. *Journal of Polymer Science Part A-1* **18**, 275-281 (1980).
172 Kudryavtsev, Y. V., Litmanovich, A. D. & Plate, N. A. On the kinetics of polyacrylamide alkaline hydrolysis. *Macromolecules* **31**, 4642-4644 (1998).
173 Zeynali, M. E. & Rabbii, A. Alkaline hydrolysis of polyacrylamide and study on poly(acrylamide-co-sodium acrylate) properties. *Iranian Polymer Journal* **11**, 269-275 (2002).

174 van Berkel, P. H. C., van Veen, H. A., Geerts, M. E. J. & Nuijens, J. H. Characterization of monoclonal antibodies against human lactoferrin. *Journal of Immunological Methods* **267**, 139-150 (2002).
175 Ng, A. H., Uddayasankar, U. & Wheeler, A. R. Immunoassays in microfluidic systems. *Analytical and Bioanalytical Chemistry* **397**, 991-1007 (2010).
176 Bright, A. M. & Tighe, B. J. The composition and interfacial properties of tears, tear substitutes and tear models *Contact Lens and Anterior Eye* **16**, 57-66 (1993).
177 Stuchell, R. N., Feldman, J. J., Farris, R. L. & Mandel, I. D. The effect of collection technique on tear composition. *Invest Ophthalmol Vis Sci* **25**, 374-377 (1984).
178 Esmaeelpour, M., Cai, J., Watts, P., Boulton, M. & Murphy, P. J. Tear sample collection using cellulose acetate absorbent filters. *Ophthalmic and Physiological Optics* **28**, 577-583 (2008).
179 Farris, R. L. Tear osmolarity—a new gold standard. *Advances in Experimental Medicine and Biology* **350**, 495-503 (1994).
180 Tomlinson, A., Khanal, S., Ramaesh, K., Diaper, C. & McFadyen, A. Tear film osmolarity: determination of a referent for dry eye diagnosis. *Investigative Ophthalmology & Visual Science* **47**, 4309-4315 (2006).
181 Versura, P., Profazio, V. & Campos, E. Performance of tear osmolarity compared to previous diagnostic tests for dry eye diseases. *Current Eye Research* **35**, 553-564 (2010).
182 Narayanan, S. Osmolarity: A diagnostic test for dry eye. *Review of Optometry* (2011).
183 Nichols, K. K. Tear Film Osmolality - A Newer Gold Standard? *Contact Lens Spectrum* (2005).
184 Tomlinson, A., McCann, L. C. & Pearce, E. I. Comparison of human tear film osmolarity measured by electrical impedance and freezing point depression techniques. *Cornea* **29**, 1036-1041 (2010).
185 Li, S. *et al.* Small proline-rich protein 1B (SPRR1B) is a biomarker for squamous metaplasia in dry eye disease. *Investigative Ophthalmology & Visual Science* **49**, 34-41, doi:10.1167/iovs.07-0685 (2008).
186 Hu, S. *et al.* Identification of autoantibody biomarkers for primary Sjögren's syndrome using protein microarrays. *Proteomics* **11**, 1499-1507 (2011).
187 Shen, L. *et al.* Novel autoantibodies in Sjogren's syndrome. *Clinical Immunology* (2012).
188 Chen, Y. T. *et al.* Immune profile of squamous metaplasia development in autoimmune regulator-deficient dry eye. *Molecular Vision* **15**, 563 (2009).
189 De Franceschi, L. *et al.* Proteome analysis of biological fluids from autoimmune rheumatological disorders. *PROTEOMICS-Clinical Applications* **5**, 78-89 (2011).
190 DeVoss, J. J. *et al.* An autoimmune response to odorant binding protein 1a is associated with dry eye in the Aire-deficient mouse. *The Journal of Immunology* **184**, 4236-4246 (2010).
191 Haneji, N. *et al.* Identification of α-fodrin as a candidate autoantigen in primary Sjögren's syndrome. *Science* **276**, 604-607 (1997).
192 Sordet, C. *et al.* Anti-α-fodrin autoantibodies are not useful diagnostic markers of primary Sjögren's syndrome. *Annals of the Rheumatic Diseases* **64**, 1244-1245 (2005).

193 Yanagi, K. *et al.* Anti-120-kDa α-fodrin immune response with Th1-cytokine profile in the NOD mouse model of Sjögren's syndrome. *European Journal of Immunology* **28**, 3336-3345 (1998).
194 Kuroda, N. *et al.* Development of autoimmunity against transcriptionally unrepressed target antigen in the thymus of Aire-deficient mice. *The Journal of Immunology* **174**, 1862-1870 (2005).
195 Li, D. *et al.* Follistatin-like protein 1 is elevated in systemic autoimmune diseases and correlated with disease activity in patients with rheumatoid arthritis. *Arthritis Research and Therapy* **13**, R17 (2011).
196 Yamaoka, K., Miyasaka, N. & Yamamoto, K. Possible involvement of epstein-barr virus in polyclonal b cell activation in Sjögren's syndrome. *Arthritis & Rheumatism* **31**, 1014-1021 (2005).
197 Tam, C., Mun, J. J., Evans, D. J. & Fleiszig, S. M. J. Cytokeratins mediate epithelial innate defense through their antimicrobial properties. *The Journal of Clinical Investigation*, 0-0 (2012).
198 Solomon, A. W., Peeling, R. W., Foster, A. & Mabey, D. C. W. Diagnosis and assessment of trachoma. *Clinical Microbiology Reviews* **17**, 982-1011 (2004).
199 Michel, C. E. C. *et al.* Field evaluation of a rapid point-of-care assay for targeting antibiotic treatment for trachoma control: a comparative study. *The Lancet* **367**, 1585-1590 (2006).
200 Buisman, N. J. F., Ossewaarde, J. M., Rieffe, M., Loon, A. M. & Stilma, J. S. Chlamydia keratoconjunctivitis determination of Chlamydia trachomatis specific secretory immunoglobulin A in tears by enzyme immunoassay. *Graefe's Archive for Clinical and Experimental Ophthalmology* **230**, 411-415 (1992).
201 Dean, D., Kandel, R. P., Adhikari, H. K. & Hessel, T. Multiple Chlamydiaceae species in trachoma: implications for disease pathogenesis and control. *PLoS Medicine* **5**, e14 (2008).
202 Thomae, M. Co-development and Regulatory Approval of Drugs, Devices and Diagnostics. *American Course on Drug Development and Regulatory Sciences* (June 14, 2011).
203 Center_for_Disease_Control. (ed Centers_for_Medicare_&_Medicaid_Services) (http://www.cms.gov/Regulations-and-Guidance/Legislation/CLIA/Downloads/HowObtainCLIACertificate.pdf, 2006).
204 (ed Centers for Medicare & Medicaid Services) (CMS.gov, http://www.cms.gov/Regulations-and-Guidance/Legislation/CLIA/How_to_Apply_for_a_CLIA_Certificate_International_Laboratories.html, 2012).
205 (ed Centers for Medicare & Medicaid Services) (http://www.cms.gov/Regulations-and-Guidance/Legislation/CLIA/Downloads/waivetbl.pdf, 2012).
206 in *GLOBE NEWSWIRE* (http://www.globenewswire.com/newsarchive/tear/xml/nitf.html?d=243546, San Diego, Jan. 24, 2012).

207 (ed Centers for Medicare & Medicaid Services) (http://www.cms.gov/Regulations-and-Guidance/Legislation/CLIA/Downloads/6064bk.pdf, 2012).
208 (ed Centers for Medicare & Medicaid Services) (http://www.cms.gov/Regulations-and-Guidance/Legislation/CLIA/Downloads/6063bk.pdf, 2012).
209 (ed US Food and Drug Administration) (http://www.fda.gov/AboutFDA/CentersOffices/default.htm, 2012).
210 (ed US Food and Drug Administration) (http://www.fda.gov/AboutFDA/CentersOffices/OfficeofMedicalProductsandTobacco/CDRH/CDRHOffices/ucm127854.htm, 2012).
211 Lemp, M. A. in *Second International Conference on the Lacrimal Gland, Tear Film and Dye Eye Syndromes.* (eds David A. Sullivan, Darlene A. Dartt, & Michael A. Meneray) (Plenum Press).
212 Duncombe, T. A. & Herr, A. E. Polyacrylamide gel moving boundary electrophoresis enables low-power protein analysis in a compact microdevice. *Analytical Chemistry* **84**, 8740-8747 (2012).
213 Breslauer, D. N., Maamari, R. N., Switz, N. A., Lam, W. A. & Fletcher, D. A. Mobile phone based clinical microscopy for global health applications. *PLoS One* **4**, e6320 (2009).
214 Renzi, R. F. *et al.* Hand-held microanalytical instrument for chip-based electrophoretic separations of proteins. *Analytical Chemistry* **77**, 435-441 (2005).
215 Kaigala, G. *et al.* Inexpensive, universal serial bus-powered and fully portable lab-on-a-chip-based capillary electrophoresis instrument. *Nanobiotechnology, IET* **3**, 1-7 (2009).
216 Poste, G. Bring on the biomarkers. *Nature* **469**, 156-157 (2011).
217 Mandrekar, S. J. & Sargent, D. J. Clinical trial designs for predictive biomarker validation: theoretical considerations and practical challenges. *Journal of Clinical Oncology* **27**, 4027 (2009).
218 Prous, J. & Williams, C. Drug discovery, personalized medicine and Thomson Reuters. *Thomson Reuters White Paper* (2010).
219 Taube, S. E. *et al.* A perspective on challenges and issues in biomarker development and drug and biomarker codevelopment. *Journal of the National Cancer Institute* **101**, 1453 (2009).
220 Jorkasky, D. Developing drugs from first in human dosing to understanding dose-response. *American Course on Drug Development and Regulatory Sciences* (2011).
221 Herr, A. E. *et al.* Microfluidic immunoassays as rapid saliva-based clinical diagnostics. *Proceedings of the National Academy of Sciences* **104**, 5268 (2007).
222 Chiem, N. H. & Harrison, D. J. Microchip systems for immunoassay: an integrated immunoreactor with electrophoretic separation for serum theophylline determination. *Clinical chemistry* **44**, 591 (1998).
223 Qiu, C. X. & Harrison, D. J. Integrated self calibration via electrokinetic solvent proportioning for microfluidic immunoassays. *Electrophoresis* **22**, 3949-3958 (2001).
224 Yue, G. E. *et al.* Protein digestion and phosphopeptide enrichment on a glass microchip. *Analytica chimica acta* **564**, 116-122 (2006).
225 Henkin, T. M. Riboswitch RNAs: using RNA to sense cellular metabolism. *Genes & Development* **22**, 3383 (2008).

226 Nahvi, A. *et al.* Genetic control by a metabolite binding mRNA. *Chemistry & biology* **9**, 1043-1049 (2002).
227 Edwards, A. L. & Batey, R. T. Riboswitches: a common RNA regulatory element. *Nature Education* **3**, 9 (2010).
228 Breaker, R. R. Prospects for riboswitch discovery and analysis. *Molecular Cell* **43**, 867-879 (2011).
229 Wickiser, J. K., Winkler, W. C., Breaker, R. R. & Crothers, D. M. The speed of RNA transcription and metabolite binding kinetics operate an FMN riboswitch. *Molecular Cell* **18**, 49-60 (2005).
230 Winkler, W. C. & Breaker, R. R. Regulation of bacterial gene expression by riboswitches. *Annual Review of Microbiology* **59**, 487-517 (2005).
231 Barrick, J. E. *et al.* New RNA motifs suggest an expanded scope for riboswitches in bacterial genetic control. *Proceedings of the National Academy of Sciences of the United States of America* **101**, 6421 (2004).
232 Weinberg, Z. *et al.* Identification of 22 candidate structured RNAs in bacteria using the CMfinder comparative genomics pipeline. *Nucleic Acids Research* **35**, 4809-4819 (2007).
233 Weinberg, Z. *et al.* Comparative genomics reveals 104 candidate structured RNAs from bacteria, archaea, and their metagenomes. *Genome Biology* **11**, R31 (2010).
234 Winkler, W. C., Nahvi, A., Roth, A., Collins, J. A. & Breaker, R. R. Control of gene expression by a natural metabolite-responsive ribozyme. *Nature* **428**, 281-286 (2004).
235 Mandal, M. *et al.* A glycine-dependent riboswitch that uses cooperative binding to control gene expression. *Science Signalling* **306**, 275 (2004).
236 Regulski, E. E. & Breaker, R. R. In-line probing analysis of riboswitches. *Methods in Molecular Biology* **419**, 53 (2008).
237 Shanahan, C. A., Gaffney, B. L., Jones, R. A. & Strobel, S. A. Differential analog binding by two classes of c-di-GMP riboswitches. *Journal of the American Chemical Society* (2011).
238 Heppell, B., Mulhbacher, J., Penedo, J. C. & Lafontaine, D. A. Application of fluorescent measurements for characterization of riboswitch-ligand interactions. *Methods in Molecular Biology* **540**, 25-37 (2009).
239 Haller, A., Rieder, U., Aigner, M., Blanchard, S. C. & Micura, R. Conformational capture of the SAM-II riboswitch. *Nature Chemical Biology* **7**, 393-400 (2011).
240 Gilbert, S. D. & Batey, R. T. Monitoring RNA–ligand interactions using isothermal titration calorimetry. *Methods in Molecular Biology* **540**, 97-114 (2009).
241 Roth, A. *et al.* A riboswitch selective for the queuosine precursor preQ1 contains an unusually small aptamer domain. *Nature Structural & Molecular Biology* **14**, 308-317 (2007).
242 Fried, M. G. Measurement of protein-DNA interaction parameters by electrophoresis mobility shift assay. *Electrophoresis* **10**, 366-376 (1989).
243 Chen, B., Zuo, X., Wang, Y. X. & Dayie, T. K. Multiple conformations of SAM-II riboswitch detected with SAXS and NMR spectroscopy. *Nucleic Acids Research* **40**, 3117-3130 (2012).
244 Heppell, B. & Lafontaine, D. A. Folding of the SAM aptamer is determined by the formation of a K-turn-dependent pseudoknot. *Biochemistry* **47**, 1490-1499 (2008).

245 Meyer, M. M. *et al.* Challenges of ligand identification for riboswitch candidates. *RNA Biology* **8**, 5 (2011).
246 Miller, O. J. *et al.* High-resolution dose–response screening using droplet-based microfluidics. *Proceedings of the National Academy of Sciences of the United States of America* **109**, 378-383 (2012).
247 Chung, K. *et al.* A microfluidic array for large-scale ordering and orientation of embryos. *Nature Methods* **8**, 171-176 (2010).
248 Lecault, V. *et al.* High-throughput analysis of single hematopoietic stem cell proliferation in microfluidic cell culture arrays. *Nature Methods* **8**, 581-586 (2011).
249 Nagrath, S. *et al.* Isolation of rare circulating tumour cells in cancer patients by microchip technology. *Nature* **450**, 1235-1239 (2007).
250 Dixon, N. *et al.* Reengineering orthogonally selective riboswitches. *Proceedings of the National Academy of Sciences of the United States of America* **107**, 2830-2835 (2010).
251 Paige, J. S., Nguyen-Duc, T., Song, W. & Jaffrey, S. R. Fluorescence imaging of cellular metabolites with RNA. *Science* **335**, 1194-1194 (2012).
252 Blount, K. F. & Breaker, R. R. Riboswitches as antibacterial drug targets. *Nature Biotechnology* **24**, 1558-1564 (2006).
253 Herr, A. E. & Singh, A. K. Photopolymerized cross-linked polyacrylamide gels for on-chip protein sizing. *Analytical Chemistry* **76**, 4727-4733 (2004).
254 Giddings, J. C. *Unified Separation Science*. (Wiley New York etc, 1991).
255 Winkler, W. C., Nahvi, A., Sudarsan, N., Barrick, J. E. & Breaker, R. R. An mRNA structure that controls gene expression by binding S-adenosylmethionine. *Nat. Struct. Biol.* **10**, 701-707 (2003).
256 Rio, D. C., Ares, M. & Nilsen, T. W. *RNA: A Laboratory Manual*. (Cold Spring Harbor Laboratory Press, 2010).
257 Willkomm, D., Hartmann, R., Bindereif, A., Schon, A. & Westhof, E. *Handbook of RNA Biochemistry*. Vol. 1 (Wiley, 2005).
258 ThermoFisherScientific. in *http://www.piercenet.com/files/TR0031-Calc-FP-ratios.pdf* (Pierce Biotechnology, Rockford, 2011).
259 Wood, B. in *http://tools.invitrogen.com/content/sfs/COAPDFs/2012/1141015_A30634.pdf* (ed Molecular Probes) (Life Technologies Corporation, 2011).
260 Invitrogen. in *http://www.invitrogen.com/etc/medialib/en/filelibrary/cell_tissue_analysis/pdfs.Par.87420.File.tmp/O-063190-Alexa-Fluor-SelectionGuide.pdf* (Molecular Probes: invitrogen detection technologies, 2005).
261 Winkler, W. C., Nahvi, A., Sudarsan, N., Barrick, J. E. & Breaker, R. R. An mRNA structure that controls gene expression by binding S-adenosylmethionine. *Nature Structural Biology* **10**, 701-707 (2003).
262 Woodson, S. A. & Koculi, E. Analysis of RNA folding by native polyacrylamide gel electrophoresis. *Methods in Enzymology* **469**, 189-208 (2009).

263 Murray, A. in *https://moore.jcvi.org/moore/SingleOrganism.do?speciesTag=PI23P* (Gordon and Betty Moore Foundation Marine Microbial Genome Sequencing Project, 2005).
264 Carreto, L. *et al.* Rubrobacter xylanophilus sp. nov., a new thermophilic species isolated from a thermally polluted effluent. *International Journal of Systematic Bacteriology* **46**, 460-465 (1996).
265 Tucker, M. P., Mohagheghi, A., Grohmann, K. & Himmel, M. E. Ultra-thermostable cellulases from Acidothermus cellulolyticus: comparison of temperature optima with previously reported cellulases. *Nature Biotechnology* **7**, 817-820 (1989).
266 Wu, M. *et al.* Life in hot carbon monoxide: the complete genome sequence of Carboxydothermus hydrogenoformans Z-2901. *PLoS Genetics* **1**, e65 (2005).
267 Hayes, R. L. *et al.* Magnesium fluctuations modulate RNA dynamics in the SAM-I riboswitch. *Journal of the American Chemical Society* (2012).
268 Mandal, M., Boese, B., Barrick, J. E., Winkler, W. C. & Breaker, R. R. Riboswitches control fundamental biochemical pathways in Bacillus subtilis and other bacteria. *Cell* **113**, 577-586 (2003).
269 Buchmueller, K. L., Webb, A. E., Richardson, D. A. & Weeks, K. M. A collapsed non-native RNA folding state. *Nature Structural Biology* **7**, 362-366 (2000).
270 Wickiser, J. K., Cheah, M. T., Breaker, R. R. & Crothers, D. M. The kinetics of ligand binding by an adenine-sensing riboswitch. *Biochemistry* **44**, 13404-13414 (2005).
271 Cann, J. R. Theory and practice of gel electrophoresis of interacting macromolecules. *Analytical Biochemistry* **237**, 1-16 (1996).
272 Omega_Optical. Curvomatic. *http://www.omegafilters.com/Products/Curvomatic* (2010).
273 Ying, B. W., Fourmy, D. & Yoshizawa, S. Substitution of the use of radioactivity by fluorescence for biochemical studies of RNA. *RNA* **13**, 2042-2050 (2007).
274 Shanahan, C. A., Gaffney, B. L., Jones, R. A. & Strobel, S. A. Differential analog binding by two classes of c-di-GMP riboswitches. *J. Am. Chem. Soc.* **133**, 15578–15592 (2011).
275 Heppell, B., Mulhbacher, J., Penedo, J. C. & Lafontaine, D. A. Application of fluorescent measurements for characterization of riboswitch-ligand interactions. *Methods Mol. Biol.* **540**, 25-37 (2009).
276 Haller, A., Rieder, U., Aigner, M., Blanchard, S. C. & Micura, R. Conformational capture of the SAM-II riboswitch. *Nat. Chem. Biol.* **7**, 393-400 (2011).
277 Hou, C. & Herr, A. E. Ultrashort separation length homogeneous electrophoretic immunoassays using on-chip discontinuous polyacrylamide gels. *Anal. Chem.* **82**, 3343-3351 (2010).
278 Rathore, A. S. & Horváth, C. Capillary zone electrophoresis of interconverting cis-trans conformers of peptidyl-proline dipeptides: Estimation of the kinetic parameters. *Electrophoresis* **18**, 2935-2943 (1997).
279 Hayes, R. L. *et al.* Magnesium fluctuations modulate RNA dynamics in the SAM-I riboswitch. *Journal of the American Chemical Society* **134**, 12043-12053 (2012).
280 Batey, R. T., Gilbert, S. D. & Montange, R. K. Structure of a natural guanine-responsive riboswitch complexed with the metabolite hypoxanthine. *Nature* **432**, 411-415 (2004).

281 Coppins, R. L., Hall, K. B. & Groisman, E. A. The intricate world of riboswitches. *Current Opinion in Microbiology* **10**, 176 (2007).
282 Bennett, B. D. *et al.* Absolute metabolite concentrations and implied enzyme active site occupancy in Escherichia coli. *Nature Chemical Biology* **5**, 593-599 (2009).
283 Gilbert, S. D., Stoddard, C. D., Wise, S. J. & Batey, R. T. Thermodynamic and kinetic characterization of ligand binding to the purine riboswitch aptamer domain. *Journal of Molecular Biology* **359**, 754-768 (2006).
284 Perchloric Acid. *http://www-safety.deas.harvard.edu/advise/PerchloricAcid.html* (2010).
285 Sellers, K. *et al. Perchlorate: Environmental problems and solutions*. (CRC, 2006).
286 Fact Sheet - Perchloric Acid Use. *http://ehs.uky.edu/ohs/perchloric.htm* (2012).
287 Hydrogen Peroxide. *http://en.wikipedia.org/wiki/Hydrogen_peroxide#Safety* (2012).